DEPARTAMENTO DE ASTROFISICA

Universidad de La Laguna

STUDY OF THE TRANSITION PHASE BETWEEN AGB STARS AND PNE

Memoria que presenta
D. Domingo Aníbal García Hernández
para optar al grado de
Doctor en Ciencias Físicas.

INSTITUTO Ð ASTROFISICA Ð CANARIAS
enero de 2006

Examination date: 17 de Junio de 2005
Thesis supervisors: Dr. Arturo Manchado
Dr. Pedro García-Lario
©Aníbal García-Hernández 2005
Front and back pages: Design and montage from Laura Ventura (IAC). Original images of PNe from Romano Corradi (IAC) and Arturo Manchado et al. (IAC). Original image of the southern sky from Roger Smith (NOAO/AURA/NSF)
ISBN: 84-689-5913-8
Depósito legal: TF-1643/2005
Some of the material included in this document has already been published (or submitted) in Astronomy & Astrophysics and aceppted for publication in The Astrophysical Journal.

A mis padres,
a mis hermanas,
a Daniela, a Chani

Agradecimientos

En primer lugar me gustaría agradecer al Instituto de Astrofísica de Canarias el haberme dado la oportunidad de poder realizar este trabajo. También quiero agradecer especialmente a mis directores de tesis Arturo y Pedro el haberme enseñado durante estos años todo lo que se sobre las estrellas post-AGB, pero sobre todo por haberme brindado su amistad y por haberme mostrado su apoyo incondicional hacia mi persona. Sin duda habeis contribuido a que continúe en el mundo de la Astrofísica. No quiero olvidarme de todos los compañeros del IAC que de una forma u otra han contribuido a la realización de esta tesis, Jonay, Ismael, y muchísimos otros que me dejo en el tintero. Gracias a Bertrand Plez por colaborar de forma determinante en esta tesis. También quiero darle las gracias a otras estupendas personas, en especial a la Iva, y a otras que he ido conociendo durante estos años en diferentes conferencias, Fran, Letizia, Denise, Guillermo, Angels, etc. Gracias a todos.

En estos momentos me acuerdo de manera muy especial de todas aquellas personas importantes en mi vida, mis padres Sarito y Vicente, mis hermanas Diana y Moneiba, mi sobrina Daniela y sobre todo de esa pequeña oruga blanca llamada Chani y que es la niña de mis ojos, sin ti esta tesis no hubiera sido posible. También quiero agradecerle y dedicarle esta tesis a todos mis amigos. Algunos en el IAC como Marla (muchísimas gracias por ser mi amiga), El Conde, El Pirata de la Paranoia, y muchos otros. Otros de mi paso por La Laguna, El Padrino, El Vela, El Guia, etc. Gracias a todos por crear mitos, por fundar "El Club de la Fufa" y por colaborar de una forma u otra a que colgaran mi camiseta en la mítica "Herradura". Y también a todos mis amigos del "Valle" y "SanBe" (el Pipa, David Paco, El Tanga, El Papa, El Daripio (aunque eres Chicha), el Taga, El Wislow, Elfidio, El Congas, etc.. Finalmente, también me acuerdo de todos aquellos que me habeis acogido tan bien en Madrid, al Morta y al Richi por recibirme en mis primeras estancias en Madriles, al Pere por enseñarme la movida madrileña, a Mar por contagiarnos toda su fuerza y por ser una tía de “uta aa”, al pikolini por estar siempre dispuesto a “armar un pollo”, a la Pili, a Celia, Jenny, Isa, Amelia, Stefano, etc. gracias a todos por hacerme sentir como en mi casa.

Gracias, muchas gracias a todos, por hacer esto posible.

Aníbal García-Hernández

Resumen

Esta tesis trata diversos aspectos relacionados con el estudio de la todavía poco conocida fase de transición comprendida entre la rama Asintótica de Gigantes (AGB, de sus siglas en inglés Asymptotic Giant Branch) y Nebulosa Planetaria (PN, de sus siglas en inglés Planetary Nebula). Para ello, hemos analizado varios tipos de objetos en esta corta fase evolutiva, incluyendo estrellas AGB/post-AGB y proto-nebulosas planetarias (PPNe), utilizando una variedad de datos observacionales.

En primer lugar, hemos analizado datos espectroscópicos en el infrarrojo cercano de una muestra representativa de objetos de transición que cubren completamente la evolución post-AGB (la muestra incluye estrellas AGB tardías, estrellas post-AGB con diferentes tipos espectrales, así como algunas de las nebulosas planetarias más jóvenes hasta ahora conocidas). Este estudio ha estado centrado en la detección de emisión de hidrógeno molecular (H_2) en estrellas post-AGB y ha explorado las correlaciones entre la presencia y naturaleza de la emisión H_2 observada y el estado evolutivo y/o morfología de las fuentes bajo análisis.

Seguidamente, la distribución del polvo alrededor de la proto−nebulosa planetaria multipolar IRAS 16594−4656 y la jóven nebulosa planetaria elíptica IRAS 07027−7934 han sido estudiadas con la ayuda de imágenes limitadas por difracción en el infrarrojo medio (a $\sim$10 μm). Hemos interpretado la morfología observada teniendo en cuenta la espectroscopía ISO disponible. Además, hemos discutido el estado evolutivo para ambos objetos.

Para concluir este trabajo, hemos analizado una larga muestra de estrellas AGB galácticas y ricas en oxígeno utilizando espectroscopía óptica de alta resolución (R$\sim$40,000–50,000) con la intención de estudiar sus abundancias de litio y/o posible enriquecimiento en elementos de procesos de tipo-s. Se ha estudiado la muestra completa en función de diversas propiedades observacionales, como su posición en el diagrama color-color IRAS ([12]−[25] *vs* [25]−[60]), distribución galáctica, velocidad de expansión (derivada de la emisión maser de OH) y período de variabilidad. Seguidamente, hemos realizado un análisis químico que combina modelos hidrostáticos clásicos de atmósferas para estrellas frías y espectroscopía sintética con extensas listas de líneas. A partir de este análisis químico hemos derivado las abundancias de litio y zirconio (tomado como representativo del enriquecimiento en procesos de tipo-s) y discutido los resultados obtenidos en el marco de los modelos teóricos de HBB (de sus siglas en inglés Hot Bottom Burning) y nucleosíntesis que predicen una segregación química en la fase AGB en función de la masa inicial de la estrella progenitora. También hemos realizado una comparación de nuestros resultados con estudios similares llevados a cabo en las Nubes de Magallanes. Las discrepancias observadas han sido explicadas como una consecuencia de la diferente metalicidad. Finalmente, hemos comparado los resultados obtenidos con los datos disponibles en la literatura para estrellas post-AGB y nebulosas planetarias en la Galaxia.

Abstract

This thesis addresses several topics in the study of the still poorly-known transition phase between the AGB ('Asymptotic Giant Branch') and the Planetary Nebula (PN) stage. In order to better understand this short evolutionary phase, we analysed various types of objects in this phase, including AGB/post-AGB stars and proto-planetary nebulae (PPNe), using a variety of observational data.

First, we analysed near-infrared spectroscopic data in a representative sample of transition objects which cover the entire post-AGB evolution. The sample includes late-AGB stars, post-AGB stars with different spectral types, as well as some of the youngest known PNe. This study has been centered on the detection of H_2 emission in post-AGB stars and has explored the correlations between the presence and the nature of the H_2 emission observed and the evolutionary stage and/or morphology of the sources under analysis.

Second, the distribution of the dust around the multipolar proto-PN IRAS 16594−4656 and the young elliptical planetary nebula IRAS 07027−7934 was studied with the help of diffraction-limited mid-IR images (at $\sim$10 μm). We interpreted the observed morphology based on the available ISO spectroscopy. In addition, we discussed the evolutionary status of both objects.

Finally, we analysed a large sample of galactic O-rich AGB stars using high resolution optical spectroscopy (R$\sim$40,000-50,000) in order to study their lithium abundances and/or possible s-process element enrichment. The complete sample was studied taking into account certain observational properties such as their position in the IRAS two colour-diagram ([12]−[25] *vs* [25]−[60]), galactic distribution, expansion velocity (derived from the OH maser emision), and period of variability. We then performed a chemical analysis by combining classical hidrostatic model atmospheres for cool stars and synthetic spectroscopy with extensive line lists. From this chemical analysis, we derived the lithium and zirconium (taken as representative for the s-process enrichment) abundances and discussed the results obtained in the framework of "Hot Bottom Burning" (HBB) and nucleosynthesis models, which predict a chemical segregation in the AGB phase as a function of the initial mass of the progenitor star. A comparison of our results with similar studies carried out in the Magellanic Clouds is also included. The discrepancies observed are explained as a consequence of different metallicities. We also compared the results obtained with the data available in the literature for galactic post-AGB stars and PNe.

Contents

1

Introduction

1.1 Stellar evolution of low- to intermediate-mass stars

Low- to intermediate-mass stars ($0.8 \leq \mathrm{M} \leq 8~\mathrm{M}_\odot$) constitute the great majority (> 90%) of the stars in the Universe. After the exhaustion of hydrogen and helium in their cores, these stars evolve towards the Asymptotic Giant Branch (AGB) phase in the Hertzsprung-Russell diagram (HR) following well-defined evolutionary paths and then pass through the Planetary Nebulae (PNe) stage before ending their lives as white dwarfs. The main evolutionary phases in the HR diagram are shown in Figure 1.1.

During the Main Sequence (MS) stage, low-mass stars ($\mathrm{M} \leq 2.5~\mathrm{M}_\odot$) and intermediate-mass stars ($2.5 \leq \mathrm{M} \leq 8~\mathrm{M}_\odot$) evolve differently as a consequence of the different hydrogen burning mechanisms in their cores. Low-mass stars burn hydrogen into helium through the "pp" cycle, while stars with higher masses convert hydrogen into helium by means of the "CNO" cycle.

When leaving the MS, the structure of low-mass stars ($\mathrm{M} \leq 2.5~\mathrm{M}_\odot$) consists of a core composed by helium and a degenerate gas of electrons, surrounded by a hydrogen burning envelope. The star ascends the Red Giant Branch (RGB) phase until a maximum luminosity of $\sim$2500 $\mathrm{L}_\odot$ is reached, while its core contracts. In addition, the so-called 1^{st} dredge-up takes place during the RGB phase where only hydrogen burning products are brought to the star's surface. At this point, the core is hot enough to break the degeneracy of the electron gas, and the helium burning in the core starts in an explosive way ("helium flash"). This "helium flash" marks the beginning of a new evolutionary stage called "Horizontal Branch" (HB). Later, the star develops a new core, this time

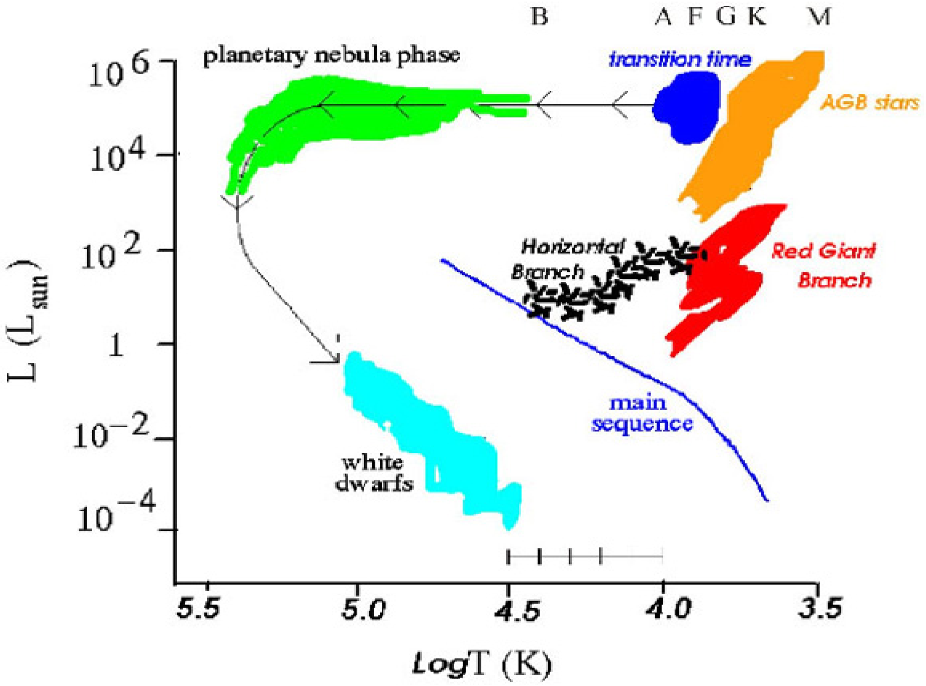

FIGURE 1.1— HR diagram displaying the main evolutionary phases in the life of low- to intermediate-mass stars.

composed of carbon and oxygen (C-O) and an electron gas, which initially is not degenerated. Eventually, the core becomes so dense that the electrons inside it attain the conditions for an electron gas to become degenerated. The star ascends now the so-called Asymptotic Giant Branch (AGB), while the C-O core contracts and the luminosity increases (up to 10^4 $L_\odot$ approximately).

In contrast, the contraction of the stellar core at the end of the MS produces higher temperatures in intermediate-mass stars ($2.5 \leq M \leq 8$ $M_\odot$). Thus, the helium ignition proceeds more gently in this case because it takes place before the degeneracy of the electron gas is reached. Therefore, these stars start their life in the HB without experiencing any "helium flash" after the exhaustion of hydrogen in their cores. They then join the AGB following the same evolutionary path as their lower mass counterparts. In contrast to low-mass stars, the so-called 2^{nd} dredge-up takes place during the early AGB (EAGB) in intermediate-mass stars.

The stellar structure in the AGB is displayed in Figure 1.2. An inert core of C-O and a degenerate gas of electrons is surrounded by two thin layers composed of helium and hydrogen which, in turn, are surrounded by an extended

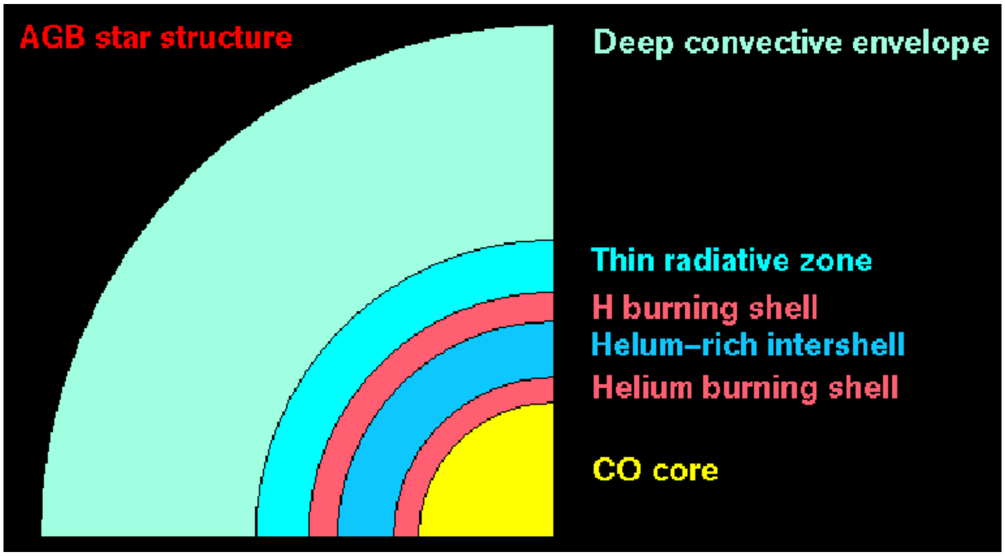

FIGURE 1.2— Sketch of the stellar structure of low- to intermediate-mass stars at the end of the AGB (adapted from Lattanzio 2003). Note that the figure is not shown at scale and the envelope in particular is much greater than the C-O core.

convective envelope of hydrogen. In addition, a stellar wind develops in the envelope of the star as it ascends the AGB. This stellar wind produces strong mass loss (10^{-6}–10^{-4} $M_{\odot} yr^{-1}$). As a consequence of the intense mass loss, the stars at the end of the AGB are in many cases highly obscured in the optical by thick dust envelopes, which often make them detectable only at infrared wavelengths. This is due to the thermal emission of the circumstellar dust present in their envelopes, which re-emits the light absorbed in the optical at IR wavelengths.

At the end of the AGB both low- and intermediate-mass stars experience a series of thermal pulses (TPs). Most of the time, the hydrogen burning shell is the main source of energy of the AGB star, but occasionally every $\sim 10^4$ yr helium ignites as a consequence of the unstable nature of the helium burning shell (Schwarzschild & Härm 1965) and results in important structural and chemical changes in the star. In between two consecutive thermal pulses ($\sim 10^4$ yr) the processed material in the hydrogen burning shell slowly increases the mass of the helium-rich intershell (interpulse phase). The new helium-rich material increases its pressure and temperature, activating the triple-α cycle in the inner helium shell. Thus, a thermal pulse is produced. In the interpulse phase, the convective envelope deepens up to the limit of the hydrogen burning shell, without an appreciable change in the stellar luminosity. The energy ex-

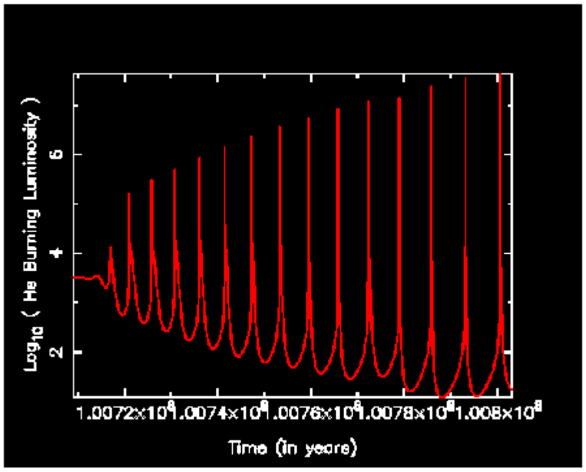

Figure 1.3— Variation of the helium burning shell luminosity during the thermal pulsing phase (TP) at the end of the AGB (adapted from Lattanzio 2003).

cess generated by the thermal pulse produces a convective transport of nuclear processed material from the hydrogen burning shell to the external layers of the stellar atmosphere while the outermost envelope expands. As a consequence, the hydrogen burning shell cools down and the nuclear helium burning is extinguished (decay of the pulse). As the temperature of the helium burning shell decreases (after-pulse stage), a new cycle begins.

During the TP phase at the end of the AGB, the star undergoes structural and thermal readjustments which change the stellar luminosity and radius after every pulse. In Figure 1.3 we show how the helium burning shell luminosity changes during the thermal pulsing phase. As a result of the penetration of the convective envelope to zones rich in nuclear-processed material, carbon, heavy elements, and s-process elements can be dredged up to the stellar surface (the so-called 3^{rd} dredge-up), altering its chemical composition. The effects of this convective envelope penetration are easily recognized through the specific chemical composition pattern which characterize AGB stars (Mowlavi 2002, 1999a).

1.2 Stellar nucleosynthesis in the AGB

When stars form, they initially display more O than C (C/O $<$ 1) reflecting the original composition of the interstellar medium (ISM), but repeated thermal pulses preferentially add C to the star's surface (the so-called 3^{rd} dredge-up). For this reason, AGB stars, originally O-rich, can turn into C-rich AGB stars (C/O $>$ 1) after a few thermal pulses. This would explain the observed spectral sequence M-MS-S-SC-C in AGB stars (Mowlavi 1999a). MS-stars have M spectral-types with C/O lower than one and small s-element overabundances ([s/Fe]$\approx$0.3) in their surfaces, S-stars display C/O ratio very close to one and higher s-element overabundances ([s/Fe] $>$ 0.5), SC-stars are C-rich stars also strongly s-element enriched but with their C/O ratio still close to $\sim$1 while C-stars are carbon-rich stars with C/O clearly larger than one . As has already been mentioned, another important characteristic of AGB stars is the presence of neutron-rich elements (s-elements) in their surface. These species are formed by slow-neutron captures (compared with the β-decay). The s-element formation results from the interaction between two consecutive thermal pulses. After a dredge-up episode, according to theoretical models, hydrogen can be partially mixed in the region between the hydrogen and helium shells, where ^{12}C- and ^{4}He-rich material exist. This region of partial mixing can arise as a consequence of semi-convection, rotation or convective "overshooting" (Mowlavi 2002; Lattanzio 2003). There, hydrogen can react with ^{12}C to form ^{13}C during the interpulse phase. ^{13}C is a good neutron source by means of the ^{13}C(α,n)^{16}O reaction. These released neutrons can be captured by iron nuclei and other heavy elements, forming s-elements which can be dredged up to the star's surface in the next thermal pulse (e.g. Straniero et al. 1995; Mowlavi 1999a; Busso et al. 2001). Another neutron source is ^{22}Ne (e.g. Straniero et al. 1995, 2000; Goriely & Mowlavi 2000), which can be formed from ^{14}N (^{14}N is formed by the CNO cycle in the hydrogen shell). From ^{22}Ne it is possible to produce other isotopes of Mg (e.g. Goriely & Mowlavi 2000), Na (e.g. Mowlavi 1999b), Al (e.g. Mowlavi & Meynet 2000), etc. ^{19}F is another element formed which is produced similarly to ^{13}C (Mowlavi et al. 2000).

In the case of the more massive O-rich AGB stars (M $>$ 4 M$_{\odot}$), the convective envelope can penetrate the H-burning shell activating the so-called "hot bottom burning" (HBB) process. HBB takes place when the temperature at the base of the convective envelope is hot enough (T $\geq 2\times10^{7}$ K) and ^{12}C can be converted into ^{13}C and ^{14}N through the CN cycle (Sackmann & Boothroyd 1992; Wood et al.1983). HBB models (Sackmann & Boothroyd 1992; D'Antona & Mazzitelli 1996; Mazzitelli, D'Antona & Ventura 1999) also predict the production of ^{7}Li by the chain ^{3}He(α,γ)^{7}Be (e^{-},v)^{7}Li, through the so-called "^{7}Be transport mechanism" (Cameron & Fowler 1971). In Figure 1.4 we display a diagram of the Cameron-Fowler beryllium transport mechanism. One of the predictions of these models is that lithium should be detectable, at least for some time, in the stellar surface together with s-elements (such as Rb, Zr, Ba,

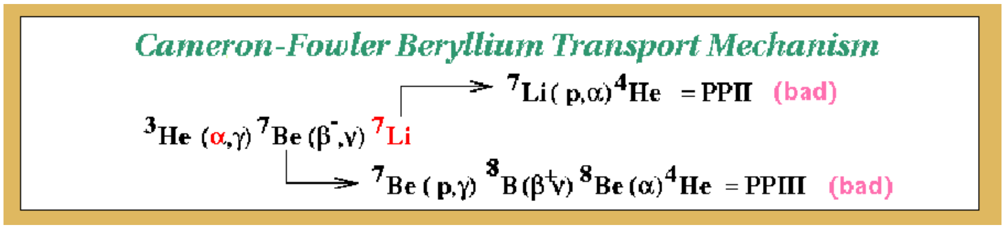

FIGURE 1.4— Diagram of the Cameron-Fowler beryllium transport mechanism (adapted from Lattanzio 2003).

Tc or Nd) which are the consequence of the neutron captures produced during the thermal pulsing phase.

The HBB activation in massive O-rich AGB stars is supported by studies on AGB stars of the Magellanic Clouds (hereafter, MCs) (Plez, Smith & Lambert 1993; Smith & Lambert 1989, 1990a; Smith et al. 1995) which show a lack of high luminosity C stars beyond the limit of $M_{bol}\sim-6$. Instead, the more luminous AGB stars in the MCs are O-rich stars. The detection of strong Li overabundances together with strong s-element enhancement in these luminous AGB stars in the LMC and in the SMC is the signature that these stars are indeed HBB AGB stars which have undergone a series of thermal pulses and dredge-up episodes in their recent past. Note that the Li abundances are much higher than those expected in the standard AGB evolution, where the lithium is destroyed and/or diluted by convection. The HBB nature of these stars is also confirmed by the detection of a very small $^{12}C/^{13}C$ ratio ($\simeq$3−4), expected only when HBB is fully active (Mazzitelli, D'Antona & Ventura 1999).

In our own Galaxy, lack of accurate information on distances has prevented the same kind of detailed analysis of optically bright AGB stars such as those in the MCs. Only a handful of Li-rich stars have been found so far (Abia et al. 1991, 1993; Boffin et al. 1993) and, unlike those detected in the MCs, they are not so luminous ($-6 \leq M_{bol} \leq -3.5$). Moreover, some of them are intermediate mass S- and SC-stars (Abia & Wallerstein 1998) and not O-rich M-type stars. Recently, research (Abia & Isern 1996, 1997, 2000) has shown that there is lithium in C-rich AGB stars with quite modest luminosities. Their galactic distribution suggests relatively low mass progenitors (1−3 $M_{\odot}$). Some of them show low $^{12}C/^{13}C$ ratios (< 30) and the presence of s-process elements. Under these conditions, however, HBB is not expected to be active and lithium production together with relatively low $^{12}C/^{13}C$ ratios is not well understood. Theoretical studies have tried to explain this phenomenon by using a non-standard mixing process known as "Cool Bottom Processing" (CBP)

(Wasserburg, Boothroyd & Sackmann 1995) or extra-mixing. Other explanations come from other scenarios such as mass transference in a binary system (Abia & Isern 2000). Some SC stars with C/O≅1 might connect the massive O-rich AGB stars (which suffer HBB) with the less massive C-rich ones (which could experience extra-mixing). There is evidence that some SC stars could represent the mass limit where HBB takes place (Bergeat et al. 2002), but a study in a more extended sample would be needed. The current HBB theoretical models have principally been tested using the results obtained from the study of the more massive AGB stars in the MCs but have never been applied to galactic sources, mainly because of the lack of observations available and of the fact that the massive AGB stars in the Galaxy could be heavily obscured by their optically thick circumstellar shells (e.g. Kastner et al. 1993; Jiménez-Esteban et al. 2005).

1.3 The transition phase AGB-PN

Stars leave the AGB when the strong mass loss (the massive wind with $\sim 10^{-4}$ – 10^{-6} M$_\odot$yr^{-1}) stops. This takes place abruptly when a minimum amount of mass (∼0.01 M$_\odot$, Blöcker 1995) is left in the envelope. At this moment, the star enters the so-called "post-AGB" stage and will no longer undergo processes such as "Hot Bottom Burning", s-element production, etc. The central star (now a post-AGB star) rapidly increases its effective temperature, reaching a value high enough to photoionize the envelope previously ejected during the AGB phase, forming a new PN. Thus, the "transition time" starts when the high mass-loss rate on the AGB terminates and it lasts until the central star reaches high enough temperatures to ionize the envelope. This "transition time" is a short-lived evolutionary stage ($\sim 10^2$–10^4 yr) and the post-AGB stars and "proto-PNe" are in this short transition phase. The mass loss determines the post-AGB evolution of the star, the internal structure, the final mass at the end of the AGB, etc. In addition, we should mention that post-AGB stars and PNe can also be divided into two separated groups (C-rich and O-rich), similar to the AGB stars, but the connection of their observed chemical composition with their precursors on the AGB is also as yet not well understood.

The main uncertainties in the evolution from the AGB to the PNe stage are associated with several factors. First, this is a short-lived evolutionary phase ($\sim 10^2$–10^4 years) and, thus, the number of transition sources in the Galaxy is small. On the other hand, many of these stars develop optically thick circumstellar shells which can completely obscure the light coming from the central star in the optical. In some cases, they are only observable in the IR domain.

FIGURE 1.5— Optical HST image of the bipolar PPN IRAS 17150−3224 (adapted from Kwok 2003).

However, this is an evolutionary stage when crucial changes occur that completely determine the subsequent evolution of the individual star as a PN. The changes affect both the morphology and the chemistry of the central star, which can later induce changes in the chemical composition of the circumstellar envelope. Eventually, this also results in changes in the overall chemical evolution of the Galaxy, since huge amounts of processed material are transferred to the interstellar medium as a consequence of the strong mass loss experienced at the very end of the AGB phase.

As we have already mentioned, the changes are also morphological. During the post-AGB phase reflection nebulosities can form prior to the ionization of the envelope. Post-AGB stars surrounded by these nebulosities are usually known as "proto-PNe" since they are thought to be the precursors of PNe. These nebulosities can display an incipient bipolar structure at a very early stage in the post-AGB phase, as has been demonstrated with HST observations for a reduced group of stars in this short evolutionary phase (Ueta et al. 2000). Subsequently, PNe with a marked bipolar structure are shaped. The formation of these bipolar structures is believed to be due to the presence of an equatorial disk/torus structure which collimates the gas flows ("outflows"), whose origin is controversial. As an example, the optical HST image of the bipolar PPN IRAS 17150−3224 is displayed in Figure 1.5.

At present, the formation of axisymmetric structures in PNe (ranging from elliptical to bipolar) is believed to occur during the post-AGB phase. But unlike in PNe, the study of these nebulosities is more difficult since the post-AGB central star (CS) is usually too cool to photoionize the gas and therefore we cannot study the formation of these axisymmetric morphologies by mapping the ionized gas. So, we must use alternative techniques based on the analysis of either the light scattered by the surrounding dust at optical wavelengths, or on the study of the neutral molecular gas in the envelope in the near-infrared (H_2), sub-millimetre (CO) or radio domain (OH), or studying the dust emission emerging at mid- to far-infrared wavelengths. The processes that lead to the different morphologies observed (Manchado et al. 2000) are not known in detail. Several models have been proposed to explain the morphologies observed in evolved PNe: the interaction of stellar winds (e.g. Mellema 1993), binary systems as central stars (e.g. Bond & Livio 1990; Morris 1987), non-radial pulsations (e.g. Soker & Harpar 1992) and the influence of magnetic fields (e.g. Pascoli 1992; Soker & Harpar 1992; García-Segura et al. 1999). To establish which one(s) of the above is the dominant mechanism, it is essential to study these morphologies as early as possible after the departure from spherical symmetry takes place, that is, in the post-AGB phase.

It is also during this short transition phase when the ionization of the gas ejected during the previous AGB phase takes place. However, it is now well established that in most cases only a small fraction of it is eventually ionized in comparison with the total amount of mass expelled by the central star during the AGB phase (tenths of a solar mass of ionized gas, compared to up to several solar masses ejected during the AGB phase in the case of the more massive progenitors) (Pottasch 1980, 1992; Kwok 1994). Most of this material remains neutral in the form of dust grains, molecules or atoms which can be detected easily at infrared or radio wavelengths even when the star has completely evolved and turned into a PN.

From the analysis of IRAS data, and especially with the advent of the higher quality ISO data, it has been possible to confirm the presence of large amounts of dust grains which emit thermally in the mid- and far-infrared in objects evolving from the AGB to the PN stage. In addition, through the analysis of the features observed in the ISO spectra, it is possible to determine the dominant molecular and solid state gas and dust chemistry (O-rich or C-rich) in the stellar photosphere and in the circumstellar envelope (Waters et al. 1999; Sylvester et al. 1999; Hrivnak et al. 2000), respectively.

The detection of molecules in the envelopes around PNe has also been successful at sub-millimetre and radio wavelengths over the last two decades. Strong CO molecular emission has been detected in a large number of C-rich PNe (Huggins & Healy 1989; Huggins et al. 1996) and is also detectable around both C-rich and O-rich post-AGB stars (Likkel et al. 1991; Loup et al. 1993; Neri et al. 1998, and references therein). Other molecules, such as HCN or CN are detected only in envelopes dominated by a C-rich chemistry (Lindqvist et al. 2000), while in the case of O-rich circumstellar envelopes, strong molecular maser emission from SiO, H_2O and OH is usually detected when the stars are still in the AGB phase (Engels 1979; Engels & Lewis 1996; Nyman et al. 1998; te Lintel Hekkert 1991; te Lintel Hekkert et al. 1991). In many cases, the OH maser emission remains detectable beyond the AGB throughout the whole post-AGB evolution (te Lintel Hekkert & Chapman 1996) and sometimes even when the object has already become an ionized PN (the so-called OHPNe, Zijlstra et al. 1989; 1991). More complex molecules are more difficult to detect, but in the circumstellar envelopes of a few objects such as IRC+10216, AFGL 618 and AFGL 2688, more than 50 different molecular species have been identified in the last few years, and the number and complexity of the new molecules found is continually increasing (Wallerstein & Knapp 1998; Bujarrabal et al. 1988; Cernicharo et al. 1999).

The presence of organic compounds with aromatic structures (the so-called PAHs) is also a common feature in the mid-IR spectra of C-rich PNe and proto-PNe (see e.g. García-Lario et al. 1999; Kwok 2003). In Figure 1.6 we display as an example the ISO spectrum of NGC 7027 which is a C-rich PN showing prominent features of PAH molecules. In contrast, strong features attributed to crystalline silicates are usually found in O-rich transition stars, sometimes also in more evolved PNe (Molster 2000). In addition, a few rare sources evolving from the AGB to the PN stage show a remarkable mixed chemistry (C-rich and O-rich) displaying both PAH and silicates features (e.g. Cohen et al. 2002) usually observed in PNe with [WC] type central stars. A strong emission at 21 μm (still of uncertain origin) observed so far only in C-rich post-AGB stars and in the young C-rich PN IC 418 (van Winckel & Reyniers 2000) has recently been identified as due to TiC clusters (Kwok 2001) although others have proposed their identification as due to SiC (Speck & Hofmeister 2003). This detection is unique to young PNe and proto-PNe and has never before been observed in the interstellar medium. The detection of these and other carbonaceous compounds in these C-rich circumstellar envelopes suggests that complex organic molecules can form in a short period of time ($\sim 10^3$ years). This process is believed to occur at the end of the AGB phase, where simple organic molecules such as acetylene (C_2H_2) formed in the AGB wind react in the envelope to produce benzene (C_6H_6) and many more other complex aromatic compounds. The post-AGB stars or proto-PNe, especially those C-rich, are thus wonderful astrophysics laboratories, very useful in the study of astromineralogy.

Since hydrogen is the main constituent of stellar atmospheres one would

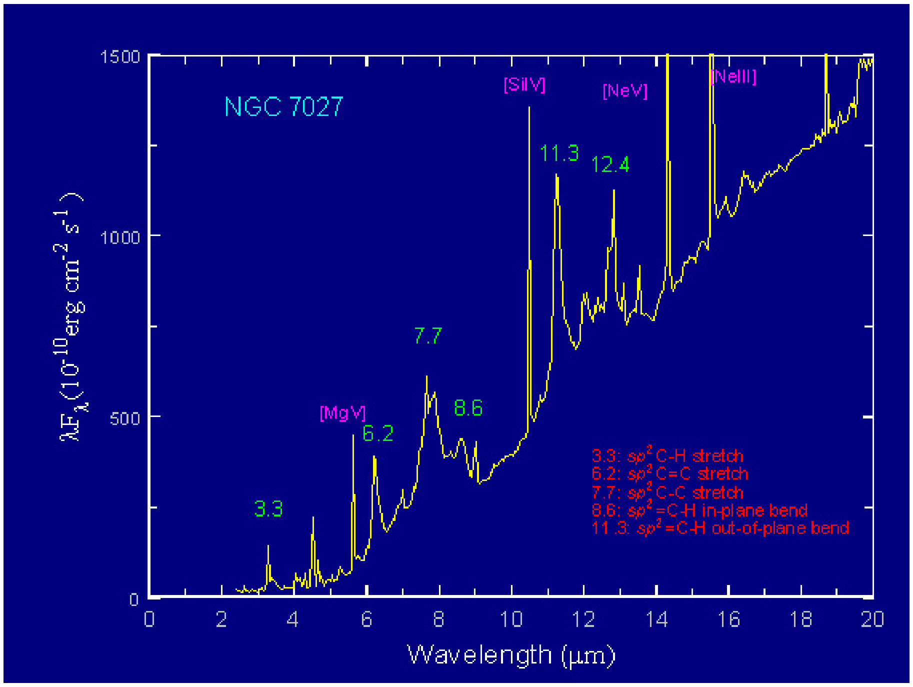

FIGURE 1.6— ISO spectrum of the C-rich PN NGC 7027 showing PAH features (marked in green) due to different stretching and bending modes (adapted from Kwok 2003).

expect to find also, at least for some time, a significant amount of neutral material locked up in the form of H_2 around transition objects between the AGB and the PN stage. Very few attempts have been made so far, however, to search for H_2 around the precursors of PNe (only 4 objects had been detected in H_2 as of 2002, see Chapter 2). The molecular hydrogen can be excited, either by fluorescence (through UV photons) or shocks (Burton 1992). In order to elucidate what excitation mechanism is responsible for the molecular hydrogen emission observed, it is very useful to compare the relative intensities of two ro-vibrational lines of H_2 (v=1→0 S(1) in 2.122 μm and v=2→1 S(1) in 2.248 μm). Fluorescence excitation can be induced by the absorption of UV photons escaping from the central star while shock excitation is the consequence of the interaction of the fast post-AGB wind with the slow wind material ejected during the AGB. A significant amount of H_2 can survive around the post-AGB stars either because the star is not hot enough to photo-dissociate this molecule or because the shielding induced by the thick equatorial disk/torus

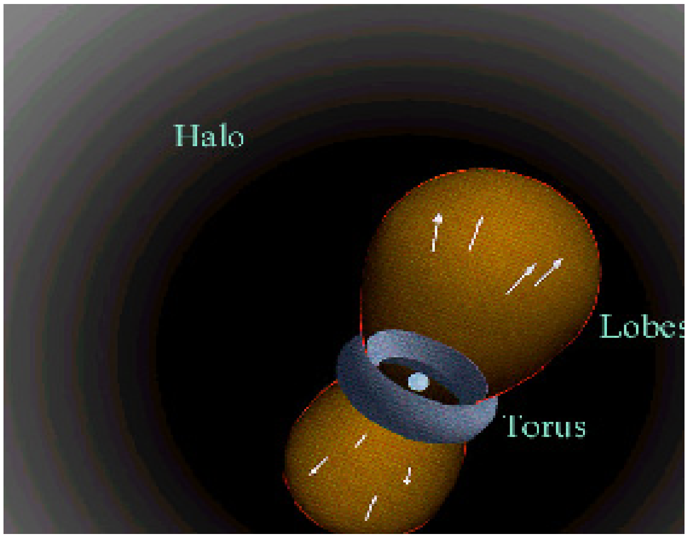

FIGURE 1.7— Illustration of the existence of thick equatorial structures (e.g. a thick equatorial torus) in PPNe (adapted from Kwok 2003).

of dense material preserves it from destruction in the case of those sources showing a bipolar morphology. Actually, it seems that the presence of this equatorial disk/torus structure is intimately related with the detection and the nature of the H_2 emission. This finding could explain why the H_2 emission is predominantly detected in type I bipolar PNe (Kastner et al. 1996). Figure 1.7 illustrates the presence of a thick equatorial torus around the central star of a PPN. Under the current theories, it is believed that the onset of the H_2 emission could take place during the post-AGB phase (Weintraub et al. 1998). Thus, the discovery and study of new transition objects showing H_2 emission at an early stage is crucial to understanding the nature of this proccess and the hydrodynamic processes shaping the PNe.

1.4 Discovery of transition objects

Stellar evolution models (Paczyński 1971; Schönberner 1979, 1981) soon showed that the central stars (CS) of PNe need a certain timescale ("transition time") in order to photoionize the circumstellar envelope previously expelled during the AGB phase and form a PN. This transition time is highly dependent on the mass of the progenitor central star and therefore, on the mass loss rate (e.g. Vassiliadis & Wood 1994).

According to the more recent interacting stellar wind (ISW) model (Kwok,

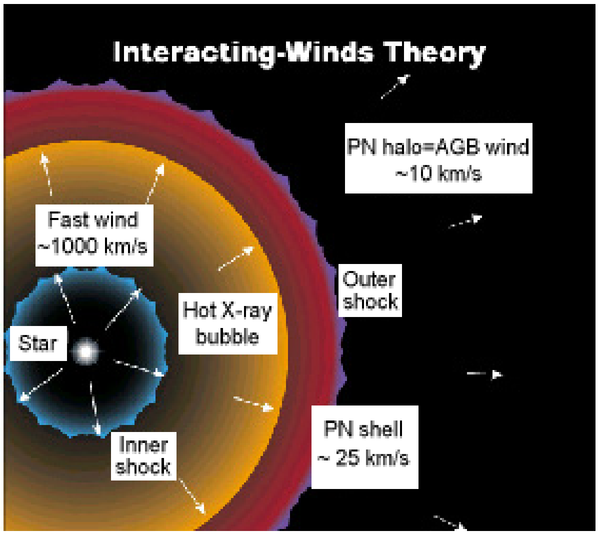

FIGURE 1.8— Qualitative sketch of the interacting stellar wind (ISW) model (adapted from Kwok 2003).

Purton & Fitzgerald 1978) PNe are the result of the interaction between a fast post-AGB wind and the remnant AGB shell. A qualitative sketch of the interacting-wind theory is displayed in Figure 1.8. Thus, the circumstellar remnant of the AGB shell should be observable during the whole transition phase and the emission of the dust present in the circumstellar envelope would make the transition objects very bright infrared sources. This fact can be used to discriminate between post-AGB candidates and ordinary stars. Only since the advent of the IRAS data has it been possible to perform systematic searches for transition objects. However, many of these searches (e.g. van der Veen, Habing & Geballe 1989; Volk & Kwok 1989) were generally biased favouring the discovery of post-AGB stars with known bright optical counterparts and ignoring those sources heavily obscured by their thick circumstellar envelopes. In the past few years, it has also been possible to discover the intrinsic axisymmetric nature of the dust shells around some PPNe (e.g. Meixner et al. 1999). The basic observational characteristics of transition objects are summarized below:

a) High luminosities ($>$ 1000$-$3000 L$_\odot$) and low gravities (luminosity classes I or Ia).

b) Intermediate effective temperatures (between 3.000 and 20.000 K) and spectral types from M to B.

c) Evidence of the remnant AGB shell (through infrared excesses or molec-

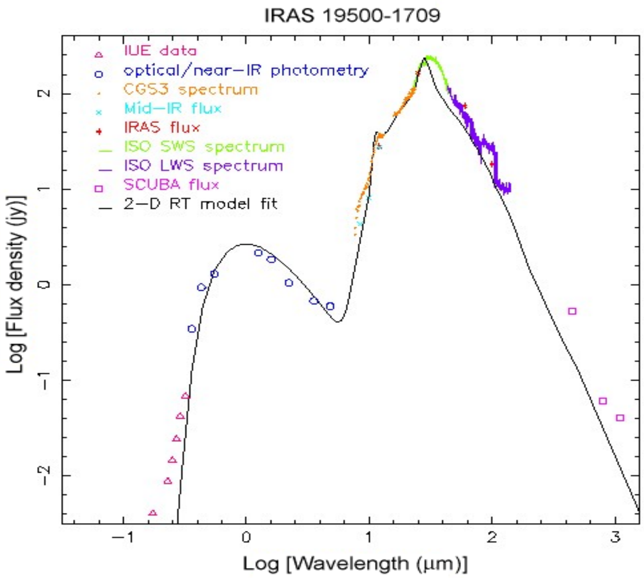

FIGURE 1.9— Example of typical double-peaked spectral energy distribution (SED) found in PPNe.

ular emission sometimes with wide velocity profiles).

d) Double-peaked[1] spectral energy distribution (SED) in many cases with evidences of a detached envelope composed by dust grains at temperatures of ∼100−200 K. An example of the typical double-peaked SED of a PPN is displayed in Figure 1.9.

e) Reflection nebulae around the central stars due to the circumstellar dust causing light to be scattered.

For the last ten years Manchado, García-Lario and collaborators have been studying a large number of IRAS sources (∼1000) with dust temperatures similar to post-AGB stars and PNe (∼100−200 K), mainly through near-infrared photometry (Manchado et al. 1989; García-Lario et al. 1990; 1997a) and optical spectroscopy (García-Lario et al. 1991; 1994; 1997b; Riera et al. 1995; Suárez 2004). As a result of this multiwavelength program, they discovered heavily obscured late AGB stars and early post-AGB stars still surrounded by

---

[1] Note that this characteristic excludes massive sources which can evolve as heavily obscured post-AGBs/PPNe all the way from the AGB to the PN stage.

thick circumstellar envelopes only detectable in the near infrared. In addition, they discovered post-AGB stars with optically bright central stars covering all possible spectral types from M to B in what it seems to be an evolutionary sequence towards the PN stage in the HR diagram (see Figure 1.1) and a small number of new extremely young PNe (García-Lario et al. 1997a; Suárez 2004), among them, the youngest PN known so far: the Stingray Nebula (Bobrowsky et al. 1998). After this study, the number of known transition objects has been duplicated. However, most of these transition objects have not yet been studied. A compilation of more than 200 transition sources discovered in a more unbiased way than previous post-AGB surveys, as well as a study of their physical properties, can be found in Suárez (2004).

1.5 Outline of this thesis

In this thesis we will address several of the still open questions in the study of this still poorly understood short transition phase between AGB and PNe, some of them already mentioned in this Introduction. To carry out this study, we will use multiwavelength observations of objects spanning a wide range of evolutionary stages covering the whole transition between AGB and PNe (AGB stars, post-AGB stars and proto-PNe).

Chapter 2 describes the search for molecular hydrogen (H_2) emission in a sample of PN precursors, including late-AGB stars, post-AGB stars with various spectral types, as well as the youngest PN known. In this Chapter we also study the correlations between the dominant excitation mechanism of the H_2 emission detected and the evolutionary stage and/or the morphology of the sources as a function of their evolution along the transition phase AGB−PN.

Chapter 3 shows the results obtained in a study of the mid-IR dust-shell structures around the multipolar proto-PN IRAS 16594−4656 and the young elliptical PN IRAS 07027−7934 using diffraction-limited mid-IR images. We complement this study with the use of the available ISO spectroscopy.

Chapters 4 and 5 present the results of a high resolution spectroscopic survey carried out in the optical for a large sample (102) of galactic O-rich AGB stars. We first characterize the sample on the basis of certain observational properties (e.g. IRAS colours, galactic distribution, etc.) and then we derive the lithium and s-process element abundances by applying state-of-the-art line-blanketed model atmospheres and spectral synthesis techniques. The interpretation of our results in the framework of current theoretical models and a comparison with the observations carried out in the past in the Magellanic Clouds and in galactic post-AGB stars and PNe are also presented.

Finally, we give a summary of the conclusions reached in this thesis in

Chapter 6 and indicate directions for future work in Chapter 7.

2

Near-IR spectroscopy of PN precursors

Most of the contents of this chapter are published in García-Hernández, D. A., Manchado, A., García-Lario, P., Domínguez-Tagle, C., Conway, G., Prada, F. 2002, A&A, 387, 955

2.1 Introduction

The short transition phase between the end of the asymptotic giant branch (AGB) and the formation of a new planetary nebula (PN) is still poorly understood. The main reason for this is probably twofold: First, only a small number of objects are known in this phase, as this is a short-lived evolutionary stage (∼10^2-10^4 years); second, in many cases, stars evolve through this phase heavily obscured by the strong circumstellar envelopes formed during the previous AGB phase, thus making observations difficult (a detailed description of the transition phase between AGB stars and PNe is presented in Section 1.3).

Since hydrogen is the fundamental component of stellar atmospheres, a significant amount of neutral material locked up in the form of molecular hydrogen is expected to be found around stars evolving from the AGB phase to the PN stage (both in O-rich and C-rich stars). Following the first detection of molecular hydrogen in the PN NGC 7027 (Treffers et al. 1976), more than 70 other PNe have been detected as H_2 emitters in the past few years by Webster et al. (1988), Zuckerman & Gatley (1988), Kastner et al. (1996), Latter et al. (1995), Hora et al. (1999) and Guerrero et al. (2000). As a general trend, it has been found that molecular hydrogen emission is predominantly detected in type I bipolar PNe, which are expected to be the result of the evolution of the more massive AGB progenitors. It remains unclear, however, whether this is just an observational selection effect.

So far very few attempts have been made to search for molecular hydrogen around post-AGB stars or proto-PNe, the precursors of PNe. Molecular hydrogen emission was first detected towards AFGL 618 by Beckwith et al. (1978) and AFGL 2688 by Gatley et al. (1988). More recently, Weintraub et al. (1998) looked at a small sample of five proto-PNe and detected molecular hydrogen emission in two of them (IRAS 17441-2411 and AFGL 6815S=IRAS 17150-3224), bringing to four the total number of bipolar proto-PNe with this type of emission. The discovery and study of new transition objects showing this emission at such an early stage is crucial for determining the mechanism of excitation of molecular hydrogen and the conditions needed to preserve this neutral material from destruction in more evolved PNe.

This Chapter extends the search for H_2 emission to a larger sample of transition objects, including late-AGB stars, post-AGB stars with various spectral types, as well as the youngest PNe known, in order to look for possible correlations between the presence/nature of molecular hydrogen emission and the evolutionary stage and/or the morphology of the sources observed.

In Section 2.2 we explain the criteria followed to select the sources in the sample. The spectroscopic observations made in the near infrared are described in Section 2.3, while the results obtained are presented in Section 2.4 and discussed in Section 2.5. The conclusions derived from these results are given in Section 2.6.

2.2 Selection of the sample

We selected a subsample of 30 stars observable from the southern hemisphere from the list of newly discovered sources in the transition phase between AGB and PNe described in Section 1.4. The subsample was taken to be representative of the various evolutionary stages mentioned above, including very late AGB stars with no optical counterpart, post-AGB stars with all kind of spectral types and proto-PNe showing a variety of morphological structures (from round/elliptical to strongly bipolar). In Figures 2.1 and 2.2 we show high resolution HST optical images for some of the objects in the sample.

In Table 2.1 we list the IRAS sources included in the study. In this Table we also indicate some of the observational characteristics which might be relevant for the discussion presented in Section 2.5, such as their apparent optical morphology (including the estimated apparent size if known, and position angle

TABLE 2.1— IRAS sources included in the survey and main observational properties. Note that the position angle of the bipolar axis (P.A.) is taken to be positive counted anti-clockwise

IRAS name	Other names	Spectral Type[1]	H_α emission[1]	Size/Morphology [P.A.]
05284+1945		OH/IR	...	No optical counterpart[1]
05341+0852		F4Iab	no	$1.1'' \times 0.8''$/Round-Elliptical[2]
06530−0213		F0I	no	$2.3'' \times 1.0''$/Bipolar[$\sim$20°][2]
06556+1623	HD 51585	B1I	yes (strong)	Unknown
07027−7934		PN (WC11)	yes (strong)	$13'' \times 15''$/Round-Elliptical[3]
07134+1005	SAO 96709	F7I	yes (weak)	$4.7'' \times 3.9''$/Round-Elliptical[2]
07331+0021	RAFGL 5236	K3-5I	yes (weak)	Unknown
08005−2356		F3I	yes (strong)	$2.6'' \times 1.2''$/Bipolar[~-45°][2]
08187−1905	HD 70379	F7I	yes (weak)	Unknown
08242−3828		OH/IR	...	No optical counterpart[1]
08425−5116		OH/IR	...	No optical counterpart[1]
09024−5019		...	...	No optical counterpart[1]
10178−5958	Hen 3−401	B1I?	yes (strong)	$2.0'' \times 14.5''$/Bipolar[$\sim$70°][4]
10197−5750	Roberts 22	A2I	yes (strong)	$7.8'' \times 4.5''$/Bipolar[$\sim$20°][5]
10215−5916	RAFGL 4106	G1I	yes (weak)	$\approx 7'' \times 7''$/Round-Elliptical[6]
11438−6330		OH/IR	...	No optical counterpart[1]
12067−4508	SAO 223245	G2w	yes (weak)	Unknown
12175−5338	SAO 239853	F2I	yes (weak)	Unknown
13421−6125		OH/IR	...	No optical counterpart[1]
14104−5819		OH/IR	...	No optical counterpart[1]
14331−6435	Hen 3−1013	B8I	yes (strong)	Unknown
16342−3814		M4	no	$2.6'' \times 0.7''$/Bipolar[$\sim$70°][2]
16594−4656		B7	yes (strong)	$5'' \times 11''$/Multipolar[$\sim$0°][7]
17119−5926	Stingray Nebula	PN (O8V)	yes (strong)	$1.6'' \times 1.4''$/Bipolar[$\sim$45°][8]
17149−3053		M4?	no	Unknown
17150−3224	RAFGL 6815S	G2I	no	$11'' \times 5''$/Bipolar[~-45°][2]
17311−4924	Hen 3−1428	B8I	yes (strong)	Unknown
17411−3154	RAFGL 5379	OH/IR	...	No optical counterpart[1]
17423−1755	Hen 3−1475	B?	yes (strong)	$3'' \times 17''$/Bipolar[~-45°][2]
18062+2410	SAO 85766	B	yes(strong)	Unknown

REFERENCES.- [1]Suárez (2004); [2]Ueta et al. (2000); [3]Zijlstra et al. (1991); [4]Sahai et al. (1999b); [5]Sahai et al. (1999a); [6]images retrieved from the HST Data Archive (Proposal 6693, PI, A. Nota); [7]Hrivnak et al. (1999); [8]Bobrowsky et al. (1998)

of the bipolar axis, if applicable), spectral type, or the presence/absence of Hα emission in their optical spectrum (all this information taken from Suárez 2004 and references therein).

2.3 Observations and data reduction

The observations were carried out in March 1993 and January 1994 with IRSPEC attached to the Nasmyth focus of the 3.5 m NTT telescope at La Silla,

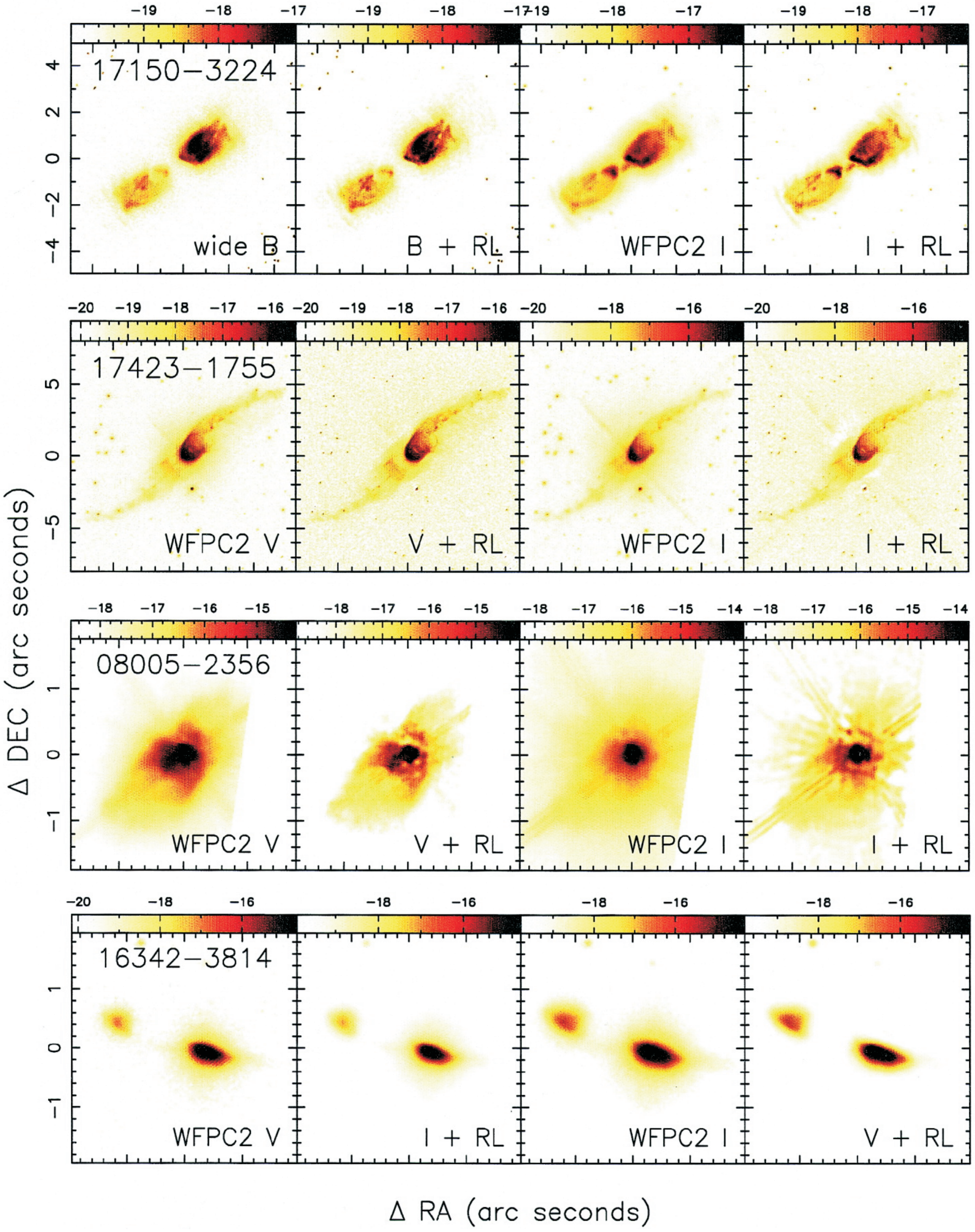

FIGURE 2.1— HST optical images of some strongly bipolar objects in the sample (adapted from Ueta et al. 2000). The leftmost frame shows the IRAS name and scale of the object. The tick marks show relative offsets in arcseconds. The filter names are shown at the bottom of each frame with "+RL" indicating Richardson-Lucy deconvolution. Wedges show the ranges of log-scaled flux density to visually illustrate the emission contrast.

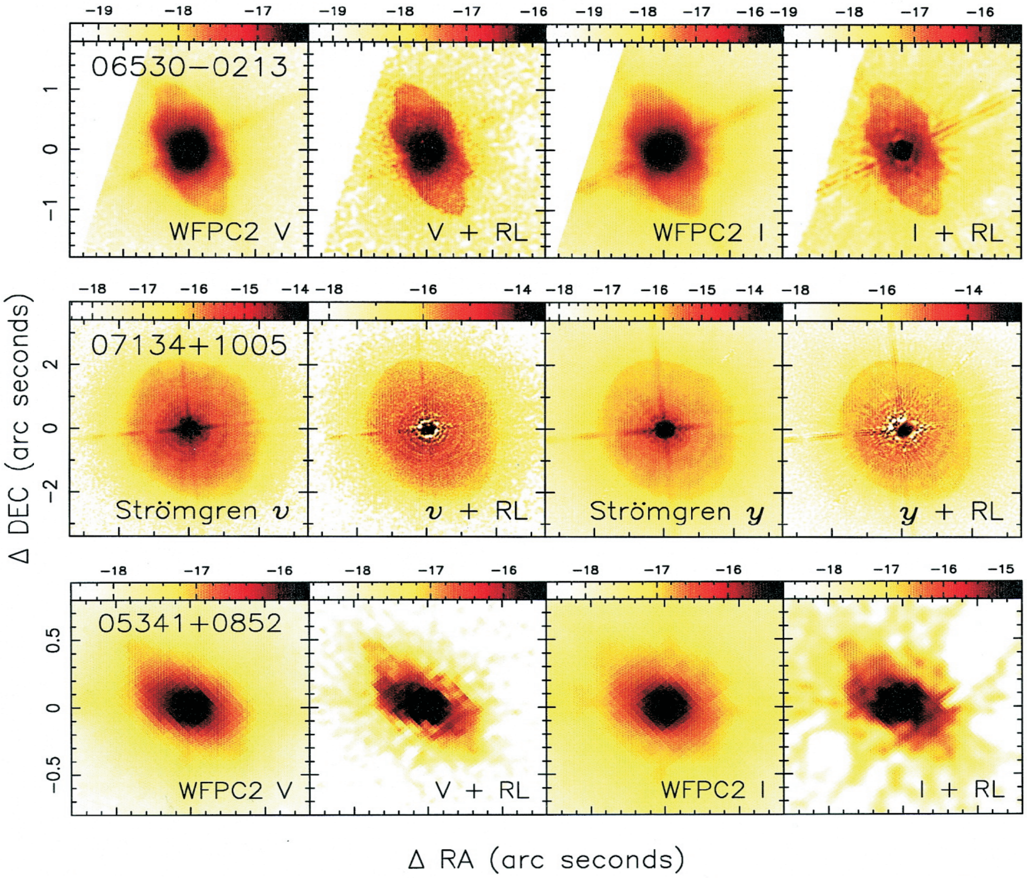

FIGURE 2.2— HST optical images of one sligthly bipolar source (at the top, IRAS 06530−0213) and some round/elliptical objects in the sample (adapted from Ueta et al. 2000). The notation is the same as in Figure 2.1.

ESO by Manchado and collaborators. IRSPEC was a cryogenically-cooled scanning grating IR spectrometer with a 58×62 pixel array from SBRC as detector (Moorwood et al. 1986). It covered the 1−5 micron wavelength range with a spectral resolution between 1500 and 2000. The spatial scale was 2.2″/pixel, the slit width was 4.5″and the unvignetted field of view was ∼100″. The array had a quantum efficiency of 0.89 at 2.85 μm, and a well capacity of 1 $10^6 e^-$. This allowed exposures up to 60 seconds per frame in the 2−2.6 μm region. For integration times around 10 seconds, the combined dark and read noise was ∼150 e^-. Owing to the poor wavelength coverage of the spectrograph in a single exposure, different exposures were needed centered at various wavelengths, each one covering a different spectral feature under analysis to reach our scientific goals. The lines observed were the molecular ro-vibrational lines of molecular hydrogen v=1→0 S(1) 2.122 μm and v=2→1 S(1) 2.248 μm, the recombination lines of hydrogen Brγ 2.166 μm, Pfγ 3.741 μm and Brα 4.052 μm, and the CO[v=2→0] 2.294 μm first overtone bandhead. Total on-source integration times were typically of 240 s with exposures ranging from 36 s to 1440 s in the most extreme cases.

The slit orientation was north-south (P.A. = 0°) in 1993 with the exception of IRAS 10178−5958 (P.A. = 70°), IRAS 16594−4656 (P.A. = 70°), IRAS 16342−3814 (P.A. = −70°) and IRAS 17423−1755 (P.A. = 55°), while in 1994 the slit orientation was always east-west (P.A. = 90°). The changes in the slit orientation during the 1993 run were in principle made in order to follow the bipolar axis of some well known extended objects, such as the ones listed above[1]. The only other known extended bipolar objects in our sample are IRAS 10197−5750 and IRAS 17150−3224. IRAS 10197−5750 was only observed in 1994, when the orientation of the slit was fixed at 90°, while the bipolar axis of this source is located at P.A. ∼ 20°. This means that the slit was positioned very close to the direction perpendicular to its bipolar axis. In the case of IRAS 17150−3224, we observed the source both in 1993 and 1994 with orientations of 0° and 90° respectively, while the actual bipolar axis of the source is now known to be very close P.A ∼ −45°. Two other sources (IRAS 10178−5958 and IRAS 16594−4656) were also observed twice. The implications of these misadjustments in the analysis of the results obtained will be discussed later. In Table 2.2 we show the log of the observations including relevant information such as the total integration time on source and the position angle of the slit for each spectral line observed.

The standard beam−switching technique was used in order to subtract the sky background. The data reduction process includes bias and flat-field correction, as well as wavelength calibration, sky subtraction, and absolute flux calibration using reference standard stars. For this we used the S/W package IRSPEC installed on MIDAS (November 1998 version). Standard tasks in IRAF[2] were also used to calculate the emission line fluxes, equivalent widths or 2σ upper limits to the expected emission line fluxes in the spectra obtained.

---

[1] However, due to a mistake in the determination of the sign, IRAS 17423−1755 was observed almost perpendicular to the actual bipolar axis in 1993.

[2] The Image Reduction and Analysis Facility software package (IRAF) is distributed by the National Optical Astronomy Observatories, which is operated by the Association of Universities for Research in Astronomy, Inc., under cooperative agreement with the National Science Foundation.

TABLE 2.2— Log of the observations: The first column gives the object name. Columns 2 to 7 give the total integration time on source (in seconds) for every spectral range observed. In column 8 we indicate the corresponding run (1993 or 1994) when the observations were made and in column 9 the position angle (in degrees) of the slit, counted anti-clockwise

IRAS name	$H_2[v=1\rightarrow0]$	Brγ	$H_2[v=2\rightarrow1]$	CO$[v=2\rightarrow0]$	Pfγ	Brα	Run	P.A.
05341+0852	240	240	...	240	...	...	1993	0
07134+1005	240	240	...	...	...	...	1993	0
08005−2356	360	240	...	360	144	96	1993	0
10178−5958*	240	240	...	480	240	192	1993	70
10215−5916	40	60	...	...	...	192	1993	0
16342−3814	240	360	...	...	...	48	1993	−70
16594−4656*	240	480	...	240	48	48	1993	70
17119−5926*	240	240	...	240	96	96	1993	0
17149−3053	240	240	...	...	...	...	1993	0
17150−3224*	240	480	...	240	...	...	1993	0
17311−4924*	240	240	...	240	72	48	1993	0
17411−3154	600	120	...	...	...	...	1993	0
17423−1755	240	360	...	240	36	48	1993	55
18062+2410	240	120	...	240	96	48	1993	0
05284+1945	...	480	...	...	...	...	1994	90
06530−0213	720	240	...	...	...	120	1994	90
06556+1623	1440	240	600	240	120	...	1994	90
07027−7934	600	240	720	720	600	360	1994	90
07331+0021	120	120	...	...	...	54	1994	90
08187−1905	240	240	...	...	...	120	1994	90
08242−3828	240	40	...	...	...	120	1994	90
08425−5116	240	240	...	240	...	720	1994	90
09024−5019	240	240	...	240	600	120	1994	90
10178−5958*	1440	480	960	...	...	...	1994	90
10197−5750	360	360	480	240	700	120	1994	90
11438−6330	240	...	...	...	120	120	1994	90
12067−4508	240	240	...	...	...	120	1994	90
12175−5338	360	240	...	240	...	120	1994	90
13421−6125	240	240	...	...	...	120	1994	90
14104−5819	240	240	...	...	...	120	1994	90
14331−6435	240	240	480	...	...	120	1994	90
16594−4656*	240	...	720	...	...	...	1994	90
17119−5926*	...	...	480	...	...	...	1994	90
17150−3224*	240	...	480	...	...	...	1994	90
17311−4924*	...	...	480	...	...	...	1994	90

Note.- ...: not observed; $*$: objects observed in both runs

2.4 Results

In Table 2.3 we list the detections/non-detections made in the different lines under analysis as a result of the observations described in Section 2.3.

TABLE 2.3— Summary table with the results obtained. Quoted values are the emission line fluxes or 2σ upper limits to the expected emission line fluxes (in units of 10^{-14} erg cm^{-2} s^{-1}). The equivalent widths (in units of Angstroms) are shown in brackets for the features detected in absorption

IRAS name	$H_2[v{=}1\rightarrow0]$		Brγ		$H_2[v{=}2\rightarrow1]$		CO[$v{=}2\rightarrow0$]		Pfγ		Brα	
05284+1945	…		n.d.	$\leq$1.3	…		…		…		…	
05341+0852	c	$\leq$0.7	A	[2.2]	…		c	$\leq$1.4	…		…	
06530−0213	c	$\leq$1.0	A	[2.1]	…		…		…		n.d.	$\leq$38.9
06556+1623	E	3.4	E	63.2	c	$\leq$2.0	c	$\leq$4.1	E	13.0	…	
07027−7934	E	2.4	E	13.4	c	$\leq$1.9	c	$\leq$4.0	E	16.4	E	62.5
07134+1005	c	$\leq$8.0	A	[3.5]	…		…		…		…	
07331+0021	c	$\leq$39.4	c	$\leq$49.4	…		…		…		c	$\leq$97.4
08005−2356	c	$\leq$9.0	c	$\leq$13.0	…		E	24.8	c	$\leq$47.5	c	$\leq$21.0
08187−1905	c	$\leq$4.2	A	[2.4]	…		…		…		c	$\leq$38.5
08242−3828	c	$\leq$30.0	c	$\leq$21.4	…		…		…		c	$\leq$32.2
08425−5116	c	$\leq$0.5	c	$\leq$0.5	…		A	[4.7]	…		c	$\leq$17.3
09024−5019	c	$\leq$0.4	E	18.8	…		c	$\leq$0.3	E	12.2	E	86.0
10178−5958	E	37.5,36.6*	E	26.7,23.3*	E	1.4	E	2.9	E	9.3	E	78.4
10197−5750	E	8.9	E	22.3	c	$\leq$3.4	c	$\leq$7.1	E	5.6	E	46.7
10215−5916	c	$\leq$203.7	c	$\leq$198.3	…		…		…		E	49.1
11438−6330	c	$\leq$0.4	…		…		…		c	$\leq$27.5	c	$\leq$55.5
12067−4508	c	$\leq$3.0	c	$\leq$4.9	…		…		…		c	$\leq$15.9
12175−5338	c	$\leq$1.4	A	[2.7]	…		c	$\leq$3.6	…		n.d.	$\leq$18.1
13421−6125	c	$\leq$0.4	c	$\leq$0.3	…		…		…		n.d.	$\leq$18.1
14104−5819	c	$\leq$1.8	c	$\leq$1.2	…		…		…		n.d.	$\leq$17.8
14331−6435	E	10.1	E	3.4	E	1.2	…		…		n.d.	$\leq$27.2
16342−3814	c	$\leq$5.1	c	$\leq$4.8	…		…		…		n.d.	$\leq$15.4
16594−4656	E	62.9,62.5*	E	9.2	E	1.9	c	$\leq$2.5	c	$\leq$15.3	E	13.3
17119−5926	E	4.1	E	43.7	E	2.7	c	$\leq$0.4	E	9.7	E	125.5
17149−3053	c	$\leq$3.2	c	$\leq$3.8	…		…		…		…	
17150−3224	E	6.7,4.2*	A	[3.1]	c	$\leq$0.7	c	$\leq$0.9	…		…	
17311−4924	E	36.3	E	2.0	E	3.2	c	$\leq$1.3	n.d.	$\leq$8.9	n.d.	$\leq$14.1
17411−3154	c	$\leq$0.4	c	$\leq$0.4	…		…		…		…	
17423−1755	c	$\leq$3.7	E	26.2	…		E	31.7	c	$\leq$27.0	E	38.1
18062+2410	E	3.0	E	0.8	…		c	$\leq$0.5	c	$\leq$14.2	n.d.	$\leq$26.7

Note.- E: emission; A: absorption; c: continuum; n.d.: not detected; …: not tried; *: line flux with 1993 slit orientation

All sources but one in the sample were observed in the wavelength region surrounding the $H_2[v{=}1\rightarrow0$ S(1)] line, resulting in positive detections in 10 cases (∼33%). All of them but one were also observed in the weaker $H_2[v{=}2\rightarrow1$ S(1)] transition, among which 5 showed some emission in this line also.

The Brγ line was detected in 17 objects, either in emission (11) or in absorption (6). In a few cases, observations were also performed in other spectral lines such as Pfγ, and Brα, or around the CO[$v{=}2\rightarrow0$] first overtone bandhead, in order to obtain complementary information.

The quantitative results are also shown in Table 2.3. Quoted values are the emission line fluxes derived by fitting gaussians to the observed line profiles or 2σ upper limits to the expected emission line fluxes in the case of those sources with no emission detected over the underlying near infrared continuum. Both are shown in units of 10^{-14} erg cm^{-2} s^{-1}. We have also estimated the equivalent widths of those features detected in absorption (in units of Angstroms). In this case the values obtained are shown in brackets in Table 2.3.

For a few sources, we did not detect any significant signal in the two-dimensional spectra (nor even a continuum) at some wavelengths. These sources have been classified in Table 2.3 as "not detected. In these latter cases we can generally infer the object's position on the two-dimensional frames based on information obtained at other spectral lines and then estimate the associated *rms* of the pixels where the feature investigated should have been detected. We used this *rms* to calculate the values quoted as 2σ upper limits to the expected emission line fluxes in Table 2.3.

We estimate that for a typical 240 s total on-target exposure and when the underlying near infrared continuum is weak, our 2σ detection threshold is of the order of $\sim 10^{-15}$ erg cm^{-2} s^{-1} for the $H_2[v{=}1{\rightarrow}0$ S(1)], Br$_\gamma$, $H_2[v{=}2{\rightarrow}1$ S(1)] and CO[$v{=}2{\rightarrow}0$] lines and of $\sim 10^{-14}$ erg cm^{-2} s^{-1} in the Pfγ and Brα regions. Note that the 2σ upper limits in Table 2.3 are very different from source to source because the rms depends on the strength of the continuum.

Three objects (IRAS 10178−5958, IRAS 16594−4656 and IRAS 17150−3224) were observed in both runs (1993 and 1994) and for them we quote in Table 2.3 the value of the integrated line fluxes for each run. The flux differences from epoch to epoch are less than 20% in IRAS 10178−5958 and IRAS 16594−4656 while in IRAS 17150−3224 is higher (probably indicating a flux loss in 1993 due to the wrong slit orientation). The emission detected was always found to be consistent with a point-like nature of the observed sources in spite of their apparent extended morphology, with the exception of IRAS 10178−5958 and IRAS 17119−5926, where the emission found is clearly resolved (see Subsection 2.5.5).

Spectra for all objects (except for IRAS 05284+1945, whose near infrared counterpart was not detected at any wavelength) in Brγ, $H_2[v{=}1{\rightarrow}0$ S(1)], $H_2[v{=}2{\rightarrow}1$ S(1)], CO[$v{=}2{\rightarrow}0$], Pfγ and Brα are presented in Figures 2.3 to 2.8. For the sources that were observed twice we show the best spectrum.

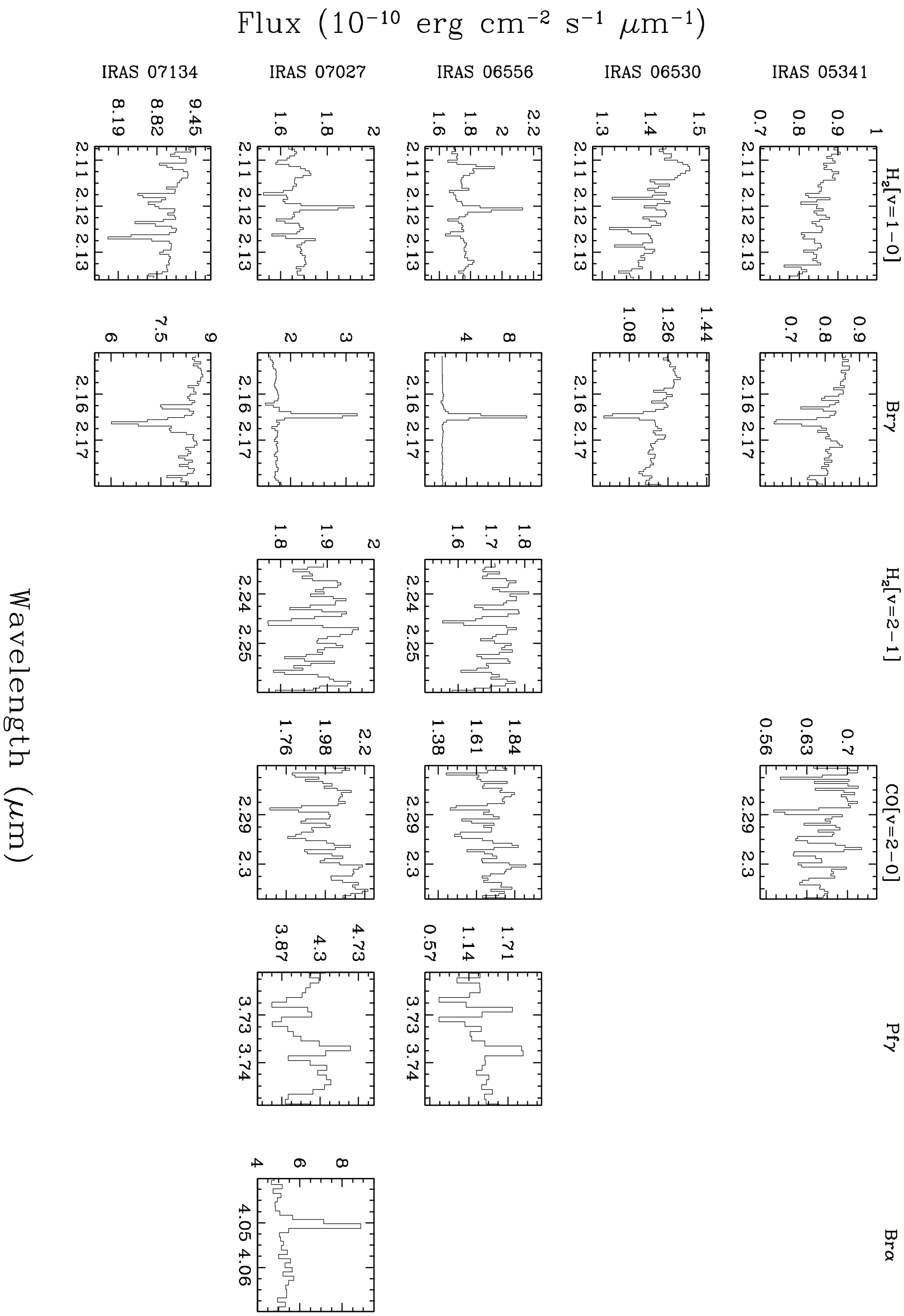

Figure 2.3— Near infrared spectra of the sources detected with IRSPEC. Each column corresponds to observations of an individual source at different wavelengths. The object name is shown at the top.

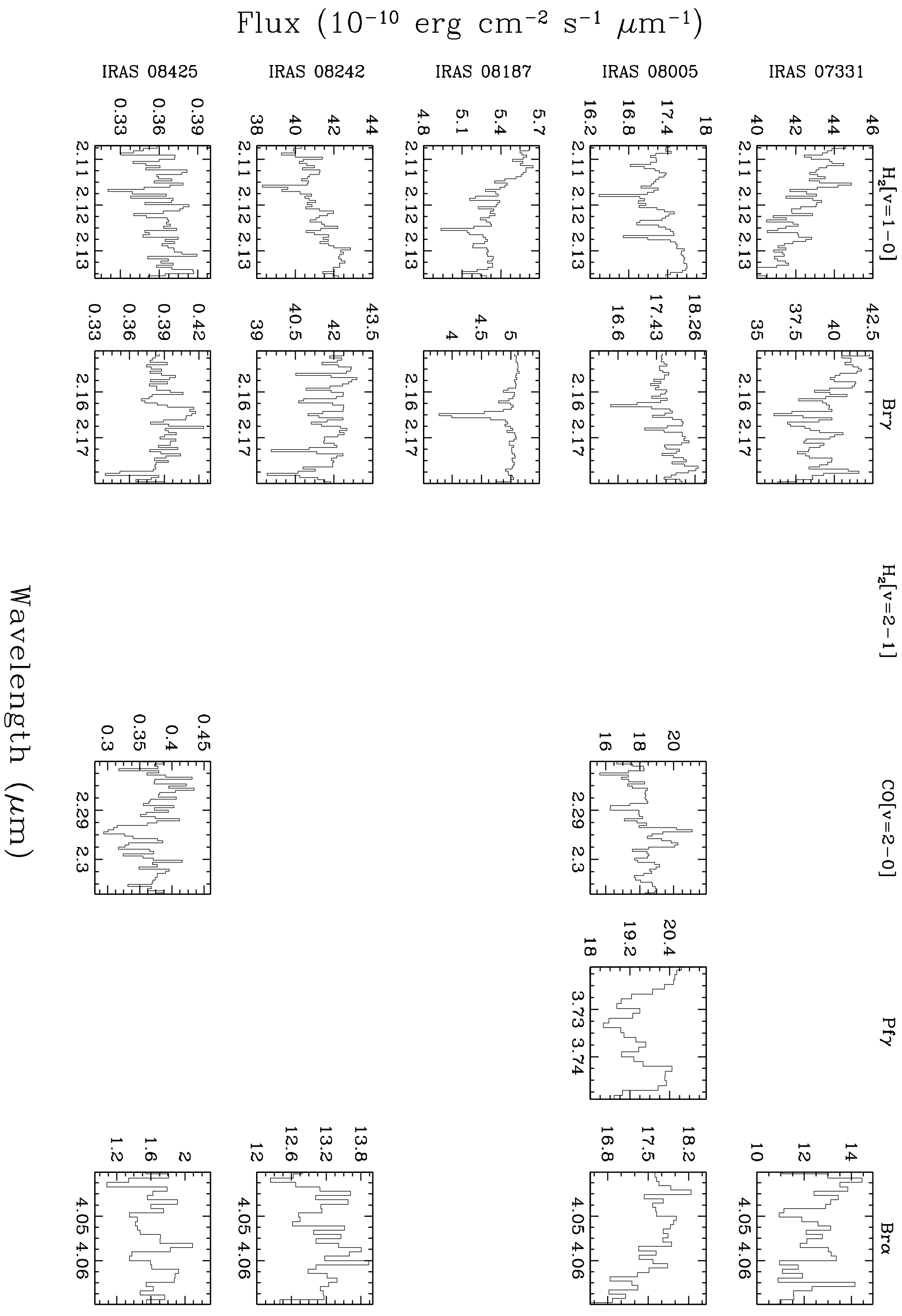

FIGURE 2.4— Near infrared spectra of the sources detected with IRSPEC (cont.).

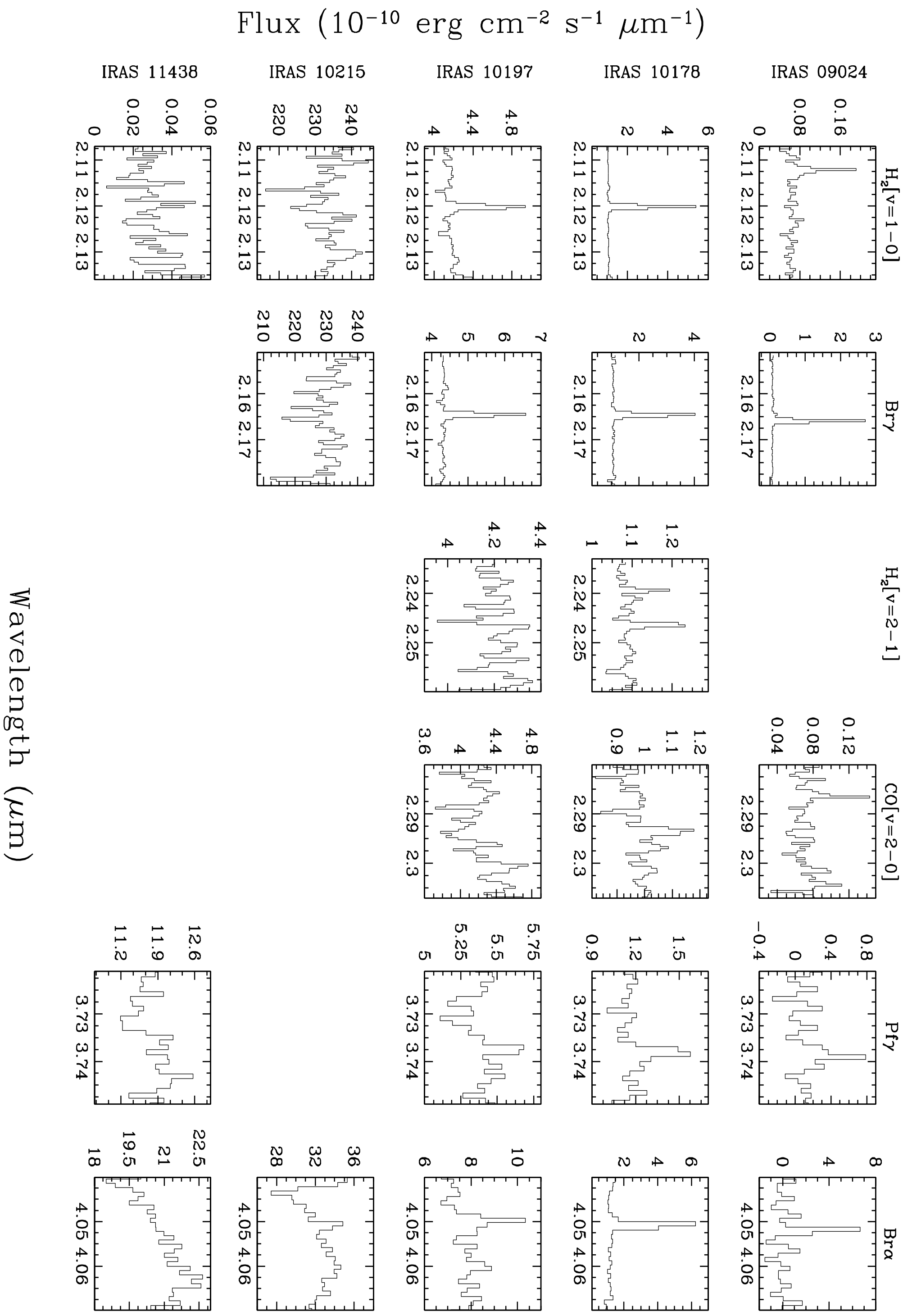

Figure 2.5— Near infrared spectra of the sources detected with IRSPEC (cont.).

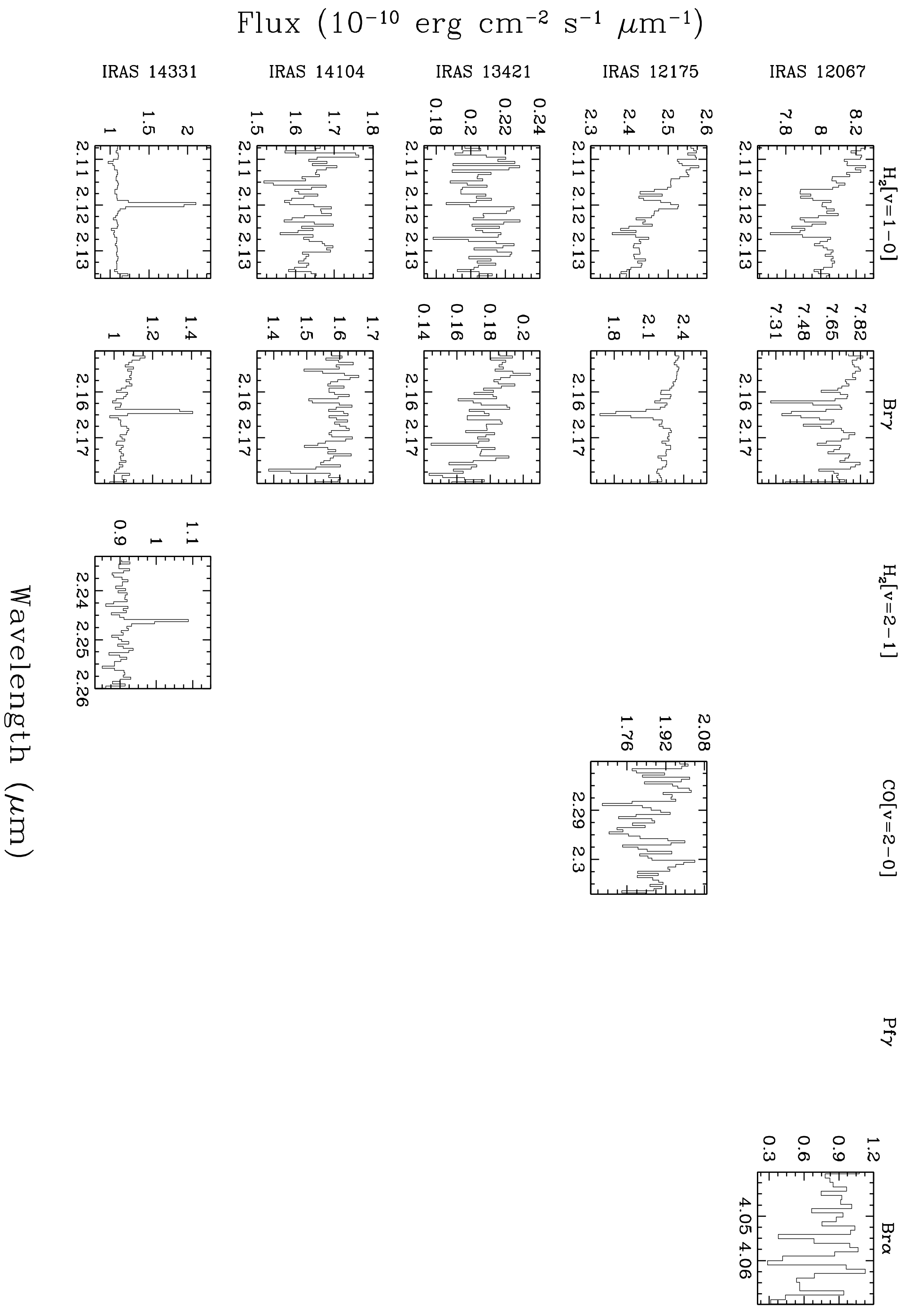

FIGURE 2.6— Near infrared spectra of the sources detected with IRSPEC (cont.).

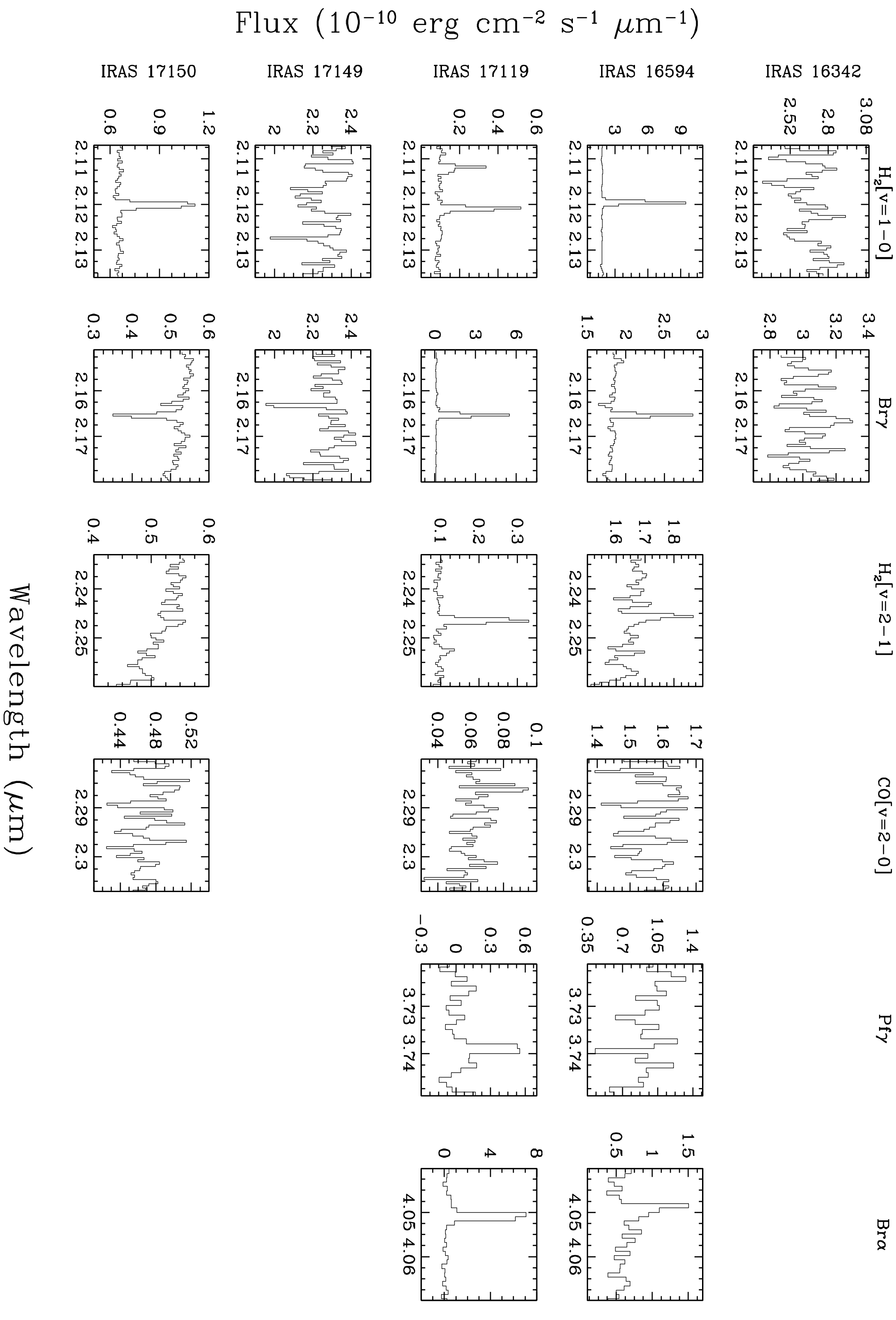

FIGURE 2.7— Near infrared spectra of the sources detected with IRSPEC (cont.).

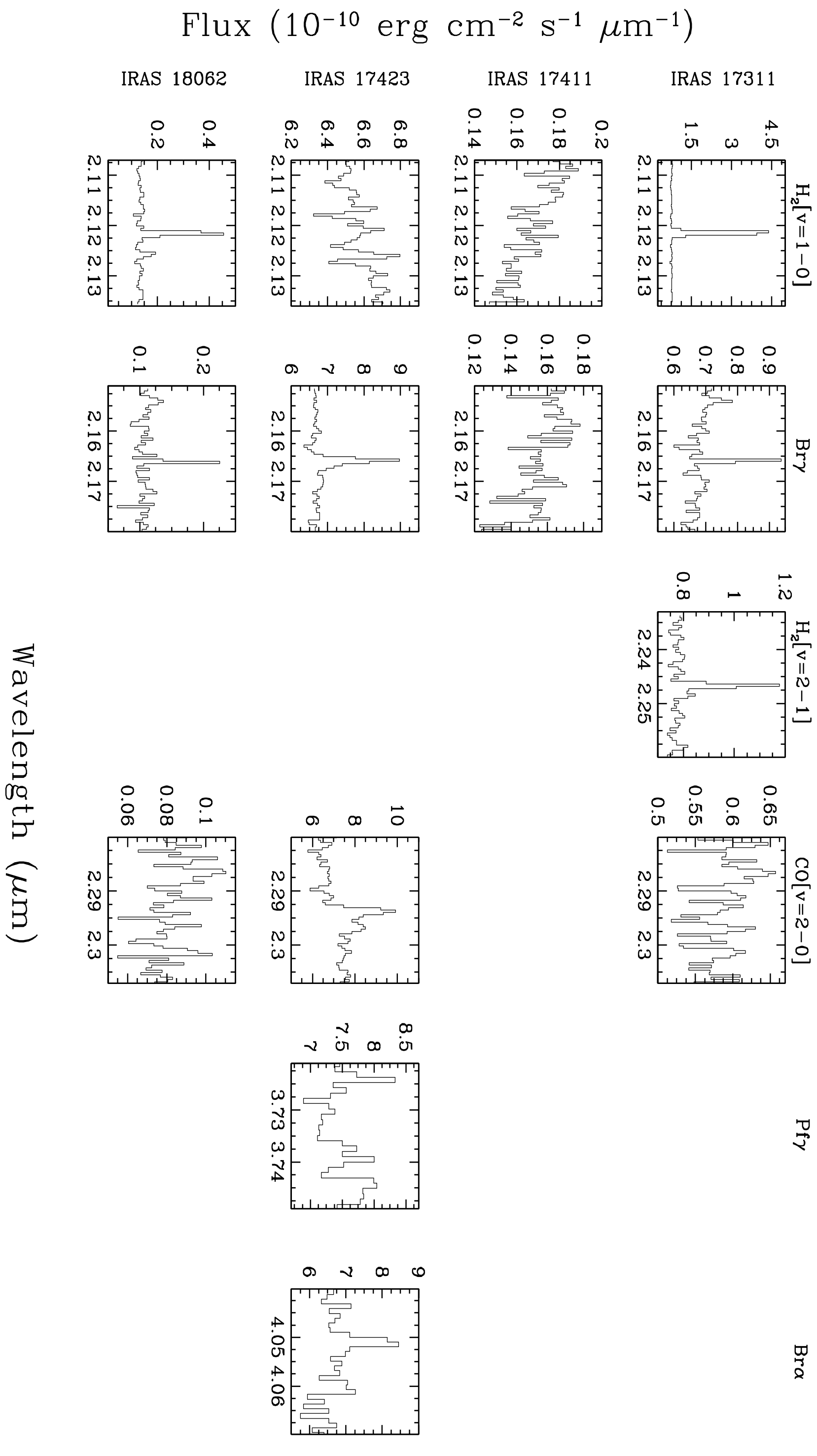

FIGURE 2.8— Near infrared spectra of the sources detected with IRSPEC (cont.).

2.5 Discussion

2.5.1 Hydrogen recombination lines

In general, the strength of the near infrared hydrogen lines detected in the stars of the sample is consistent with the spectral types derived from optical data. All objects where a Brγ absorption was detected show also Hα in absorption in the optical or very weak emission, while those with Brγ strongly in emission in the near infrared are also strong Hα emitters in the optical, as expected.

In the case of the late AGB stars included in the study (those classified as OH/IR stars in Table 2.1) the Brγ line region is veiled by the strong dust continuum emission. These are late type, pulsating stars with very long periods, so heavily obscured by their circumstellar envelopes that they usually do not show any optical counterpart. As such, they are not expected to show any signature of hydrogen recombination lines, in any case.

The same veiling effect might be the reason why IRAS 08005$-$2356 shows a featureless continuum around the Brγ line as well as at other near infrared hydrogen recombination lines, while in the optical a relatively strong Hα emission is detected. Another possibility is that the emission is just strong enough to fill in the photospheric absorption and, thus, both components compensate each other, leading to a flat continuum.

IRAS 09024$-$5019 seems to be also a remarkable case, since it shows a clear emission in the light of Brγ and Brα while it does not have any (known) optical counterpart. This star could be a heavily obscured transition object in which the onset of the ionization is now taking place.

2.5.2 CO first overtone

The effective temperature of late AGB stars is expected to be very low ($\leq$2500 K). Consistent with this, a strong CO photospheric absorption was detected in IRAS 08425$-$5116 at 2.29 μm, the only late AGB star included in the sample for which we were able to obtain a meaningful spectrum at this wavelength.

This feature corresponds to the CO first overtone bandhead, which is expected to be visible in stars with effective temperatures below 5000 K. However, IRAS 17150$-$3224, a post-AGB star with a cool central star (G2I), did not show any signature of this bandhead, probably because of the veiling produced by the strong thermal emission from the hot dust formed in the circumstellar envelope, which completely dominates the observed spectral energy distribution at this wavelength.

Notably, in three of the post-AGB stars with the earlier spectral types in the sample we detected the CO first overtone bandhead in emission. This has previously been observed in a few other transition objects (Oudmaijer et al.

1995) and it has been interpreted as the result of active post-AGB mass loss, the CO lines being formed in the dense outflow.

2.5.3 H_2 emission and evolutionary stage

In order to understand the mechanism of excitation of molecular hydrogen it may help to try to find a possible correlation between the frequency of positive detections and the evolutionary stage (spectral type of the central star) of the sources observed.

Starting from the less evolved objects, we find that none of the late-AGB stars included in the sample show any indication of the presence of H_2 emission at 2.122 μm. However, it is important to note that, as for the hydrogen recombination lines discussed above, the spectral region around this molecular hydrogen line usually appears completely dominated by the thermal emission coming from the hot dust in the envelope, making the detection of any spectral feature difficult in these kinds of objects.

More interesting is the fact that, with the only exception of IRAS 17150−322 4, which will be discussed below, none of the post-AGB stars in the sample with spectral types later than A showed any detectable emission in this line. This includes 6 F-type, 2 G-type, 1 K-type and 1 M-type post-AGB stars. It should be noticed that in these optically-bright post-AGB stars the veiling effect from the circumstellar dust is slight and cannot justify the non-detections.

In contrast, all the stars identified as post-AGB candidates in the list with spectral types earlier than A were detected in molecular hydrogen at 2.122 μm. In this case, the only exception was IRAS 17423−1755, whose central star has tentatively been classified as A-type or B-type and it shows no evidence of H_2 emission at 2.122 μm. If this emission comes mainly from the bipolar lobes, it may not have been covered by the slit because it was mistakenly positioned perpendicular to the bipolar axis (see Section 2.3). Consistently, we did not detect any extended emission from this object in any other spectral line (nor even in Brγ which is very strongly detected in emission). In addition, this is also a quite peculiar, extended bipolar proto-PN which shows a very high velocity outflow and a strong near infrared excess (Riera et al. 1995; García-Lario et al. 1997a). Thus, the H_2 emission may be veiled by the strong underlying continuum and/or the molecular hydrogen molecules may have been destroyed by the strong stellar wind[3].

Out of the 10 objects in which we detected molecular hydrogen emission, 9 are new detections (only IRAS 17150−3224 was previously reported by Wein-

---

[3] Davis et al. (2005) have very recently detected H_2 emission in the north-western outflow lobe confirming our first suggestion.

traub et al. 1998). This brings the total number of transition stars in which molecular hydrogen emission has been detected from four to thirteen[4].

The results above are consistent with the non-detection of molecular hydrogen emission in the bipolar proto-PNe OH 231.8+4.2, IRAS 07131−0147 or IRAS 09371+1212 by Weintraub et al. (1998), all of which have late-type M central stars.

However, IRAS 17150−3224 is not the only post-AGB star with a spectral type later than A showing H_2 emission in the short list of known H_2 emitters. There is another discrepant case in the literature, the well-known PPN CRL 2688 (Sahai et al. 1998), whose central star is classified as F5Iae, although it is suspected to be a binary.

2.5.4 H_2 emission and morphology

It has been suggested that molecular hydrogen emission is a signpost for bipolarity in evolved PNe (Kastner et al. 1996). In order to explore the validity of this statement in the precursors of PNe as well, we can investigate whether a correlation exists between the detection rate of molecular hydrogen emission and the morphology of the sources included in the sample. In order to do this, we will restrict the analysis to those sources for which morphological information exists. Naturally this means that we will not consider any of the heavily obscured objects in the list which do not show any optical counterpart (all of the late-AGB stars plus IRAS 09024−5019), nor will we study the objects classified as of unknown size/morphology in Table 2.1. Note that this class of objects may actually contain a mixture of round/elliptical and bipolar sources, as deduced from recent observations of similar objects made with HST, even though they might look like point sources in ground-based CCD images (see some examples in Figures 2.1 and 2.2).

The remaining sources in the sample were classified as round/elliptical or bipolar depending on the morphological properties derived from ground-based or HST observations (see again Table 2.1).

If we concentrate our attention now on the ten sources showing H_2 emission in the sample, we can see that morphological information is available for six of them, out of which five are classified as bipolar in Table 2.1, while only one is considered to be round/elliptical.

However, among the bipolar objects in the sample (eight in total), there are three of them which were not detected in H_2. This argues against the idea of a one-to-one correlation between H_2 emission and bipolarity.

---

[4] Note that the H_2 emission in IRAS 10178−5958 was previously presented by our research group in García-Lario, Riera & Manchado (1999).

In summary, the main conclusion is that although there seems to be an association between bipolarity and the presence of H_2 emission, the correlation is not so strong as previously reported by Kastner et al. (1996), who derived this conclusion from the observations of well-evolved PNe.

2.5.5 The excitation mechanism of H_2

Molecular hydrogen can be excited either in shocks or by fluorescence (Burton 1992). In order to investigate which of these two possible mechanisms is responsible for the bulk of the emission observed in the objects included in the sample it is useful to compare the relative strength of the $H_2[v{=}1{\rightarrow}0\ S(1)]$ and $H_2[v{=}2{\rightarrow}1\ S(1)]$ lines. From the analysis of this diagnostic ratio it is possible to determine whether the excitation is produced by shocks (Burton, Hollenbach & Tielens 1992) or by fluorescence through the absorption of UV photons coming from the central star (Black & van Dishoeck 1987; Sternberg & Dalgarno 1989). For moderate UV radiation fields and gas densities lower than 10^5 cm^{-3}, shock−excited emission is expected to be associated to flux ratios $H_2[v{=}1{\rightarrow}0\ S(1)/v{=}2{\rightarrow}1\ S(1)] \sim 10$ while in the case of emission induced by fluorescence a value of ~ 2 (Aspin et al. 1993; Ramsay 1993; Burton et al. 1998) is predicted. In Table 2.4 we show the ratios derived for 9 out of the 10 post-AGB stars in the sample detected in molecular hydrogen for which data is available. The estimated uncertainty is $\sim$20%. For those objects in which the $H_2[v{=}2{\rightarrow}1\ S(1)]$ line was not detected lower limits are given.

As we can see in Table 2.4 a wide range of values is obtained. If the above-mentioned models are applied to the stars in the list we deduce that shock−excited H_2 emission must be the dominant excitation mechanism in at least three of the objects in the sample with a clearly marked bipolar morphology: IRAS 10178−5958 (possibly B-type central star), IRAS 16594−4656 (B-type central star) and IRAS 17150−3224 (G-type central star) as well as in two other objects of unknown morphology: IRAS 14331−6435 and IRAS 17311−4924 (both with B-type central stars), while fluorescence excitation seems to be the prevalent excitation mechanism in the Stingray Nebula (IRAS 17119−5926), which is a very young PN showing an incipient bipolar morphology. For the remaining objects the lower limits found are too ambiguous to support either fluorescence or shock excitation.

From the results obtained, there seems to be a prevalence of shocked-excitation in those objects showing the most extreme bipolar morphologies. However, the results are not conclusive since the statistics are very poor. There is also no evident connection between the excitation mechanism derived from the analysis of the $H_2[v{=}1{\rightarrow}0\ S(1)/v{=}2{\rightarrow}1\ S(1)]$ ratio and the spectral type

TABLE 2.4— Flux ratios observed in the sources showing molecular hydrogen emission and prevalent excitation mechanism tentatively inferred from the data

Object	$H_2[v{=}1\rightarrow0]^1$	$H_2[v{=}1\rightarrow0/v{=}2\rightarrow1]$	$H_2[v{=}1\rightarrow0]/\mathrm{Br}\gamma$	Excitation
IRAS 06556+1623	3.4	>1.7	0.05	Fluorescence
IRAS 07027−7934	2.4	>1.3	0.18	Fluorescence
IRAS 10197−5750	8.9	>2.6	0.40	Fluorescence**
IRAS 17119−5926	4.1	1.5	0.09	Fluorescence
IRAS 10178−5958	37.5	27	1.40*	Shock
IRAS 14331−6435	10.1	8.4	2.97	Shock
IRAS 16594−4656	62.9	33	6.84	Shock
IRAS 17150−3224	6.7	>9.6	…[2]	Shock
IRAS 17311−4924	36.3	11.3	18.2	Shock
IRAS 18062+2410	3.0	…[3]	3.75	Shock?

Notes.- [1]: Emission line flux in units of 10^{-14} erg cm^{-2} s^{-1}. [2]: Brγ detected in absorption. [3]: Not observed in the $H_2[v{=}2\rightarrow1]$ line. *: The $H_2[v{=}1\rightarrow0]/\mathrm{Br}\gamma$ is equal to 1.57 in 1993 observations. **: Shock-excited emission can be present in the outer lobes as deduced from recent HST images but they were not covered by our slit.

of the central star in which molecular hydrogen has been detected. However, in this latter analysis we must be careful since it is well known that episodic mass loss during the post-AGB phase can induce significant spectral changes which may alter for some time the observable spectral type and, thus, taking the spectral type as an indicator of the evolutionary stage might be not the best choice (Bobrowsky et al. 1998; Suárez 2004).

In addition, an important caveat needs to be considered when interpreting the data in Table 2.4. This is the fact that the models mentioned above lose their validity at very high densities ($n_e > 10^5$ cm^{-3}) and we know that some of the post-AGB stars and transition objects under study could be surrounded by regions of these very high densities. In this case, collisional de-excitation of fluorescence excited levels (“collisional fluorescence) might take on importance, increasing the v=0 and 1 populations over the pure fluorescent values, leading to higher $H_2[v{=}1\rightarrow0\ S(1)/v{=}2\rightarrow1\ S(1)]$ ratios (Sternberg & Dalgarno 1989; Burton et al. 1990) which could mimic shock-excitation.

In order to address the problem from a different point of view, it is also useful to study the detailed spatial distribution of the molecular hydrogen emission and compare this, whenever possible, with the spatial distribution observed in the light of Brγ.

The $H_2[v{=}\ 1\rightarrow0\ S(1)]/\mathrm{Br}\gamma$ ratio has recently been found to be correlated both with the evolutionary stage and the degree of bipolarity in a sample of well-known bipolar PNe (Guerrero et al. 2000). Bipolar PNe with small size, poorly defined rings and bright central stars exhibit small $H_2[v{=}1\rightarrow0\ S(1)]/\mathrm{Br}\gamma$

ratios ($\sim$ 0.1$-$0.5) while those with large, well defined rings and faint central stars showed larger $H_2[v{=}1{\rightarrow}0$ S(1)]/Brγ ratios (>5).

Guerrero et al. (2000) suggest that the excitation of the molecular hydrogen in each of these groups turns from fluorescence excitation at the early stages of PNe to shocked-excited emission as the bipolar PNe evolve. This is supported by the different spatial distribution of the observed molecular hydrogen emission.

H_2-dominated bipolar PNe are found to show different morphological and physical properties. Their central regions have low surface brightness, in agreement with their low densities while Brγ-dominated bipolar PNe have a high surface brightness and larger densities.

If this effect is interpreted as an evolutionary sequence (Balick 1987) then the less evolved bipolar PNe with molecular hydrogen emission would start their evolution as Brγ dominated later becoming H_2-dominated.

Note, however, that this scenario does not apply to all PNe. Well-evolved, low-mass density-bounded round/elliptical PNe are not expected to preserve hydrogen in the form of molecules since most (if not all) of the hydrogen in the circumstellar envelope becomes ionized as the ionization front passes through the gas. These PNe will end their lives as Brγ-dominated, unlike the group of PNe with more massive progenitors. Those with more massive progenitors are expected to develop ionization-bounded nebulae, where a substantial fraction of the mass ejected will never become ionized. This enables the detection of neutral material in the circumstellar gas even at a very late stage as PNe, provided the UV radiation field from the central star is hard enough to produce fluorescence excitation. In the subgroup of bipolar PNe, the shielding provided by the dense equatorial regions that collimate the outflow from the UV photons escaping from the central star would also favour the preservation of hydrogen in molecular state. This would explain the high detection rate of molecular hydrogen emission in bipolar type I PNe, which are suspected to be the result of the evolution of stars with large progenitor masses. In this latter case, molecular hydrogen can also be excited by shocks formed in the high velocity outflow.

Applying the above considerations to the analysis of the molecular hydrogen emission observed in precursors of PNe it would be natural to expect fluorescence to be activated when the radiation coming from the central post-AGB star becomes hard enough to produce a significant number of UV photons as the central star moves in the HR diagram towards hotter effective temperatures on its way to becoming a PN. On the other hand, the interaction of the fast post-AGB wind with the slow-moving material ejected during the previous AGB phase would favour the formation of shocks, specially in those objects showing a strong collimation induced by the presence of a thick equatorial disk or torus, in the process of developing a bipolar morphology.

In order to check whether this scenario is consistent with the data obtained for the stars in the sample, we have derived the $H_2[v{=}1{\rightarrow}0\ S(1)]/Br\gamma$ ratios for the objects that exhibit H_2 emission. The results obtained are presented in Table 2.4, where we can see that, as for the $H_2[v{=}1{\rightarrow}0\ S(1)/v{=}2{\rightarrow}1\ S(1)]$ ratio, a wide range of values is found (the quoted values, not corrected for extinction, again have an estimated uncertainty of ∼20%).

Only four sources (out of ten) are found to be Brγ-dominated. These are: IRAS 06556+1623, IRAS 07027−7934, IRAS 10197−5750 and IRAS 17119−5926. Detailed morphological information exists for the latter three sources. IRAS 07027−7934 is known to be a very young PN showing a round/elliptical shape (see Chapter 3). The bipolar morphology is only incipient in IRAS 17119−5926 which otherwise would look also quite round/elliptical. The only source in this short list with a marked bipolar morphology is IRAS 10197−5750 (Sahai et al. 1999a), which is seen almost edge-on. This source has recently been imaged with HST (NICMOS) in the light of $H_2[v{=}1{\rightarrow}0\ S(1)]$ (Sahai et al. 2000) and the spatial distribution of the emission in this line has been found to be very similar to the distribution of scattered light in the bright lobes, suggesting that fluorescence excitation is the main mechanism contributing to the overall observed emission. However, a clear enhancement of emission is observed at two localized point-symmetric regions distant from the central star which unfortunately have not been covered by the slit (the slit orientation was 90° and its bipolar axis is orientated $\sim +20°$), which we interpret as shock-excited emission probably originated by the interaction of the high velocity post-AGB wind with the slow moving old AGB shell. Interestingly, the four Brγ-dominated sources show $H_2[v{=}1{\rightarrow}0\ S(1)/v{=}2{\rightarrow}1\ S(1)]$ ratios compatible with fluorescence excitation (see Table 2.4).

Three other sources in the list have also been imaged in the light of $H_2[v{=}1{\rightarrow}0\ S(1)]$ with HST (NICMOS). These are IRAS 16594−4656 (see Chapter 3), IRAS 10178−5958 (Sahai et al. 2000) and IRAS 17150−3224 (Su et al. 2000) belonging to the group of H_2-dominated sources in the sample.

In all cases, the spatial distribution of the molecular hydrogen emission suggests a shock-excited origin. In the multipolar PPN IRAS 16594−4656 the H_2 emission is mainly localized in one of the bipolar lobes, although four additional clumps of H_2 emission are also observed at the end of another two bipolar lobes (Hrivnak, Kelly & Su 2004−see Chapter 3). In IRAS 10178−5958, the molecular hydrogen emission comes mainly from the walls of the bipolar lobes (García-Lario, Riera & Manchado 1999), while in IRAS 17150−3224 the bulk of the detected emission arises in an expanding molecular torus surrounding the central star (Weintraub et al. 1998), although several clumps of molecular hydrogen emission are also detected in the outer regions of the bipolar lobes according to Su et al. (2000). A similar spatial distribution was also found by Sahai et al. (1998) in the case of AFGL 2688, where the emission observed was also interpreted as due to shock excitation.

Unfortunately, none of the three other H_2-dominated sources in Table 2.4 have been imaged in molecular hydrogen with HST. All of them (namely IRAS 14331−6435, IRAS 17311−4924 and IRAS 18062+2419) are sources not spatially resolved from ground-based observatories. All of them show large H_2 [v=1 →0 S(1)/v=2→1 S(1)] ratios which are consistent with shock excitation[5].

The emission seems to be extended only in the case of IRAS 10178−5958 and IRAS 17119−5926 but we did not find any spatial dependence of the measured H_2[v=1→0 S(1)/v=2→1 S(1)] ratios along the nebulae. This confirms shock excitation as the prevalent mechanism of excitation for the molecular hydrogen in IRAS 10178−5958 throughout its whole nebular extension. On the other hand, fluorescence excitation seems to be the mechanism through which molecular hydrogen gets excited in the case of IRAS 17119−5926. For IRAS 17119−5926, two-dimensional spectra of both H_2 lines were taken with different (perpendicular) slit orientations in 1993 and 1994. Remarkably, the molecular hydrogen emission seems to be quite homogeneous independent of the slit orientation considered and extends well beyond the limits of the Brγ emission. This suggests that most of the emitting molecular hydrogen is located outside the small ionized region of this very young PN, in the still neutral outer shell. In Figure 2.9 we display the H_2[v=1→0 S(1)] 2D spectra for both sources.

In summary, when the integrated emission detected in each line is considered, we systematically find either high H_2[v=1→0 S(1)/v=2→1 S(1)] and H_2[v=1→0 S(1)]/Brγ ratios which are consistent with the prevalence of shock excitation, or low ratios which indicate fluorescence as the dominant mechanism for the observed H_2 emission. And this is supported by the different spatial distribution seen in those objects with existing H_2 NICMOS images.

In general, considering the data obtained on our small sample and the rest of available data we find different type of sources that exhibit H_2 emission during the post-AGB phase.

1) The H_2 emission that comes from bipolar sources with later than A spectral types (e.g. AFGL 2688 and IRAS 17150−3224) must be essentially shock-excited because the central post-AGB star is still not hot enough to produce fluorescence emission. The presence of shock-excited emission early in

---

[5] In the case of IRAS 18062+2419, Kelly et al. (2004) suggested a contribution from both excitation mechanisms to the observed H_2 emission.

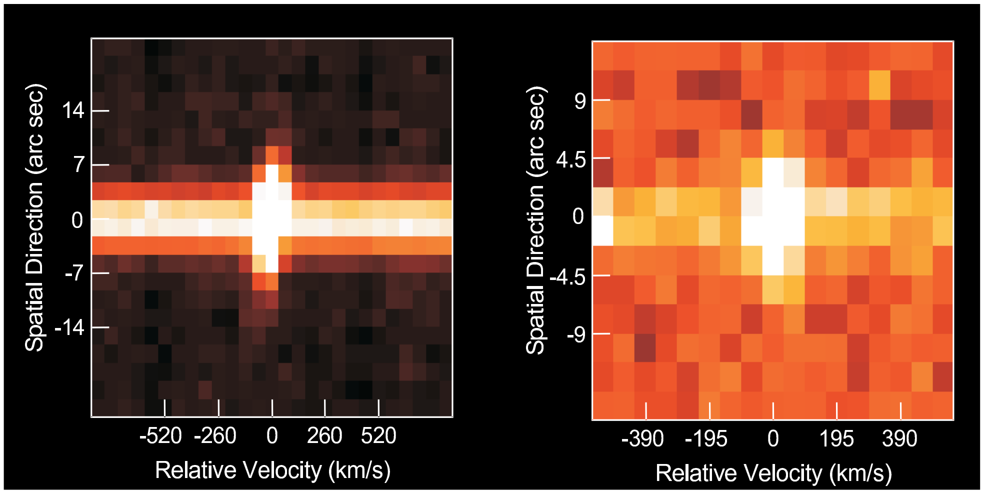

FIGURE 2.9— H_2 [v=1→0 S(1)] 2D spectra for IRAS 10178-5958 (left) and IRAS 17119-5926 (right). The scales are approximated. The spatial scale y-axis is oriented along: P.A.=70° for IRAS 10178−5958 and P.A.=0° for IRAS 17119−5926.

the post-AGB phase must be indicative of an advanced evolutionary stage of the nebulosity that surrounds the central post-AGB star from the morphological point of view. However, it remains unclear if the early development of such marked bipolar morphologies during the post-AGB phase could be a signature of the high mass of the central progenitor star.

2) The fluorescence-excited H_2 emission is mainly detected in non-bipolar sources. In addition, the detection of H_2 emission towards many well-evolved bipolar PNe could be indicative that the destruction of neutral material around the non-bipolar ones (e.g. IRAS 07027−7934 or even IRAS 17119−3224) is more efficient and can roughly coincide with the photoionization of the circumstellar shell. This could indicate that the fluorescence-excited H_2 emission detected in non-bipolar sources is observed only during a short period of time in the post-AGB phase. Later, H_2 would be destroyed unless the morphology is bipolar. Where the wind is strongly collimated by the presence of an optically thick equatorial disc or torus, the molecular material can be shielded from the ionizing photons coming from the central star.

3) In strongly bipolar sources with early spectral types, there must be a contribution from the two excitation mechanisms in the observed emission (e.g. IRAS 10197−5750). It is very difficult to distinguish the contribution of both excitation mechanisms but it seems clear that the shocked H_2 emission must be more intense than the fluorescence-excited emission in many cases, leading

to high $H_2[v{=}1{\rightarrow}0\ S(1)/v{=}2{\rightarrow}1\ S(1)]$ and $H_2[v{=}1{\rightarrow}0\ S(1)]/Br\gamma$ ratios.

This entire hypothesis deserves further study to understand better the physical and chemical processes acting during the short transition phase from the AGB phase to the PN stage. At present, the number of known transition objects is continually growing, as is the amount of high quality data. A detailed spatially resolved spectroscopic analysis of the H_2 emission line spectra in a large sample of planetary nebula precursors would be needed in order to reach a definitive conclusion.

2.6 Conclusions

With the data presented here we have extended the number of post-AGB stars and/or proto-PNe where molecular hydrogen emission has been detected from four to thirteen.

The results confirm the previous finding by Weintraub et al. (1998) made on a smaller sample of sources that the onset of emission from molecular hydrogen takes place during the post-AGB phase. In many cases this occurs well after the generation of the bipolar structure takes place and before the nebular envelope becomes ionized.

In the past it has been suggested that molecular hydrogen emission is a signpost for bipolarity in PNe (Kastner et al. 1996). We find that the detection of molecular hydrogen strongly depends on the excitation mechanism.

The detection of fluorescence-excited molecular hydrogen emission in precursors of PNe is strongly correlated with the evolutionary stage of the central star (spectral type), independent of the morphology of the source considered. The fluorescence excitation of molecular hydrogen emission is produced as a consequence of the absorption of the increasing number of UV photons escaping from the relatively hot, rapidly evolving central post-AGB star by the hydrogen molecules present in the circumstellar shell. As a general trend, we find that fluorescent H_2 emission becomes active when the central post-AGB star reaches a certain temperature that corresponds to an A-spectral type.

On the other hand, shock-excited emission is only detected in objects with a marked bipolar morphology, sometimes at a very early stage during the post-AGB phase, when the star is still very cool. This can be localized along the waist and/or in specific regions of the bipolar lobes (either at the walls, as in IRAS 10178−5958, or at the tips, as in IRAS 10197−5750), where a physical interaction exists between fast- and slow-moving material.

Bipolarity also helps preserve the molecular hydrogen from destruction, favouring its detection in well-evolved bipolar PNe. With very few exceptions, the brightest H_2 emission, shock-excited, is actually detected toward the waist of bipolar PNe (Kastner et al. 1996). The high correlation found between bipolarity and molecular hydrogen emission seems to be just the consequence of the bias induced by this fact.

The diagnostic ratios $H_2[v{=}1{\rightarrow}0\ S(1)/v{=}2{\rightarrow}1\ S(1)]$ and $H_2[v{=}1{\rightarrow}0\ S(1)]$/Br γ are shown to be very good indicators of the prevalent mechanism of excitation in proto-PNe. Unfortunately, the information on the relative spatial distribution of the different molecular hydrogen lines with respect to the hydrogen recombination lines is still sparse. Without this information we cannot determine the precise localization of shock-excited and fluorescence-excited regions on individual sources. As we have shown through this work, this is a strong limitation if we want to understand the physical processes which are taking place in this still poorly known transition phase which precedes the formation of PNe. This is specially important for interpreting the emission observed in complex objects like IRAS 10197−5750, where both fluorescence- and shock-excited regions may coexist. High spatial resolution images (e.g. with NICMOS on board HST) in the three emission lines mentioned above for a statistically significant number of transition objects and young PNe will provide this crucial information. This would be an ideal way to test the scenario proposed here.

3

Revealing the mid-infrared emission structure of IRAS 16594-4656 and IRAS 07027-7934

Most of the contents of this chapter have been accepted for publication in ApJ García-Hernández, D. A., Manchado, A., García-Lario, P., Acosta-Pulido, J. A., Benítez-Cañete, A., Pérez-García, A. M. (astro-ph/0512064)

3.1 Introduction

As already mentioned in Chapter 1, Planetary nebulae (PNe) are the result of the evolution of low- to intermediate-mass stars (0.8–8 $M_\odot$). These stars experience a phase of extreme mass loss during the previous Asymptotic Giant Branch (AGB) that causes the ejection of the stellar envelope. When this mass loss ceases the AGB phase ends and the star evolves into a short-lived evolutionary stage called the 'post-AGB' or 'proto-PN' phase (PPN) just before the star becomes a PN. At present, the formation of axisymmetric structures in PNe (ranging from elliptical to bipolar) is believed to occur during this PPN phase. But unlike for PNe, the study of PPNe is more difficult since their central stars (CS) are usually too cool to photoionize the gas and we cannot therefore study the formation of axisymmetric morphologies by mapping the ionized gas. Thus, we must use alternative techniques based on the analysis of: (i) the light scattered by the surrounding dust at optical wavelenghts; (ii) the study of the neutral molecular gas in the envelope in the near-infrared (H_2), sub-millimetre (e.g. CO) or radio domain (e.g OH, SiO, H_2O, CO); and (iii) the dust emission emerging at mid- to far-infrared wavelengths.

PPNe generally show a double-peaked spectral energy distribution (SED) (Volk & Kwok 1989; van der Veen, Habing, & Geballe 1989) with the photospheric emission coming from the central star dominating in the optical range and a strong infrared excess indicating the presence of a cool detached envelope ($T_d \sim 150-300$ K). This strong infrared excess is produced by the thermal emission of the dust present in their circumstellar shells previously expelled during the AGB phase. In order to reproduce the wide variety of morphologies observed in PNe, a generalization of the interacting stellar wind (ISW) model originally proposed by Kwok, Purton & Fitzgerald (1978) is required. In this model the fast post-AGB wind is assumed to interact directly with the axisymmetric dust shell formed early during the PPN phase. Additional scenarios have also been invoked (i.e. binary systems, magnetic fields - see Section 1.3). Therefore the study of the dust shells around PPNe provides fundamental information about the shaping mechanisms which are responsible for the wide variety of morphologies observed in PNe. Unfortunately, the intrinsically compact nature of the PPN dust shells have prevented the discovery of extended mid-IR emission in PPNe in the past, but more recent high spatial resolution observations have shown the intrinsic axisymmetric nature of the dust shells around a few compact PPNe at subarcsec level (Meixner et al. 1997; Meixner et al. 1999; Ueta et al. 2001).

In this Chapter, we present mid-infrared images (8–13 μm) of the PPN IRAS 16594−4656 (hereafter I16594) and of the very young [WC] PN IRAS 07027−7934 (hereafter I07027) with the aim of mapping the dust emission originated in the innermost regions of their circumstellar dust shells. I16594 is a C-rich multipolar PPN with a strong 21 μm dust emission feature (García-Lario et al. 1999). All previous studies of I16594 suggest that a dust torus could obscure the central star in the visible light and at the same time collimate the fast wind coming from the central star. This model can be tested by obtaining high-resolution mid-infrared images of the circumstellar shell. On the other hand, I07027 possesses a [WC]-type central star surrounded by a circumstellar shell where the simultaneous presence of oxygen and carbon-rich dust was recently revealed by ISO (Cohen et al. 2002). Determining the dust distribution in the mid-IR may be crucial to determining the nature and evolutionary status of I07027 and to understanding the origin of the dual-chemistry characteristics observed in most of the [WC] PNe observed so far in the mid-infrared.

3.2 Mid-IR observations

The observations were carried out on October 9 and 10, 2001, using the imaging mode of TIMMI2 (Reimann et al. 2000; Käufl et al. 2003) attached to the ESO 3.60 m telescope (La Silla, Chile). TIMMI2 has an array of 320 × 240 pixels with a pixel scale of $0.2'' \times 0.2''$ resulting in a field of view of $64'' \times 48''$. The observational conditions were very good (photometric and with a stable seeing of around $0.5''$), thus we were able to obtain mid-infrared images (at 8.6 μm [N1-filter], 11.5 μm [N11.9-filter] and 11.7 μm [SiC-filter]) of I16594 and I07027 at the diffraction limit of the telescope. The standard nodding/chopping observational technique was used in order to cancel the thermal emission from the atmosphere and from the telescope. Due to the short integration times required to avoid saturation in the mid infrared, each image is a combination of a large number of individual sub-images, each one with a typical integration time between 100 and 500 ms (approximately the atmospheric coherence time at 10 μm). Total on-source integration times were typically of $\sim$2 minutes. Mid-infrared photometric standard stars[1] were also observed at different air masses every night to determine the photometric flux conversion (from ADUs to Jy) and to measure the telescope point spread function (PSF).

3.3 Data reduction

The basic data reduction process includes bad pixel correction and the combination of all the images into one single image per filter. The flux calibration was made using the conversion factors (from ADUs to Jy) derived from the observation of standard stars at different air masses. The variation of these conversion factors with air mass was slightly different during the two nights of observation due to the different atmospheric conditions. On October 9 this variation was very small ($\leq$10%), so a single averaged conversion factor was used for all the observations performed during the night. However, on October 10 we found larger variations ($\sim$30%). Thus, for each observation we took the conversion factors derived from the observations of the standard stars located in the same region of the sky and at the same or a similar air mass. The size and morphology of the target stars in our programme was compared to the PSF derived from the observation of the standard stars used for the flux calibration using standard tasks in IRAF[2]. The object name, observing date, filters, central wavelength and width of the different filters used, total on-source integration time, object size, PSF size, integrated and peak fluxes, are listed in Table 3.1.

---

[1] The standard stars were taken from the web page of TIMMI2 (www.ls.eso.org/lasilla/sciops/timmi) (Doublier et al. 2005)

[2] The Image Reduction and Analysis Facility software package

TABLE 3.1— Summary of the ESO 3.6m/TIMMI2 mid-infrared observations.

Object	Date	Filter	$\lambda_c(\Delta\lambda)$ (μm)	T_{Total} (s)	Size[a] (")	PSF[b] (")	Flux[c] (Jy)	Peak (Jy arcsec^{-2})
I16594	9/10/01	N1	8.6(1.67)	120.4	∼1.7 x 1.6	0.57	14	5
...	...	N11.9	11.5(1.89)	107.5	∼1.8 x 1.6	0.73	40	13
...	...	SiC	11.7(3.21)	161.3	∼1.8 x 1.6	0.75	35	11
I07027	10/10/01	N1	8.6(1.67)	120.4	0.65	0.57	19	23
...	...	N11.9	11.5(1.89)	107.5	0.83	0.73	19	17

[a] Major and minor axis length at 40% of the peak intensity or FWHM in the case of IRAS 07027−7934.

[b] FWHM of the standard star.

[c] The fluxes are not colour corrected

From the internal consistency of the measurements made on the standard stars we estimate that the photometric uncertainty of our observations is in the order of ∼10%.

The observed PSFs are dominated by diffraction effects. Thus, the Lucy-Richardson deconvolution algorithm as implemented in IRAF (task LUCY) was used in order to recover the actual emission structure of the targets in each filter and remove the effects induced by the telescope PSF, which was found to be very stable. In order to study the goodness of the deconvolution process a subset of the standard stars observed for flux calibration purposes were also deconvolved with the same PSF used for the target stars. This exercise is useful for confirming that undesired artifacts are not introduced in the deconvolution process. We found that in all cases the deconvolved images of the standard stars spread over only one or two pixels, showing a quasi-point-like brightness distribution. As an example, one of the deconvolved standard stars is shown together with its corresponding raw image in Figure 3.1.

3.4 Results and data analysis

3.4.1 Mid-IR morphology of IRAS 16594−4656

Figure 3.2 shows the raw images of I16594 taken with TIMMI2 (left panel) together with the images obtained after applying the Lucy-Richardson deconvolution algorithm (right panel) mentioned above. The PSFs used for the deconvolution are also shown for comparison. I16594 already shows in the raw images an extended elongated morphology surrounding a complex inner core emission which is resolved in more detail after deconvolution. The source center has been determined by averaging the central coordinates of the elliptical isophotes within 20–40% of the peak intensity (thus avoiding any contamina-

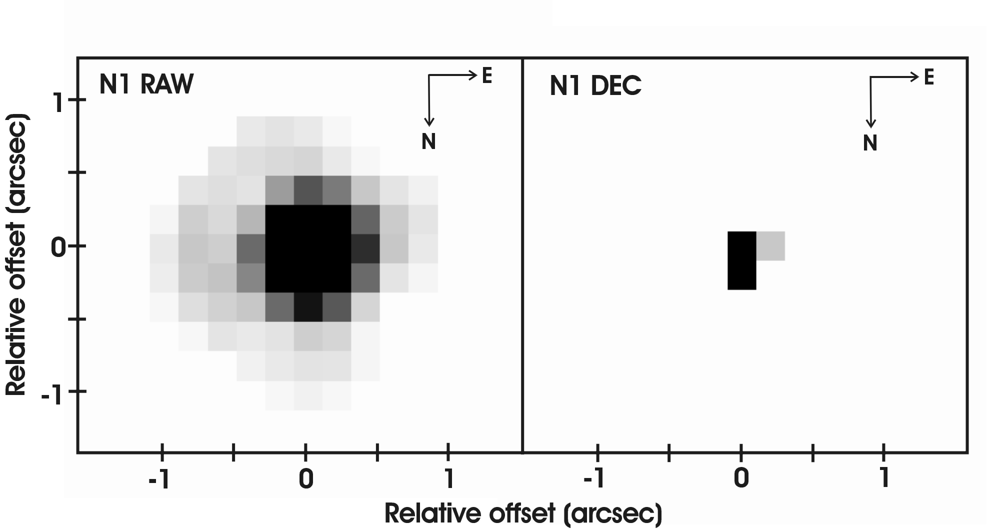

FIGURE 3.1— Illustrative example of the deconvolution of one of the observed standard stars showing the goodness of the deconvolution process. Raw mid-IR image in the N1 (8.6 μm) filter (left) and the corresponding deconvolved image using the Lucy-Richardson algorithm (right).

tion from the core structure). The images displayed in Figure 3.2 have been centred at this position.

The deconvolved 8.6, 11.5 and 11.7 μm images are shown in the right panel of Figure 3.2. The overall elliptical shape of the nebula is clear in all three filters with its major axis oriented along the east-west direction (P.A.∼80°) and extends out to at least 3.5″ x 2.1″ at 5% of the peak intensity at 8.6 μm. In addition, a conspicuous double-peaked morphology in the innermost region of the nebulosity is also recovered. The two detected peaks are oriented approximately along the north-south direction (P.A.∼−10°) perpendicular to the axis of symmetry defined by the outer elliptical emission. The measured separation between the two peaks is ∼0.8″. We are confident that the deconvolved structure is real because a very similar emission structure is observed in all three filters. A negligible contribution to the observed flux at 10 μm is expected from the central star of I16594 if this has a B7 spectral type as suggested by van de Steene, Wood & van Hoof 2000. Hrivnak, Kwok & Su (1999) found that the central star only contributes 3% to the total flux detected in the mid-IR. For this reason, the photospheric emission can be considered negligible in our images and we can therefore safely assume that we are observing the emission structure of the dust in the shell alone. The mid-IR morphology seen in the

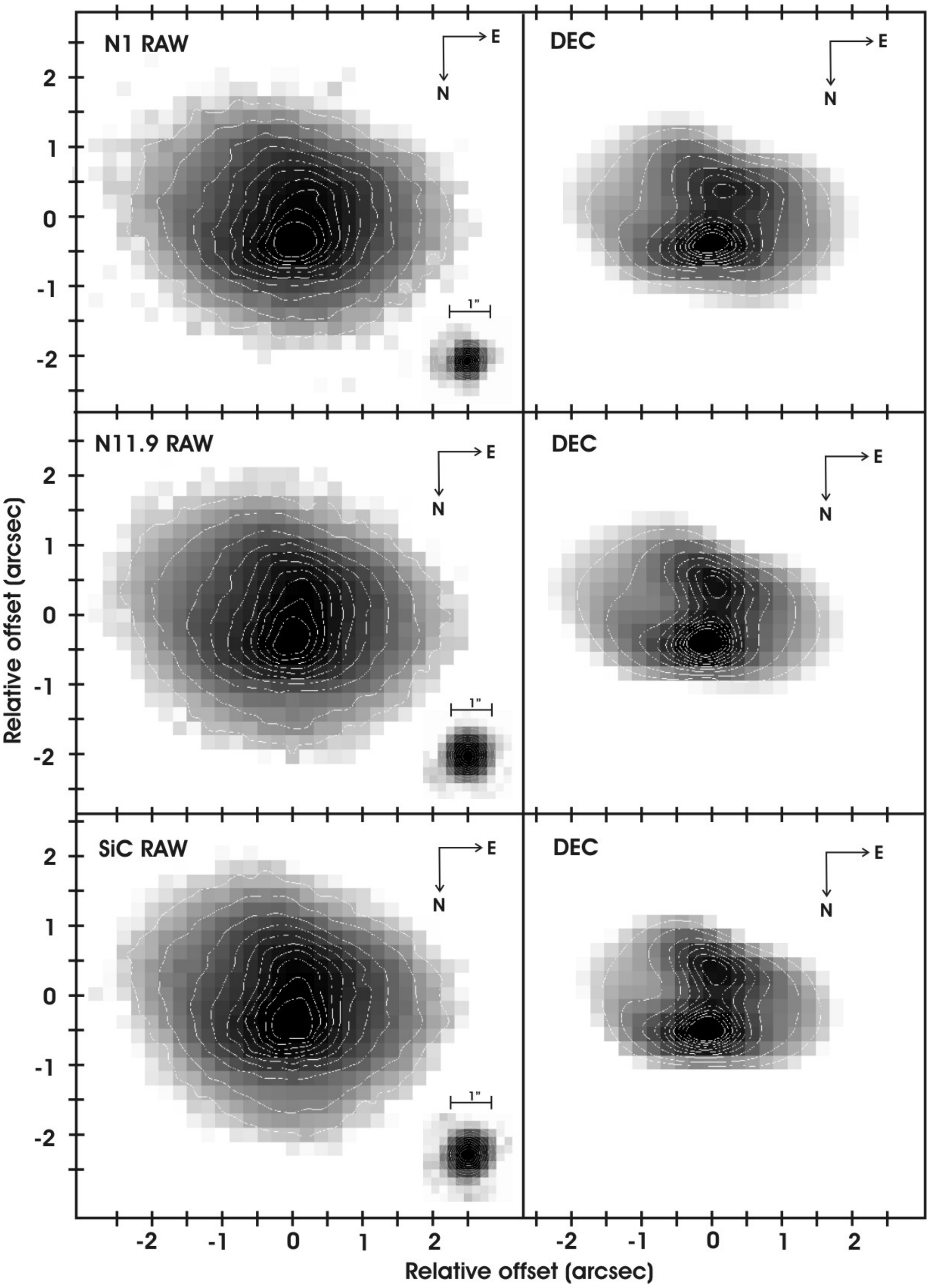

FIGURE 3.2— From top to bottom, raw mid-IR images of IRAS 16594−4656 in the N1 (8.6 μm), N11.9 (11.5 μm) and SiC (11.7 μm) filters (left) and the corresponding deconvolved images using the Lucy-Richardson algorithm (right). The tick marks show relative offsets from the centre of the nebula in arcseconds. Contours range from 10% to 90% of the peak intensity (in steps of 10%) plus the outermost contour, which corresponds to 5% of the peak intensity. The insets show the standard star PSFs in each filter.

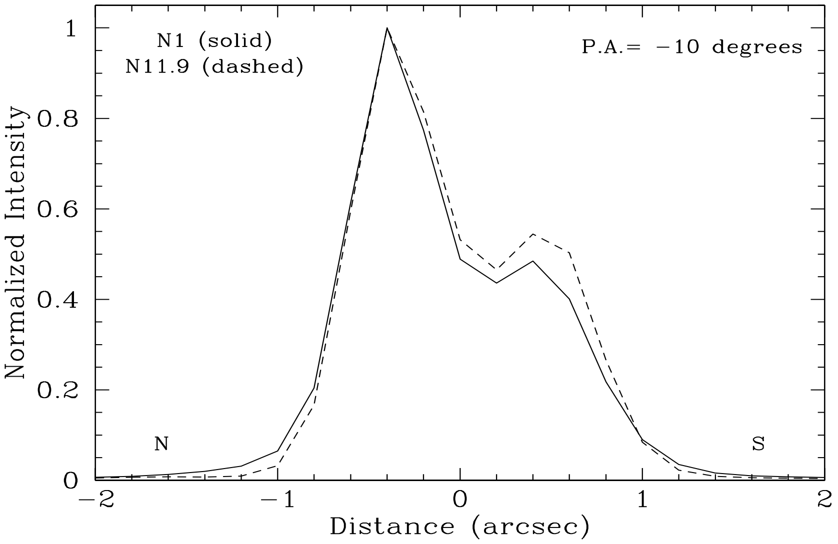

FIGURE 3.3— Normalized surface intensity profiles along the dust torus direction (from north to south) in IRAS 16594−4656. The solid and dashed lines correspond to the N1 (8.6 μm) and N11.9 (11.5 μm) filters, respectively. The centre of the nebula (tentatively identified as the central star position) corresponds to distance 0.

deconvolved images is thus interpreted as the evidence of the presence of a dusty toroidal structure with a ∼0.4″ radius size seen nearly edge-on. In addition, the north-peak (P.A.∼−10°) is about a factor 2 brighter than the south peak (see Figure 3.3). This finding is not unique to I16594. Indeed, Ueta et al.(2001) found a similar asymmetric profile in IRAS 22272+5435. The origin of this asymmetric appearance of the dust torus is still unclear. Ueta et al. (2001) argued that this can be attributed to asymmetric mass loss and/or an inhomogeneity in the dust distribution.

3.4.2 Mid-IR morphology of IRAS 07027−7934

The mid-IR morphology of I07027 is clearly less complex than the one observed in I16594 as deduced already from the raw images shown in Figure 3.4 (left). In this case, only a slightly extended source is detected in the two images available, which correspond to the filters N1 and N11.9 (centred at 8.6 and 11.5 μm, respectively).

The deconvolved images of I07027 in the 8.6 and 11.5 μm filters are shown in Figure 3.4 (right). After the deconvolution, a very bright and slightly elongated (in the north-south direction), marginally extended (FWHM=0.3″) emission is

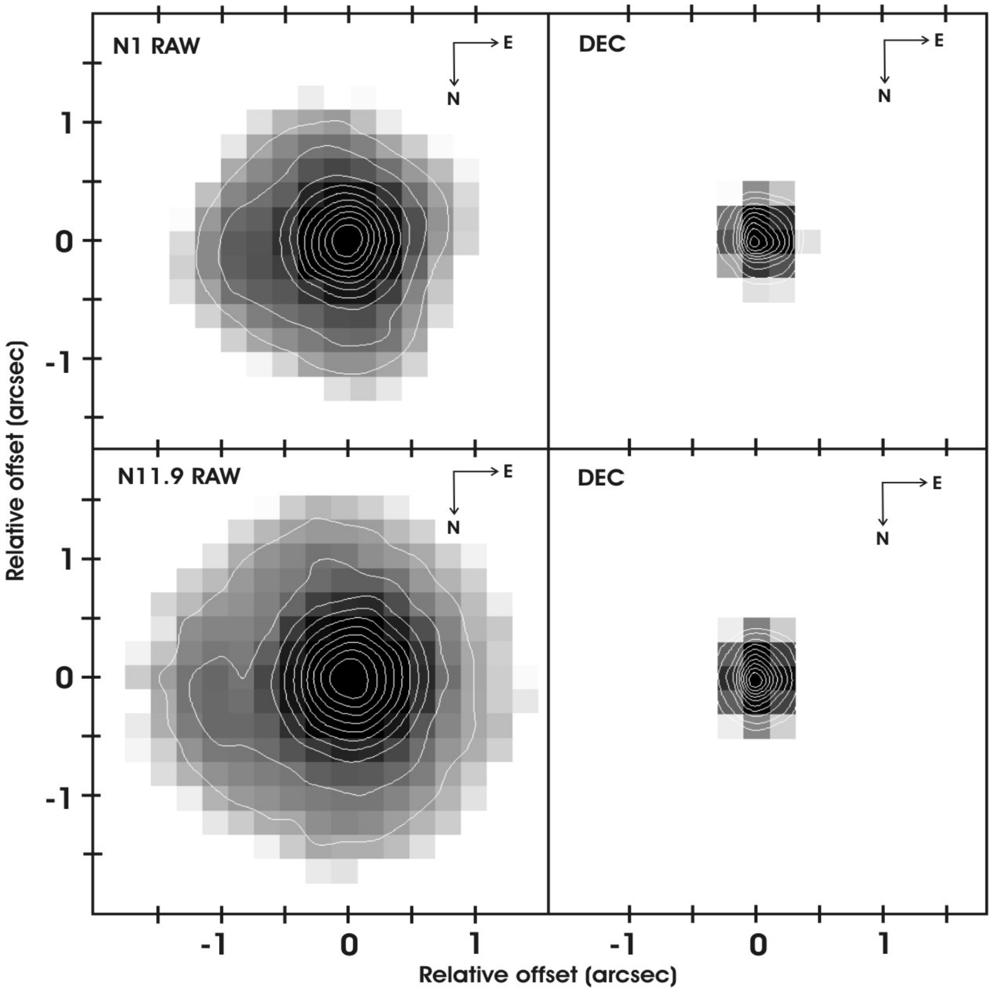

FIGURE 3.4— From top to bottom, raw mid-IR images of IRAS 07027−7934 in the N1 (8.6 μm), and N11.9 (11.5 μm) filters (left) and the corresponding deconvolved images using the Lucy-Richardson algorithm (right). The tick marks show relative offsets from the centre of the nebula in arcseconds. Contours range from 10% to 90% of the peak intensity (in steps of 10%) plus the outermost contour, which corresponds to 5% of the peak intensity.

recovered in both filters. Remarkably, the core of this mid-IR emission is not located in the central position derived by fitting ellipsoidal isophotes to the faint emission detected in the raw images. A similar result was previously reported by Zijlstra et al. (1991) based on optical images taken in the light of H_α. In this case, a non-resolved ionized core was detected off-centre, together with a faint, slightly elongated halo of scattered light emission, oriented also along the north-south direction. The same orientation is confirmed in recent HST-NICMOS images of I07027 taken in the near-infrared (see Section 3.6.1). We propose that the emission core which is detected in the mid-IR must be coincident with the non-resolved ionized core detected in the optical. Thus, the images showed in Figure 3.4 (right) have been centred at this core position.

3.5 Discussion I: IRAS 16594−4656

3.5.1 A dusty toroidal structure around IRAS 16594−4656

I16594 (=GLMP 507) was first identified as a PPN candidate on the basis of its IRAS colours by Volk & Kwok (1989) and van der Veen, Habing & Geballe (1989). It shows a double-peaked spectral energy distribution dominated by a strong mid- to far- infrared dust emission component which is much brighter than the peak in the optical (van de Steene, van Hoof & Wood 2000). The first indication of the C-rich chemistry of I16594 was the detection of CO molecular emission in its envelope (with V_{exp}~16 km s^{-1}) by Loup et al. (1990), in agreement with the non-detection of OH maser emission (te Lintel Hekkert et al. 1991). More recently, García-Lario et al. (1999) studied the ISO spectrum of this source and confirmed this classification based on the detection of the characteristic IR emission features generally attributed to PAHs (at 3.3, 6.2, 7.7, 8.6 and 11.3 μm) together with relatively strong features at 12.6 and 13.4 μm which indicates a high degree of hydrogenation in these PAHs. The ISO spectrum also reveal the presence of strong 21, 26 and 30 μm dust emission features (see Fig.3.5), adding I16594 to the short list of known PPNe displaying this set of still unidentified features.

The optical spectrum of I16594 shows only the hydrogen Balmer emission lines over an extremely reddened stellar continuum (E_{B-V}=1.8, van de Steene & van Hoof 2003) consistent with a B7 spectral type if dereddened. The H_α emission has a P-Cygni type profile indicative of a stellar wind with a velocity of ~126 km s^{-1} (van de Steene, Wood & van Hoof 2000). HST optical images show the presence of a bright central star surrounded by a multiple-axis bipolar nebulosity (seen in scattered light) with a complex morphology at some intermediate viewing angle. The size of this optical nebulosity is $6.3''$ x $3.3''$ at $3\sigma_{sky}$ level (Hrivnak, Kwok & Su 1999).

In the literature there are several indications of the presence of a circumstellar disc or a torus (an equatorial density enhancement) in I16594. The highly collimated structure seen in the HST optical images and the non-detected radio-continuum emission by van de Steene & Pottasch (1993) suggest that the emission lines observed in the optical spectrum are the result of shock excitation produced by a fast bipolar wind from the central source in interaction with the slow AGB wind. In agreement with this hypothesis García-Hernández et al. (2002) reported the detection of H_2 shock-excited emission in I16594 (see Chapter 2), later confirmed by van de Steene & van Hoof (2003) through a more detailed analysis of the H_2 spectrum. They postulate that the H_2 emission originates mainly where the stellar wind is funnelled through a circumstellar disc or torus. More recently, Hrivnak, Kelly & Su (2004) presented HST-NICMOS near-IR images of I16594 which show that this emission originates in regions where shocks must be taking place (see Section 3.5.5). Polarization measurements carried out by Su et al. (2003) revealed a 10% polarization value around the central source. The polarization vectors show both centrosymmetric and pointsymmetric patterns which clearly suggest the presence of a circumstellar torus. However, van de Steene, van Hoof & Wood (2000) failed to detect any extended emission in their N-band TIMMI images of I16594 in a previous attempt to search for mid-IR emission coming from this torus, but they observed with a lower spatial resolution (pixel scale of $0.66''$), and under poor weather conditions.

Our deconvolved mid-IR images of I16594, of much better quality, reveal directly for the first time the presence of a dusty toroidal structure with a radius of $\sim 0.4''$. Unfortunately, there are no parallax measurements for this object and the distance determinations to I16594 are quite uncertain. Su, Hrivnak & Kwok (2001) estimated a distance of 2.5 ${L_4}^{1/2}$ kpc (where L_4 is in units of 10^4 $L_\odot$) to I16594 based on the dereddened bolometric flux. On the other hand, van de Steene & van Hoof (2003) determined a total extinction (i.e., interstellar plus circumstellar) of $A_V=7.5\pm0.4$ (with $R_V=4.2$) such that the intrinsic color matched the dereddened color only at distance of (2.2 ± 0.4) ${L_4}^{1/2}$ kpc. We have tried to derive another distance estimate to I16594. To derive this distance, we have put together the IRAS fluxes at 12, 25, 60 and 100 μm, the near-IR JHK magnitudes from García-Lario et al. (1997) and the BVRI magnitudes from Hrivnak, Kwok & Su (1999). The observed BVRI and JHK fluxes were corrected for extinction according to the value of the total extinction ($A_V=7.5$ with $R_V=4.2$) determined by van de Steene & van Hoof (2003) and adopting the extinction law from Cardelli, Clayton & Mathis (1989). Then, we calculated a distance-dependent luminosity by integrating the observed flux at all wavelengths. This way, a distance of 2.1 ${L_4}^{1/2}$ kpc was obtained, in good agreement with the previous determinations mentioned above. Assuming a luminosity of 6000 $L_\odot$, which is the theoretical luminosity for a post-AGB star with a core mass of 0.60 $M_\odot$ (Schönberner 1987), a distance of 1.6 kpc to I16594 is derived, a value that will be adopted in the following discussion.

At a distance of 1.6 kpc, the extended emission detected in our deconvolved mid-IR images of I16594 would correspond to a dusty toroidal structure with a radius of ∼640 AU. Considering a 50% error on the assumed distance, a dusty torus radius in the range of ∼320–960 AU is obtained. Assuming that the CO emission detected towards I16594 is a good tracer of the dusty torus structure and considering the CO expansion velocity of 16 km s^{-1} measured by Loup et al. (1990), a dynamical age of the dusty torus structure of ∼190 yr can be estimated. This dynamical age is quite consistent with a source which has left the AGB very recently.

3.5.2 Dust temperature

The radiation transfer equation in the interior of a dust cloud adopts a simple form when the energy source is a single exciting star under the optically thin approximation and assuming thermal equilibrium. Under these conditions, the mean colour temperature of the dust can be obtained from a simple equation (see e.g. Evans 1980) which relates the measured fluxes $S_{\nu1,2}$ at two different wavelenghts $\lambda_{1,2}$ and the dust emissivity index (which depends on the assumed dust model), assuming a homogeneous dust distribution throughout in the cloud. We decided to use a basic dust model composed by hydrogenated amorphous carbon grains (HACs; type BE of Colangeli et al. 1995) of a standard size of 0.01 μm, whose emissivity index is ∼1 for I16594. The selection of this dust model is justified for several reasons: first, the PAH emission features at 3.3, 6.2, 7.7, 8.6, and 11.3 μm and the strong emission at 12.7 and 13.4 μm seen in the ISO spectrum indicates a C-rich chemistry and the presence of highly hydrogenated PAHs in the envelope (García-Lario et al. 1999); second, previous works dealing with similar sources have shown that amorphous carbon grains with a size of 0.01 μm reproduce reasonably well the dust emission structures and the spectral energy distribution usually observed in PPNe with the 21 μm dust emission feature (Meixner et al. 1997). In principle, one could construct the colour temperature map which results from this analysis using the 8.6 and 11.5 μm TIMMI2 images of any given source. Unfortunately, in the case of I16594, the 8.6 and 11.5 μm emission is strongly affected by the PAH emission features which are clearly visible in the ISO spectrum (see Fig.3.5). Thus, the temperature values derived this way are not expected to represent realistic estimations of any physical temperature in the shell. The same problem is found if we try to derive the dust temperature from the IRAS photometry at 12 and 25 μm, since both filters are also strongly affected by the presence of dust features, as ISO spectroscopy reveals. This is confirmed by the strongly different mean dust temperatures $T_{8.6/11.5}$ of 227 K and $T_{12/25}$ of 129 K, derived from our mid-IR data and from the IRAS photometry at 12 and 25 μm, respectively.

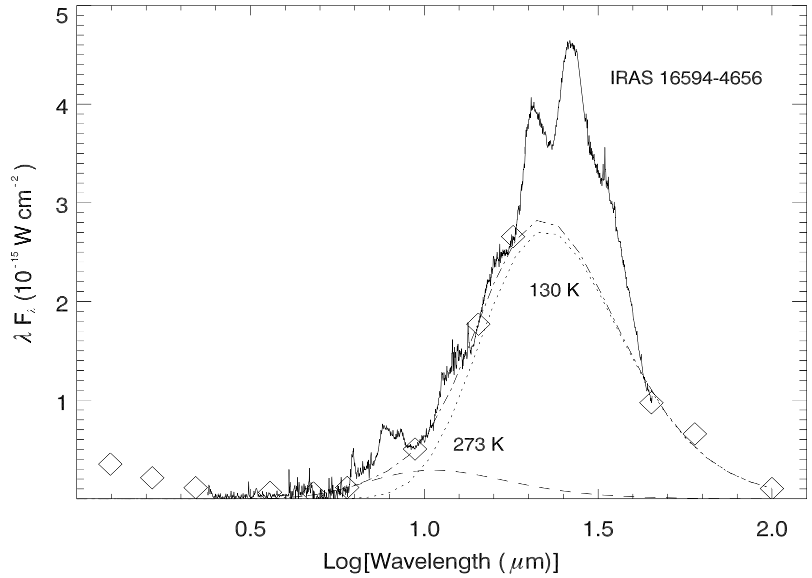

FIGURE 3.5— Two blackbody fitting of the SED of IRAS 16594−4656. The diamond symbols are the dereddened BVRIJHK photometry; the continuum points that were taken at carefully selected wavelengths used for the fitting, from the SWS ISO spectrum and the IRAS photometry at 60 and 100 μm, respectively.

A reliable dust temperature measurement can only be derived by fitting one (or more) blackbodies to the ISO data by considering fluxes representative of the underlying continuum at carefully selected wavelengths not affected by any dust feature. We did this by selecting only the ISO fluxes at 6, 9.4, 14.3, 18, and 45 μm plus the IRAS fluxes at 60 and 100 μm. The best fit is obtained with the combination of two blackbodies with temperatures of 273 K and 130 K, respectively, as we can see in Figure 3.5, where we display the SED of I16594 from the blue up to 100 microns together with the two blackbodies. We find that actually the warm component (at 273 K) dominates in the wavelength range of the N1-filter (at 8.6 μm) while the cool component (at 130 K) dominates in the N11.9-filter range (at 11.5 μm).

3.5.3 Dust equilibrium radius

An important parameter which can be estimated from the available images is the dust equilibrium radius. Based on the formula worked out by Scoville & Kwan (1976), this can be calculated for an emissivity index of 1 for each dust component using the equation:

$$r_{eq} = 3.44 f^{-1/2} T_d^{-5/2} L_*^{1/2} \tag{3.1}$$

where r_{eq} is the equilibrium radius in pc, f is the emissivity of the dust, T_d is the dust temperature in K, and L_* is the source luminosity in $L_\odot$.

In order to calculate the dust emissivity, the mass extinction coefficient value for hydrogenated amorphous carbon was taken from appendix A of Colangeli et al. (1995) at the central wavelength between the two filters. Then, a typical grain density of 1.81 g cm^{-3} (Koike, Hasegawa & Manabe 1980) was assumed. Finally, this quantity was multiplied by an assumed standard grain size of 0.01 μm, obtaining a dust emissivity of 9.8 10^{-3}. The equilibrium radius of the dust at the two reference temperatures calculated in the previous Section can then be derived using the mean dust temperature obtained from the two blackbody fitting (T_{BB1} and T_{BB2}) and the assumed luminosity of the source (6000 $L_\odot$).

The dust equilibrium radius at T_{BB1}=273 K is found to be ~451 AU, which corresponds to ~0.3$''$ at the assumed distance, which is just slightly below of the measured radius of the dusty torus in our deconvolved I16594 images and both values are consistent within the errors. The asymmetric appearance of the dust torus could indicate inhomogenities in the dust distribution and by simply adopting a smaller size grain of 0.005 μm, an equilibrium radius of ~0.4$''$ would be obtained, in perfect agreement with the observations.

Actually, a much larger equilibrium radius of ~3737 AU, or ~2.3$''$ for T_{BB2}=130 K was obtained. This means that the bulk of the dust emission in thermal equilibrium at 273 K probably originates at the dusty torus while the cooler dust in thermal equilibrium at 130 K would be located outside this internal region and can be identified as the remnant AGB shell (not detected in our images).

The similar extension and morphology of the shell at 8.6, 11.5 and 11.7 μm confirms that the mid-IR emission that we see in our TIMMI2 images is in all cases dominated by the PAHs and that these are preferentially distributed along the torus.

3.5.4 Comparison with other PPNe with mid-IR toroidal structures

Only a few other PPNe have been resolved in the mid-IR so far, which represents ~30% of the total number of PPNe in which extended emission has been searched for (Meixner et al. 1999; Ueta et al. 2001). Among them, Meixner et al. (1999) found two different classes of mid-IR morphologies. They distinguish those sources with a mid-IR core/elliptical structure from those with a toroidal one and they argue that this morphological dichotomy is due to a

TABLE 3.2— Mid-IR toroidal PPN/PNe sample

IRAS Name	Tor[a]	STyp[b]	Chem[c]	Type[d]	Morph.[e]	PAHs[f]	21 μm[g]	Ref.[h]
07134+1005	R	F5 Iab	C	PPN	S+B	y	y	1
16594−4656	R	B7	C	PPN	S+M	y	y	2
17436+5003	R	F3 Ib	O	PPN	S+B	n	n	3
19114+0002	U	G5 Ia	O	PPN/SG	S+M	n	n	3
21282+5050	R	O9	C	Young PN	S+B	y	n	4
22223+4327	U	G0 Ia	C	PPN	S+M	y	y	5
22272+5435	R	G5	C	PPN	S+M	y	y	6

[a] Toroidal. R: Two emission peaks clearly resolved. U: The two emission peaks are not resolved but there is evidence for the presence of a toroidal structure. The mid-IR images available are shown or described in Meixner et al. (1997, 1999), Ueta, Meixner & Bobrowsky (2000), Ueta et al. (2001), and this work for IRAS 16594−4656.
[b] Spectral types taken from SIMBAD.
[c] Chemistry. C: C-rich; O: O-rich.
[d] Evolutionary classification.
[e] Morphology. S+B: Star + bipolar. S+M: Star + multipolar. Optical morphology taken from Meixner et al. (1999). For IRAS 22223+4327 and IRAS 16594−4656 the HST images were retrieved from the HST Data Archive.
[f] Presence of the dust features at 3.3, 6.2, 7.7, 8.6 and 11.3 μm generally attributed to PAHs.
[g] Presence of the unidentified dust emission feature at 21 μm.
[h] References for the mid-IR spectra: 1) Hrivnak, Volk & Kwok (2000); 2) García-Lario et al. (1999); 3) Molster et al. (2002a); 4) Justtanont et al. (1996); 5) Kwok, Hrivnak & Geballe (1995); 6) Hrivnak, Volk & Kwok (1999).

difference in dust shell density. Moreover, in their sample there are only 4 out of 6 toroidal PPN/PNe in which the central dust torus is well resolved in two emission peaks. This work adds I16594 to this short list. In Table 3.2 we list the few known toroidal PPN/PNe sample together with some other observational characteristics of interest such as the spectral type of the central star, C/O ratio, evolutionary classification, optical morphology, and the list of mid-IR dust emission features detected.

Table 3.2 clearly indicates that I16594 is now the toroidal-PPN with the earliest spectral type known. The other PPNe with mid-IR toroidal structures have all F-G spectral types, while IRAS 21282+5050 is already a young PN with an O9-type central star. Thus, I16594 could represent the evolutionary link between the F-G mid-IR toroidal PPNe and the young PN IRAS 21282+5050. Interestingly, it seems that many of these sources show a C-rich chemistry (indicated by the presence of PAH emission features) but the number of objects is small and the statistics are very poor. More interesting is the fact that all mid-IR toroidal-PPN/PNe have bipolar/multipolar optical morphologies where the central star is clearly seen. In contrast, the central star is rarely seen in the mid-IR core/elliptical class sources described by Meixner et al. (1999) and almost all of them display bipolar morphologies in the optical. In addition, the mid-IR core/elliptical sources are typically O-rich and show deep silicate absorption features at 9.8 μm in their mid-IR spectra, indicating that they may be optically thick at mid-infrared wavelengths (Meixner et al. 1999). However, IRAS 17436+5003, which is the only O-rich mid-IR toroidal PPN known, does not display this silicate absorption feature at 9.8 μm in the ISO spectrum (e.g. Molster et al. 2002a). The different optical morphology (with or without a visible central star) and the apparent differences in the dust properties (optical thickness in the mid-IR) suggest that mid-IR toroidal PPNe might be surrounded by a dust torus optically thin at mid-IR wavelengths and, thus, not able to obscure the central star in the optical domain, while, in contrast, mid-IR core/elliptical PPNe may be surrounded by an optically thick dust torus/disk which would completely obscure the central star in the optical. The optically thick dust torus of mid-IR core/elliptical PPNe would be the responsible for the generation of the bipolar morphology observed in the optical, but the torus itself would only be detected at longer wavelengths (i.e. in the far infrared) as cooler material. For this reason, the detection of this type of collimating structures at mid-IR wavelengths would be easier in PPNe/PNe with a relatively low enhancement of the equatorial density.

3.5.5 Evidence for precession in IRAS 16594−4656

I16594 has also been observed by the HST in the optical, through the broad F606W continuum filter with the Wide Field Planetary Camera (WFPC2) under proposal 6565 (P.I.: Sun Kwok), and in the near-infrared, through the narrow F212N (H_2) and F215N (H_2-continuum) filters with the Near Infrared Camera and Multi Object Spectrometer (NICMOS) under proposal 9366 (P.I.: Bruce Hrivnak). In the optical, I16594 shows a flower-shaped morphology where several petals (or bipolar lobes) can be identified at the opposite sides of the central star with different orientations (Hrivnak, Kwok, & Su 1999). From the HST optical images (taken from the HST Data Archive) we identify pairs of elongated structures with at least four different bipolar axes at P.A.∼34°, ∼54°, ∼84° and ∼124°. The presence of multiple bipolar axes has usually been interpreted in the literature as the result of episodic mass loss from a precessing central source (e.g. García-Segura & López 2000). Similar structures have also been detected in other PPNe (e.g. Hen 3-1475; Riera et al. 2003) and in more evolved PNe (e.g. NGC 6881; Guerrero & Manchado 1998).

In Figure 3.6 we have displayed the contour map of the deconvolved mid-IR images of I16594 obtained with TIMMI2 in the N1 and N11.9 filters overlaid

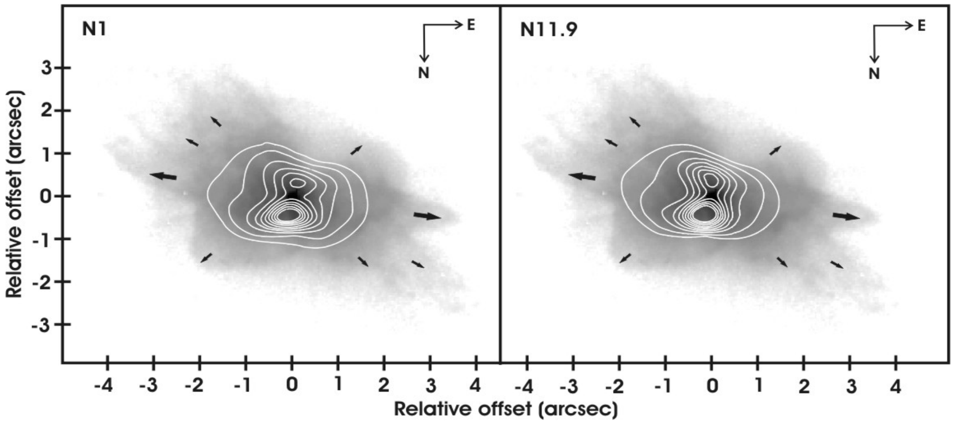

FIGURE 3.6— Contour maps of the deconvolved mid-IR images taken in the N1 (8.6 μm) and N11.9 (11.5 μm) filters overlaid on the optical HST image of IRAS 16594−4656 in the F606W filter (taken from the HST Data Archive). Contours range from 10% to 90% of the peak intensity (in steps of 10%) to which we have added the contour corresponding to a 5% of the peak intensity. The tick marks show relative offsets from the centre of the nebula in arcseconds. The arrows indicate the direction of the various bipolar lobes identified in the optical images. The big one marks the lobe whose orientation is remarkably coincident with the mid-IR axis defined by the dust torus.

on the optical HST-WFPC2 image taken in the F606W filter. Remarkably, we can see that the axis of symmetry defined by the mid-IR emission nicely coincides with only one of the bipolar axes that can be identified in the optical images, in particular with that oriented at P.A.∼84°. If this emission is a good tracer of the hot dust in the envelope and we accept that this hot dust must have been recently ejected from the central star we can interpret the observed spatial distribution in the mid-IR as the result of the preferential collimation of the outflow material along this direction in the most recent past.

Remarkably, the H_2 shocked emission detected with HST-NICMOS in the near-IR is also found mainly distributed following the same bipolar axis. This is shown in Figure 3.7, where the H_2 continuum-subtracted HST-NICMOS image (taken also from the HST Data Archive) is shown together with the same optical HST image of I16594 used in Figure 3.6. The H_2 emission is mainly coming from the walls of the bipolar lobe oriented at P.A.∼84° identified in the HST optical images. In addition, four additional clumps of much weaker H_2 emission are detected at the end of each of the other two point-symmetric outflows associated to I16594 (Hrivnak, Kelly & Su 2004). The stronger emission detected along the walls of this bipolar lobe would suggest that the interaction of the fast wind from the central star with the slowly moving AGB wind is currently

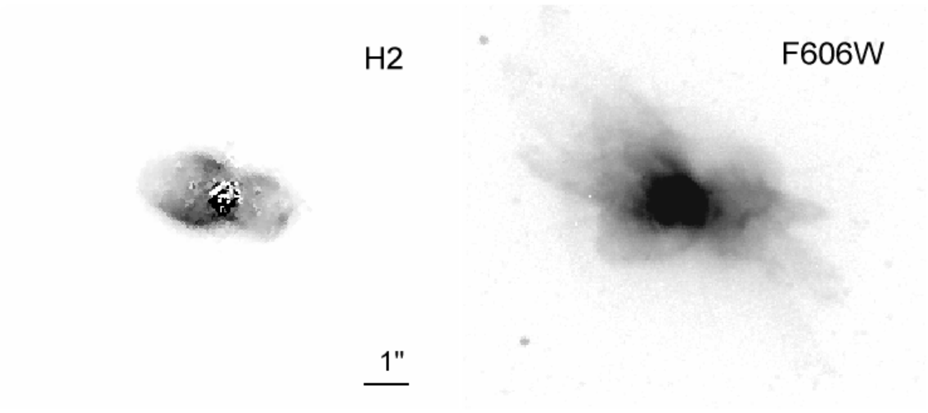

FIGURE 3.7— HST-NICMOS image showing the near-IR H_2 emission at 2.122 μm detected in IRAS 16594−4656 (left) and the optical HST-WFPC2 image taken in the broad F606W filter (right). Both images were taken from the HST Data Archive. The orientation is the same to that of Figure 3.6 (north is down, east to the right) and the images are displayed on logarithmic scale. Remarkably, the H_2 emission is mainly distributed along the walls of the lobe at P.A.∼84° identified in IRAS 16594−4656. Note that the H_2 image was continuum-subtracted using the HST-NICMOS image containing the emission in the adjacent continuum at 2.15 μm.

taking place preferentially also along this axis of symmetry. The rest of bipolar outflows observed at other orientations in the optical images taken with HST must then be interpreted as the result of past episodic mass loss ejections. As such, they must contain much cooler dust grains which are then only detectable in the optical because of their scattering properties.

3.6 Discussion II: IRAS 07027−7934

3.6.1 The marginally extended mid-IR core of IRAS 07027−7934

I07027 (=GLMP 170) is a very peculiar young PN. It has a [WC] central star that was classified by Menzies & Wolstencroft (1990) as of [WC11]-type. Their classification was based on the spectral characteristics of the visible spectrum. This corresponds to a PN with prominent nebular hydrogen and [N II] lines, together with stellar carbon and helium lines over a weak continuum. The detection of OH maser emission at 1612 MHz by Zijlstra et al. (1991), together with the strong PAH features seen in the IRAS Low Resolution Spectrum (Olnon et al. 1986) and in the ISO spectrum (Cohen et al. 2002; Peeters et al. 2002) indicate the simultaneous presence of oxygen and carbon-rich dust in the envelope. At present, there are only about half a dozen PNe whose central star has been classified as [WC11]. They all have stellar temperatures between ∼28,000 and 35,000 K (Leuenhagen & Hamann 1998) and are thought to be in the earliest observable phase of its PN evolution, soon after the onset of the ionization in their circumstellar envelopes. I07027 is also among the brightest IRAS PNe and it has IRAS colours similar to young post-AGB stars (Zijlstra 2001). Remarkably, all other [WC] CSPNe observed with ISO show a mixed chemistry as well (Cohen et al. 2002) but I07027 is the only known [WC] star belonging to the rare group of OHPN, and therefore it links OH/IR stars with carbon-rich PNe (Zijlstra et al. 1991).

Unfortunately, I07027 has not been imaged yet with the HST in the optical; however, it has very recently been observed in the near-infrared through the broad F110W and F160W continuum filters with NICMOS under proposal 9861 (P.I.: Raghvendra Sahai). In Figure 3.8 we have displayed the near-IR HST images of I07027 (taken from the HST Data Archive) together with their corresponding contour levels. They resolve, for the first time, the near-infrared morphology of I07027. In the F160W filter, I07027 shows a bright core (with FWHM=0.25″), which is elongated along the north-south direction surrounded by a fainter elliptical halo with a total size of ∼1.6″ × 2.1″ at 1% of the peak intensity. However, the HST image in the F110W filter shows a slightly less extended emission of ∼1.1″ × 1.5″ (at 1% of the peak intensity) and a central point source which corresponds very probably to the central star. This could probably indicate that the F160W (H-band) filter is already dominated by the hot dust emission (∼1000−2000 K).

Zijlstra et al. (1991) also published an H_α image of I07027 taken with the ESO 3.5m NTT telescope. This image shows an ionized core, surrounded by a very large round/elliptical halo of ∼13″ x 15″ oriented also along the north-south direction. Because in the optical image at 5000 Å (where an intense [O III] nebular line is located) only the central star can be seen, this halo may be mostly due to light scattered by neutral material and dust grains in the envelope. Based on the observed OH profile, the difference between the CO and OH velocities and the off-centre location of the ionized core in the H_α halo, Zijlstra (2001) suggested that I07027 could have a bipolar morphology. García-Hernández et al. (2002) detected H_2 fluorescence-excited emission from this source, in agreement with the round/elliptical H_α morphology of the nebula and the temperature of the central star (see Chapter 2). At present, the evolutionary status of I07027 is not well understood. The PAH emission observed in the mid-IR requires a moderate UV radiation field while the OH 1612 MHz emission detected at radio wavelengths requires much lower temperatures (Field 1985). Note that ultraviolet irradiation from the central star is generally thought to be the excitation mechanism of PAHs. However, if the UV radiation field becomes

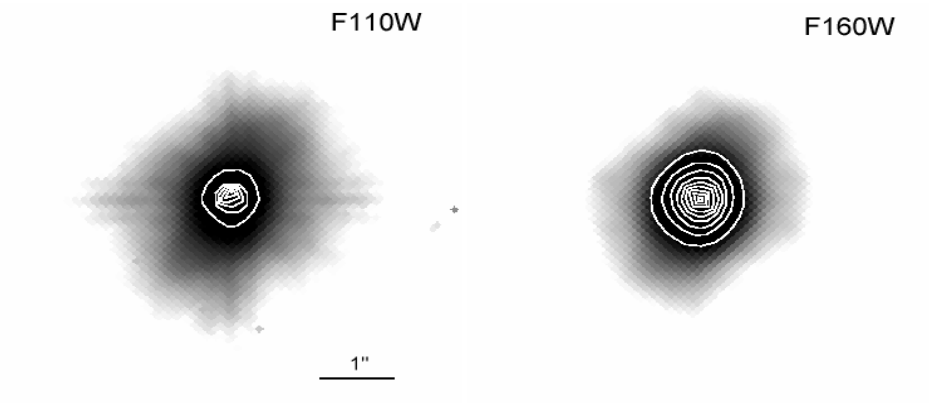

FIGURE 3.8— Logarithmic-scale near-IR HST-NICMOS images of IRAS 07027−7934 (taken from the HST Data Archive) in the F110W (left panel) and F160W filters (right panel) with contours corresponding to 10% to 90% of the peak intensity (in steps of 10%). The orientation is the same as that of Figure 3.4 (north is down, east to the right).

too strong the PAH molecules can be destroyed, specially the small ones with a size ∼20−30 carbon atoms (see e.g. Allain, Leach & Sedlmayr 1996). This may indicate that the C-rich dust seen in the ISO spectrum must be located close to the central source and subject to the mild UV irradiation coming from the central star, but shielded from the stronger ISM UV radiation field by the outer layers of the circumstellar shell, while the O-rich emission is expected to come from the external cooler regions. I07027 had never been imaged in the mid-IR before. Thus, our observations are the first attempt to reveal the spatial distribution of the warm dust in this peculiar object.

The deconvolved mid-IR images of I07027 displayed in Figure 3.4 show a slightly extended and elongated mid-IR emission core at 8.6 and 11.5 μm. This mid-IR emission core is only marginally resolved (with a FWHM=$0.3''$ as compared to the typical PSF size of FWHM$\leq 0.2''$ measured in the deconvolved standard stars) and is elongated in the north-south direction consistent with the overall morphology observed in the near-IR with HST-NICMOS. Zijlstra et al. (1991) predicted a radio flux density of 10 mJy assuming E_{B-V}=1.1 and $T_e=10^4$ K. In addition, by using a plausible radio brightness temperature of 10^3 K they predicted an angular diameter of $\sim 0.3''$ for the ionized region. This predicted size for the ionized region is also consistent with the measured size of the bright mid-IR core seen in our deconvolved images of I07027. The distance determination to I07027 is, as usual, quite uncertain, and was estimated by Zijlstra et al. (1991) through the measurement of E_{B-V} in nearby stars. They obtained a distance of 3–5 kpc for I07027 using this method. We carried out a similar procedure for I16594, and we have also constructed the SED of I07027 by combining the available IRAS fluxes at 12, 25, 60 and 100 μm with the JHKL and BVRI photometry taken from García-Lario et al. (1997) and Zijlstra et al. (1991), respectively. The observed fluxes were also corrected for extinction by adopting the extinction law from Cardelli, Clayton & Mathis (1989) with R_V=3.1. Then, a distance of 4.1 $L_4{}^{1/2}$ kpc (with L_4 in units of 10^4 $L_\odot$) is obtained. Note that I07027 is located at a much higher galactic latitude (b=$-26°$) than I16594 (b=$-3°$) and at such high galactic latitudes this much interestellar reddening is unexpected. Thus, we interpret that the observed reddening E_{B-V}=1.1 is mainly circumstellar in origin. On the other hand, most of the flux is emitted in the infrared where the effect of the interstellar/circumstellar extinction is mild. This distance is in good agreement with the value of 4.2 $L_4{}^{1/2}$ kpc derived by Surendiranath (2002). Assuming a luminosity of 10^4 $L_\odot$ for I07027, a distance of 4.1 kpc is derived. At this distance, the determined core size would correspond to ~1230 AU.

3.6.2 Dust temperature

As in the case of I16594, we cannot interpret our mid-IR observations of I07027 in terms of dust temperatures in the shell because the ISO spectrum of I07027 (Cohen et al. 2002) shows that the 8.6 and 11.5 μm filters are also strongly affected by strong PAH emission features. In particular, the PAH emission features, around 8 μm (at ~7.7 and 8.6 μm), are much stronger in this case than the feature located at 11.3 μm. Thus, the dust temperature values derived would be unrealistically high.

Again, using IRAS data, a mean dust temperature $T_{12/25}$ of 148 K is derived, while the TIMMI2 data gives a $T_{8.6/11.5}$ of ~363 K. The strong differences in the derived temperatures confirm that the PAH emission is dominating the emission observed in the mid-IR. In order to confirm this hypothesis, the ISO spectrum originally published by Cohen et al. (2002) was examined. As we did in the case of I16594, the SED can be fitted by a two-component dust continuum with temperatures of T_{BB1}=430 K and T_{BB2}=110 K, respectively. The warm component dominates in the wavelength range of our TIMMI2 observations (where the PAH features are found) while the cool component dominates at longer wavelengths where the crystalline silicate dust features are detected.

3.6.3 Dust equilibrium radius

In contrast to I16594, the ISO spectrum of I07027 shows the non-detection of the emission features at 12.6 and 13.4 μm, which are the signatures of the CH out-of-plane bending vibrations for hydrogens in positions duo and trio, respectively (Pauzat, Talbit & Ellinger 1997) and indicate that the PAH population in I07027 is largely dehydrogenated. So, for the modelling of the dust emitting at T_{BB1}=430 K we made the same assumptions as in the case of I16594 (see Section 3.5.3) but this time we adopted a composition dominated by dehydrogenated amorphous carbon grains (type ACAR of Colangeli et al. 1995). Under these assumptions, we obtain a dust equilibrium radius of ∼228 AU or only 0.05″ assuming a distance of 4.1 kpc. Note that if we consider a larger grain size of 0.1 μm an even smaller dust equilibrium radius is derived. In order to get a dust equilibrium radius consistent with the observed extension of ∼0.3″ seen in our mid-IR deconvolved images we need to assume a very small grain size of <0.001 μm. This suggests that the mid-IR emission at ∼430 K is dominated by small PAH molecules located very close to the central star, consistent with the narrow features detected by ISO, where the UV radiation field is strong. Actually, the ISO spectrum of I07027 shows also that the PAH emission features at 3.3 and 11.3 μm are weak compared with the emission features located at 6.2, 7.7, and 8.6 μm, indicating a high degree of ionization in the population of PAHs (see Figure 2 in Allamandola, Hudgins & Sandford 1999), in agreement with our interpretation of the observed mid-IR emission.

For the cool dust component at 110 K, a different dust model was assumed, composed mainly of astronomical silicates. This choice was made in order to take into account the O-rich nature of the dust detected at wavelengths longer than 25 μm. The crystalline silicates are expected to be formed in the circumstellar dust shells of evolved stars at temperatures in the range 60−160 K (Molster et al. 2002b). The mean emissivity value adopted between 25 and 60 μm was taken from Figure 5 in Draine & Lee (1984) and in this case two grain sizes of 0.1 and 0.01 μm were considered. A dust equilibrium radius of ∼0.02 pc and of ∼0.06 pc (or 1.1″ and 3.4″ at 4.1 kpc) for a grain size of 0.1 and of 0.01 μm, respectively is then derived. Our calculations indicate that this cool dust must be located much further away from the central source than the warm dust emission (at 430 K) detected in the mid-IR.

These results favour the hypothesis that I07027 may have experienced a late thermal pulse which has produced the recent switch to a C-rich chemistry. All C-rich material would then be warm as a consequence of its very recent formation and, thus, located very close to the central source while the cooler O-rich material, must have been ejected a long time ago, during the previous AGB phase and therefore now it can only be found further away from the central source.

3.6.4 Evolutionary status of IRAS 07027−7934

As we have already mentioned, the evolutionary status of I07027 is not yet well understood. The hydrogen-deficiency of the central star together with the mixed dust chemistry (C-rich and O-rich) is a common finding among the limited sample of known [WC] PNe (De Marco & Soker 2002; Cohen et al. 2002). The most promising scenarios to explain the current observational properties of this rare class of PNe are the so-called 'disk-storage' scenario (Jura, Chen & Plavchan 2002; Yamamura et al. 2000), a final thermal pulse while the star was still in the AGB or a late thermal pulse during the post-AGB evolution (Herwig et al. 1997, 1999; Herwig 2000, 2001; Blöcker 2001).

The disk-storage scenario invokes the presence of a binary system in which the O-rich silicates are trapped in a disk formed by a past mass transfer event, with the C-rich particles being more widely distributed in the nebula as a result of recent ejections of C-rich material. This type of dusty disk structure has been detected in some PPN/PNe with binary [WC] central stars like CPD−56°8032 (De Marco, Barlow & Cohen 2002) or in the Red Rectangle (HD44179) (Waters et al. 1998). However, an AGB final thermal pulse or a late thermal pulse during the post-AGB phase can produce both the switch to a C-chemistry and a strong stellar wind, which is characteristic of these [WC] CSPNe. The off-centre location of the ionized core detected in I07027 could suggest the presence of a binary system but no firm evidence for the binarity of I07027 exists as yet. As we have discussed in Section 3.6.3, the emission detected in our mid-IR images can be attributed to ionized PAH plus thermal emission from relatively warm dust ($\sim$430 K) located very close to the central source. In contrast, the typical disk sources with dual chemistry which are known to be binary systems show a completely different relative distribution of O-rich and C-rich dust. Waters et al. (1998) found that the PAH emission at 11.3 μm has a clumpy nature and comes from the extended nebula around HD44179, while the O-rich material is located in a circumbinary disk. More recently, the bipolar post-AGB star IRAS 16279−4757 has been studied in the mid-IR by Matsuura et al. (2004). They found that the PAH emission is enhanced at the outflow, while the continuum emission is located towards the centre. Thus, they suggest the presence of a dense O-rich torus around an inner, low density C-rich region and a C-rich bipolar outflow resembling the morphology attributed to HD44179.

The observational characteristics of I07027 indicate a totally different formation mechanism, which is only consistent with a very recent change of chemistry from O-rich to C-rich. Because of the very small size of the C-rich emitting region we favour the late thermal pulse (probably at the end of the previous AGB phase) scenario, a process which could also be the origin of most of the CSPNe displaying [WC]-type characteristics and a dual chemistry.

3.7 Conclusions

We have presented diffraction limited mid-IR images of the PPN I16594 and the [WC] PN I07027 at 8.6, 11.5 and 11.7 μm taken under exceptionally good seeing conditions ($\leq$0.5$''$). By applying the Lucy-Richardson deconvolution algorithm, we have resolved, for the first time, the subarcsecond dust shell structures around both objects.

I16594 displays two emission peaks in the innermost region of the circumstellar dust shell at the three wavelengths observed. This two-peaked mid-IR morphology is interpreted as the presence of a dusty toroidal structure with a 0.4$''$ radius size (or $\sim$640 AU corresponding to a dynamical age of $\sim$190 yr at the assumed distance of 1.6 kpc). The observed mid-IR emission is dominated by PAH emission which is mainly distributed along the torus. We have also found that the axis of symmetry observed in the mid-IR is well aligned with one of the bipolar outflows identified in the HST optical images (at P.A.$\sim$84°) and we suggest that, at present, the outflow material is being collimated by the dust torus in this direction. Consistently, the H_2 shocked-emission seen in the HST NICMOS image is mainly distributed along the same bipolar axis where the fast post-AGB wind is interacting with the slow moving material ejected during the previous AGB phase. The presence of several other bipolar outflows at a variety of P.A. may be the result of past episodic mass loss events in a precessing system.

I07027 exhibits a slightly asymmetric mid-IR emission core which is only marginally extended with FWHM=0.3$''$ at 8.6 and 11.5 μm. This mid-IR core is probably coincident with the off-centre ionized core detected in ground-based H_α images. The mid-IR emission is attributed to a combination of emission from highly ionized, small PAH molecules plus relatively warm dust continuum located very close to the hot central star. Finally, we propose that the dual chemistry observed in I07027 can be interpreted as the consequence of a late thermal pulse (probably at the end of the previous AGB phase) which has recently switched the chemistry of the central star from the original O-rich composition to a C-rich one. It is suggested that this might be the commom mechanism which originates the dual chemistry and strong stellar winds usually observed in other [WC]-type CSPNe.

4

Li and s-elements in massive galactic O-rich AGB stars: A qualitative approach

Most of the contents of this chapter have been submitted for publication to A&A García-Hernández, D. A., García-Lario, P., Plez, B., Manchado, A., D'Antona, F., Lub, J., Habing, H.

4.1 Introduction

The Asymptotic Giant Branch (AGB) is formed by stars with initial masses in the range between 0.8 and 8 $M_\odot$ in a late stage of their evolution. The internal structure of an AGB star consists of an electron-degenerate C-O core surrounded by a shell of He. During most of the time H burning is the main source of energy for the AGB star but, occasionally, the inner He shell ignites in a "thermal pulse" and, eventually, the byproducts of He burning may reach the outer layers of the atmosphere in a "dredge-up" of processed material transforming O-rich M giants into ^{12}C- and s-process-rich C or S stars.

Recent studies of AGB stars in the Magellanic Clouds (hereafter, MCs) (Plez, Smith & Lambert 1993; Smith & Lambert 1989, 1990a; Smith et al. 1995) show a lack of high luminosity C stars (brighter than $M_{bol} \sim -6$). This has been interpreted as the consequence of the transformation of ^{12}C into ^{14}N via the CN cycle in massive AGB stars, where the temperature of the convective envelope is hot enough ($T \geq 2 \times 10^7$ K) (Sackmann & Boothroyd 1992; Wood et al. 1983). These *hot-bottom burning* (HBB) models predict the production of ^{7}Li, through the "^{7}Be transport mechanism" (Cameron & Fowler 1971), which should be detectable for a short time in the atmosphere of the star, together with the s-process heavy elements formed by the capture of the neutrons produced during the thermal pulses, such as Rb, Zr, Ba, Tc or Nd. In addition, as a consequence of the activation of HBB and, therefore, of the CN cycle, a very low ^{12}C/^{13}C ratio ($\sim$3$-$4) is also predicted by these models (Mazzitelli, D'Antona & Ventura 1999).

Extensive surveys have been carried out searching for lithium on AGB stars in the MCs (Plez, Smith & Lambert 1993; Smith & Lambert 1989, 1990a; Smith et al. 1995) resulting in the detection of strong Li lines in luminous O-rich AGB stars in the range $-7 \leq M_{bol} \leq -6$, which are also enriched in s-process elements, while brighter stars do not show lithium.

In our Galaxy only a handful of Li-rich stars have been found so far (e.g. Abia et al. 1993), and, unlike those detected in the MCs, they are not so luminous. Most of them are intermediate mass C-stars and S-stars with a modest luminosity. However, hot bottom-burning is expected to be active in the most massive (and luminous) AGB stars (from $\sim$4 to 7 $M_\odot$) (Mazzitelli, D'Antona & Ventura 1999), which might not be C-rich, but O-rich. The best candidates are the so-called *OH/IR stars*, luminous O-rich AGB stars which are extremely bright in the infrared and show a characteristic double-peaked OH maser emission at 1612 MHz. These stars are also known to be very long period variables (LPVs), sometimes with periods of more than 500 days and large amplitudes of up to 2 bolometric magnitudes. However, they experience very strong mass loss rates (up to several times 10^{-5} $M_\odot yr^{-1}$) and most of them are usually heavily obscured at this stage by thick circumstellar envelopes, making optical observations very difficult. Thus, as yet no information exists on their Li abundances and/or possible s-process element enrichment.

In this Chapter, we present the qualitative results obtained from a wide observational programme based on high resolution optical spectroscopy of a carefully selected sample of galactic AGB stars suspected to be massive according to their observational properties. In Chapter 5 we will describe the results found in a more detailed and quantitative way, applying model atmospheres for cool stars and spectral synthesis techniques in order to determine their atmospheric parameters and derive their lithium abundances, as well as their enrichment in s-process elements (or upper limits) with respect to the Fe-peak elements.

4.2 Selection of the sample

A large sample (more than 100 sources) of long-period (300−1000 days), large amplitude variability (up to 8−10 magnitudes in the V band), late-type (> M5) O-rich AGB stars displaying OH maser emission with a wide range of expansion velocities (from just a few km s^{-1} to more than 20 km s^{-1}) was carefully selected. Some of them were so strongly reddened that they do not show any optical counterpart in the Digitized Sky Survey[1] (DSS) plates, although in a few cases optical detections have been reported in the literature.

Stars were included in the sample if satisfying at least one of the above criteria and ideally as many of them as possible, which guarantees that they are definitely massive stars. It should be noted that 9 stars classified as Mira-type stars in the SIMBAD[2] database and included in the initial sample were found to exhibit properties of C-rich stars during our observations (see Section 4.3). These stars have been separated from the O-rich ones in this study. In Table 4.1 we list the 102 O-rich stars selected according to the above criteria, where we give the IRAS name together with other names taken from the literature when relevant, the galactic coordinates, the variability type, the spectral type, and the IRAS colour index [12]−[25] and [25]−[60][3]. Similar information for a few well known galactic M-supergiants and S-, SC- and C-type AGB stars selected for comparison is presented in Table 4.2. In Table 4.3 we also list this information for the few peculiar stars mentioned above which were found to be carbon stars. The OH expansion velocities (or from CO data in the case of C-rich stars) and the pulsational periods together with literature references are given in Tables 4.5, 4.6, 4.7, 4.8 and 4.9.

The position of the selected stars in the IRAS two colour-diagram [12]−[25] *vs* [25]−[60] is shown in Figure 4.1. Most of them fall, as expected, along the observational "O-rich AGB sequence" (García-Lario 1992). This sequence agrees very well with the model predictions by Bedijn (1987) and it is interpreted as a sequence of increasing thickness of the circumstellar envelopes and/or mass loss rates in O-rich AGB stars.

We also show the galactic distribution of the sample in Figure 4.2. There we can see that most of the stars must be members of the galactic disk population. However, it should be noted that the sample contains a significant number of nearby OH/IR stars (especially among the stars with bright optical counterparts

---

[1] The Digitized Sky Survey was produced at the Space Telescope Science Institute under U.S. Government grant NAG W-2166.

[2] Set of Identifications, Measurements, and Bibliography for Astronomical Data, operated at CDS, Strasbourg, France.

[3] defined as $[12]-[25]=-2.5\log(F_{12}/F_{25})$ and $[25]-[60]=-2.5\log(F_{25}/F_{60})$, where F_{12},F_{25} and F_{60} are the IRAS flux densities at 12, 25 and 60 μm, respectively.

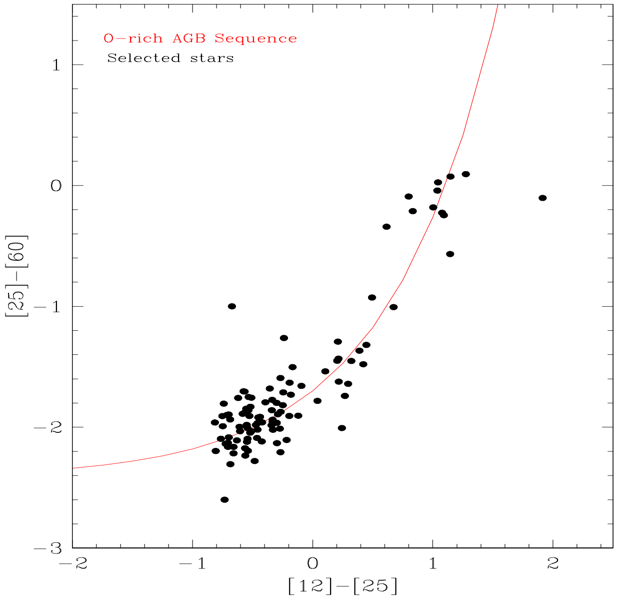

FIGURE 4.1— IRAS two-colour diagram [12]−[25] *vs* [25]−[60], where the positions of all the sources in the sample are represented (black dots). The red continuum line is the "O-rich AGB sequence" (see text) which indicates the sequence of colours expected for O-rich AGB stars surrounded by envelopes with increasing thickness and/or mass loss rates (Bedijn 1987).

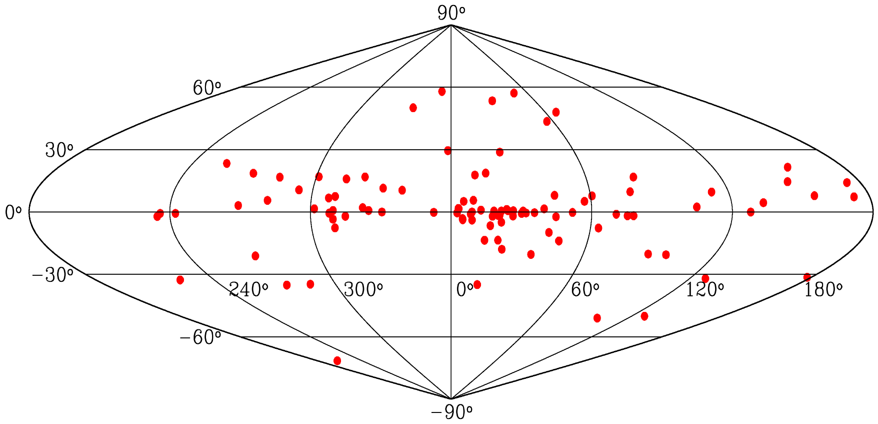

FIGURE 4.2— Galactic distribution of the sources in the sample (red dots).

located at high galactic latitudes).

The distribution of OH expansion velocities and periods for all the sources

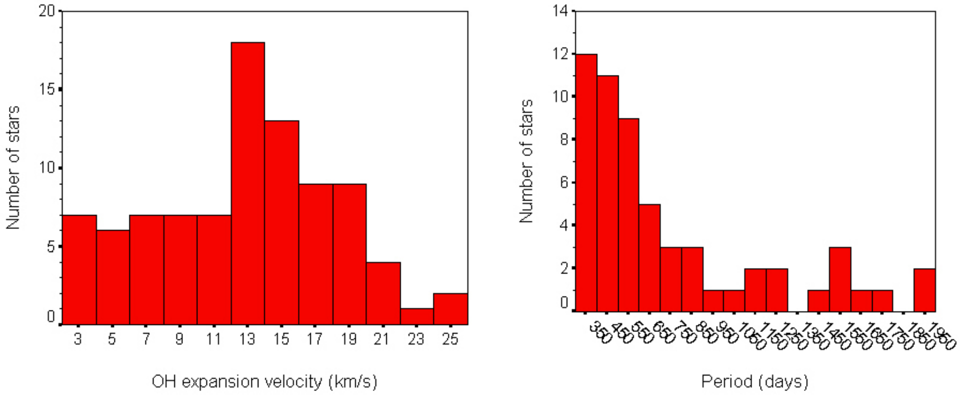

FIGURE 4.3— Distribution of OH expansion velocities (in km s^{-1}, left panel) and periods (in days, right panel) for the sources in the sample. The bin size is 2 km s^{-1} and 100 days for the OH expansion velocity and period distribution, respectively.

in the sample is displayed in Figure 4.3. These distributions show the wide range of expansion velocities (ranging from 3 to 25 km s^{-1}) and periods (from 300 to 2000 days) covered by our programme stars.

4.3 Observations and data reduction

The observations were carried out during several observing periods in 1996-1997. High-resolution spectra were obtained using the Utrecht Echelle Spectrograph (UES) installed at the Nasmyth focus of the 4.2 m William Herschel Telescope at the Spanish Observatorio del Roque de los Muchachos (La Palma, Spain) over three different observing runs in August 1996 (run #1), June 1997 (run #2) and August 1997 (run #3) and the CAsegrain Echelle SPECtrograph (CASPEC) of the ESO 3.60 m telescope at the European Southern Observatory (La Silla, Chile) in February 1997 (run #4). The full log of the spectroscopic observations is shown in Table 4.4, including more detailed information on the telescopes, dates of the observations, instrumentation used in each run, spectral dispersion, as well as on the spectral range covered.

We used a TEK 1124 × 1124 CCD as a detector during the first run at the 4.2m WHT using UES in August 1996 and a SITe1 2148 × 2148 CCD during the second and third runs in June 1997 and August 1997, respectively. Since we were mainly interested in the spectral range between 6000 Å and 8200 Å, we used the 31.6 lines/mm grating in order to provide the full coverage of this spectral region in a single spectrum. With a central wavelength around

Table 4.1— The sample of galactic O-rich AGB stars

IRAS name	Other names	Galactic Coord.	Var[1]	SpTyp[2]	[12]−[25]	[25]−[60]
01037+1219	WX Psc	128.64 −50.11	Mira	M10	−0.192	−1.632
01085+3022	AW Psc	127.96 −32.04	Mira	M9	−0.331	−2.021
01304+6211	V669 Cas	127.81 −0.02	Mira	...	+0.494	−0.927
02095−2355	IRC−20029	206.68 −71.55	...	M6	−0.748	−1.992
02316+6455	V656 Cas	133.61 +4.46	Mira	M8	−0.463	−2.089
03507+1115	IK Tau	177.95 −31.41	Mira	M9e	−0.725	−2.137
04404−7427	SY Men	286.97 −34.74	Mira	...	−0.297	−2.132
05027−2158	T Lep	222.67 −32.71	Mira	M7e	−0.706	−2.129
05073+5248	NV Aur	156.44 +7.83	Mira	M10	+0.204	−1.450
05098−6422	U Dor	274.30 −35.16	Mira	M7e	−0.510	−1.756
05151+6312	BW Cam	148.28 +14.57	Mira	M9	−0.698	−2.084
05559+3825	V373 Aur	173.24 +7.27	Mira	M9−10	−0.563	−2.174
06297+4045	IRC+40156	174.11 +14.12	...	M8	−0.094	−1.658
06300+6058	AP Lyn	154.31 +21.52	Mira	M7+	−0.357	−1.680
07080−5948	NSV 3436	270.50 −21.14	...	...	−0.631	−2.109
07222−2005		234.58 −2.16	...	M9	−0.733	−2.600
07304−2032	Z Pup	235.90 −0.69	Mira	M5e	−0.752	−1.908
07445−2613	SS Pup	242.43 −0.69	Mira	M6e	−0.807	−2.197
09194−4518	MQ Vel	269.09 +3.10	Mira	...	−0.273	−2.012
09429−2148	IW Hya	255.80 +23.35	Mira	M9	−0.217	−2.106
10189−3432	V Ant	271.03 +18.61	Mira	M7e	−0.561	−2.235
10261−5055	VZ Vel	281.31 +5.57	SRa	M6e	−0.542	−2.096
11081−4203		283.71 +16.75	...	Me	−0.699	−1.895
11525−5057		294.00 +10.65	...	...	−0.299	−1.964
12377−6102		301.63 +1.52	Mira	...	−0.195	−1.907
12384−4536		301.08 +16.94	...	...	−0.120	−1.905
13203−5536		307.45 +6.71	...	...	−0.249	−1.818
13328−6244		308.00 −0.56	...	...	+0.295	−1.641
13341−6246		308.14 −0.63	L	...	−0.300	−1.799
13379−5426		310.14 +7.48	...	...	−0.290	−1.893
13442−6109	OH309.6+.7	309.62 +0.73	...	M10	−0.337	−1.774
13475−4531	V618 Cen	313.60 +15.88	Mira	Me	−0.764	−2.096
13517−6515		309.51 −3.46	...	...	+0.040	−1.782
14086−0730	IO Vir	334.78 +50.12	Mira	M8	−0.333	−1.938
14086−6907		310.04 −7.61	...	...	−0.333	−1.955
14247+0454	RS Vir	352.67 +57.97	Mira	M5e	−0.553	−1.847
14266−4211		321.67 +16.84	...	...	−0.547	−2.121
14337−6215		314.87 −2.09	...	...	−0.518	−1.831
15099−5509	RAFGL 4212	322.26 +2.10	...	...	−0.267	−1.873
15193+3132	V S CrB	49.47 +57.17	Mira	M6e	−0.510	−2.034
15211−4254		330.43 +11.47	...	...	−0.609	−1.997
15255+1944	WX Ser	29.51 +53.48	Mira	M8e	−0.483	−2.280
15303−5456		324.83 +0.69	...	...	+0.421	−1.479
15576−1212	FS Lib	358.44 +29.52	Mira	M8−9	−0.535	−1.860
15586−3838	NSV 7388	338.79 +10.48	...	...	−0.672	−1,785
16030−5156	V352 Nor	330.50 +0.01	Mira	M4e	−0.438	−1.914
16037+4218	V1012 Her	66.88 +48.00	...	M8	−0.549	−1.981
16260+3454	V 697 Her	56.37 +43.53	Mira	M9	−0.245	−1.712
16503+0529	RX Oph	23.69 +28.78	Mira	M5	−0.687	−1.936
17034−1024	V850 Oph	10.68 +17.76	Mira	M8	−0.543	−2.007
17103−0559		15.57 +18.70	...	...	−0.539	−2.195
17239−2812		352.61 −0.18	...	...	−0.268	−1.593

IRAS name	Other names	Galactic Coord.	Var[1]	SpTyp[2]	[12]−[25]	[25]−[60]
17359−2138		5.40 +5.09	...	M7	−0.705	−2.163
17433−1750	GLMP 637	9.56 +5.61	...	...	+1.144	−0.567
17433−2523		3.10 +1.68	...	...	−0.421	−1.960
17443−2519	RAFGL 5386	3.29 +1.52	...	...	+0.322	−1.452
17501−2656	V4201 Sgr	2.58 −0.43	SR	M8−9	−0.239	−1.262
18025−2113	IRC−20427	8.93 −0.01	...	cM4	−0.167	−1.503
18050−2213	VX Sgr	8.34 −1.00	SRc	M4eIa	−0.740	−1.805
18057−2616	SAO 186357	4.89 −3.18	...	M	−0.575	−1.703
18071−1727	OH 12.8+.9	12.75 +0.89	...	...	+1.275	+0.094
18083−2630	NSV 24316	4.97 −3.73	...	M6	+0.243	−2.007
18172−2305		8.95 −3.89	...	...	−0.459	−2.020
18198−1249	OH 18.3+.4	18.30 +0.43	...	...	+1.092	−0.246
18257−1000	V441 Sct	21.46 +0.49	Mira	...	+1.038	−0.042
18273−0738	V436 Sct	23.73 +1.23	Mira	...	+0.105	−1.538
18276−1431	V445 Sct	17.68 −2.03	Mira	...	+1.914	−0.103
18304−0728	IRC−10434	24.21 +0.63	...	M5r	−0.394	−1.794
18312−1209		20.18 −1.70	...	...	+0.447	−1.319
18314−1131	NSV 24500	20.76 −1.46	...	M6	−0.533	−1.750
18348−0526	V437 Sct	26.54 +0.62	Mira	...	+0.615	−0.341
18413+1354	V837 Her	44.56 +8.02	Mira	M8III	−0.424	−2.118
18429−1721	V3952 Sgr	16.84 −6.60	Mira	M9	−0.527	−1.907
18432−0149	V1360Aql	30.71 +0.42	Mira	...	+0.799	−0.091
18437−0643	V440 Sct	26.42 −1.93	Mira	...	+0.389	−1.367
18454−1226	IRC−10463	21.53 −4.92	...	M6	−0.685	−2.306
18460−0254	V1362 Aql	30.09 −0.68	Mira	...	+1.003	−0.181
18488−0107	V1363 Aql	31.99 −0.49	Mira	...	+1.043	+0.026
18549+0208	OH 35.6−.3	35.57 −0.34	...	...	+0.833	−0.212
18560+0638	V1366 Aql	39.71 +1.50	Mira	...	+0.210	−1.292
19059−2219	V3880 Sgr	14.66 −13.61	Mira	M8	−0.343	−1.984
19129+2803		60.67 +7.74	...	...	−0.521	−2.045
19147+5004	TZ Cyg	81.22 +16.80	Lb	M6	−0.659	−2.163
19157−1706	RAFGL 2361	20.53 −13.55	...	...	−0.458	−1.965
19161+2343	RAFGL 2362	57.12 +5.12	...	...	+0.217	−1.623
19192+0922	NSV 24761	44.79 −2.31	...	...	+0.215	−1.433
19254+1631	GLMP 915	51.80 −0.22	...	...	+1.077	−0.226
19361−1658	NSV 24833	22.74 −17.93	...	M8	−0.268	−2.207
19412+0337	V1415 Aql	42.34 −9.86	Mira	M9	−0.583	−1.889
19426+4342		77.48 +9.73	...	...	−0.659	−2.216
20052+0554	V1416 Aql	47.37 −13.95	Mira	M9	−0.453	−1.919
20077−0625	V1300 Aql	36.36 −20.42	Mira	M	−0.182	−1.731
20109+3205	V557 Cyg	70.47 −1.08	Mira	M7	−0.562	−1.876
20181+2234	V371 Vul	63.44 −7.72	Mira	...	+0.268	−1.741
20272+3535	GLMP 999	75.27 −1.84	...	...	+1.147	+0.074
20343−3020	RT Mic	13.59 −34.91	Mira	...	−0.605	−2.033
20350+3741	V1828 Cyg	77.90 −1.84	Mira	M7	−0.814	−1.961
22177+5936	NSV 25875	104.91 +2.41	...	...	+0.673	−1.006
22180+3225	YZ Peg	89.60 −20.24	...	...	−0.620	−1.758
22466+6942		112.69 +9.59	...	...	−0.472	−1.981
22510+3614	NSV 14347	97.90 −20.56	...	M7	−0.567	−1.705
23492+0846	DO 8089	99.10 −51.03	...	M5	−0.716	−1.900

[1] Variability types taken from the Combined General Catalogue of Variable Stars (GCVS, Kholopov 1998). Mira: Mira-type variable; SRa, SRb, SRc: A-, B- or C-type semiregular variable; L, Lb: irregular variable.

[2] Spectral types taken from Kwok et al. (1997) and references therein.

TABLE 4.2— The sample of comparison stars

IRAS name	Other names	Galactic Coord.	Var[1]	SpTyp[2]	[12]−[25]	[25]−[60]
00213+3817	R And	117.07 −23.98	Mira	S5/4.5e	−0.723	−2.104
02192+5821	S Per	134.62 −2.19	SRc	M4eIa	−0.407	−1.897
10436−3459	Z Ant	275.86 +20.94	SR	S5.4	−0.830	−2.172
18397+1738	V821 Her	47.78 +10.01	Mira	Ce	−0.873	−1.499
19133−1703	T Sgr	20.32 −13.01	Mira	S5/6e	−1.125	−1.372
20166+3717	WX Cyg	75.43 +0.87	Mira	C9,2eJ	−1.191	+1.445
23416+6130	PZ Cas	115.06 −0.05	SRc	M3vIa	+0.070	−1.538
23554+5612	WY Cas	115.57 −5.62	Mira	S6/6e	−0.633	−1.286
23587+6004	WZ Cas	116.76 −1.91	SRc	SC7/10e	−1.280	−1.348

[1] Variability types: see note in Table 4.1.
[2] Spectral types taken from Kwok et al. (1997) and references therein. C: carbon star; S: star with s-process enrichment.

TABLE 4.3— The sample of peculiar carbon AGB stars

IRAS name	Other names	Galactic Coord.	Var[1]	SpTyp[2]	[12]−[25]	[25]−[60]
00247+6922	V668 Cas	120.86 +6.87	Mira	C	−0.774	−1.762
04130+3918	RAFGL 6312	160.41 −8.09	...	C	−1.273	−1.633
09425−6040	GLMP 260	282.04 −5.88	...	C	+0.790	−1.045
17297+1747	V833 Her	40.80 +25.30	Mira	C	−0.340	−1.859
19321+2757	V1965 Cyg	62.57 +3.96	Mira	C	−0.703	−1.598
19594+4047	V1968 Cyg	76.52 +5.59	Mira	C	−0.285	−1.594
20072+3116	V1969 Cyg	69.35 −0.87	Mira	C	−0.644	−1.483
23166+1655	LL Peg	93.53 −40.35	Mira	C	+0.101	−1.238
23320+4316	LP And	108.46 −17.15	Mira	C	−0.777	−1.555

[1] Variability types: see note in Table 4.1.
[2] Spectral types taken from Kwok et al. (1997) and references therein. C: carbon star.

TABLE 4.4— Log of the spectroscopic observations

Run	Telescope	Instrumentation	Dates	Dispersion (Å/pix)	Spectral Range (Å)
#1	4.2m WHT	UES	16-17 August 1996	0.065	5300-9400
#2	4.2m WHT	UES	10-12 June 1997	0.065	4700-10300
#3	4.2m WHT	UES	18-20 August 1997	0.065	4700-10300
#4	3.6m ESO	CASPEC	21-24 February 1997	0.085	6000-8200

6700 Å our spectra extended over ∼4000 Å during the first run and ∼6000 Å during the second and third runs. The spectra were taken with a separation between orders of around 21 pixels (or 7.5”), which is large enough to allow sky subtraction, taking into account the fact that the targets in our sample are non-extended. The resolving power was around 50,000, equivalent to a spectral resolution of 0.13 Å around the Li I line at 6708 Å. The selected setup covered the spectral regions from 5300 Å to 9400 Å in about 47 orders with small gaps in the redder orders for the first run, while the 4700–10300 Å region was covered in about 61 orders without any gaps for the second and third runs.

The CASPEC spectra, taken at the ESO 3.6m telescope, covered the wavelength range from 6000 Å to 8200 Å. The red cross-disperser (158 lines/mm) was used, which gave a resolving power of ∼40,000 (equivalent to a spectral resolution of ∼0.17 Å around the Li I line at 6708 Å) and an adequate interorder separation, using the TEK 1024 × 1024 CCD as a detector. With this setup, we covered the selected spectral region in about 27 orders with small gaps only in the redder orders.

The observational strategy was similar in all runs. Since the stars of the sample are known to be strongly variable, typically 3–4 magnitudes in the R band and in the V band sometimes more than 8 magnitudes, once at the telescope, we determined the exposure time according to the brightness of the source at the moment of the observation. First we took one very short exposure (2 to 5 minutes) intented to i) confirm the identification of the source as a very late-type M star; ii) better estimate the exposure time of the longer exposure (avoiding saturation in the red if possible). Many of these stars can saturate the detector at the red end of the spectral range covered, while no signal is detected in the blue. If the image was saturated in the red with such a short exposure, we took another, even shorter one. The last exposure was always long enough to obtain a high S/N ratio ($\geq$100 if possible) in the region around 6708 Å (the lithium line) in order to resolve this narrow absorption line, which is usually veiled at these wavelengths by the characteristic molecular bands which dominate the optical spectrum of these extremely cool stars. The typical exposure times ranged between 10 and 30 minutes, according to the brightness of the source. However, for a few very faint stars, two 30-minute spectra were taken (and later co-added in order to increase the S/N ratio of the final spectrum). Adopting this strategy, typical S/N ratios of $50-150$ were achieved around the Li I line at 6708 Å. Because of the very red colours of the sources observed, the S/N ratios achieved in the reduced spectra can strongly vary from the blue to the red orders. Typically, at ∼6000 Å the S/N ratio can be as low as only 10-20, while at ∼8000 Å the S/N ratio is usually much higher than 100.

All the 102 O-rich stars (see list in Table 4.1) were tried, but useful spectra were obtained only for 57 (56%). The remaining 45 (44%) sources were either too red to obtain any useful information on the strength of the Li I line at

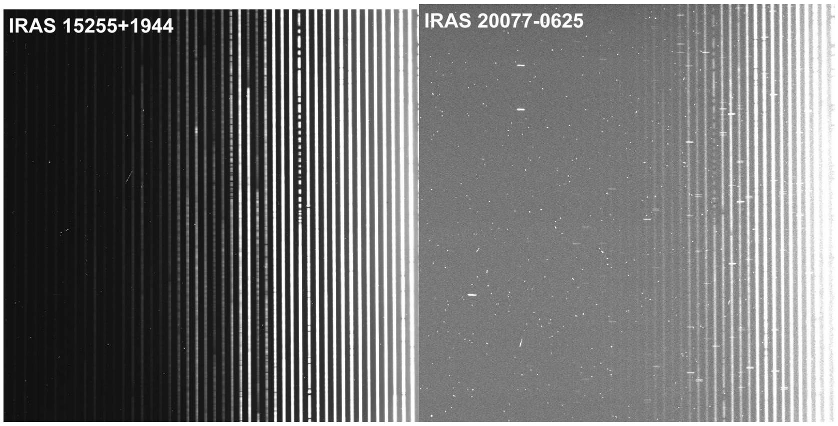

FIGURE 4.4— UES echelle spectra of the two observed O-rich AGB stars IRAS 15255+1944 (blue example, left panel) and IRAS 20077−0625 (red example, right panel). The orders are in the vertical direction, with the wavelength increasing from the bottom to the top and from the left to the right. The spectra cover the range from 5300 to 9400 Å. The 6700 Å region is located close to the center of the CCD.

6708 Å or the optical counterpart was simply not found, in the most extreme cases. Two examples, one of a "blue" echelle spectrum and another one of a "red" echelle spectrum are displayed in Figure 4.4. The spectra correspond to IRAS 15255+1944 (left panel), which shows an intense lithium absorption line and IRAS 20077−0625 (right panel) which was too red at this wavelength range to make any kind of analysis. The integration time for these spectra was 30 minutes in both cases. A few bright galactic M-supergiants together with some known galactic C-, SC-, and S-type AGB stars were also observed for comparison (see list in Table 4.2). Some of them were known to be among the most Li-rich stars in the Galaxy. As we have already mentioned in Section 4.2, 9 stars in the initial sample turned out to be carbon stars when observed and not O-rich, as initially suspected (see list in Table 4.3). Finally, some hot stars with high rotation velocity were also observed for calibration purposes. They were used to identify and subtract the contribution from telluric absorptions (sometimes very strong in the red) from the target stars. Thus, the total number of objects observed considering all runs was 120.

During the observations, some targets with known, relatively bright optical counterparts (in the Digitized Sky Survey 'DSS') did not show any optical counterpart. On the other hand, some other targets without any optical counterpart in the DSS appeared as considerably bright stars at the telescope. In Figure 4.5, the DSS finding charts of two of the O-rich AGB stars in the sample

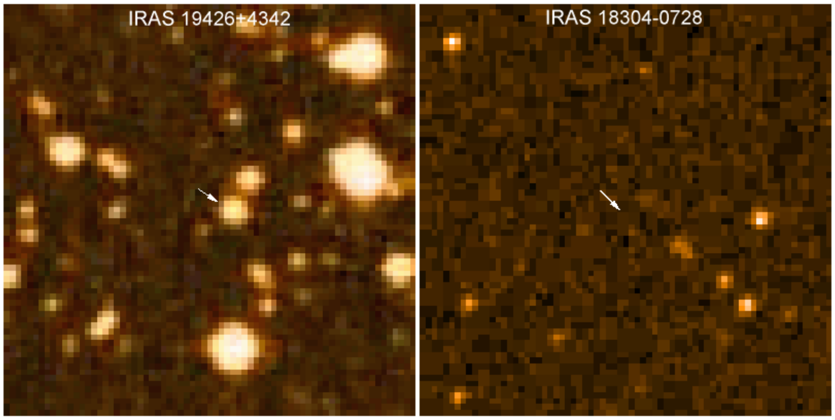

FIGURE 4.5— DSS finding charts of two O-rich AGB stars in the sample showing a strong variability: IRAS 19426+4342 (left panel), not detected during our observations, and IRAS 18304−0728 (right panel), found to be considerably bright at the telescope. The image size is 2 × 2 arcmin in both cases and the position of the target is marked with a white arrow.

are displayed. IRAS 19426+4342 (left panel) is a relatively bright source in the optical DSS image but no optical counterpart was found during our first and third observing campaigns. In contrast, the DSS image of the field around IRAS 18304−0728 (right panel) did not exhibit any optical counterpart while it was clearly detected as a bright optical source during our third run observations.

For wavelength calibration purposes, several Th–Ar calibration lamp exposures were also taken every night during the UES runs. In the case of the CASPEC observations, these calibration lamp exposures were taken before or after any science exposure at the position of the target in order to keep control of possible dispersion changes with the telescope position. Note that with UES the system is more stable because the instrumentation is located at the Nasmyth focus of the 4.2m WHT telescope. Finally, the corresponding bias and flat–field images were also taken at the beginning of the night (or at the end). Photometric standard stars were not observed because we were not interested in absolute flux calibration.

The two-dimensional frames containing the echelle spectra were reduced to single-order one-dimensional spectra using the standard ECHELLE software package as implemented in IRAF[4]. The data reduction process can be summa-

---

[4] Image Reduction and Analysis Facility (IRAF) software is distributed by the National Optical Astronomy Observatories, which is operated by the Association of Universities for Research in Astronomy, Inc., under cooperative agreement with the National Science Foundation.

rized as follows:

a) Bias-level subtraction (IRAF task CCDPROC).

b) Search and trace of apertures using a reference bright star in all orders (IRAF tasks APFIND and APTRACE).

c) Scattered-light subtraction (IRAF task APSCATTER).

d) Construction of a normalized flat-field image to remove pixel-to-pixel sensitivity fluctuations (IRAF task APNORMALIZE).

e) Extraction of the orders (IRAF task APSUM).

f) Wavelength calibration. The wavelength calibration was made using the Th-Ar comparison lamps. We selected non-saturated Th-Ar emission lines and adjusted third-fourth order polynomials. The calibration fit accuracy was always better than 20 m$\AA$ (IRAF tasks ECIDENTIFY, ECREIDENTIFY and DISPCOR).

g) Identification of terrestrial features (telluric absorption lines) comparing the target spectra with the spectrum of a hot, rapidly rotating star. However, it should be noted that the majority of the spectral ranges which were used in the abundance analysis are not significantly affected by these terrestial features. The IRAF task TELLURIC was used for instance to eliminate the telluric absorption lines around the K I line at 7699 Å.

4.4 A qualitative approach

4.4.1 Overview of the main spectroscopic properties

We detected the presence of the Li I resonance line at 6708 Å in 25% of the sources in the sample (25 stars) with a wide variety of strengths, while we did not find any signature of this line in 31% (32 stars) of the stars. The remaining 44% (45 stars) were too red or simply the optical counterpart was not found at the moment of the observations. Sample spectra of stars showing increasing strengths in the Li I line at 6708 Å are presented in Figure 4.6.

In general, all stars (with or without lithium) show extremely red spectra with the flux level falling dramatically at wavelengths shorter than 6000 Å. In addition, the spectra are severely dominated by strong molecular bands mainly due to titanium oxide (TiO), as a consequence of the very low temperature and the O-rich nature in these stars[5]. The bandheads of TiO at ∼6651, 6681, 6714,

---

[5] Note that, in contrast, the spectra of the few C-rich AGB stars found in our survey (see list in Table 4.3) are completely dominated by CN and C_2 absorption bands.

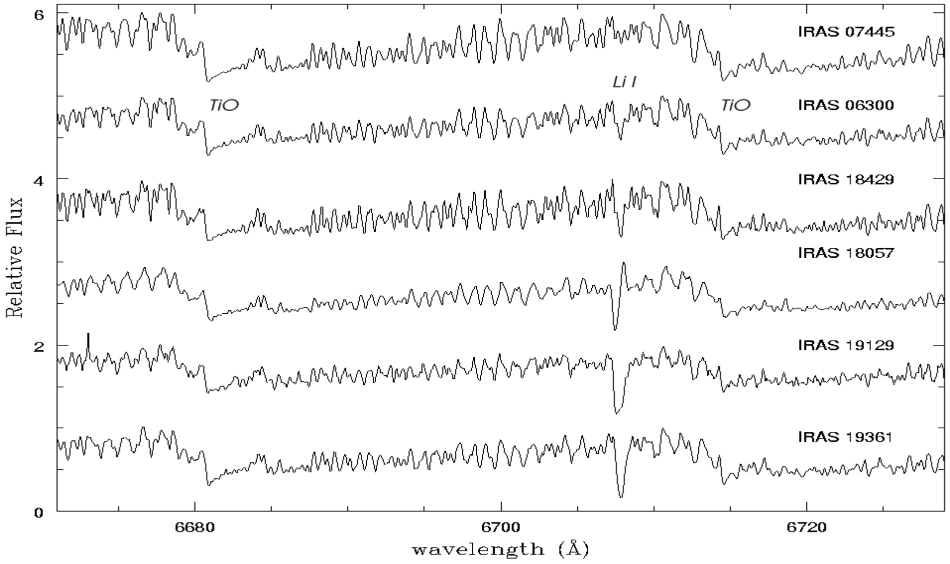

FIGURE 4.6— High resolution optical spectra of sample stars displaying increasing strengths of the Li I line at 6708 Å. Note the P-cygni type profile of the Li I line in IRAS 18057−2616. The jumps at 6681 and 6714 Å correspond to the bandheads of the TiO molecule.

7055, and 7125 Å are clearly present in all spectra. Interestingly, the bandheads of ZrO at ~6378, 6412, 6474, 6495, 6505 and 6541 Å seem to be absent. These ZrO bandheads (together with those corresponding to other s-element oxides such as LaO or YO) are very strong in galactic S-stars. The absence of these bands in our galactic O-rich AGB stars is clearly evidenced in Figure 4.7, where we show the spectral region around the ZrO bandheads at 6474 and 6495 Å in several sample stars compared to the well known S-stars WY Cas and R And. The TiO veiling effect is so intense that it is very difficult to identify individual atomic lines in the spectra of these stars, with the exception of the Li I line at 6708 Å, the Ca I lines at 6122 and 6573 Å, the K I line at 7699 Å, the Rb I line at 7800 Å and a few strong Fe I lines. In addition, the K I and Rb I lines are generally blue-shifted with respect to the Li I and Ca I lines and show complex profiles (with emission over absorption), indicating that their origin is probably circumstellar while the atmospheric layers where the Li I and Ca I lines are formed are deeper (see Subsection 4.4.3). Finally, some stars display H$_\alpha$ emission, which in this type of stars is generally interpreted as the consequence of the propagation of shock waves through the outer layers of the stellar atmosphere (see Subsection 4.4.4).

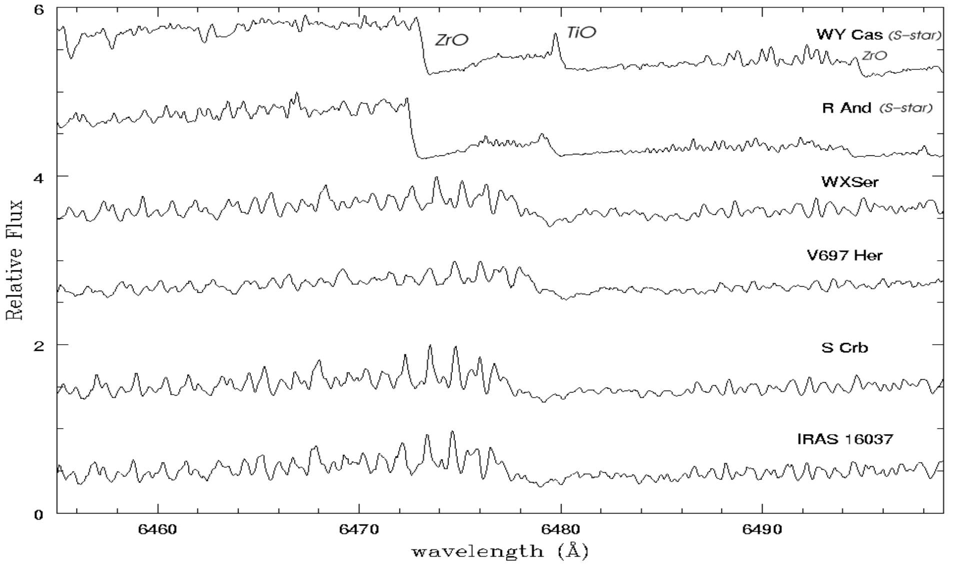

FIGURE 4.7— High resolution optical spectra of sample stars displaying the lack of the ZrO absorption bands at 6474 and 6495 Å compared with two galactic S-stars (WY Cas and R And). WX Ser (IRAS 15255+1944) and V697 Her (IRAS 16260+3454) are Li-detected while S CrB (IRAS 15193+3132) and IRAS 16037+4218 are Li non-detected. The absorption band at ~6480 Å correspond to the TiO molecule.

The complete sample has been divided in different groups on the basis of the detection or non-detection of the lithium line in Tables 4.5 and 4.6, respectively. A third group is formed by the stars that were too red (or which did not show any optical counterpart at the telescope), and they are listed in Table 4.7. The IRAS name, the run in which the stellar field was observed, the OH expansion velocities and the pulsational periods are listed in every table. The same information is also presented for the comparison stars in Table 4.8, which includes, as we have already mentioned, a few M-supergiants, bright C-, SC-, and S-AGB stars. For the sample of peculiar C-rich AGB stars found during the survey the same information is given in Table 4.9.

One source (IRAS 13442−6109) in our sample has been identified as a possible supergiant star. Supergiant stars are characterized by very high expansion velocities (> 20 km s^{-1}) and small and irregular photometric fluctuations with an amplitude of a few tenths of a magnitude, unlike AGB stars, which display quasi-sinusoidal and regular variations of several magnitudes in the optical and periods typically between 250 and 500 days. Another two stars (IRAS 18454−1226 and IRAS 23492+0846) with bright optical counterparts but un-

TABLE 4.5— Galactic O-rich AGB stars with lithium detected

IRAS name	Run	$v_{exp}(OH)$ (km s^{-1})	Ref.[1]	Period (days)	Ref.[1]
01085+3022	3	13.0	3	560	1
02095−2355	1	...	...	...	...
04404−7427*	4	7.7	1	534	2
05027−2158	4	7.9	1	368	1
05559+3825	3	single peak	4	590	3
06300+6058	3	12.3	2	440	4
07222−2005*	4	8.2	1	1245	10
07304−2032	4	7.4	5	509	1
09429−2148	4	12.0	2	650	1
11081−4203	4	single peak	1	...	...
11525−5057	4	single peak	1	...	...
12377−6102*	4	20.4	1	...	...
14337−6215	4	19.7	9	...	...
15211−4254	4	11.0	1	...	...
15255+1944	1	7.4	2	425	1
15576−1212	4	9.9	2	415	1
16030−5156	4	single peak	1	...	...
16260+3454	1	12.3	2	475	1
18025−2113	1	10.6	1	...	...
18057−2616	1	18.7	1	...	...
18413+1354	2	14.7	4	590	3
18429−1721	1	6.9	1	1508	10
19129+2803	2	single peak	1	423	10
19361−1658	2,3	7.5	1	...	...
20052+0554	2	15.6	12	450	3

[1] Reference for the OH expansion velocity and period of variability.

* Tentative classification because of the poor S/N ratio.

REFERENCES.-

a) OH expansion velocity: 1) te Lintel Hekkert et al. (1991); 2) te Lintel Hekkert et al. (1989) 3) Chengalur et al. (1993); 4) Slootmaker et al. (1985); 5) Sivagnanam et al. (1989); 6) Lewis, Eder & Terzian (1990); 7) Lewis, David & Le Squeren (1995); 8) Groenewegen et al. (2002) (CO data); 9) Sevenster et al. (1997); 10) Groenewegen & de Jong (1998); 11) Nyman et al. (1992); 12) Lewis (1994).

b) Period: 1) Combined General Catalogue of Variable Stars (GCVS), Kholopov (1998); 2) Whitelock et al. (1994); 3) Jones et al. (1990); 4) Lockwood (1985); 5) Engels et al. (1983); 6) Nakashima et al. (2000); 7) Slootmaker et al. (1985); 8) Le Bertre (1993); 9) Herman & Habing (1985); 10) Jiménez-Esteban (2004).

known expansion velocities and periods are also marked with a double asterisk as possible supergiants in Table 4.6. The reddened objects of our sample are more difficult to classify but they are expected to be extreme AGB stars (usu-

TABLE 4.6— Galactic O-rich AGB stars without lithium

IRAS name	Run	$v_{exp}(OH)$ (km s^{-1})	Ref.[1]	Period (days)	Ref.[1]
03507+1115	3	16.5	2	470	1
05098−6422	4	6.0	2	394	2
05151+6312	1	14.5	2	...	3
07080−5948	4	5.0	1	...	...
07445−2613	4	4.8	2	391	1
10189−3432	4	3.4	2	303	1
10261−5055	4	3.7	1	317	1
13379−5426	4	10.2	1	...	...
13442−6109**	4	23.7	1	...	...
13475−4531	4	3.7	1	...	...
14086−0730*	4	13.7	2	...	...
14086−6907*	4	13.4	1	...	...
14247+0454	4	4.0	2	354	1
14266−4211	4	9.1	1	...	...
15193+3132	1	3.3	2	360	1
15586−3838	4	9.3	1	...	...
16037+4218	1	3.5	1	365	10
16503+0529	2	3.8	3	323	1
17034−1024	2	single peak	1	346	1
17359−2138*	2	8.5	1	...	...
18050−2213	3	19.8	2	732	1
18304−0728	3	15.3	2	...	...
18454−1226**	3	single peak	1	...	...
19147+5004	1	12.6	1	...	...
19157−1706	2	14.7	1	...	...
19412+0337	2	14.5	6	440	3
20343−3020	3	8.4	1	349	2
20350+3741	3	...	...	450	3
22180+3225	1	4.3	3	...	...
22466+6942	1	5.6	1	408	6
22510+3614	1	2.8	3	...	...
23492+0846**	1	...	...	...	...

[1] See references in Table 4.5.
* Tentative classification because of the poor S/N ratio.
** Possible supergiant star.

ally supergiant stars have a bright optical counterpart). This is supported by the long periods (> 500 days) and large variability amplitudes which have been determined in many cases from the monitoring of their OH maser emission.

The detection of a strong Li I line in S Per (IRAS 02192+5821), classified in the literature as a possible galactic supergiant, is remarkable. Supergiant stars

TABLE 4.7— Galactic O-rich AGB stars for which no analysis was possible

IRAS name	Run	$v_{exp}(OH)$ (km s^{-1})	Ref.[1]	Period (days)	Ref.[1]	Opt.Count.
01037+1219	1,3	18.2	2	660	2	Too red
01304+6211	3	11.0	2	1994	7	...
02316+6455	3	15.5	7	534	3	Too red
05073+5248	3	16.9	2	635	1	Too red
06297+4045	3	12.0	2	536	10	Too red
09194−4518	4	11.3	1	...	...	Too red
12384−4536	4	13.2	1	...	...	Too red
13203−5536	4	12.7	1	...	...	...
13328−6244	4	25.1	1	...	...	...
13341−6246	4	16.7	1	...	...	Too red
13517−6515	4	17.9	1	...	...	...
15099−5509	4	18.8	1	...	...	Too red
15303−5456	4	24.0	1	...	...	...
17103−0559	2,3	15.3	1	425	10	...
17239−2812	3	20.7	1	...	...	...
17433−1750	3	15.0	1	...	...	Too red
17433−2523	3	19.9	1	...	...	Too red
17443−2519	3	16.1	1	...	...	...
17501−2656	3	23.0	1	928	8	Too red
18071−1727	3	11.0	2	1488	9	...
18083−2630	2,3	18.2	2	...	...	...
18172−2305	3	15.9	1	...	...	...
18198−1249	3	15.3	2	845	9	...
18257−1000	2,3	19.1	2	1975	9	...
18273−0738	2	14.3	2	700	5	Too red
18276−1431	2	12.0	2	890	9	Too red
18312−1209	3	12.3	1	...	...	...
18314−1131	3	single peak	1	...	...	Too red
18348−0526	2,3	13.9	2	1575	3	...
18432−0149	2,3	17.5	2	1140	5	...
18437−0643	2,3	12.1	2	652	9	...
18460−0254	2,3	20.2	2	1730	5	...
18488−0107	3	20.5	1	1540	4	...
18549+0208	3	13.7	1	840	9	...
18560+0638	1,2,3	16.0	2	1033	5	...
19059−2219	2,3	13.3	2	510	1	Too red
19161+2343	2,3	17.9	2	...	...	...
19192+0922	2,3	16.5	2	552	9	...
19254+1631	2	19.0	2	1162	9	Too red
19426+4342	1,3	8.6	1	...	...	Too red
20077−0625	1,3	12.3	2	680	1	Too red
20109+3205	3	5.7	1	382	1	...
20181+2234	1,3	11.2	2	...	...	...
20272+3535	3	12.0	2	1603	9	...
22177+5936	3	15.1	2	1215	9	...

[1] See references in Table 4.5.

Table 4.8— Comparison stars

IRAS name	Run	$v_{exp}(OH)$ (km s^{-1})	Ref.[1]	Period (days)	Ref.[1]
00213+3817	1	9.0	10	409	1
02192+5821[2]	1	14.5	2	822	1
10436−3459	4	11.3	1	104	1
18397+1738[3]	2	13.4	8	511	3
19133−1703	1	10	10	395	1
20166+3717	3	...	...	410	1
23416+6130[2]	1	26.5	2	925	1
23554+5612	1	15.5	10	477	1
23587+6004	1	...	...	186	1

[1] See references in Table 4.5.
[2] Star identified for the first time as a genuine AGB star.
[3] Note that for this C-rich star the expansion velocity was derived from CO data.

Table 4.9— Peculiar C-rich AGB stars

IRAS name	Run	$v_{exp}(CO)^2$ (km s^{-1})	Ref.[1]	Period (days)	Ref.[1]	Opt.Count.
00247+6922	3	17.2	8	650	3	...
04130+3918	3	...	...	470	10	Bright
09425−6040	4	...	...	...	...	Bright
17297+1747	2	15.2	11	520	3	Too red
19321+2757	2	24.4	8	625	3	Too red
19594+4047	3	20.5	8	783	3	...
20072+3116	2	25.6	8	550	3	Too red
23166+1655	3	15.1	8	520	3	...
23320+4316	3	14.7	8	620	3	Too red

[1] See references in Table 4.5.
[2] Note that for these C-rich stars the expansion velocity was derived from CO data.

are not expected to show a strong Li I line. According to our data, it looks like a true AGB star. Similarly, PZ Cas (IRAS 23416+6130), another source classified as a supergiant in the literature, shows a strong Li I absorption line and it is clearly identified as a SC-star and thus, we also identify it, for the first time, as a genuine AGB star, and not as a supergiant. Consistent with our AGB identification for the latter two sources, they are the only two stars with periods well beyond 500 days in Table 4.8. More interesting are the new detections of lithium lines in the peculiar mixed chemistry (C-rich and O-rich) stars IRAS 09425−6040 and IRAS 04130+3918. The detection of lithium is weak in the

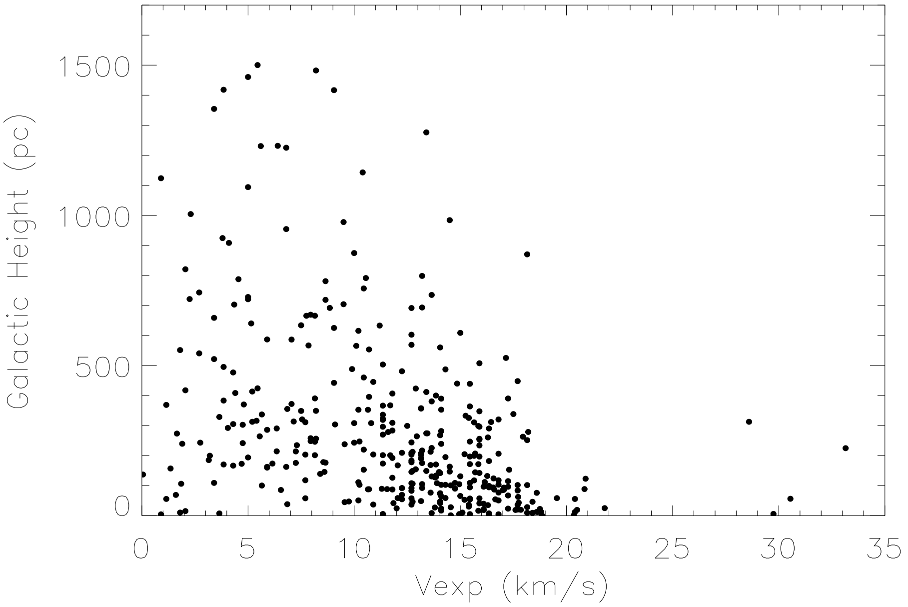

FIGURE 4.8— Galactic height distribution as a function of the OH expansion velocity for a large sample of OH/IR stars in the Galaxy (taken from Jiménez-Esteban 2004).

case of IRAS 04130+3918 but it is very strong in IRAS 09425−6040, which is studied in detail in García-Hernández et al. (2006). In addition, we also detected for the first time a strong lithium line in the C-rich AGB stars IRAS 20072+3116 (V1969 Cyg) and IRAS 23320+4316 (LP And) but the S/N ratios around 6700 Å are too poor to make a quantitative analysis. Finally, the S-star IRAS 10436−3459 (Z Ant) was observed for the first time with high resolution. IRAS 10436−3459 shows intense molecular bands of s-element oxides (like ZrO and LaO) but no lithium; it will be studied in detail elsewhere.

4.4.2 O-rich AGB stars and progenitor masses

Based on the fact that the group of OH/IR stars with the longer periods and larger expansion velocities shows a galactic distribution which corresponds to a more massive population, i.e. Baud et al. (1981), Baud & Habing (1983), Chen et al. (2001), it has been suggested that the periods of variability and the expansion velocities of the circumstellar envelopes of AGB stars showing OH maser emission must be correlated with the progenitor mass. Jiménez-

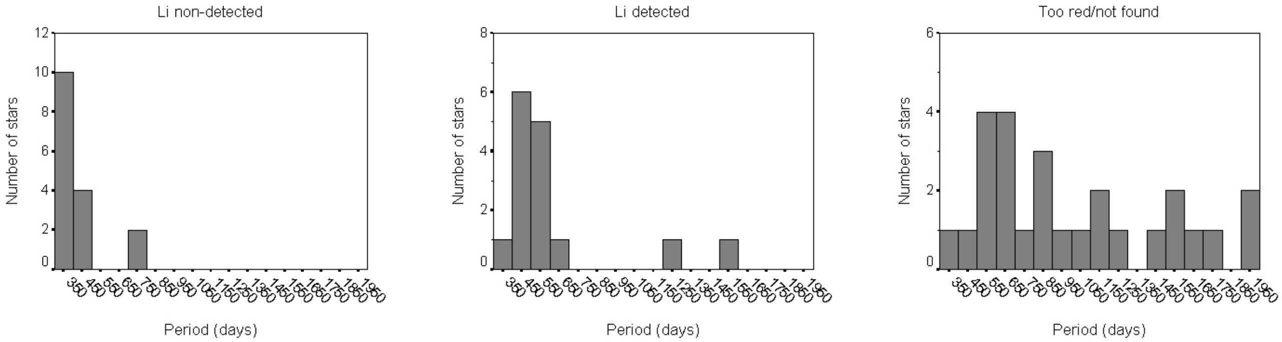

FIGURE 4.9— Distribution of periods (in days) for the Li non-detected (left panel), Li detected (middle panel) and too red/not found (right panel) sources. The bin size is 100 days in all cases.

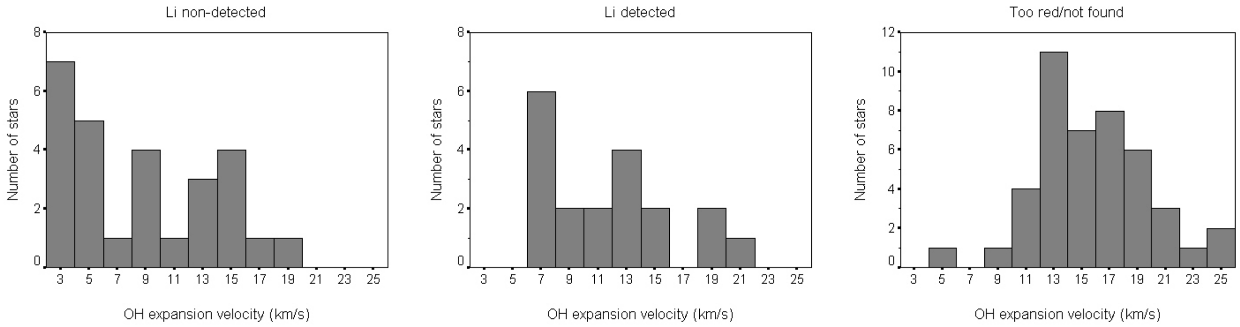

FIGURE 4.10— Distribution of OH expansion velocities (in km s^{-1}) for the Li non-detected (left panel), Li detected (middle panel) and too red/not found (right panel) sources. The bin size is 2 km s^{-1} in all cases.

Esteban (2004) has recently confirmed this hypothesis as far as the expansion velocities are concerned by studying a large sample (∼400 sources) of galactic OH/IR stars where a clear correlation is found between the galactic height and $v_{exp}(OH)$ (see Figure 4.8). In the following discussion we will assume that the period and the OH expansion velocity can be taken as valid distance-independent mass indicators and at the end we will review whether the results obtained are consistent with this hypothesis.

The distribution of variability periods and OH expansion velocities found for each of the subgroups identified in our sample are displayed in Figures 4.9 and 4.10, respectively. The same results are presented in a different way in Table 4.10 where we show how the sources with similar OH expansion velocity or variability properties are distributed among the different subtypes.

TABLE 4.10— Distribution of sources showing the same OH expansion velocity or variability properties among the different subgroups identified in the sample.

Period (days)	Observed	Li not detected	Li detected	Too red/Not found
<400	12	10 (84%)	1 (8%)	1 (8%)
400−700	26	4 (15%)	12 (46%)	10 (39%)
>700	18	1 (6%)	2 (11%)	15 (83%)

$v_{exp}(OH)$ (km s^{-1})	Observed	Li not detected	Li detected	Too red/Not found
<6	13	12 (92%)	0 (0%)	1 (8%)
6−12	25	6 (24%)	11 (44%)	8 (32%)
>12	53	10 (19%)	8 (15%)	35 (66%)

From Table 4.10, we can conclude that most of the AGB stars with the lower OH expansion velocities ($v_{exp}(OH) < 6$ km s^{-1}) are among those not detected in the Li I line (92%) while 44% of stars with OH expansion velocities between 6 and 12 km s^{-1} (but still observable in the optical) are detected as Li-strong sources. However, there are also stars with non-detection of lithium (24%) and stars too red or not found (32%) within this group. On the other hand, the majority of the stars in the group of heavily obscured sources (too red or not found) shows OH expansion velocities higher than 12 km s^{-1} (66%).

Similar statistics are obtained attending to the period of variability. Sources with relatively short periods, i.e. below 400 days, are predominantly non-Li detections (84%), while almost half of the stars showing periods between 400 and 700 days are Li detected (46%). Again, the same observational problems arise when we try to analyse the stars with the longer periods ($P > 700$ days), since most of them are completely obscured in the optical (83%).

Figure 4.11 (left panel) shows the distribution of the sources in the sample for which OH expansion velocities are available in the IRAS two colour-diagram [12]−[25] *vs* [25]−[60]. As can be seen from this diagram, on average, the sources with OH expansion velocities between 6 and 12 km s^{-1} are located towards higher [12]−[25] and [25]−[60] colour indexes (with a mean value of $<[12]-[25]>=-0.168$ and $<[25]-[60]>=-1.713$, respectively) with respect to those sources with OH expansion velocities below 6 km s^{-1} (which have a mean value of $<[12]-[25]>=-0.595$ and $<[25]-[60]>=-1.972$, respectively), which implies thicker circumstellar envelopes and/or larger mass loss rates. The sub-sample of stars with OH expansion velocities beyond 12 km s^{-1} is clearly located at even redder IRAS colour indexes (the mean values are $<[12]-[25]>=+0.007$ and $<[25]-[60]>=-1.495$). The position of the sources with the redder IRAS

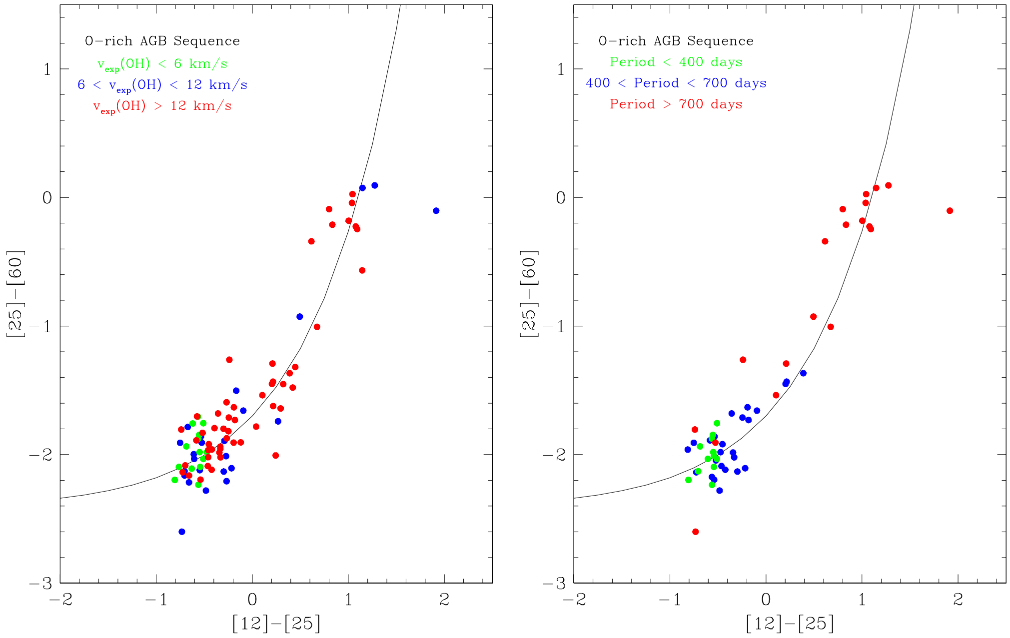

FIGURE 4.11— Distribution of the sources included in our sample in the IRAS two-colour diagram [12]−[25] *vs* [25]−[60] as a function of the OH expansion velocities (left panel) and periods (right panel). The continuum line is the "O-rich AGB sequence" (see text) which indicates the sequence of colours expected for O-rich AGB stars surrounded by envelopes with increasing thickness and/or mass loss rates (Bedijn 1987).

colour indexes would be consistent with a more advanced stage on the AGB if we assume that mass loss rate increases along this evolutionary phase. Alternatively, they may be among the more massive AGB stars, since in principle, they should be able to develop thick circumstellar envelopes even at an early stage in their AGB evolution, i.e. not necessarily in the late AGB phase. A similar behaviour is observed attending to the period of variability but the number of stars with known periods is significantly smaller (see Figure 4.11, right panel).

As we have already mentioned, it has been reported that the galactic distribution of OH/IR stars with large OH expansion velocities and periods of variability (e.g. $v_{exp}(OH)$ larger than ∼10−15 km s^{-1} and P > 500−600 days, respectively) is more concentrated towards the galactic plane with respect to the galactic distribution of the stars with lower OH expansion velocities and periods (Baud et al. 1981; Chen et al. 2001; Jiménez-Esteban 2004). Stars in

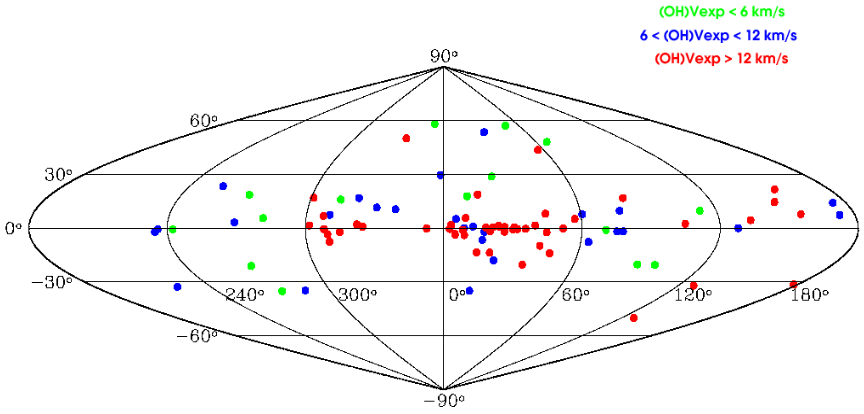

FIGURE 4.12— Galactic distribution of the sources in the sample as a function of the OH expansion velocities: $v_{exp}(OH) < 6$ km s^{-1} (green dots), $6 < v_{exp}(OH) < 12$ km s^{-1} (blue dots) and $v_{exp}(OH) > 12$ km s^{-1} (red dots).

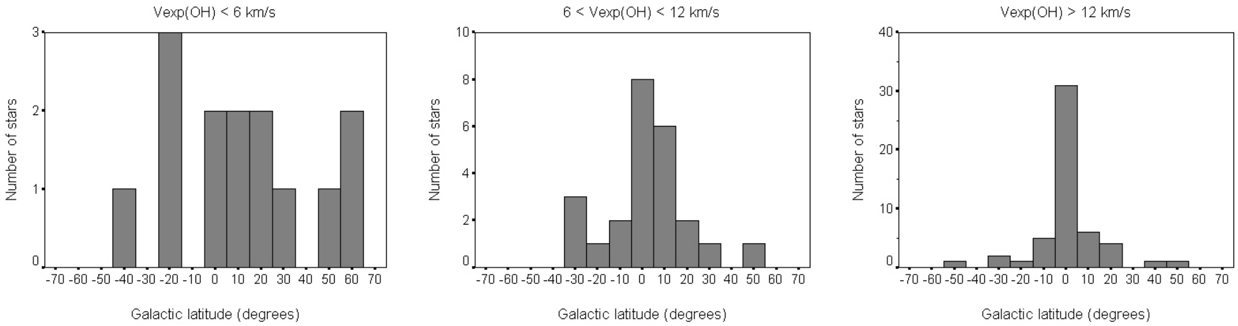

FIGURE 4.13— Galactic latitude distribution (in degrees) of the sources in our sample as a function of the OH expansion velocities: $v_{exp}(OH) < 6$ km s^{-1} (left panel), $6 < v_{exp}(OH) <$ 12 km s^{-1} (middle panel) and $v_{exp}(OH) > 12$ km s^{-1} (right panel). The bin size is 10 degrees in all cases.

our sample follow the same behaviour, although due to the limited number of stars considered we are unable to extract any statistical conclusion based on our data alone. This is illustrated in Figures 4.12 and 4.13, which show the galactic distribution of the sources in our sample as a function of $v_{exp}(OH)$.

If the detection of lithium is taken as a signature of HBB and the period and the OH expansion velocity are accepted as valid mass indicators, our results indicate that there are not HBB stars among those AGB stars in our sample with periods lower than 400 days and $v_{exp}(OH) < 6$ km s^{-1}, while some of the AGB stars with periods in the range 400−700 days and expansion velocities between 6 and 12 km s^{-1} may be HBB stars. According to the most recent HBB models (Mazzitelli, D'Antona & Ventura 1999) this would imply a minimum progenitor mass of ∼4 M$_{\odot}$. But, as we can see in Table 4.10, AGB stars within these range of periods and expansion velocities are also found among the stars in the other two subsamples. In addition, there are AGB stars in our sample with very long periods (P > 700 days) and very high expansion velocities ($v_{exp}(OH)$ > 12 km s^{-1}) for which lithium is not detected suggesting that a more detailed analysis is needed to reach any conclusion.

An important point to consider is that the non-detection of lithium does not necessarily imply a strong lithium underabundance; a more detailed analysis is always needed (see Chapter 5).

4.4.3 Origin of the atomic line absorptions

In order to determine the origin of the few atomic line absorptions detected in the stars in our sample we have computed the associated Doppler velocities. The atomic lines studied are the Li I line at 6707.8 Å, the Ca I lines at 6122.2 and 6572.8 Å, the K I line at 7699 Å and the Rb I line at 7800.3 Å. To do this, gaussian fits to these lines were performed using the task SPLOT in IRAF. Surprisingly, all Li detected stars (with the exception of IRAS 05027−2158) show considerable Doppler shifts in the K I, Rb I lines group with respect to the Li I and Ca I lines. The atomic lines of K I and Rb I are systematically blue-shifted with respect to the Li I and Ca I lines. Remarkably, the Doppler velocity of the TiO bandheads seen in all spectra coincide with that of the Li I and Ca I lines with just three exceptions (IRAS 14337−6215, IRAS 18025−2113 and IRAS 19129+2803). Only the latter three stars in our sample display a lithium line in which two absorption components (circumstellar and stellar) were resolved. The Doppler velocity of the circumstellar component coincides with that of the K I and Rb I lines, while the Doppler velocity of the lithium stellar component is the same observed in the TiO bandheads and Ca I lines. The values derived for each individual line under analysis, the mean Doppler velocity associated to the circumstellar K I, Rb I lines and to the stellar Li I, Ca I lines, and the difference between these mean Doppler velocities are presented in Table 4.11. Note that these velocities were not converted to any standard reference system, i.e. the local standard of rest "LSR" or the heliocentric system, because we are only interested in the detection of relative velocity shifts between atomic lines. Stars only tentatively classified as Li detected (IRAS 04404−7427, IRAS

Table 4.11— Doppler velocities[1] derived for stars in the Li detected subsample of galactic O-rich AGB stars

IRAS name	6122Å Ca I	6573Å Ca I	6708Å Li I	<V$_{stellar}$>	7699Å K I	7800Å Rb I	<V$_{circumstellar}$>	Δv[2]	V_{exp} (OH)
01085+3022	...	−54.8	−57.3	−56.0	−70.3	−60.9	−65.6	9.6	13.0
02095−2355	+38.7	+38.4	+39.9	+39.0	+32.8	+26.5	+29.7	9.3	6.0
05027−2158	+13.2	+14.8	+15.9	+14.6	+10.7	+12.3	+11.5	3.1	7.9
05559+3825	−48.6	−48.0	−49.1	−48.5	−61.4	−57.3	−59.3	10.8	...
06300+6058	...	−40.6	−40.4	−40.5	−57.2	−45.7	−51.4	11.0	12.3
07304−2032	+38.7	+44.3	+36.9	+40.0	+28.5	+35.4	+32.0	8.0	7.4
09429−2148	...	+56.6	+55.2	+55.9	+41.3	+43.8	+42.6	13.3	12.0
11081−4203	+46.9	+51.8	+50.5	+49.8	+35.2	+43.4	+39.3	10.4	...
11525−5057	+26.1	+28.8	+31.0	+28.6	+16.5	+19.9	+18.2	10.4	...
14337−6215[3]	...	−40.9	−41.4	−41.1	−65.3	−55.9	−60.6	19.5	19.7
15211−4254	...	−49.9	−49.5	−49.7	−63.0	−62.5	−62.8	13.1	11.0
15255+1944	+19.3	+20.6	+19.7	+19.9	+3.9	+6.0	+5.0	14.9	7.4
15576−1212	...	−42.5	−44.3	−43.4	−47.7	−47.8	−47.7	4.4	9.9
16030−5156	...	−32.3	−35.2	−33.8	−52.9	−38.9	−45.9	12.1	...
16260+3454	+56.3	+59.1	+59.3	+58.2	+41.6	+45.3	+43.4	14.8	12.3
18025−2113[3]	+32.4	+29.3	+31.2	+31.0	+1.6	+0.4	+1.0	30.0	10.6
18057−2616	+23.9	+22.1	+8.3	+22.1	+8.7	+16.7	+8.5	13.4	18.7
18413+1354	−42.2	−44.6	−44.2	−43.6	−60.2	−55.4	−57.8	14.1	14.7
18429−1721	...	+9.3	+9.9	+9.6	−2.6	+8.8	+3.1	6.5	6.9
19129+2803[3]	...	−3.0	0.8	−1.1	−15.1	−11.5	−13.3	12.2	...
19361−1658[4]	+32.8	+34.8	+33.0	+33.6	+22.0	+22.2	+22.1	11.4	7.5
19361−1658[5]	+65.9	+66.2	+65.6	+65.9	+53.6	+54.6	+54.1	11.8	7.5
20052+0554	...	−101.2	−101.6	−101.4	−118.9	−109.5	−114.2	12.8	15.6

[1] The estimated errors are expected to be less than 1 km s^{-1}.

[2] Difference between the mean Doppler velocities for each group of lines (stellar and circumstellar).

[3] The lithium line has a circumstellar component and the Doppler velocity corresponds to the stellar component.

[4] Observed during the second run.

[5] Observed during the third run.

07222−2005 and IRAS 12377−6102) were excluded from this analysis because of the poor S/N ratio. For the majority of the stars, the difference between the mean Doppler velocities of the stellar and circumstellar lines is of the order of the expansion velocity derived from the OH maser emission, which is also displayed in Table 4.11. In conclusion, our results confirm that the origin of the K I and Rb I absorption lines is very probably circumstellar and that the Li I and Ca I lines (as well as the TiO molecular bands) must be formed deeper in the stellar atmosphere.

4.4.4 H_α emission

Some of the stars included in our sample show in addition intense and variable H_α emission. Sometimes the H_α line is split into several components or shows complex profiles. The detection of variable H_α emission in late-type and variable stars has been the subject of studies by several authors during the past fifty years (Alvarez et al. 2001a, and references therein). The appearance/disappearance of hydrogen and metallic emission lines and the splitting of the Balmer emission lines into several components is a common feature in long-period variables (LPVs). Strong H_α emission is clearly observed only before the minimum brightness (phase ∼0.4) in late M-type Miras while it is already obvious at maximum brightness (phase ∼0.0) in early M- and S-type stars (e.g. Gillet 1988a, 1988b). Absorption line Doppler shifts correlated with the excitation potential of the lines and doubling of several absorption components around maximum light are also observed. This is interpreted as a clear signature of shock waves which propagate through the stellar photosphere (e.g. Alvarez et al. 2000b, 2001a, 2001b). However, Alvarez et al. (2001a) found that the line-doubling phenomenon is less frequent among the most extended and coolest LPVs (with periods higher than 250 days and spectral types later than M3). The stars in our sample are among the most extended and coolest LPVs ever studied. Thus, spectral changes are expected to be restricted to H_α. The detection of H_α emission in some of our stars might actually be an indication that they are being observed near their minimum brightness.

In Figure 4.14 we show the spectra of IRAS 19361−1658, taken in June and August 1997 (second and third runs, respectively). Both spectra only differ in the presence of a strong H_α emission line split into several components during the third run of observations, while H_α was not present during the second run. Unfortunately, the period and the variability type of this source are unknown. Nevertheless, we know that the source was considerably brighter in June 1997. This finding suggests that the star may have been near to its minimum brightness in August 1997.

4.5 Galactic S-stars versus Magellanic Cloud S-stars

4.5.1 Stellar masses

As we have mentioned in the introduction of this work, very strong Li overabundances are observed only in very few stars in our Galaxy. These are usually C-stars, SC-stars or S-stars, which are not among the most massive AGB stars; see for example Catchpole & Feast (1971,1976) and Abia et al. (1991). The low-mass nature of galactic S-stars is deduced from their galactic scale height

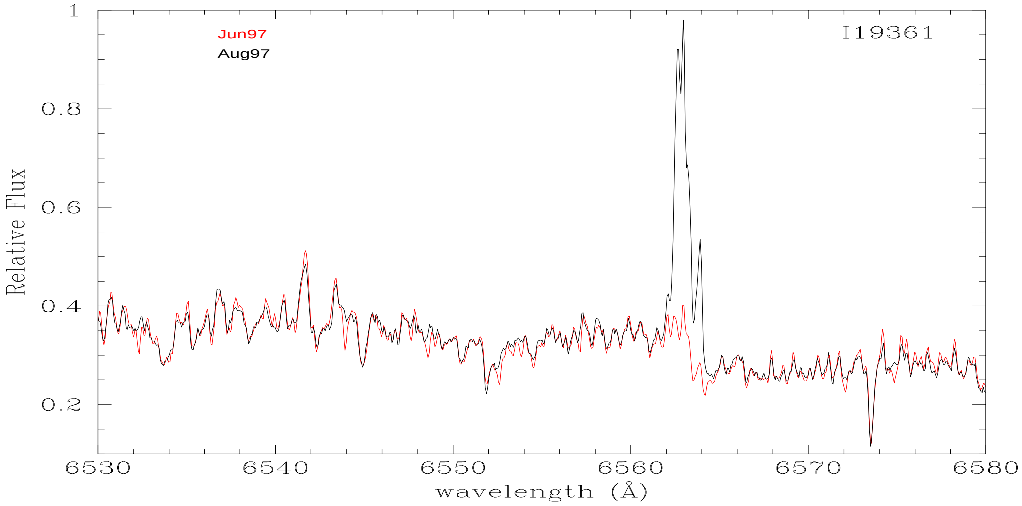

FIGURE 4.14— High resolution optical spectra of IRAS 19361−1658 taken during the second run in June 1997 (red line) and third run in August 1997 (black line) around H_α at 6563 Å. The absorption line at ∼6573 Å is from Ca I. Note the strong variations in the H_α line.

(H=200 pc according to Jura 1988 and Van Eck & Jorissen 2000), comparable to that of optical carbon stars, which are also considered to be low-mass stars. Actually, only ∼2−5% of the known galactic S-stars (from a sample of ∼200 S-stars) shows a strong lithium overabundance (Catchpole & Feast 1976; Boesgaard 1970). In constrast, practically all massive AGB stars of the MCs are S-type stars. They are O-rich, s-process enriched and most of them are also strongly Li-enriched (e.g. Plez et al. 1993; Smith et al. 1995). Our preliminary conclusion is that S-stars in our Galaxy seem to be completely different in nature to the S-stars in the MCs.

4.5.2 Li strengths

A rough estimate of the abundance of lithium in our galactic sample before a more detailed analysis is made (see Chapter 5) can be derived from the ratio of the equivalent widths of Li I 6708 Å to Ca I 6573 Å (Catchpole 1982). The Li I/Ca I line ratios are typically ∼1.0 in galactic S-SC stars which show lithium abundances less than or close to the solar value (Catchpole & Feast 1971; Catchpole 1982; Boesgaard 1970). This has usually been used to show that these S-SC stars are not among the most Li-rich stars in our Galaxy.

For this purpose, the equivalent widths of the Li I and Ca I lines at 6708 Å and 6573 Å measured with respect to the local continumm were derived for

TABLE 4.12— Equivalent widths of Li I 6708Å and Ca I 6573Å, together with the Li I/Ca I ratios derived for the galactic O-rich AGB stars in our sample belonging to the Li-detected group.

IRAS name	EW(Li I) (Å)	EW(Ca I) (Å)	EW(Li I)/EW(Ca I)[1]
01085+3022	0.245	0.134	1.82±0.41
02095−2355	0.247	0.402	0.61±0.01
05027−2158	0.448	0.342	1.31±0.02
05559+3825	0.315	0.319	0.99±0.05
06300+6058	0.383	0.306	1.25±0.11
07304−2032	0.359	0.211	1.70±0.06
09429−2148	0.329	0.232	1.42±0.11
11081−4203	0.393	0.333	1.18±0.07
11525−5057	0.088	0.225	0.39±0.02
14337−6215[2]	<0.630	0.256	<2.46±0.26
15211−4254	0.284	0.171	1.66±0.18
15255+1944	0.424	0.378	1.12±0.03
15576−1212	0.346	0.339	1.02±0.11
16030−5156	0.339	0.178	1.90±0.23
16260+3454	0.393	0.212	1.85±0.07
18025−2113[2]	<0.262	0.369	<0.71±0.03
18057−2616[3]	0.326	0.254	1.28±0.09
18413+1354	0.236	0.262	0.90±0.08
18429−1721	0.170	0.110	1.54±0.11
19129+2803[2]	<0.499	0.151	<3.30±0.46
19361−1658[4]	0.393	0.169	2.32±0.09
19361−1658[5]	0.425	0.158	2.69±0.16
20052+0554	0.349	0.183	1.90±0.36

[1] The error in the equivalent width is always less than 10% and it mainly depends on the S/N ratio of the spectrum.
[2] The lithium line has a circumstellar component and the EW is thus an upper limit.
[3] The lithium line has a P-cygni type profile.
[4] Observed during the second run.
[5] Observed during the third run.

all sources in the Li detected sample from the available spectra if the S/N ratio was good enough to obtain a reliable value. Note that the true "continuum" in these extremely cool stars is located well above the observed continuum. Therefore, the measured 'equivalent widths' shown in Table 4.12 are merely indicators of the relative strength of the Li I and Ca I lines and cannot be taken as absolute measurements. Remarkably, only 3 stars (14%) show Li I/Ca I ratios below 0.90, while 11 stars (50%) have Li I/Ca I ratios higher than 1.5, indicating that they may be more strongly lithium enriched than the galactic

S-SC stars studied by Catchpole & Feast (1976) and Boesgaard (1970).

The equivalent widths of the Li I line in our sample stars range from ∼0.20 to 0.60 Å . A similar range of equivalent widths for the lithium line were also found in the massive O-rich AGB stars HV 1719 (with 0.287 Å) and HV 11452 (with 0.638 Å) in the SMC. Their effective temperatures are ∼3200 K, i.e. approximately that expected for an M6 giant. Smith et al. (1995) estimated the lithium abundance for HV 1719 and HV 11452 as $log\ \varepsilon(Li)$∼1.5 and 3.8 respectively[6]. Thus, the subsample of Li detected galactic AGB stars in our sample may have a very similar range of Li overabundances.

In summary, the equivalent widths of the Li I line together with the Li I/Ca I ratios found in the stars listed in Table 4.12 suggest that the group of Li-detected O-rich AGB stars of our Galaxy must be Li-rich. In Chapter 5 we will derive the atmospheric parameters of these stars in order to estimate the Li abundances more quantitatively.

4.5.3 Enrichment in s-elements.

Concerning s-process elements, we can use the ZrO band at 6474 Å as an s-process enhancement indicator. Surprisingly, this band was not detected in any of the sources observed (see sample spectra around the 6474 Å region in Figure 4.7), nor were any of the atomic lines corresponding to s-process elements (e.g. Rb, Zr, Ba, Tc or Nd) in the classical spectral window 7400−7600 Å. In contrast, these s-element atomic lines and the ZrO band at 6474 Å are very strong in the galactic S-stars observed for comparison and in the massive MC AGB stars. Sample spectra of the region around 7565 Å are shown in Figure 4.15 where the position of some atomic lines of Zr I, Nd II and Fe I are indicated.

A qualitative study of the enrichment in s-process elements with respect to the Fe-peak elements can be made through the analysis of the ZrO/TiO absorption bands ratio using the ZrO band at 6474 Å and the TiO band at 7055 Å, respectively, as the most representative ones. The ZrO/TiO absorption band ratios can actually be used to separate s-process enriched AGB stars from normal s-process abundance supergiants (see Fig. 4 in Smith et al. 1995). Smith et al. (1995) found that all stars in the MCs with detectable Li I lines were true AGB stars, showing ratios ZrO/TiO ≥ 2. However, they also reported a considerable number of S-type stars with ZrO/TiO ≥ 2 without detectable Li I lines. In contrast, in our program stars ZrO bands were not detected in any of the target stars. The complete absence of detectable ZrO absorption bands together with the non-detection of atomic lines coming from s-process elements

---

[6] The lithium abundance is given in the usual scale 12+$log\ N(Li)$. In this scale the solar lithium abundance is 1.1.

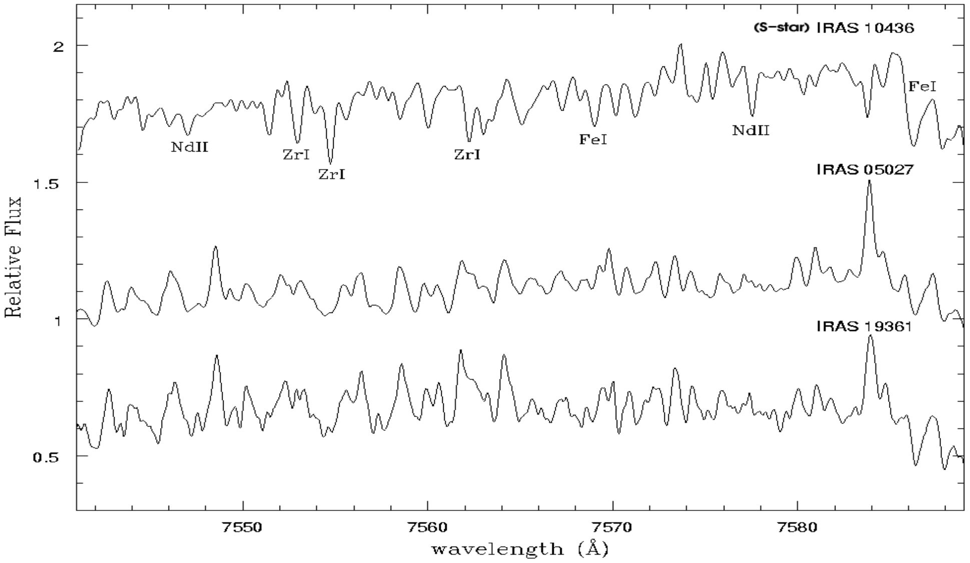

FIGURE 4.15— High resolution optical spectra of two stars in our sample where the lack of s-process element atomic lines (e.g. from Zr and Nd) around the 7565 Å region is shown in comparison with the galactic S-star IRAS 10436−3459. IRAS 05027−2158 and IRAS 19361−1658 show lithium lines with very different strengths. The positions of some atomic lines of Zr, Nd and Fe are indicated.

in the 7400−7600 Å spectral region suggest that the most massive O-rich AGB stars in our Galaxy are not S-stars, unlike those in the Magellanic Clouds. As for the lithium abundances, we will discuss in detail the s-element enrichment in our sample of galactic O-rich AGB stars in Chapter 5, where we will present a detailed abundance analysis.

4.6 Preliminary conclusions

We have carried out a qualitative analysis of a sample of 102 galactic O-rich AGB stars using high resolution optical spectroscopy (R∼40,000–50,000) aimed at studying their lithium abundance and enrichment in s-process elements in comparison with previous observations made on a similar group of massive AGB stars in the Magellanic Clouds.

We have detected the Li I 6708 Å line in ∼25% of the AGB stars in the sample with a wide variety of strengths while 31% did not show any signature of it. The remaining 44% of the sample was too faint at optical wavelengths at the moment when the observations were performed.

With just one exception, the O-rich AGB stars with the shorter periods (P < 400 days) and lower OH expansion velocities (v_{exp} < 6 km s^{-1}) did not show the Li I line at 6708 Å. However, half of stars with periods from ∼400 to 700 days and OH expansion velocities between 6 and 12 km s^{-1} were lithium detected. Stars with longer periods and larger OH expansion velocities were usually too red/not found at optical wavelengths and, therefore, we could not perform any kind of analysis on them. The non-detection of lithium in some stars with high expansion velocities and long periods will be discussed in the next Chapter.

The position of the sources with the larger OH expansion velocities (v_{exp} > 6 km s^{-1}) and longer periods (P > 400 days) in the IRAS two colour-diagram [12]−[25] *vs* [25]−[60] relative to the sources with lower OH expansion velocities and shorter periods indicates that these stars possess on average thicker circumstellar envelopes and/or have experienced higher mass loss rates in the recent past. In addition, their galactic distribution (especially for those stars with higher OH expansion velocities and longer periods) is closer to the galactic plane, suggesting that they represent a more massive progenitor population. These results confirm the validity of the assumptions made at the beginning of this Chapter that the period of variability and the OH expansion velocity of these stars are good distance-independent mass indicators. The three subsamples of galactic O-rich AGB stars defined on the basis of their different OH expansion velocities and periods are then suggested to represent stellar populations with different progenitor masses.

The Doppler velocity shifts found in the K I and Rb I absorption lines are attributed to their circumstellar origin. In contrast, the Li I and Ca I lines are formed deeper in the stellar atmosphere and, thus, show the same Doppler velocities as the molecular bands. We have also briefly discussed the origin of the strong, variable H_α emission detected in some of the AGB stars included in the sample. This is interpreted as the result of shock waves propagating through the stellar atmosphere.

The detection of strong Li I lines in a fraction of stars in our sample is interpreted as a clear signature of the HBB activation and, therefore, this group must be formed by massive O-rich AGB stars (M > 4 $M_\odot$). The measured Li I/Ca I ratios suggest that these stars are even more Li-enriched than the low- and intermediate-mass galactic S-SC stars previously studied in the literature. Contrary to what has previously been reported for massive AGB stars in the Magellanic Clouds, the galactic O-rich AGB stars do not show any enrichment in s-process elements; in other words, the most massive AGB stars in our Galaxy are not S-stars.

5

Li and s-elements in massive galactic O-rich AGB stars: A chemical abundance analysis

Most of the contents of this chapter have been submitted for publication to A&A García-Hernández, D. A., García-Lario, P., Plez, B., Manchado, A., D'Antona, F., Lub, J., Habing, H.

5.1 Introduction

Atmospheres of cool pulsating AGB stars present a major challenge for realistic, self-consistent modelling. At present, two types of self-consistent models exist: classical hydrostatic models and time-dependent dynamical models. Classical hydrostatic model atmospheres include a sophisticated treatment of micro-physical processes and radiative transfer, but neglect the effects of dynamics due to pulsation and winds (e.g. Plez, Brett & Nordlund 1992). Time-dependent dynamical models for stellar winds (Winters et al. 2000; Höfner et al. 2003, and references therein), on the other hand, tend to be based on crude descriptions of radiative transfer, pulsation, dust formation, and simplified micro-physics.

Propagating shock waves caused by stellar pulsation modify the structure of the atmosphere on local and global scales ("creating an extended atmosphere"), which can give rise to strong deviations from a hydrostatic stratification. The radiative field is dominated by the effect of molecular opacities or even by the dust grains forming in the cool outer layers of these atmospheres. Important micro-physical processes like chemistry and dust formation may be severely out of equilibrium. Given the performance of existing computers it is not feasible at present to model the coupled system of time-dependent hydrodynamics, detailed non-LTE radiative transfer and chemical non-equilibrium (Höfner et al. 2003).

However, the hydrostatic model atmospheres based on the MARCS code (Plez, Brett & Nordlund 1992) reproduce satisfactorily the observed spectra of C-rich AGB stars (e.g. Loidl, Lancon & Jörgensen 2001) and O-rich AGB stars (e.g. Alvarez et al. 2000a) in the optical domain. The optical spectra of massive O-rich AGB stars in the Magellanic Clouds (hereafter, MCs), for instance, have been successfully modelled with these hydrostatic models (e.g. Plez, Smith & Lambert 1993). For galactic O-rich AGB stars, however, most of the recent work has concentrated on the longer infrared wavelengths observed with the ISO satellite, where O-rich dust formation effects are stronger. A comparison of these models with existing high resolution observational data in the optical is unfortunately still lacking.

In Chapter 4, we presented a qualitative analysis of the results derived from the first high resolution spectroscopic survey in the optical range of a large sample of galactic O-rich AGB stars. Basically, we found that some of the AGB stars observed are Li-strong but contrary to what has previously been reported for luminous AGB stars in the MCs, they do not show enrichment in s-process elements. The latter was deduced from the lack of any spectral signature of s-process atomic lines and/or ZrO molecular bands.

In this Chapter, we will perform a more detailed, quantitative analysis by adopting certain atmospheric parameters for all the stars in the sample for which a good enough S/N spectrum was obtained in order to derive the lithium and s-process element abundances. To do this, hydrostatic model atmospheres for cool stars (MARCS models) and synthetic spectroscopy with extensive linelists were applied. Initial estimates of the stellar fundamental parameters were obtained using the available photometry together with the study of the influence of the variations of these stellar parameters on the synthetic spectra. This initial plausible range of stellar parameters was used to construct a grid of MARCS model spectra which were then confronted with the real data. A statistical goodness-of-fit test (the χ^2 minimisation) was applied to this grid of spectra in order to select the theoretical spectrum which is the “best” representation of the observed data. We will focus our study on the determination of the lithium abundance and on the enrichment in s-process elements and discuss our results in the context of HBB and nucleosynthesis models.

5.2 MARCS model atmospheres and synthetic spectra

Our analysis combine state-of-the-art line blanketed model atmospheres and synthetic spectroscopy with extensive linelists. Note that an 'equivalent width approach' cannot be used in cool M-type stars like the ones in our sample due to the strong veiling by molecular lines. First, we have estimated a range of values of the stellar parameters to be adopted in all the stars in our sample: effective temperature T_{eff}, surface gravity *log g*, mass M, metallicity z, microturbulent velocity ξ and C/O ratio. Then we have used the 'MARCS' model atmospheres for cool stars and the 'TURBOSPECTRUM' spectral synthesis code (Plez, Brett & Nordlund 1992) to derive the lithium and s-process element abundances.

MARCS model atmospheres are calculated with the SOSMARCS code developed by Plez, Brett & Nordlund (1992). The simple assumptions of: i) spherical stratification in stationary homogeneous layers; ii) hydrostatic equilibrium; and iii) local thermodynamic equilibrium (LTE), are made. Convection is treated through a local mixing-length theory (Henyey, Vardya & Bodenheimer 1965) and energy conservation is imposed for radiative and convective flux. Turbulent pressure is, however, not considered (see Plez, Brett & Nordlund 1992, for more details). The models are designed with the notation *(T_{eff}, log g, M, z, ξ, C/O)*, where T_{eff} is the effective temperature of the star in K, g is the surface gravity in cm s^{-2}, M is the stellar mass in $M_{\odot}$, z is the metallicity, ξ is the microturbulent velocity in km s^{-1} and C/O is the ratio between the C and O abundances.

The synthetic spectra are generated with the TURBOSPECTRUM program package which shares much of its input data and routines with SOSMARCS (e.g., the continuous opacities and the spherical transfer routines, see Plez, Brett & Nordlund 1992, for a more detailed description). The program can handle millions of lines in a reasonable amount of time and has been tested against the widely used MOOG (Sneden 1973), and no significant differences have been found in the output synthetic spectra (Plez, Smith & Lambert 1993).

The atomic and molecular equilibrium constants of Tsuji (1973) for 65 molecules and 38 atoms are included in order to consider most of the molecular species which are formed at these low temperatures. The original data of Tsuji for the equilibrium constants are adapted, including the dissociation constants provided by Huber & Herzberg (1979). Solar abundances of Grevesse & Sauval (1998) are adopted, except for the iron abundance, *log ε(Fe)*=7.50, which is obtained from meteoritic data. Most opacity sources for cool M-type stars are included and taken from the literature, except for TiO, ZrO, VO and H_2O, for which new linelists were calculated (see Plez, Brett & Nordlund 1992 for more details). All opacities are treated by means of the opacity sampling method (OS; Sneden et al. 1976). Finally, other lines which are also included are: the lines of CO (the vibration-rotation fundamental bands, as well as the first and second overtones), CN (violet and red system), C_2, CH, OH, MgH, NH, SiH and SiO, all taken from Gustafsson et al. (1975), while the HCN lines are taken from Jörgensen et al. (1985).

For atomic lines, the primary source of information was the VALD-2 database (Kupka et al. 1999). The NIST[1] atomic spectra database was also consulted for comparison. The identification of features was made using the Solar Atlases by Moore, Minnaert, & Hootgast (1966) and Wallace, Hinkle & Livingston (1993, 1998). We used the observed solar spectrum of Neckel (1999) and the TURBOSPECTRUM program was run using the abundances from Grevesse & Sauval (1998) together with the solar model atmosphere by Holweger & Müller (1974) with parameters T_{eff}=5780 K, *log g*=4.44 and a variable microturbulence as a function of the optical depth. VALD-2 *gf*−values taken from Kurucz (1993, 1994) were often erroneous and did not fit the atomic lines of the solar spectrum. When possible, *gf*−values were checked by fitting the solar spectrum.

The whole machinery was tested on the high resolution optical spectrum (R$\sim$150,000) of the K2 IIIp giant Arcturus (α Boo) from Hinkle et al. (2000). Basically, a MARCS model atmosphere with the same fundamental parameters found by Decin (2000) was used. Decin (2000) derived T_{eff}=4300 K, *log g*=1.50, z=−0.5, M=0.75 $M_\odot$, ξ=1.7 km s^{-1}, *C/N/O*=7.96/7.55/8.67 and $^{12}C/^{13}C$=7 from the ISO-SWS spectrum of Arcturus. These fundamental stellar parameters for Arcturus are in excellent agreement with other determinations reported in the literature. In addition, some Kurucz *gf*−values of metallic lines of Fe I, Ni I, Co I, Cr I, Ti I, Zr I and Nd II, which were too weak in the solar spectrum, were adjusted so as to yield a good fit to the Arcturus spectrum in several regions (specially in the 7400−7600 Å and 8100−8150 Å regions); otherwise we used the *gf*−values given in the VALD-2 database. This exercise was very useful for confirming the lack of s-process atomic lines in the 7400−7600 and 8100−8150 Å spectral windows in the galactic O-rich AGB stars in our sample, relative to the S-stars observed for comparison, as we will see later.

5.3 Modelling the galactic O-rich AGB stars in our sample

The input parameters needed to generate the synthetic spectra by means of the TURBOSPECTRUM program are T_{eff}, *log g, M, z,* ξ, *C/O*, while the output parameters are the chemical abundances of any element of our interest. Note

---

[1] National Institute of Standards and Technology (NIST). http://physics.nist.gov/cgi−bin/AtData/linesform.

that the synthetic spectra must be convolved with a gaussian profile (with a certain *FWHM*) which accounts for the instrumental profile and the large-scale motions expected in the stellar atmosphere (macroturbulence, rotation, etc.).

The best set of input parameters can be selected by comparing the synthetic spectra with the observations at different wavelength regions, until a good set of stellar parameters is chosen which describes the star's atmosphere. However, the solution is usually not unique and different sets of stellar parameters can produce synthetic spectra which fit the observations reasonably well. A first guess can be obtained from our knowledge of the main characteristics of our stars. In order to decide on the most adequate initial set of parameters and define their plausible range of variation, an exhaustive analysis of the dependence of the output synthetic spectra on the assumed stellar parameters is usually performed.

5.3.1 Spectral regions of interest

For the determination of the abundance measurements we concentrated our attention on the following spectral regions:

Lithium

We used the Li I resonance line at ∼6708 Å to derive the lithium abundance. The selected spectral region ranges from 6670 to 6730 Å, which has the advantage of covering in addition a couple of TiO molecular bands at ∼6681 and 6714 Å, which are strongly sensitive to variations in the effective temperature (see Section 5.3.3). In addition, the spectral regions around the subordinate Li I lines at ∼6103 and 8126 Å could have also been inspected. However, we decided to drop them from the analysis because the latter lines are much weaker than the Li I resonance line at ∼6708 Å. Moreover, the S/N ratio is usually very low around 6103 Å in our sources and the contamination of terrestrial lines at 8126 Å is very strong.

s-process elements

The study of the s-process elements was carried out through the analysis of several ZrO absorption bands in the region from 6455 to 6499 Å. In particular we used the strong ZrO absorption band around ∼6474 Å, expected to be very strong in s-process enriched O-rich AGB stars (see Chapter 4) to determine the Zr elemental abundance, taken as representative of all other s-process elements. Surprisingly, this band was not detected in any star in our sample, nor did they show any signature from the atomic lines of the most abundant s-process elements like Zr, Nd, Ba, etc. in the spectral windows 7400−7600

Å and 8100−8150 Å,where many atomic lines of Zr I, Nd II, Ba II could have potentially been found.

Other additional spectral regions inspected were:

The K I λ7699 and Rb I λ7800 region

We also synthesised the spectral regions around the resonance lines of K I and Rb I at ∼7699 Å and 7800 Å, with the intention of using the elemental abundance of these lines as metallicity and neutron density indicators, respectively. Synthesis of these regions was also used to check that the model which best fit in the lithium region would also fit these spectral regions reasonably well, e.g. to further constrain the value of the effective temperature through the analysis of the TiO molecular bands, also included in these spectral regions. Two intervals of the order of 60 Å in the regions 7670−7730 Å and 7775−7835 Å were selected for study. The detection of circumstellar components in these two lines as we reported in Chapter 4 prevented the use of these lines for our initial purposes. The presence of a circumstellar contribution to the observed K I and Rb I lines was actually found to be a common feature among the O-rich AGB stars in the sample.

5.3.2 A first photometric approach to the stellar parameters

As we have already mentioned, in order to generate a MARCS model atmosphere, a set of fundamental stellar parameters have to be provided first as input. These are generally not available in the literature for the stars in our sample. Moreover, the stellar effective temperature and the radius (and hence the surface gravity) of our stars are expected to be subject to variations during the stellar pulsation cycle. In spite of this, we can still roughly estimate plausible ranges for both the effective temperature and the surface gravity of our stars based on the observed V−K colours using the empirical relations applicable to KM giants which relate the $(V-K)_0$ color with T_{eff} or radius. These empirical relations were established by van Belle et al. (1999) using the infrared flux method (IRFM) and interferometric data.

We corrected the observed V−K colours from interstellar extinction following the method outlined by Vanture & Wallerstein (2002). For those stars with $|b| \geq 10^{\circ}$, an estimation of the colour excess E(B−V) can be taken from the extinction galactic maps of Burstein & Heiles (1982). Unfortunately, there are not known Hipparcos parallaxes for practically any of the stars in the sample and we cannot then correct the colour from distance effects. The colour excess E(B−V) estimated in this way is converted to E(V−K) following the prescription of Bessell, Castelli & Plez (1998) and the extinction-corrected $(V-K)_0$ is then directly obtained from the definition of the colour excess E(V−K). For those stars with $|b| < 10°$ that are not on the Burstein & Heiles maps, we used the relation for A_V given by Chen, Wang & Xiong (1998). A_V values can be transformed to A_K according to Cohen et al. (1981). Finally, as was previously mentioned, the stellar effective temperature and the radius of the star are obtained from the empirical relationships between $(V-K)_0$ and T_{eff} or radius given in van Belle et al. (1999).

Once the stellar radius is known, the surface gravity can easily be determined using the Newton's universal gravitation law. Taking into account a possible mass range from 1 to 8 solar masses for our target stars (the range of masses expected for stars in the AGB) and based on the derived values of $(V-K)_0$, we end up with $2800 < T_{eff} < 3600$ K and $-1.0 < log\ g[\mathrm{cm\ s^{-2}}] < 1.0$ as the most plausible values for T_{eff} and *log g*, respectively, for the stars in our sample.

Van Belle, Thompson & Creech-Eakman (2002) actually measured the radii of the sample stars IRAS 15193+3132 (S CrB) and IRAS 14247+0454 (RS Vir) from interforemetric data at 2.2 μm. The measured radii in these two stars result in values of *log g* between −1.0 and 0.0 (for a mass range from 1 to 8 $M_\odot$, respectively), in very good agreement with the above estimations. Nevertheless, we must keep in mind once more the variable character of the stars in our sample as well as the fact that the photometry can be affected by the thermal emission from the circumstellar hot dust specially in the K band, and by the extra contribution from the circumstellar dust to the extinction. In addition, some of the observations available in the literature at V and K bands used in the application of this method are not simultaneous and not all stars in the sample have been observed photometrically. This implies that the values derived using the photometric method above described need to be considered with some caution. This initial range of variation for T_{eff} and *log g*, however, can be considered as a plausible starting point for our subsequent analysis, where we will show how these parameters can be more accurately determined through detailed spectral synthesis.

5.3.3 Derivation of the stellar parameters using spectral synthesis

In order to analyse how the variations of the stellar parameters influence the output synthetic spectra, we constructed a grid of MARCS model atmospheres and generated the associated synthetic spectra with the following specifications:

i) The stellar mass was in all cases taken to be 2 $M_\odot$ (see text below).

ii) T_{eff} values ranging from 2500 to 3800 K in steps of 100 K.

iii) *C/O* ratio values of 0.5, 0.7, 0.8 and 0.9.

iv) *log g* values between −0.5 and 1.6 dex in steps of 0.3 dex.

v) The more plausible value of the microturbulent velocity ξ was considered to be 2 km s^{-1} in the model atmospheres, but it was changed in the TURBOSPECTRUM program to values between 1 and 6 km s^{-1} in steps of 0.5 km s^{-1} in order to check the effect on the synthetic spectra.

vi) Metallicity z values between 0.0 and −0.3 dex.

vii) *log ε(Zr)* values[2] from 1.6 to 3.6 dex in steps of 0.25 dex.

viii) CNO abundances shifted ±1.0 dex (in steps of 0.5 dex) from the solar values of Grevese & Sauval (1998).

ix) $^{12}C/^{13}C$ ratio values of 10 (as expected for HBB stars) and 90 (the solar value).

This results in an extremely large grid of synthetic spectra containing more than ∼80,000 possible combinations of the above parameters. In order to reduce the number of spectra to be considered in our analysis, further constraints can be imposed on the above set of parameters by studying their effect on the spectral synthesis.

Stellar mass

As we have already mentioned, the stellar mass was in all cases selected to be 2 $M_\odot$. The main reason for this selection is that the temperature and pressure structure of the model atmosphere is practically identical for a 1 $M_\odot$ and 10 $M_\odot$ model atmosphere (see Figure 1 in Plez 1990) and the output synthetic spectra are not sensitive to the mass of the star (Plez 2003, private communication).

Effective temperature

The synthetic spectra are specially sensitive to T_{eff}, which determines the overall strength of the molecular absorption over the continuum (mainly, from TiO molecules but also from VO, and from ZrO if the Zr elemental abundance is increased above a certain limit). Thus, we decided to keep the whole range of values initially considered, i.e., T_{eff} from 2500 to 3800 K in steps of 100 K. The depth of the molecular bands (specially the TiO molecular bands) increases

---

[2] The zirconium abundance is given in the usual scale 12+*log N(Zr)*. In this scale the solar zirconium abundance is 2.6 dex.

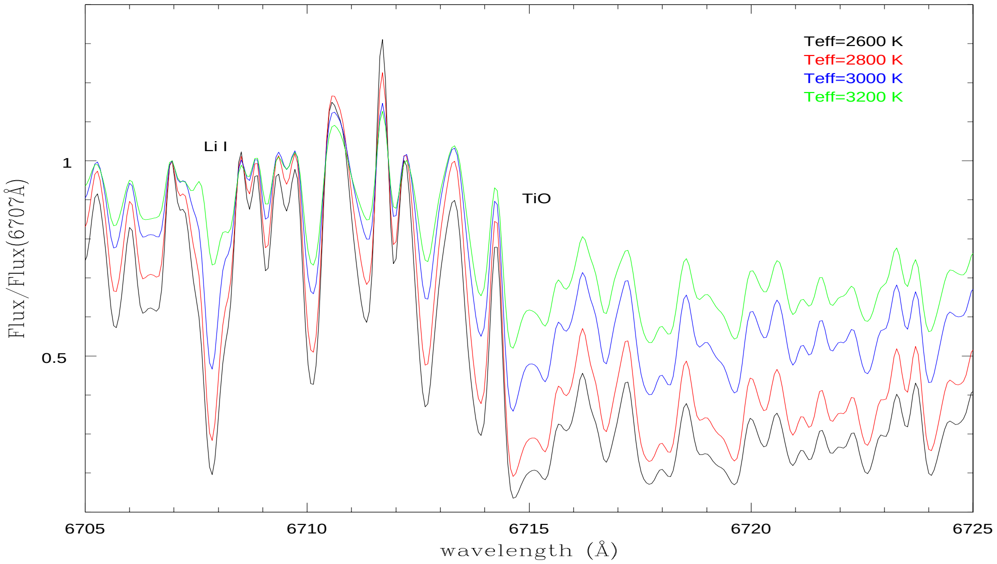

FIGURE 5.1— Comparison of different synthetic spectra in the Li I 6708 Å region generated from MARCS model atmospheres at the resolution of the observations. The effective temperatures (in K) used are indicated in the legend. The values taken for the other fundamental parameters of the model atmosphere are $log\ g$=-0.5, M=2 $M_\odot$, z=0.00, ξ=3 km s^{-1}, C/O=0.5, solar CNO abundances and $^{12}C/^{13}C$ ratio, $log\ \varepsilon(Zr)$=2.6 dex and $FWHM$=300 mÅ. The choice of these values is discussed in the text. The synthetic spectra are normalised by dividing each of them by the continuum flux at 6707.0 Å (taken as the pseudocontinuum around the Li I line) in order to make the comparison easier.

considerably with decreasing temperature. The effect is shown in Figure 5.1, where we can see that the effective temperature has also a large impact on the strength of the Li I line at 6708 Å in the synthetic spectrum. From this Figure it is clear that a decrease of T_{eff} has the effect of increasing the TiO veiling, as well as the strength of the Li I line, as a consequence of the changes in the Li I/Li II population equilibrium.

C/O ratio

The C/O ratio basically determines the prevalence of O-rich molecules (C/O<1) against C-rich molecules like CN, C_2, etc. which dominate when this ratio is larger than one. In the case of our O-rich AGB stars, the precise value of the C/O ratio adopted, always <1, affects mainly the strength of the TiO veiling and of the Li I line in the synthetic spectrum. An increase of the C/O ratio will decrease the TiO veiling and increase the Li I line strength relative to the adjacent continuum in a very similar way as a decrease in T_{eff}. This is a good example of how the set of parameters giving a good match between the observed and the synthetic spectra for a given spectral region is not necessarily unique. A good fit is obtained in both cases but they correspond to quite different Li abundances. Fortunately, one of these two sets of parameters does not provide acceptable fits for other spectral regions. In particular, the presence of detectable atomic lines in the synthetic spectrum is very sensitive to variations of the C/O ratio: an increase of C/O ratio will lower the TiO veiling, making the detection of atomic lines easier. This is the natural consequence of the less availability of oxygen atoms to form the TiO molecule. According to the models, the immediate effect should be the detection of much stronger atomic lines of K I, Fe I, Zr I, Nd II etc. Since we do not see such an effect in our spectra, we assume that C/O must always be $\leq$0.75 in our stars. Abundances derived from models with C/O between 0.15 and 0.75 actually show little difference (Plez, Smith & Lambert 1993). Given that all the stars in the sample are clearly O-rich and taking into account all previous considerations, we decided to use C/O=0.5 in all cases, as a constant value. This selection is in agreement with other more detailed determinations made in massive O-rich AGB stars in the MCs (e.g. Plez, Smith & Lambert 1993; Smith et al. 1995) and in a few low-mass M-type stars studied in our Galaxy (Smith & Lambert 1985, 1990b)[3].

Surface gravity

The surface gravity also affects the appearance of the output synthetic spectra but its effect is small compared to that of the effective temperature. Looking at Figure 5.2, it is obvious that the influence of a change in the value adopted for the surface gravity within the range of values (*log g* between -0.5 and 0.5 dex) under consideration is not as severe as a temperature change. The molecular absorption becomes slightly weaker at higher surface gravities. For example, an increase of the surface gravity of 0.5 dex has approximately the same impact as an increase of 100 K in effective temperature. However, for a fixed temperature we found that the lowest gravities in general fit better both the TiO band strength and the pseudocontinuum around the 6708 Å Li I line. As the appearance of the spectra is not so dependent on the surface gravity and considering that its value must be low in these mass-losing stars, a constant surface gravity of *log g*=-0.5 was adopted for all the stars in the

---

[3] This is the only other chemical analysis previously carried out in galactic O-rich AGB M-type stars (only 6 stars!) before the work presented here. However, these are low-mass stars (M $\lesssim$ 1.5$-$2 M$_\odot$) and their study was focussed on the determination of CNO abundances through near-IR spectra and the s-process enrichment, but they did not study the lithium enrichment in particular.

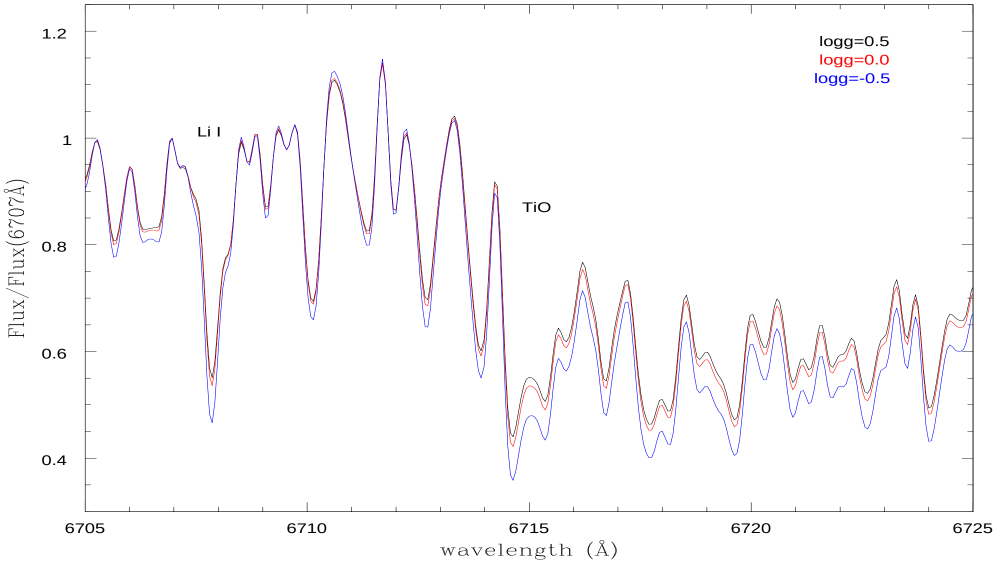

FIGURE 5.2— Comparison of different synthetic spectra in the Li I 6708 Å region generated from MARCS model atmospheres at the resolution of the observations. The surface gravities used are indicated. The values taken for the other fundamental parameters are T_{eff}=3000 K, M=2 $M_\odot$, z=0.00, ξ=3 km s^{-1}, C/O=0.5, solar CNO abundances and $^{12}C/^{13}C$ ratio, *log ε(Zr)*=2.6 dex and $FWHM$=300 mÅ. The choice of these values is discussed in the text. The synthetic spectra are normalised dividing each spectrum by an estimation of the pseudocontinuum flux (at 6707 Å) around the Li I line at 6708 Å, in order to facilitate the comparison.

sample. This selection seems to be appropriate if we compare it with the values adopted by Plez, Smith & Lambert (1993) of $-0.33 \leq log\ g \leq 0.0$ for O-rich AGB stars in the MCs with effective temperatures between 3300 and 3650 K.

Microturbulent velocity

The microturbulent velocity is usually derived by demanding no correlation between the abundance of iron derived from individual lines and their reduced equivalent widths. Previous studies of O-rich AGB stars found microturbulent velocities between 2 and 4 km s^{-1} (Plez, Smith & Lambert 1993; Smith & Lambert 1985, 1989; Smith et al. 1995; Vanture & Wallerstein 2002). Unfortunately, we cannot estimate the microturbulent velocity in the stars in our sample due to the lack of useful Fe I atomic lines (the small number of detectable Fe I lines does not cover a wide range of equivalent widths). Thus, we will assume in the following a microturbulent velocity ξ=3 km s^{-1}, which is a typical value generally adopted for AGB stars (e.g. Aringer, Kerschbaum

& Jörgensen 2002). Higher values of ξ would strengthen all atomic lines in the synthetic spectra and we do not see this effect in our observations.

Metallicity

The metallicity of the galactic O-rich AGB stars in a first approximation is assumed to be solar, as expected for disk stars. A lower metallicity may be unlikely since all the stars in the sample are expected to be considerably massive (M $\gtrsim$ 2−3 $M_\odot$). This assumption is in good agreement with the typical metallicities found in AGB stars in our Galaxy (e.g. Abia & Wallerstein 1998; Vanture & Wallerstein 2002). The Ca I lines at ∼6122 Å and 6573 Å generally used for this determination in other studies, are unfortunately not sensitive to the metallicity nor to the surface gravity at the very low temperature of our sample stars (i.e. see Figure 7 in Cenarro et al. 2002). This was checked by running different test models and spectral synthesis in the 6100−6160 Å and 6535−6585 Å regions where these lines fall. A decrease of the metallicity would imply less availability of metals like Ti, and thus, lower the TiO veiling, making the detection of atomic lines easier. Actually, this may be the main reason why we can easily detect atomic lines in O-rich AGB stars at the metallicity of the MCs (e.g. z=−0.5 in the SMC, Plez, Smith & Lambert 1993), while they are not detected in our spectra.

Zirconium

The synthetic spectra are also very sensitive to changes in the zirconium elemental abundance, specially at those wavelength regions where ZrO molecular bands are present. For a set of fixed stellar parameters, an increase of the zirconium abundance greatly increases these bands. Thus, we decided to use a large set of zirconium abundances with *log ε(Zr)* between 1.6 and 3.6 dex in steps of 0.25 dex. The effect of changing the zirconium abundance is shown in Figure 5.3 in the spectral range covering the strong ZrO band at 6474 Å. It should be noted that, according to the models, the effect of a variation in the zirconium elemental abundance on the strength of the ZrO molecular bands is stronger than that associated to variations in the T_{eff} or C/O ratio. In contrast, even at relatively high zirconium abundance, the corresponding Zr atomic lines are more difficult to detect at low T_{eff} or C/O ratio because there is less availability of zirconium atoms and more availability of oxygen atoms, respectively. This is because at low T_{eff} or C/O ratio the formation of ZrO molecules is favoured.

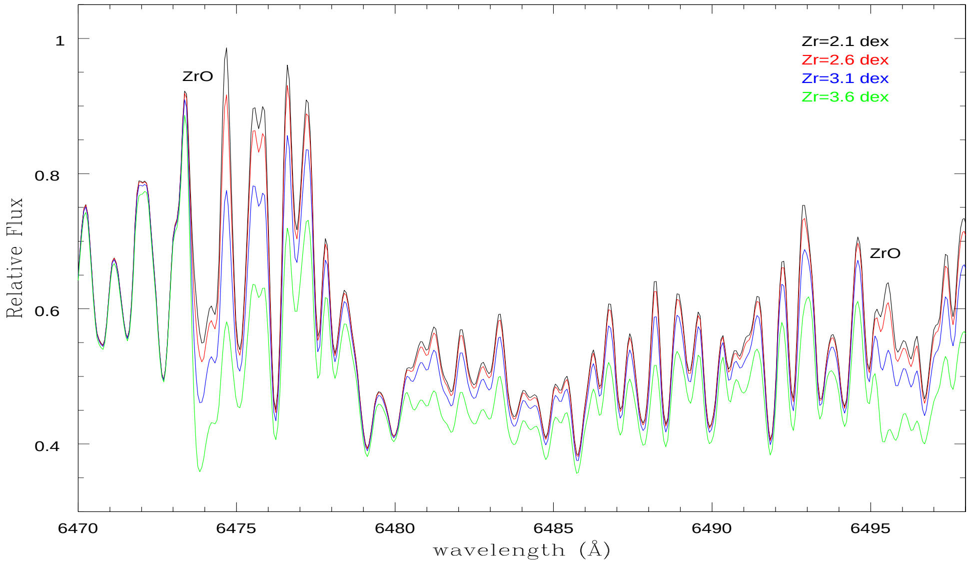

FIGURE 5.3— Comparison of different synthetic spectra in the ZrO 6474 Å region generated from MARCS model atmospheres at the resolution of the observations. The zirconium abundances (in the scale *log* $\varepsilon(Zr)$, see text) are denoted in the legend. The values for the other fundamental parameters are T_{eff}=3000 K, *log* g=−0.5, M=2 $M_\odot$, z=0.00, ξ=3 km s^{-1}, C/O=0.5, solar CNO abundances and $^{12}C/^{13}C$ ratio and $FWHM$=300 mÅ. The choice of these values is discussed in the text.

CNO abundances and $^{12}C/^{13}C$ *ratio*

As we have already mentioned, we have adopted solar CNO abundances and $^{12}C/^{13}C$ ratio from Grevesse & Sauval (1998). However, different test models and spectral syntheses were also run with different CNO abundances and $^{12}C/^{13}C$ ratios to investigate the possible dependence of the synthetic spectra on these parameters. The synthetic spectra are not altered by changes of the nitrogen and carbon abundances and of the $^{12}C/^{13}C$ ratio within a reasonable range of adopted values (see Section 5.3.3) in any of the spectral regions of our interest. Basically, this is due to the strong TiO veiling, which dominates completely in the optical region. However, changes of the oxygen abundance can modify the appearance of the synthetic spectra, and indeed this has the same effect as a change in the titanium abundance. Increasing the oxygen abundance will also increase the TiO veiling, modifying the overall strength of the molecular absorption over the continuum whereas the relative strength of the TiO bandheads with respect to the local continuum remains practically unaffected. Given that our stars are all O-rich AGB stars, we can safely assume that their photospheric oxygen abundances were not affected significantly by its passage along the RGB (first dredge-up) and the early-AGB (second dredge-up) or by the effects of the third dredge-up and/or HBB during the thermal pulsing AGB phase. In the synthetic spectra, variations of the carbon and nitrogen abundances and of the $^{12}C/^{13}C$ ratio are completely negligible with respect to other stellar fundamental parameters.

5.4 Abundance determination

5.4.1 Overall strategy

Based on the above considerations, we now have estimates of, and/or lower/upper limits for, all the required stellar fundamental parameters to create a more reduced grid of MARCS model spectra for all the O-rich AGB stars of the sample with useful spectra. For each observed spectrum we can now try to find the best fitting synthetic spectrum from the grid.

After imposing these further constraints, the grid of MARCS model spectra is now composed of ‘only’ ∼650 spectra, with effective temperatures in the range T_{eff}=2500−3800 K in steps of 100 K, $log\ \varepsilon(Zr)$ between 1.6 and 3.6 dex in steps of 0.25 dex, $FWHM$ in the range 200−600 mÅ in steps of 50 mÅ, and keeping all the other stellar fundamental parameters fixed: $log\ g$=−0.5, M=2 $M_{\odot}$, solar metallicity z=0.00, ξ=3 km s^{-1}, C/O=0.5, solar CNO abundances and solar $^{12}C/^{13}C$ ratio.

A procedure based on the comparison between synthetic and observed spectra was developed in order to find the theoretical spectrum which better fits the observed spectrum. The method is a modified version of the standard χ^2 test. When fitting observed data $Yobs_i$ to model data $Ysynth_i$, the quality of the fit can be quantified by the χ^2 test. The best fit corresponds to that leading to the minimum value of χ^2. This test is used here in a modified way an is mathematically expressed as:

$$\chi^2 = \sum_{i=1}^{N} \frac{[Yobs_i - Ysynth_i(x_1...x_M)]^2}{Yobs_i} \tag{5.1}$$

with N the number of data points, and M the number of free parameters.

The observed spectra were fully reduced (see a description of the data reduction process in Section 4.3) and shifted to rest-wavelength using the mean Doppler velocity shift derived from the Li I and Ca I lines. In addition, they were re-binned to the same resolution as the synthetic ones (0.06 Å/pix) and normalized in order to make the comparison easier. The observed spectra were then compared to the synthetic ones in intervals of ∼60 Å which allowed the analysis of their overall characteristics as well as the relative strength of the TiO molecular bands.

The fitting-procedure places special emphasis on the goodness of the fit in the lithium region (6670−6730 Å). In this spectral range the goal was to fit the relative strength of the TiO bandheads at ∼6681 and 6714 Å, which are very sensitive to the effective temperature, together with the pseudocontinuum around the Li I line. We first determined by χ^2 minimisation which of the spectra from our grid of models provide the best fit, fixing mainly the T_{eff}. The best fits resulting from the χ^2 minimisation were also judged by eye in order to test the method. Then the lithium content was estimated by changing the lithium abundance. This procedure was repeated on each star of the sample for which an acceptable S/N ratio was achieved around the Li I 6708 Å line. Unfortunately, we could not analyse the few AGB stars with a low signal-to-noise ratio in their spectra (IRAS 04404−7427, IRAS 07222−2005, IRAS 12377−6102, IRAS 14086−0730, IRAS 14086−6907 and IRAS 17359−2138) (see Table 5.1). IRAS 18025−2113, IRAS 03507+1115 and IRAS 18304−0728 show unusual spectra, very different from the rest of the stars in our sample and a good fit from our grid of MARCS model spectra was not possible. The spectra of these stars show unusual TiO band strengths plus a combination of narrow and broad atomic lines. Their complicated spectra suggest that they are most likely double lined spectroscopic binaries, i.e. consisting of a main sequence F- or G-type star plus an AGB M-type companion.

The best fitting model spectrum in the Li I spectral region (6670−6730 Å) is usually found to fit also reasonably well the wavelength regions around the ZrO bandhead and the K I and Rb I resonance lines. In general, the overall shapes of the spectrum (including the TiO bandheads) are well described. As an example, the fits made in different spectral regions for the star IRAS 11081−4203 are presented in Figures 5.4 to 5.8. All best fits in the 6670−6730 Å spectral region around the Li I line are presented in Appendix A and B for each star in the sample for which a fitting could be done. The effective temperatures of the best fitting model spectra together with the lithium abundances (or upper limits) derived following the above procedure are listed in Table 5.1 where we have separated the Li detected stars from the Li non-detected ones.

Then, we attempted the measurement of the zirconium abundance from our spectral synthesis in the 6455−6499 Å spectral region. In this case, the goal was to obtain the best fit around the ZrO molecular bands at 6474 Å and 6495 Å. The non-detection of these features in any of the stars analysed imposed severe upper limits to the zirconium abundance, as we will see later. We also ruled out the possibility of the Zr not being part of the ZrO molecule but free in the form of Zr I atoms by looking at the 7400−7600 and 8100−8150 Å spectral regions

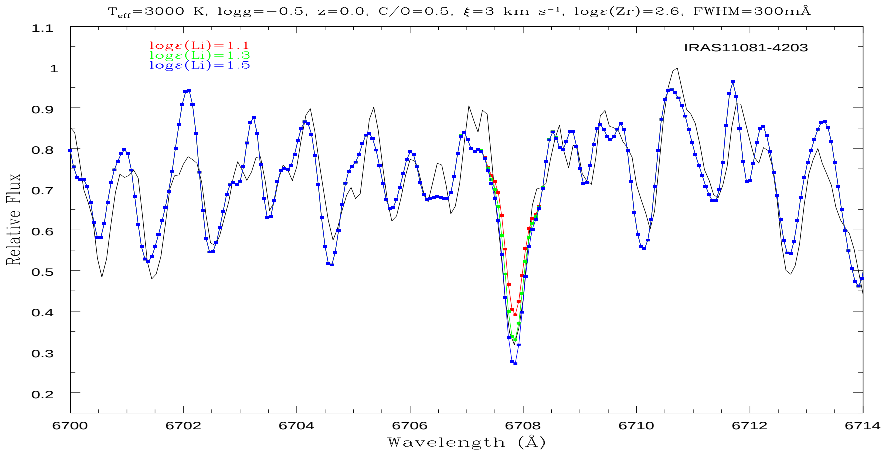

FIGURE 5.4— Best model fit and observed spectrum around the Li I line (6708 Å) for the star IRAS 11081−4203. The Li abundance derived from this spectrum was *log ε(Li)*=1.3. The synthetic spectra obtained for Li abundances shifted +0.2 dex and −0.2 dex from the adopted value are also shown. The parameters of the best model atmosphere fit are indicated in the top label.

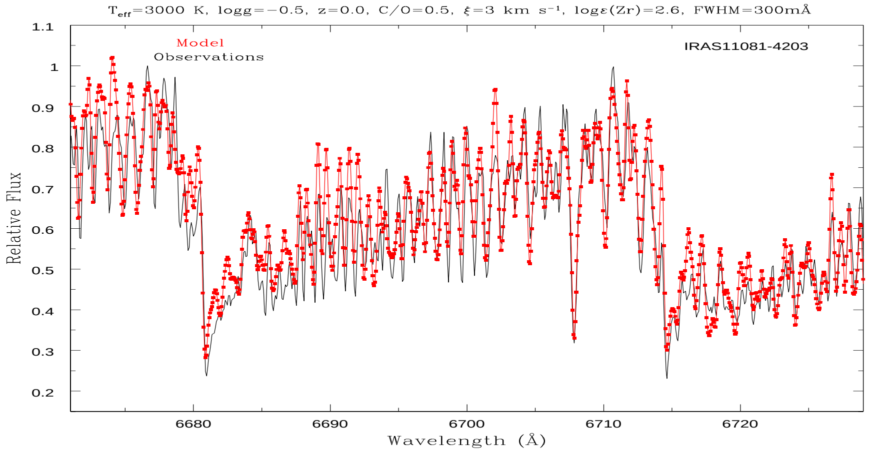

FIGURE 5.5— Best model fit and observed spectrum in the region 6670−6730 Å for the star IRAS 11081−4203. The T_{eff} derived from this spectrum was 3000 K. The parameters of the best model atmosphere fit are indicated in the top label.

where strong Zr I atomic lines should have been detected in that case. However, we must note that the continuum emission at these latter wavelength regions is not well reproduced in the O-rich AGB stars in our sample, in contrast with the perfect agreement obtained in some of the comparison stars observed, like

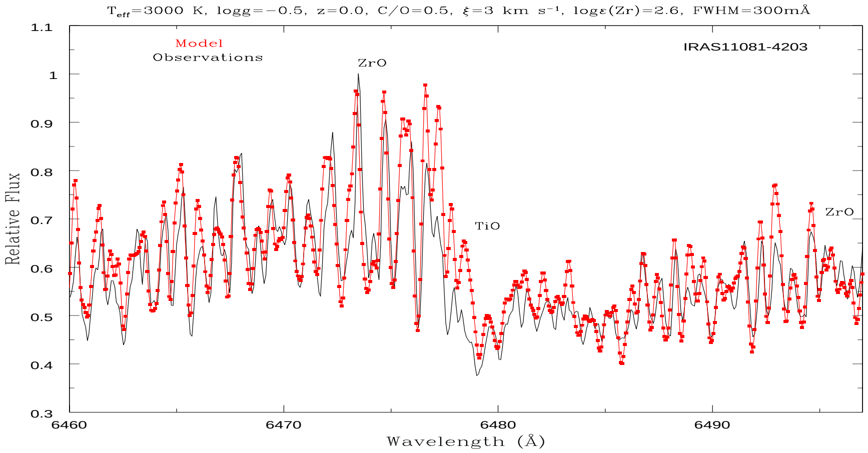

FIGURE 5.6— Best model fit and observed spectrum in the region 6460−6499 Å for the star IRAS 11081−4203. The Zr abundance derived from this spectrum was *log ε (Li)*=2.6 which corresponds to the solar value. The parameters of the best model atmosphere fit are indicated in the top label. Note the non-detection of the characteristics strong ZrO bandheads typical of galactic S-stars.

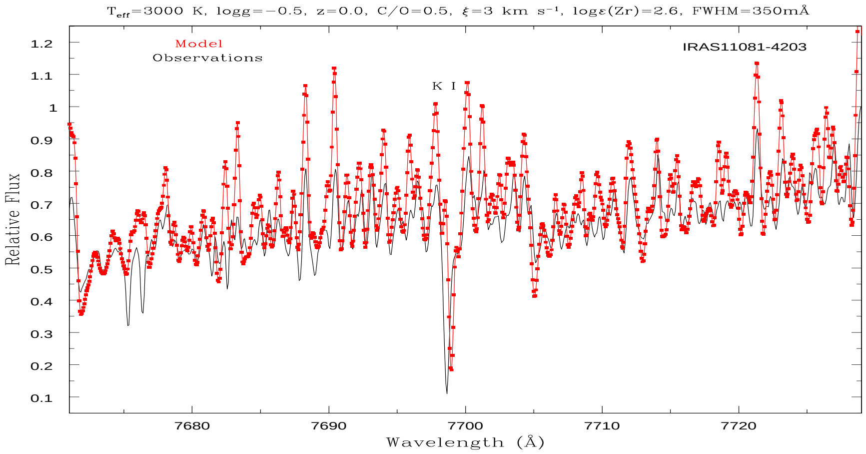

FIGURE 5.7— Best model fit and observed spectrum in the region 7670−7730 Å (around the K I line at 7699 Å) for the star IRAS 11081−4203. The synthetic spectrum obtained for solar K abundance (*log ε (K)*=5.12 dex) is shown. The parameters of the best model atmosphere fit are indicated in the top label. Note the Doppler shift, which is interpreted as a result of the circumstellar origin of the K I line. The narrow features seen at ∼7675−77 Å, which are not adjusted by the model, are telluric lines.

the S-star IRAS 10436−3454, for which a perfect fit is obtained both for the

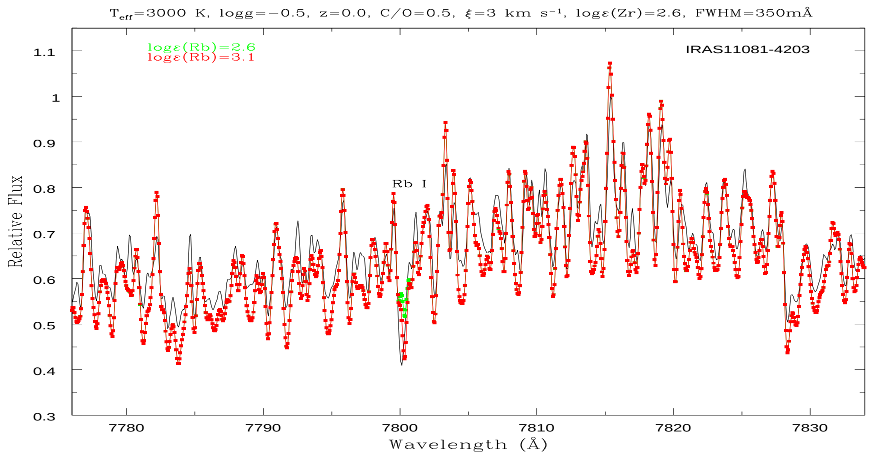

FIGURE 5.8— Best model fit and observed spectrum in the region 7775−7835Å (around the Rb I line at 7800 Å) for the star IRAS 11081−4203. The synthetic spectra obtained for solar Rb abundance (*log ε(Rb)*=2.6 dex) and shifted +0.5 dex (*log ε(Rb)*=3.1 dex) are shown. The parameters of the best model atmosphere fit are indicated in the top label. Again, the Doppler shift observed suggests a circumstellar origin of the Rb I line.

ZrO bandheads at 6455−6499 Å (see Figure 5.11) and for the Zr I atomic lines in the 7400−7600 and 8100−8150 Å spectral regions (not shown). The stars in our sample are the coolest O-rich AGB stars ever studied (with effective temperatures between 2700 K and 3300 K; see Section 5.4.2) and we believe that the discrepancies observed in the continuum shape are mainly due to the non-inclusion of the H_2O molecule linelists in our modelling. The effect of this molecule may be ignored in S-stars, where the C/O ratio is close to one, but it can be dominant in the case of our O-rich stars at these very low temperatures, preferentially at the longer wavelengths (see e.g. Allard, Hauschildt & Schwenke 2000; Decin et al. 2003a, 2003b).

5.4.2 Lithium and s-element abundances

The derived Li abundances are displayed in Table 5.1. From Table 5.1 it is clear that almost all Li detected stars have unusual Li abundances (*log ε(Li)* $\geq$ 1), larger than solar, but smaller than those found in the few so-called 'super Li-rich' AGB stars (with *log ε(Li)* $>$ 3−4) in our Galaxy. A very similar range of Li overabundances, for instance, is found in the massive O-rich AGB stars studied in the MCs (Plez, Smith & Lambert 1993; Smith & Lambert 1989, 1990a; Smith et al. 1995). We generally find equally good fits for effective temperatures shifted ±100 K from the best fit. Even for the coolest stars of

TABLE 5.1— Spectroscopic T_{eff} and lithium abundances derived for the subgroup of Li detected (left) and Li non-detected stars (right)

Li detected IRAS name	T_{eff} K	$log\ \varepsilon(Li)^1$ 12+$log\ N(Li)$	Li non-detected IRAS name	T_{eff} K	$log\ \varepsilon(Li)^1$ 12+$log\ N(Li)$
01085+3022	3300	2.4	03507+1115[3]	...	...
02095−2355	3300	1.6	05098−6422	3000	<-1.0
04404−7427*	...	...	05151+6312	3000	<0.0
05027−2158	2800	1.1	07080−5948	3000	<0.5
05559+3825	2900	0.6	07445−2613	2900	<-1.0
06300+6058	3000	0.7	10189−3432	2900	<-1.0
07222−2005*	...	...	10261−5055	3000	<-1.0
07304−2032	2700	0.9	13379−5426	2900	≤ 0.0
09429−2148	3300	2.2	13442−6109**	3000	<-1.0
11081−4203	3000	1.3	13475−4531	2900	<-1.0
11525−5057[2]	3300	≤ 0.9	14086−0730*	...	...
12377−6102*	...	...	14086−6907*	...	...
14337−6215	3300	≤ 2.4	14247+0454	2700	<0.5
15211−4254	3300	2.3	14266−4211	2900	<0.0
15255+1944	2900	1.0	15193+3132	2800	<0.0
15576−1212	3000	1.1	15586−3838	3000	<0.0
16030−5156	3000	1.5	16037+4218	2900	<-1.0
16260+3454	3300	2.7	16503+0529	2800	<-1.0
18025−2113[3]	...	...	17034−1024	3300	<0.0
18057−2616[4]	3000	...	17359−2138*	...	...
18413+1354	3300	1.8	18050−2213	2900	<-1.0
18429−1721	3000	1.2	18304−0728[3]	...	...
19129+2803	3300	≤ 3.1	18454−1226**	3300	<0.0
19361−1658[5]	3000	1.9/2.0	19147+5004	3000	<0.0
20052+0554	3300	2.6	19157−1706	3300	<0.0
			19412+0337	3300	<0.0
			20343−3020	3000	<-1.0
			20350+3741	3000	<0.0
			22180+3225	3300	<0.0
			22466+6942	3300	<0.0
			22510+3614	3000	<-1.0
			23492+0846**	3000	<-1.0

---

[1] The uncertainty is estimated to be around ±0.4−0.6 dex in all cases.

[2] The fit is also consistent with no lithium.

[3] Possible double lined spectroscopic binary.

[4] The lithium line has a P-cygni-type profile.

[5] Observed Li abundances in two different runs.

[*] The S/N ratio is too low to derive any reliable T_{eff} and/or lithium abundance estimate.

[**] Possible supergiant star.

TABLE 5.2— Sensitivity of the derived Li abundance (in dex) to slight changes in the atmosphere parameters used for the modelling of the star IRAS 15255+1944.

Adopted value	Change	Abundance
T_{eff}=2900 K	$\Delta T_{eff}=\pm100$ K	$\Delta log\ \varepsilon(Li)=\pm0.3$
z=0.0	$\Delta z=\pm0.3$	$\Delta log\ \varepsilon(Li)=\pm0.2$
ξ=3 km s^{-1}	$\Delta\xi=\pm1$ km s^{-1}	$\Delta log\ \varepsilon(Li)=\mp0.1$
$log\ g=-0.5$	$\Delta log\ g=+0.5$	$\Delta log\ \varepsilon(Li)=+0.1$
$FWHM$=300 mÅ	$\Delta FWHM=\pm50$ mÅ	$\Delta log\ \varepsilon(Li)=\pm0.1$

the sample with T_{eff} < 2900 K we still found reasonably good fits for T_{eff} changes of up to ±200 K. The effect of the uncertainty in the location of the pseudocontinuum around the Li I line on the measured abundances is negligible compared with any change in the other stellar parameters. The final error in the derived Li abundance mainly depends on the uncertainty of the effective temperature (±100−200 K) and metallicity (±0.3) while it is less sensitive to the microturbulent velocity (±1 km s^{-1}), surface gravity (±0.5) and $FWHM$ determination (±50 mÅ) uncertainties. If we consider these typical uncertainties in the atmosphere parameters as independent sources of error, the resulting uncertainty in the Li abundances given in Table 5.1 is estimated to be in the order of 0.4−0.6 dex. This error reflects mostly the sensitivity of the derived abundances to changes in these specific atmospheric parameters taken for the modelling. The uncertainty is larger in the coolest stars. As an example, the changes in the derived Li abundance induced by slight variations of each of the atmospheric parameters used in our modelling are displayed in Table 5.2 for the star IRAS 15255+1944.

Note, however, that the estimated errors do not reflect possible non-LTE effects, dynamics of the stellar atmosphere, nor errors in the model atmospheres or in the molecular/atomic linelists themselves. In particular, overionization and overexcitation of Li is predicted to occur under non-LTE conditions both in C-rich and O-rich AGB stars (Pavlenko 1996) although the effect is expected to be more pronounced in metal-deficient stars (i.e. MC AGBs). Use of LTE in super Li-rich AGB stars is then likely to lead to an underestimation of the Li abundance (Abia, Pavlenko & Laverny 1999).

Concerning s-process elements, the non-detection of the ZrO molecular bands at 6474 Å and 6495 Å is consistent with upper limits for the Zr abundance around 0.0−0.5 dex with respect to the solar value of $log\ \varepsilon(Zr)$=2.6 dex. The synthetic spectra predict detectable ZrO bandheads at 6474 Å and 6495 Å for Zr abundances above 0.00−0.25 dex for $T_{eff} \geq 3000$ K and 0.25−0.50 dex for T_{eff}

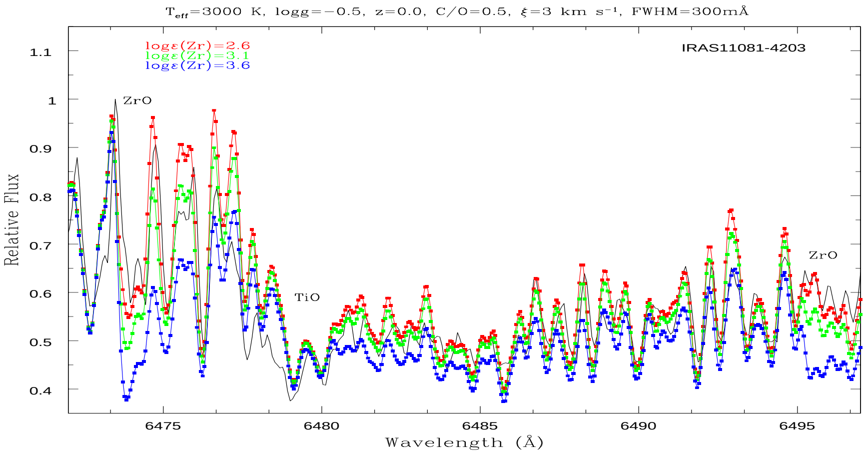

FIGURE 5.9— Synthetic and observed spectra in the region 6460−6499 Å for the star IRAS 11081−4203, one of the Li detected stars in our sample. The synthetic spectra corresponding to Zr abundances shifted +0.5 dex and +1.0 dex from the solar value (*log ε(Zr)*=2.6 dex) are also shown. The parameters of the best model atmosphere fit are indicated in the top label.

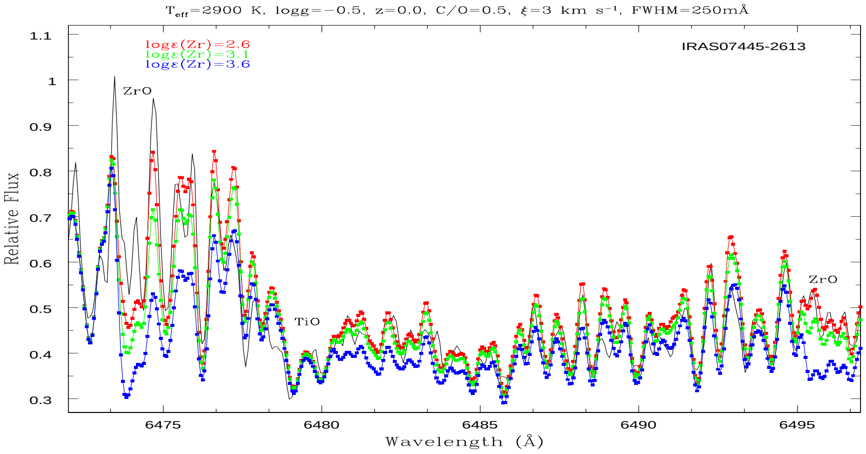

FIGURE 5.10— Synthetic and observed spectra in the region 6460−6499 Å for the star IRAS 07445−2613, one of the Li non-detected stars in our sample. The synthetic spectra corresponding to Zr abundances shifted +0.5 dex and +1.0 dex from the solar value (*log ε(Zr)*=2.6 dex) are also shown. The parameters of the best model atmosphere fit are indicated in the top label.

< 3000 K. In fact, the fits are also reasonably good even if we do not include any ZrO in the synthesis. We found the same results both in the Li non-detected stars and in the Li detected ones. The effect of varying the Zr abundance for

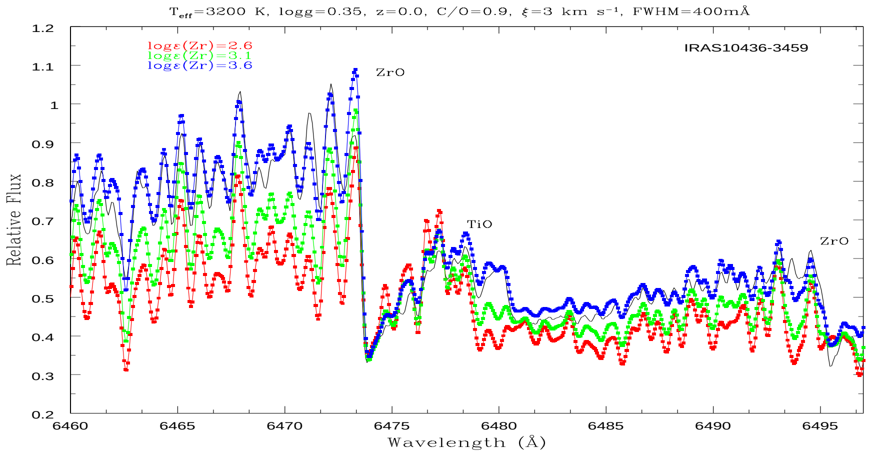

FIGURE 5.11— Synthetic and observed spectra in the region 6460−6499 Å for the galactic S-star IRAS 10436−3454. The synthetic spectra corresponding to Zr abundances shifted +0.5 dex and +1.0 dex from the solar value (*log ε(Zr)*=2.6 dex) are also shown. The parameters of the best model atmosphere fit are indicated in the top label. Note the strong overabundance (*log ε(Zr)*=3.6 dex) needed to fit the observations.

the Li detected star IRAS 11081−4203 and for the Li non-detected star IRAS 07445−2613 is displayed in Figures 5.9 and 5.10, respectively. The best model spectrum fit for the galactic S-star IRAS 10436−3454 is also shown in Figure 5.11, for comparison. As we can see, strong ZrO bandheads are only detected in IRAS 10436−3454, while these are completely absent from the spectra of IRAS 11081−4203 and IRAS 07445−2613. According to the models, at least a small enhancement (with respect to the solar value) of Zr is required for the ZrO molecular bands to show up in our sample stars because of the strong veiling produced by the TiO molecule (see Figures 5.9 and 5.10). In contrast, a lower Zr abundance is enough when the C/O ratio is ∼1 (see Figure 5.11) because of the weaker TiO veiling in the S-star. This also favours the visibility of the Zr I atomic lines in the 7400−7600 and 8100−8150 Å spectral regions.

5.5 Discussion

In this section, we will first discuss our abundance results in the framework of “Hot Bottom Burning” models. Then, we will compare our results with the previous studies made on massive AGB stars in the MCs. Finally, we will try to interpret the overall results obtained in the context of stellar evolution.

5.5.1 Lithium production and HBB model predictions

At present, it is generally accepted that lithium production in massive O-rich AGB stars (> 4 M$_\odot$) is due to the activation of the so-called "hot bottom burning" (HBB) process at the bottom of the convective mantle, which prevents the formation of luminous C-rich AGB stars (see details in Section 1.2.). Modelling of HBB started thirty years ago with envelope models including non-instantaneous mixing coupled to the nuclear evolution (Sackmann, Smith & Despain 1974). More recent models (Sackmann & Boothroyd 1992; Mazzitelli, D'Antona & Ventura 1999, hereafter SB92 and MDV99, respectively) seem to work well reproducing the lithium production observed in massive O-rich AGB stars in the MCs. Although the precise determination of the lithium production depends on the input physics (stellar mass, metallicity, mass loss rate, overshooting, etc.), the strongest dependence is with the convection model assumed. SB92 model predicts lithium production in intermediate mass stars assuming the so-called "Mixing Length Theory" (MLT) framework for convection. But these models require a fine tuning of the mixing length parameter α, with $\alpha = l/H_p > 2$, where l is the mixing length and H_p is the thickness of the mixing layer. The present assumption for the Sun is a value of α in the range 1.5−1.7. However, MDV99 explored lithium production in intermediate mass stars according to a more modern treatment of turbulent convection, known as the "Full Spectrum of Turbulence" (FST) model (D'Antona & Mazzitelli 1996, and references therein). The latter model is more appropriate to predict the lithium production in intermediate mass stars because they do it without the need of adjusting the α parameter. In fact, MDV99 model is able to reproduce the strong Li enhancement observed in massive O-rich LMC AGB stars satisfactorily well and seems to be able to give a theoretical explanation of the existence in the LMC of a few sources with extreme luminosities of up to $M_{bol} = -7.3$ and -7.6, which are long period, obscured AGB stars (Ventura, D'Antona & Mazzitelli 2000), but this has as yet not been tested against their galactic analogs.

For solar metallicity, MDV99 predict lithium production as a consequence of the activation of HBB for stellar masses $\gtrsim 4.5$ M$_\odot$ without core overshooting, and for M $\gtrsim 4$ M$_\odot$ including core overshooting. The amount of lithium produced during the AGB is independent of the assumed initial lithium abundance as the star structure loses all memory of the previous history of lithium at the beginning of the AGB phase. As an example, according to this model, the lithium surface abundance drops to $log\ \varepsilon(Li) \sim 0.3$ for a 6 M$_\odot$ star after the second dredge-up, at the beginning of the AGB phase. If overshooting from below the convective envelope is allowed, an important decrease of the number

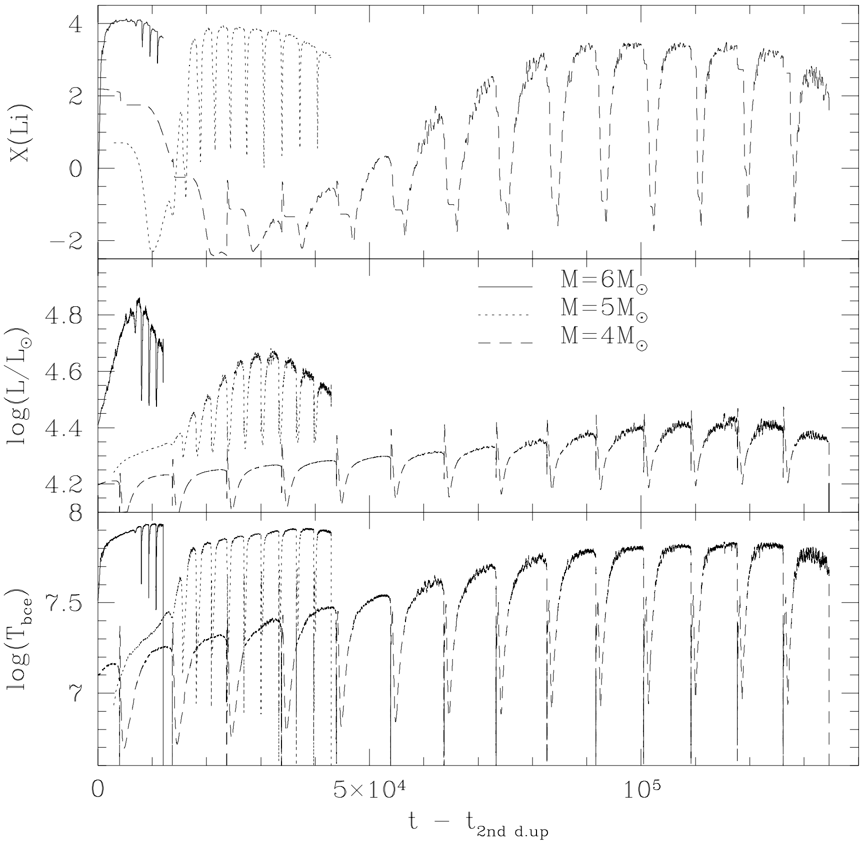

FIGURE 5.12— Variation with time of the lithium abundance, stellar luminosity and temperature at the base of the convective envelope (T$_{bce}$) for different stellar masses and solar metallicity when core overshooting is allowed (taken from MDV99). Note that the times refer to the time after the 2nd dredge-up and the lithium abundance X(Li) is in the usual scale of 12+*log N(Li)*.

of thermal pulses is predicted by the model and lithium production takes place before the first thermal pulse. The variation with time of the lithium abundance, total luminosity and temperature at the base of the convective envelope (T$_{bce}$) for different masses is shown in Figure 5.12. As we can see, a stronger Li-overabundance, faster increase of the luminosity at the beginning of the AGB phase and higher T$_{bce}$ are predicted when the mass of the star is increased.

Mass loss rates and metallicities also play an important role, according to MDV99. A low mass loss rate leads to a longer run of TPs, and to a lithium

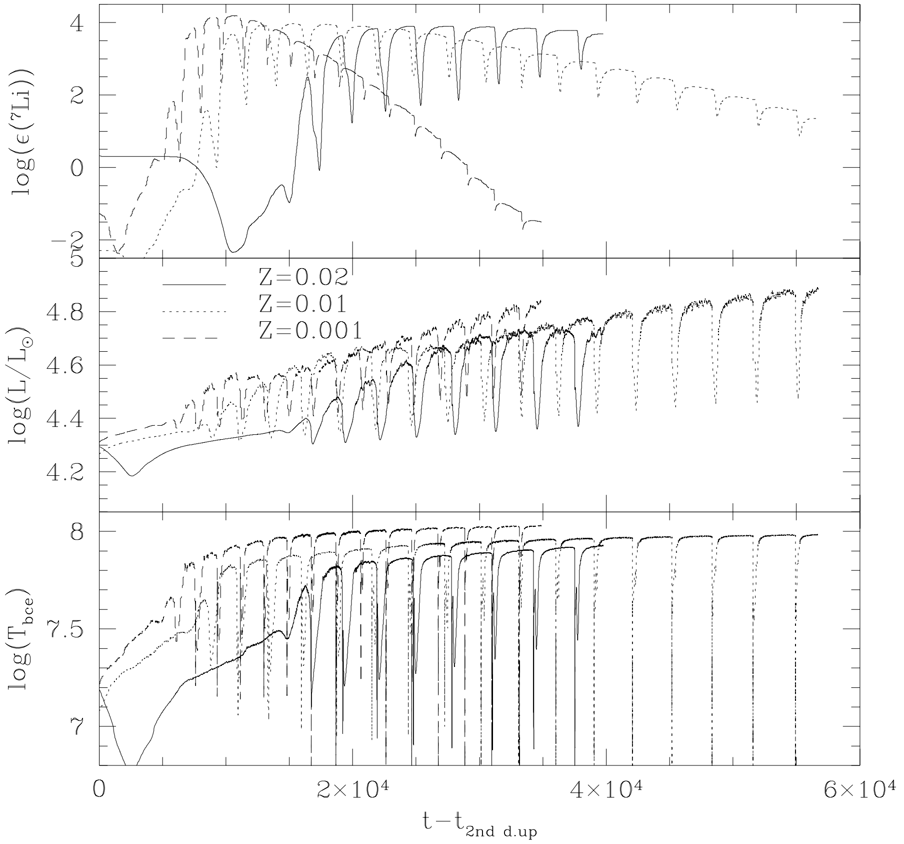

FIGURE 5.13— Variation with time of the lithium abundance, stellar luminosity and temperature at the base of the convective envelope (T$_{bce}$), computed for a 6 M$_\odot$ star model with different metallicities (taken from MDV99). Note that solar metallicity corresponds to Z=0.02. Computations were made without including mass loss and overshooting in this case. Note that the times refer to the time after the 2^{nd} dredge-up and the lithium abundance *log ε(Li)* is in the usual scale of 12+*log N(Li)*.

abundance which remains large for the entire TP-AGB lifetime. In contrast, for high mass loss rates, the HBB process is stopped only after a few pulses (∼5 for a 6 M$_\odot$ star). Models with strong mass loss show oscillations of the Li abundance by orders of magnitude on short scales of $\sim10^4$ years (even within a single TP! - see Figure 5.12). The temperature at the bottom of the convective envelope, T$_{bce}$, varies so much that the lithium production is temporarily stopped while the lithium already produced is diluted. When T$_{bce}$ increases, the lithium abundance increases again. The consequence is that, at least for 20% of the time, there is negligible lithium in the envelope (at a level of approximately *log* $\varepsilon(Li) \lesssim 1.0$). This implies that the distribution of Li abundances derived from the observations can only be analysed statistically.

On the other hand, the activation of HBB takes place at a lower mass limit of only 3.0−3.7 $M_\odot$ at the metallicity of the LMC (Ventura, D'Antona & Mazzitelli 2000). Low-metallicity models predict larger values of T_{bce} and higher luminosities, and as a consequence, higher lithium production for a given stellar mass. In addition, this accelerates Li-production and a maximum value of *log* $\varepsilon(Li) \sim 4.3$ is reached in a shorter time scale with respect to the solar metallicity case. The variation with time of the surface lithium abundance, stellar luminosity and T_{bce}, computed for a 6 $M_\odot$ model and different metallicities is shown in Figure 5.13. We can see that lower metallicity models essentially produce lithium faster due to the larger temperature at the base of the convective envelope.

5.5.2 Period and OH expansion velocity versus HBB

In contrast to the studies made in the past on AGB stars in the Magellanic Clouds, for which a common distance can be assumed, leading to relatively well-determined absolute luminosities, the estimation of absolute luminosities and masses for the stars in our galactic sample is hampered by the large uncertainty in the distance determination[4]. We can try to estimate the luminosity as a first approach using the so-called period-luminosity relationship (for those sources with a well-determined period), taking the period as a distance-independent mass/luminosity indicator. If the P−L relationship for galactic Mira variables found by Groenewegen & Whitelock (1996) is applied to our sample of OH/IR stars, we obtain M_{bol} around ~ -6 for those stars with periods of 400−600 days while a M_{bol} of ~ -5.5 is derived for periods around ~300 days. Similar values were found among the more massive AGB stars in the MCs. However, if we take those stars with the longer periods in the sample ($\gtrsim$ 1000 days), we derive $M_{bol} \lesssim -7$, which seems unrealistically high. This suggests that the period-luminosity relationship may not be applicable to the most extreme OH/IR stars (Wood, Habing & McGregor 1998). On the other hand, there is recent observational evidence for the existence of low-metallicity (e.g. in the LMC) HBB AGB stars with luminosities brighter than the predictions of the core-mass luminosity relation which have been attributed to an excess flux from

---

[4] Note that, in addition, AGB stars are also expected to be strongly variable. Engels et al. (1983) found a M_{bol} variation of 2 magnitudes between the minimum and maximum light (from −5.0 to −7.1 mag respectively) in the galactic OH/IR star OH 32.8−0.3.

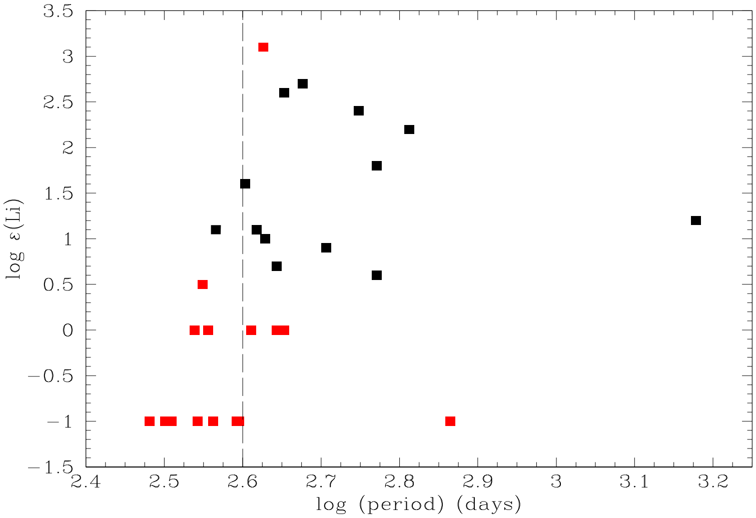

FIGURE 5.14— Observed Li abundance vs. period. Upper limits to the Li abundance are shown in red. The dashed vertical line marks the point where the period is 400 days (see text).

HBB (Whitelock et al. 2003), which could explain the detection of HBB AGB stars with high M_{bol} also in our Galaxy. As we can see in Figure 5.14, we find no correlation at all between the precise value of the Li abundance and the period in our target stars. However, it is interesting to note that for periods below 400 days ($log\ P < 2.6$), only one star out of 12 is Li detected.

Alternatively, we can try with another distance-independent mass/luminosity indicator, such as the expansion velocity derived from OH maser measurements (Baud & Habing 1983; Jiménez-Esteban 2004). The observed lithium abundances are plotted against the OH expansion velocity in Figure 5.15. Again, we find that there is not a clear correlation between OH expansion velocities and the Li abundances derived. Only a trend is detected in which a maximum Li abundance increases with the OH expansion velocity, suggesting that the most massive AGB stars can experience a higher lithium enrichment. However, the most interesting result is the non-detection of Li in any star in the sample with $v_{exp}(OH) < 6$ km s^{-1}. As we have already suggested in Chapter 4, considered all together, the non-detection of Li in stars with periods < 400 days and $v_{exp}(OH) < 6$ km s^{-1} could indicate that these stars do not develop HBB, i.e. they must be stars with M $\lesssim$ 4 $M_{\odot}$.

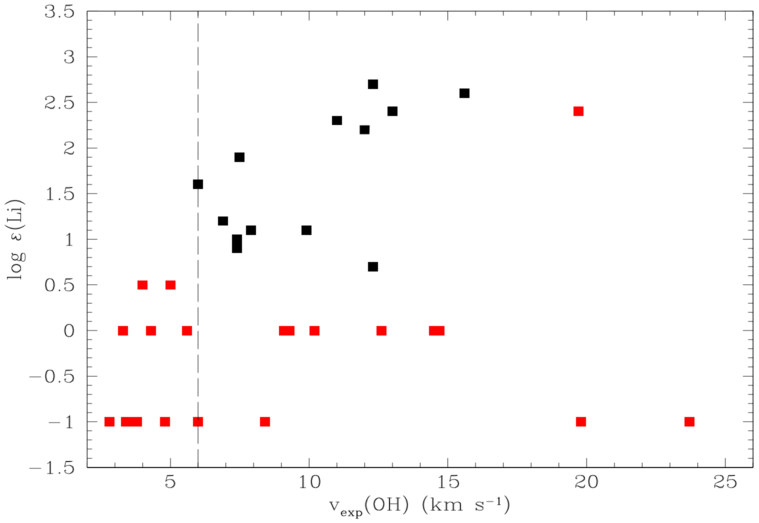

FIGURE 5.15— Observed Li abundance vs. OH expansion velocity. Upper limits to the Li abundance are shown in red. The dashed vertical line marks the point where the OH expansion velocity is 6 km s^{-1} (see text).

5.5.3 Li I/Ca I versus Li abundances

As we have already mentioned in Chapter 4, we have also studied the behaviour of the measured Li I 6708Å /Ca I 6573Å equivalent width ratio in the stars in our sample in connection with the observed Li abundances, and the results are displayed in Figure 5.16. From this diagram, it seems that a fine correlation exists, with a very wide dispersion. This correlation shows that the high Li abundance observed is not an artifact of Li I and Ca I lines appearing strong because of some atmospheric effect (in that case both lines would become stronger). Two different groups of stars are tentatively distinguished. The group of stars with the highest observed Li abundances corresponds to those stars showing the largest OH expansion velocities (>10 km s^{-1}) while the group of stars with lower Li abundances also have lower OH expansion velocities. Our observations also confirm that Li I/Ca I can be used as a rough estimation of the Li abundance as previously suggested in the literature (e.g. Catchpole & Feast 1971; Catchpole 1982; Boesgaard 1970).

5.5.4 Theory versus observations

Globally considered, our results confirm our previous finding that below a certain value of the period and the OH expansion velocity our stars do not show

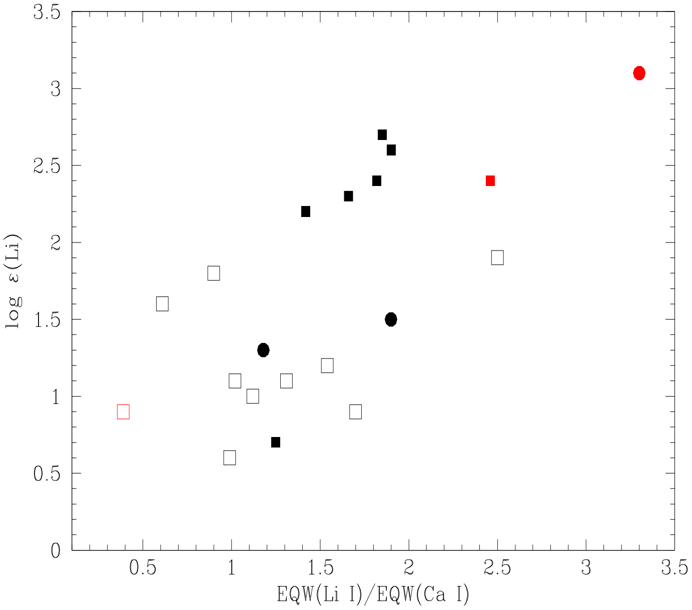

FIGURE 5.16— Observed Li abundance vs. measured ratio of the equivalent widths of Li I 6708 Å to Ca I 6573 Å. Solid squares correspond to those stars with $v_{exp}(OH) > 10$ km s^{-1}, while the group of stars with lower $v_{exp}(OH)$ are represented by open squares. The dot symbols correspond to those stars with unknown $v_{exp}(OH)$. Upper limits to the Li abundance and the measured EQW(Li I)/EQW(Ca I) ratio are shown in red.

any Li enhancement. However, not all the stars above these values show a detectable Li. In fact, the observed Li overabundances are never extremely large ($log\ \varepsilon(Li) \leq 3$), compared to the abundances observed in the so-called 'super Li-rich' stars in our Galaxy. These are C-stars, S-stars or SC stars, which are not among the most massive AGB stars in our Galaxy. Taking into account the strong fluctuations of the Li abundances predicted by the models while the stars evolve along the thermal pulsing AGB phase (see Figures 5.12 and 5.13) it is not possible *a priori* to determine whether the observed stars are at the beginning of the Li-production phase within a thermal pulse or at the end. The absence of s-process enrichment in our stars could in principle indicate that they are at the initial stages of the AGB when the third dredge-up has just been activated and there has been no time yet for a significant surface enrichment in s-process elements. However, the strong IR excesses associated with most of the stars in our sample suggest that they are actually at the end of their evolution as AGB stars. It should be noted that, contrary to the effects of HBB which are soon detectable in the surface of the star after its activation, the effects of the third dredge-up require some time to become observable at the surface of the star (essentially, as a strong s-process element enhancement) and they may only be detectable after a few thermal pulses. Classic stellar modelling (e.g. Becker & Iben 1980; Iben 1991) predicts a rapid activation of the third dredge-up in stars with large core masses. Surprisingly, none of the stars in our sample show a strong s-process enhancement as would have been expected if they were stars at the end of their AGB evolution. In the case of the more massive stars in our sample one could argue that the mass loss is so strong at the high metallicity of our Galaxy (compared to the MCs metallicity) that their AGB lifetime may become shortened significantly, so that they will end this phase experiencing only very few thermal pulses before they completely lose their envelope. However, the lack of s-process enhancement is also observed in the group of stars in which no lithium has been detected.

In order to interpret these results, several scenarios can be proposed:

i) All the stars in the sample are HBB stars, and thus, considerably massive ($M \gtrsim 4\ M_\odot$). The difference between the Li detected and the Li non-detected ones would be simply that the non-detected ones are in a very early stage as AGB stars. This hypothesis would explain the absence of s-process enhancement in all the stars in the sample, but it would not be consistent with the non-detection of lithium in the group of stars with the shorter periods and lower OH expansion velocities. HBB models predict a considerable Li enhancement just after the arrival at the AGB. Statitiscally there should be no difference in the behaviour of the Li abundances for any star in the sample, and this is not observed.

ii) The sample is composed of a combination of low-mass ($M \lesssim 1.5\ M_\odot$) and high mass ($M \gtrsim 4\ M_\odot$) stars. In this scenario, the optically bright O-rich AGB stars in our sample with the shorter periods and lower OH expansion velocities, non-detected in Li, would belong to the population of low-mass stars in the Galaxy which do not experience HBB and evolve all the way along the AGB as O-rich stars. However, these stars are expected to evolve very slowly and develop a large number of thermal pulses during the AGB. At the end of their AGB evolution they are expected to become strongly enhanced in s-process elements as a consequence of the dredge-up of processed material induced by the many thermal pulses experienced. But the Li non-detected stars in our sample do not show this enhancement in s-process elements. The only way to reconcile this result with their status as low-mass stars would imply to assume that they are at a very early stage as AGB stars, which again seems to be incompatible with the strong IR excess detected by IRAS. Such strong excess is only expected in low-mass stars at the very end of the AGB. Alternatively, they could experience fewer thermal pulses than predicted by the model or the dredge-up process could be very inefficient. But this is not what we observe in other low- and intermediate-mass stars in the Galaxy, such as the S-stars and many C-rich stars, which show the strong s-process enhancement which is not observed in our stars. Therefore, we must conclude that the hypothesis of these stars being identified as low-mass AGB stars would not seem to be plausible.

iii) All the stars in the sample are considerably massive (M $\gtrsim$ 3 M$_\odot$) but only a fraction of them, the more massive ones (M $\gtrsim$ 4 M$_\odot$), experience HBB. This scenario would explain why the sources with lower periods and OH expansion velocities in our sample are non-detected in the Li I line, while at the same time, they do not show any s-process enhancement. These stars, although slightly below the minimum mass needed to develop HBB, would also experience a very strong mass loss rate and only a few thermal pulses ($\sim$5$-$10) before the early termination of the AGB as a consequence of this strong mass loss. Busso et al. (1988) predict that an important s-process enhancement is only expected after $\sim$10 thermal pulses or so, under solar metallicity conditions. Alternatively, ^{22}Ne might be favoured as a neutron source to form s-process elements in massive AGB stars (M $\gtrsim$ 3 M$_\odot$) because of the higher temperature during the thermal pulses (e.g. Straniero et al. 2000). In contrast, ^{13}C would be the preferred neutron source in lower mass stars (M $\lesssim$ 3 M$_\odot$) (e.g. Straniero et al. 1995; Busso et al. 2001). Busso et al. (1988) also predict that ^{22}Ne seems to be unable to produce strong s-process overabundances in massive AGB stars. But how can we explain the large spread of Li abundances observed in the group of sources in our sample with longer periods and larger OH expansion velocities? All of these are supposed to be HBB stars. Moreover, HBB models predict a large fluctuation of the Li abundance as the star evolves along the TP-AGB (see Figure 5.12) between two consecutive pulses. In fact, the timescale of the Li production phase in the TP-AGB is predicted to be in the order or slightly smaller than the timescale between pulses ($\sim$10^4 years for a massive star with M $\gtrsim$ 4 M$_\odot$). In addition, as the AGB evolution proceeds the surface Li abundances decrease again very rapidly because of ^{3}He is almost completely burned in the envelope and the Li production is ceased (e.g. MDV99; Forestini & Charbonnel 1997). This would be consistent with the detection of strong Li abundances in $\sim$50% of the stars in which HBB is active. Under this scenario, the strongly obscured sources in the sample for which we were not able to obtain an optical spectrum would also be interpreted as a population of high mass stars developing HBB with even more extreme observational properties. They are sources with longer periods ($>$ 700 days) and larger OH expansion velocities ($>$ 12 km s^{-1}) which have developed thick circumstellar envelopes as a consequence of the huge mass loss experienced in the AGB. These stars must also be detectable as Li-rich at least for some time during their AGB evolution but, unfortunately, they are so strongly reddened in the optical range that their study is only possible in the infrared, where no strong Li lines are present. Finally, we propose that the HBB nature of these obscured stars can be elucidated by determining their $^{12}C/^{13}C$ ratios, which can also be used as a HBB indicator, through near infrared spectroscopy (the H and K bands include several bandheads of the first and second overtones of ^{12}CO and ^{13}CO).

5.5.5 Comparison with the O-rich AGB stars in the Magellanic Clouds

The situation is quite different for the AGB stars in the MCs. In contrast with their galactic analogues, the more luminous AGB stars in the MCs (with $-7 \leq M_{bol} \leq -6$) are O-rich stars showing s-process elements enhancement (S-stars). In addition, a higher proportion of them (∼80% compared to ∼50% in our Galaxy) shows lithium enhancement also. The lithium enhancement indicates that they are also HBB stars but, why are these stars also enriched in s-process elements?

The answer to this question must be related to the different metallicity of the stars in the MCs with respect to our Galaxy. Actually, theoretical models predict a higher efficiency of the dredge-up in low metallicity atmospheres (e.g. Herwig 2004) with respect to those with solar metallicity (e.g. Lugaro et al. 2003). Under low metallicity conditions Busso et al. (1988) predict a significant enrichment in s-process elements after only a few (∼4−5) thermal pulses.

Moreover, there is increasing observational evidence that lower metallicity environments are also less favourable to dust production, as is suggested by the very small number of heavily obscured AGB stars in the MCs (Trams et al. 1999; Groenewegen et al. 2000). This is supported by the lower dust-to-gas ratios derived by van Loon (2000) in the few obscured AGB stars in the MCs for which this analysis has been made.

If mass loss is driven by radiation pressure on the dust grains, this might be less efficient with decreasing metallicity (Willson 2000). In that case, longer AGB lifetimes would be expected, which could increase the chances of nuclear-processed material to reach the stellar surface. This would also explain the larger proportion of luminous C-rich stars (up to $M_{bol}\sim-6$) observed in the MCs (Plez, Smith & Lambert 1993; Smith & Lambert 1989, 1990a; Smith et al. 1995) with respect to the Galaxy. The slow evolution predicted for AGB stars in the MCs as a consequence of the less efficient mass loss leaves time for more thermal pulses to occur during the AGB lifetime and, therefore, a more effective dredge-up of s-process elements to the surface can be expected before the envelope is completely gone at the end of the AGB. This would explain why even the more massive stars in the MCs show a strong s-process enrichment in contrast to their galactic counterparts. In our Galaxy the only AGB stars showing a similar overabundance in s-process elements seem to be the result of the evolution of low- to intermediate-mass stars ($M \lesssim 1.5-2.0\ M_{\odot}$), while no or very litle s-process enhancement is observed in galactic AGB stars with higher main sequence masses.

In addition, the lower critical mass needed to develop HBB ($M \gtrsim 3\ M_{\odot}$ at the metallicity of the LMC, compared to the $\sim$4 $M_{\odot}$ limit in our Galaxy) would favour the simultaneous detection of s-process elements and Li enrichment in a larger number of AGB stars in the MCs. In our Galaxy, the Li rich sample of AGB stars is restricted to the fraction of stars with main sequence masses $M \gtrsim 4\ M_{\odot}$. In contrast to their MC counterparts, these stars evolve so rapidly (because of the strong mass loss) that there is no time for a significant enhancement in s-process elements, as the results presented here seem to demonstrate.

5.5.6 An evolutionary interpretation

The well known existence of at least two different chemical branches of AGB stars (C-rich and O-rich) and the dependence of this chemical segregation on the main sequence mass and on the environmental conditions in which these stars evolve (such as the metallicity) is a long debated issue in stellar evolution. Efforts have been made to improve nucleosynthesis models which are now able to explain roughly the observational properties of AGB stars in a quite satisfactory way. However, there are still a large number of physical processes, such as the treatment of the convection by the models or the effects of overshooting, which are not yet fully understood and may have an enormous impact on the chemical properties observed at the stellar surface (e.g. Mazzitelli, D'Antona & Ventura 1999; Lugaro et al. 2003). In general, current models are often lacking in that they are not contrasted with observations, a problem that we have tried to alleviate with the data presented in this work. So far, only studies based on MC AGB stars have been published in the literature (Plez, Smith & Lambert 1993; Smith & Lambert 1989, 1990a; Smith et al. 1995). Moreover, the connection with the chemical composition observed in post-AGB stars and/or well evolved

PNe has never been addressed in detail from an overall perspective (van Winckel 2003; Pottasch 1990).

Observationally we can distinguish up to three different chemical evolutionary paths in the AGB stars of our Galaxy. Which path is followed by a given source is mainly a function of their main sequence mass (García-Lario & Perea Calderón 2003):

i) Low mass stars ($0.8\ M_\odot < M < 1.5\ M_\odot$; $-4.0 > M_{bol} > -5.0$). They evolve as optically bright O-rich Mira variable stars along the AGB, with periods typically in the order to 200 to 350 days. Only a very small fraction of these stars are expected to develop OH masers. The more massive stars in this group may be able to increase their C/O ratio to values close to one at the end of the AGB phase and eventually become S-stars (C/O$\sim$1) or low-mass C-rich stars (C/O $>$ 1).

ii) Intermediate mass stars ($1.5\ M_\odot < M < 3.0\ M_\odot$; $-5.0 > M_{bol} > -5.5$). Shortly after entering the TP-AGB phase, they become carbon stars as a consequence of an efficient dredge-up. Typical variability periods are expected to be in the range of 300$-$500 days. Most of them will evolve as optically bright carbon stars all the way along the AGB. Only the more massive stars in this group may become heavily obscured at the end of the AGB phase, turning into 'infrared carbon stars'.

iii) High mass stars ($M > 3\ M_\odot$; $-5.5 > M_{bol} > -7.0$). Most of the stars in this group evolve as OH/IR stars while they are in the AGB phase, with variability periods longer than 350 days. Because of the strong mass loss they develop thick circumstellar envelopes which eventually hide them from detection in the optical range. The lower mass fraction of stars in this group with $3\ M_\odot < M < 4\ M_\odot$ will not develop hot-bottom burning, and they will not experience enough (and less efficient because of the high metallicity) thermal pulses to produce a significant enrichment in carbon and s-process elements in the stellar atmosphere, remaining as O-rich stars during the whole AGB phase. The higher mass fraction of stars in this group (with $M > 4\ M_\odot$) will develop HBB and show a strong lithium enhancement at least during the Li production phase ($\sim$50% of the time). They are expected to become heavily obscured and evolve as optically invisible O-rich stars (probably N-rich too, as a consequence of the activation of the HBB) all the way until the end of the AGB.

The observational properties of the stars in our sample indicate that they belong to the latter group of high mass stars. The fraction of stars with periods shorter than 400 days and $v_{exp}(OH) < 6$ km s^{-1} are identified as stars with progenitor masses in the 3$-$4 M$_{\odot}$ range, while those with longer periods and higher $v_{exp}(OH)$ must be HBB stars with M > 4 M$_{\odot}$. In our sample there is an additional group of sources showing even more extreme properties (P > 700 days and $v_{exp}(OH) > 12$ km s^{-1}) which are found to be completely obscured in the optical and could not be studied. This latter group may represent the more massive fraction of AGB stars in our Galaxy.

Our results also suggest that the segregation of AGB stars in these different chemical evolutionary paths is strongly modulated by the metallicity. The dramatically different abundance patterns found in AGB stars belonging to the MCs and to our Galaxy can only be explained in terms of the different metallicity conditions under which these stars evolved.

Additional observational constraints can be extracted from the analysis of the chemical abundances found in galactic post-AGB stars and PNe, as they are expected to be the result of the evolution of AGB stars with a wide variety of masses.

Stars classified as post-AGB stars in the literature are mainly low mass stars, according to their wide galactic distribution. They represent the fraction of stars which evolve so slowly that they are still visible for some time as stars with intermediate spectral types before they become PNe. Many of these stars are C-rich and show strong s-process element enhancements [s-process/Fe]$\sim$+1.5 (van Winckel & Reyniers 2000; Reddy, Baker & Hrivnak 1999; Klochkova et al. 1999), in agreement with what we would expect if they were the final product of the evolution of low-mass AGB stars. However, another group does not show the characteristic signatures of the third dredge-up. In the non-enriched sources the s-process element abundances can be as low as [Zr/Fe] $\lesssim$ 0.2 (Luck et al. 1990; van Winckel 1997). A similar result is found in a group of hot B-type post-AGB stars (e.g. Conlon et al. 1993; Mooney et al. 2001), which show strong carbon deficiencies and no third dredge-up pattern. These objects might be extremely low-mass post-AGB stars (M$\sim$0.8$-$1.0 M$_{\odot}$) which have evolved off the AGB before the third dredge-up could occur (Marigo, Girardi & Bressan 1999). In the more extreme cases they will probably never become PNe.

A chemical segregation is also observed in galactic PNe. Classically, they are classified as type I, II and III as a function of their chemical abundance properties (Peimbert 1978). They are expected to cover a wide range of progenitor masses and, thus, show different chemical signatures as a consequence of their previous passage along the AGB.

Type III PNe are members of the halo population and, thus, expected to represent the fraction of lower mass PNe. Their progenitor masses must be in the order of M$\sim$1.0$-$1.5 $M_\odot$.

Type II PNe are the result of the evolution of stars with progenitor masses between 1.5 $M_\odot$ and 4 $M_\odot$. Among them we should expect to find C-rich and O-rich stars, with a wide variety of s-process enrichment patterns, depending on whether they evolved along the AGB as low-mass O-rich stars, intermediate-mass C-rich stars or high-mass O-rich stars (without the HBB activated).

Finally, Type I PNe are characterized by their large He abundances (He/H > 0.10) and N/O ratios (Manchado 2003, 2004; Mampaso 2004, and references therein). They are suspected to represent the fraction of the more massive PNe in the Galaxy, as is confirmed by their strong concentration at low galactic latitudes. Their strong N overabundances would be consistent with their identification as the result of the evolution of HBB AGB stars.

But how can we test the chemical connections suggested above between AGB stars and PNe?

A first attempt has recently been made through the obtention of ultra-deep near-infrared spectra of a sample of bright PNe, which resulted in the detection of atomic lines corresponding to s-process elements (Dinerstein 2001; Dinerstein & Geballe 2001). Despite the crude ionization correction factors adopted, Sterling & Dinnerstein (2004) found that PNe with WC-type central stars (thus, C-rich) tend to exhibit stronger s-process element enhancements while bipolar nebula (usually considered to represent a more massive population of PNe) display lower s-process abundances than elliptical PNe. When reliable atomic data for a quantitative analysis becomes available for these lines, the possibility will open to test whether the abundances observed are consistent with the evolutionary scenario predicted for their immediate precursors in the AGB.

Another test could consist of the determination of the ^{12}C/^{13}C ratio in different types of PNe, used as an alternative HBB indicator. This ratio is expected to vary according to the mass of the progenitor star as a consequence of the activation of HBB in the more massive AGB stars (M > 4 $M_\odot$). HBB models predict the production of ^{7}Li while the carbon is cycled to nitrogen and low values for the ^{12}C/^{13}C ratio ($\sim$3$-$4) should be attained (Mazzitelli, D'Antona & Ventura 1999). So far, the measurement of this ratio in PNe has been restricted to the ultraviolet and submillimeter wavelength range (Palla et al. 2000, 2002; Balser, McMullin & Wilson 2002). At least two type I bipolar PNe included in the limited observed sample (NGC 2440 and M 1-16) have ^{12}C/^{13}C ratios near to the equilibrium value of $\sim$3$-$4 predicted by HBB models (Mazitelli, D'Antona & Ventura 1999).

5.6 Conclusions

With the help of MARCS model atmospheres and synthetic spectroscopy we have been able to derive the main physical parameters (T_{eff}, *log g, C/O,* ξ, etc.) and determine the Li and Zr abundances of a large sample of massive galactic O-rich AGB stars. Our chemical abundance analysis detected Li overabundances in half of the stars for which an optical spectrum could be obtained, with *log* ε*(Li)* in the range of +0.0 to +3.0 dex. This is interpreted as a clear signature of the activation of HBB in the more massive O-rich AGB stars in the Galaxy. On the other hand, we have found that our observations are also consistent with no significant s-process enhancement (assuming that Zr abundances are representative of s-process element abundances) in strong contrast with the observations of the more luminous AGB stars in the Magellanic Clouds. The discrepancies observed are attributed to the different metallicity.

From the comparison of our results with the theoretical predictions of HBB and nucleosynthesis models and assuming that the variability period and the OH expansion velocity can be taken as distance independent mass indicators we conclude that the stars in our sample are all considerably massive ($M > 3$ $M_\odot$), but only the more massive ones ($M > 4$ $M_\odot$; with periods longer than 400 days and v_{exp}*(OH)* > 6 km s^{-1}) experience HBB and lithium production. The lack of lithium in some stars suspected to belong to the group of more massive AGB stars in the sample is explained as the consequence of the timescale of the Li production phase (being of the order or slightly smaller than the interpulse time $\sim 10^4$ years) and/or by the ^{3}He exhaustion in the envelope ceasing Li production, in agreement with the predictions made by the models.

A significant number of stars in the sample were too red to derive any information on their physical properties and/or chemical abundances in the optical range. They belong to the group showing the most extreme observational properties (with periods sometimes longer than 700 days and v_{exp}*(OH)* > 12 km s^{-1}) and are believed to represent the more massive AGB stars in our Galaxy. According to their high mass they should also be HBB stars and display strong Li overabundances and no s-process element enhancement. Observations of these stars at near infrared wavelengths are strongly indicated in order to confirm the HBB nature of these stars through the measurement of the ^{12}C/^{13}C ratios.

Considered overall, our results are consistent with the observational data available on galactic post-AGB stars and PNe. In particular, the AGB stars in our sample in which HBB is thought to be activated (i.e. those with periods longer than 400 days and v_{exp}*(OH)* > 6 km s^{-1}) are suggested to be the predecessors of the N-rich type I PNe, while the rest of AGB stars in our sample would evolve into O-rich type II PNe.

6

Conclusions

6.1 Molecular hydrogen emission from the AGB phase to the PN stage

Based on the analysis of our near-IR spectroscopic data, we have increased from four to thirteen the total number of proto-PNe detected in H_2, confirming the previous finding, made on a smaller sample of objects, that the onset of H_2 emission takes place during the transition phase between AGB and PNe. In addition, we have used the diagnostic ratios $H_2[v{=}1{\rightarrow}0\ S(1)/v{=}2{\rightarrow}1\ S(1)]$ and $H_2[v{=}1{\rightarrow}0\ S(1)]/Br\gamma$ as indicators of the prevalent mechanism of the H_2 excitation. Interestingly, we have found that the onset of the molecular hydrogen emission strongly depends on the excitation mechanism.

When the H_2 is fluorescence-excited the detection rate is found to be directly correlated with the evolutionary stage of the central star (spectral type), rather than with the nebular morphology. We have found that fluorescent molecular hydrogen emission becomes active, as a consequence of the absorption of UV photons coming from the central star, when the rapidly evolving post-AGB central star attains a temperature value which corresponds to an A-spectral type.

In contrast, shock-excited H_2 emission is detected only in strongly bipolar proto-PNe, sometimes even at a very early stage in the post-AGB phase when the post-AGB central star is still very cool. Shock-excited H_2 emission is interpreted as the result of the interaction of the fast post-AGB wind with the slow wind material previously expelled during the AGB phase. This type of emission is often localized in those regions where the physical interaction between these two winds is taking place (i.e., along the walls or at the tip of the bipolar lobes). Bipolarity also protects the molecular hydrogen from destruction, favouring its detection in the waist of well evolved bipolar PNe. The strong correlation found between shock-excited H_2 emission and bipolarity seems to explain the high detection rate of H_2 emission found in bipolar PNe.

6.2 Mid-infrared structures around IRAS 16594−4656 and IRAS 07027−7934

The presence of a double-peaked mid-IR emission in the central region of the C-rich multipolar proto-planetary nebula IRAS 16594−4656 is interpreted as the result of the presence of a dusty toroidal structure with a $0.4''$ radius size (or ∼640 AU at an assumed distance of 1.6 kpc). The dynamical age of this dusty torus structure is estimated to be ∼190 yr adopting the expansion velocity measured from CO data. This adds IRAS 16594−4656 to the short list of known PPN/PNe (only 4 sources previously known!) in which a dusty toroidal structure has been imaged. The torus is oriented perpendicular to one of the bipolar outflows (at P.A.∼84°) identified in the HST optical images. The other bipolar outflows identified in the HST optical images may have been formed as a consequence of past episodic mass loss events and are an indication of the presence of a central precessing system.

In IRAS 07027−7934, a young elliptical planetary nebula showing mixed chemistry (C-rich and O-rich, [WC]), we have identified/detected a slightly asymmetric marginally extended emission at 8.6 and 11.5 μm (FWHM=$0.3''$), coincident with the off-centre ionised core emission identified in the ground-based Hα images. The mid-IR emission is interpreted as due to a mixture of highly ionised PAHs and warm dust continuum. In addition, we suggest that IRAS 07027−7934 may have recently experienced a late thermal pulse (likely at the end of the previous AGB phase) which has produced a switch in the dominant chemistry of its central star (from O-rich to C-rich).

6.3 Lithium and s-process element abundances in massive galactic O-rich AGB stars

As a result of a high resolution spectroscopic survey carried out in the optical for a large sample (102) of massive galactic O-rich AGB stars, we have detected the Li I resonance line at 6708 Å in 25 stars, while 32 stars did not display this Li I line. The rest of the stars observed (45 stars) were heavily obscured by their thick circumstellar envelopes and they were too red/not found at optical wavelengths.

We have classified the sample in three subgroups on the basis of their OH expansion velocity and variability period. From their relative distribution in the IRAS two-colour diagram [12]−[25] vs [25]-[60] and galactic distribution, we conclude that they must represent populations of galactic O-rich AGB stars with different progenitor masses.

Combining MARCS model atmospheres and synthetic spectroscopy with extensive linelists we have been able to derive the stellar fundamental parameters (T_{eff}, *log g, C/O,* ξ, etc.) and obtain the Li and Zr abundances in those stars for which an optical spectrum could be obtained. Our chemical abundance analysis shows that half of the stars show Li overabundances in the range between $log\ \varepsilon(Li){\sim}{+}0.0$ and +3.0 dex. These are interpreted as a signature of the activation of "Hot Bottom Burning" (HBB), confirming that they are massive AGB stars. However, these stars do not show any zirconium enhancement (taken as a representative for the s-process element enrichment), as predicted by the models, indicating that they behave differently from the more massive (and luminous) AGB stars in the Magellanic Clouds. The discrepancies observed are attributed to the different metallicity environment.

Assuming that the variability period and the OH expansion velocity can be taken as distance independent mass indicators and by comparing our results with the theoretical predictions of HBB and nucleosynthesis models, we conclude that the O-rich AGB stars in our sample are all considerably massive (M > 3 M$_\odot$), even those with non Li detected, but only the more massive ones (M > 4 M$_\odot$; with periods longer than 400 days and $v_{exp}(OH) > 6$ km s^{-1}) experience HBB. The non lithium enrichment found in some of the stars suspected to belong to the group of more massive AGB stars in the sample is explained as the consequence of the timescale of the Li production phase (being of the order or slightly smaller than the interpulse time $\sim$10^4 years) and/or by the ^{3}He exhaustion in the envelope ceasing Li production, in agreement with the predictions made by the models.

The group of stars displaying the most extreme observational properties (with periods sometimes longer than 700 days and $v_{exp}(OH) > 12$ km s^{-1}) are believed to represent the more massive AGB stars in our Galaxy. Unfortunately, these stars are strongly obscured by their thick circumstellar envelopes and we could not carry out any type of analysis in the optical range. This very high mass population should also experience HBB and show strong Li enhancement but no s-process element overabundances. We propose that the HBB status of these obscured stars can be determined by measuring their ^{12}C/^{13}C ratios in the near-infrared, which can also be used as a HBB indicator.

Globally considered, our results are in good agreement with the observational data available in the literature on galactic post-AGB stars and PNe. In particular, the O-rich AGB stars in our sample with periods longer than 400 days and $v_{exp}(OH) > 6$ km s^{-1} are suggested to be the precursors of N-rich type I PNe, while the non-HBB O-rich AGB stars in our sample (i.e. those with lower periods and OH expansion velocities) would evolve into O-rich type II PNe.

7

Future work

As a natural continuation of the work presented in this thesis, new research areas have emerged.

Regarding the analysis of the molecular hydrogen emission in sources evolving from the AGB phase to the PN stage, it will be very useful to obtain near infrared spectroscopy of a larger sample of stars to improve the still poor statistics derived from the results so far obtained. This will help to establish a conclusive relationship between the detection of H_2 emission and the evolutionary stage of the sources studied as well as between the characteristics of the H_2 emission and the morphology. To this end, the use of LIRIS, now installed at the WHT (La Palma, Spain) is planned in the near future for the observation of extended sources. For the more compact sources, NICMOS onboard HST (for which a Cycle 14 proposal has been submitted) or adaptive optics observations using e.g. NAOMI+INGRID at the WHT with subarcsec resolution will be needed.

Concerning the study of dust shells around proto-PNe, we plan to extend the analysis carried out on IRAS 16594−4656 and IRAS 07027−7934 to other transition sources, using the images at 10 microns already obtained in 2004 using TIMMI2 at the ESO 3.6m telescope (La Silla, Chile). The detection of mid-IR extended structures around proto-PNe (such as the dust torus in IRAS 16594−4656) can be crucial for studying the collimating processes in bipolar PNe at a very early stage of development. In the future, VISIR at the VLT (Paranal, Chile) or CANARICAM at the GTC (La Palma, Spain) can also be used to extend the observations to a larger sample and/or improve the spatial resolution of the images already obtained up to the subarcsec level. With these two instruments we can also determine the overall morphology of these sources using narrow-band filters, which will provide information about the relative distribution of the gas and dust in the envelope, leading to the determination of the physical conditions of the emitting atoms, molecules and grains.

As we have shown in this thesis, the more massive AGB stars in our sample are so heavily obscured that their analysis in the optical range was not possible. Many of these extremely reddened stars are, in contrast, extremely bright in the near infrared. Thus, an observational programme at this wavelength range using the same sample of galactic O-rich AGB stars studied in this thesis has been started. The intention is to determine the $^{12}C/^{13}C$ ratio (used as a HBB indicator) in these sources, giving priority to the more extremely obscured ones that were not studied in the optical. For this study, near infrared spectroscopy in the H and K bands of a first group of ~30 sources has already been obtained using NICS (R~2,500) at the TNG (La Palma, Spain) in 2004 and additional observing time has been granted to observe the southern sources in the sample using ISAAC (R~9,000) at the VLT (Paranal, Chile) in May 2005. These observations will allow us to study the hidden chemical properties of these massive stars and will pose important constraints on the theoretical models.

Bibliography

[1] Abia, C., Boffin, H.M.J., Isern, J. & Rebolo, R. 1991, A&A, 245, L1

[2] Abia, C., Boffin, H.M.J., Isern, J. & Rebolo, R. 1993, A&A, 272, 455

[3] Abia, C. & Isern, J. 1996, ApJ, 460, 443

[4] Abia C. & Isern J. 1997, MNRAS, 289, L11

[5] Abia, C. & Wallerstein, G. 1998, MNRAS, 293, 89

[6] Abia, C., Pavlenko, Y. & de Laverny, P. 1999, A&A, 351, 273

[7] Abia, C. & Isern, J. 2000, ApJ, 536, 438

[8] Allain, T., Leach, S. & Sedlmayr, E. 1996, A&A, 305, 616

[9] Allamandola, L.J., Hudgins, D.M. & Sandford, S.A. 1999, ApJ, 511, L115

[10] Allard, F., Hauschildt, P.H. & Schwenke, D. 2000, ApJ, 540, 1005

[11] Alvarez, R., Lancon, A., Plez, B. & Wood, P. R.. 2000a, A&A, 353, 322

[12] Alvarez, R., Jorissen, A., Plez, B., Gillet, D. & Fokin, A. 2000b, A&A, 362, 655

[13] Alvarez, R., Jorissen, A., Plez, B., Gillet, D., Fokin, A. & Dedecker, M. 2001a, A&A, 379, 305

[14] Alvarez, R., Jorissen, A., Plez, B., Gillet, D., Fokin, A. & Dedecker, M. 2001b, A&A, 379, 288

[15] Aringer, B., Kerschbaum, F. & Jörgensen, U.G. 2002, A&A, 395, 915

[16] Aspin, C., Schwarz, H.E., Smith, M.G., Corradi, R.L.M., Mountain, C.M., Wright, G.S., Ramsay, S.K., Robertson, D., Beard, S.M., Pickup, D.A., Geballe, T.R., Bridger, A., Laird, D., Montgomery, D., Glendinning, R., Pentland, G., Griffin, J.L. & Aycock, J. 1993, A&A, 278, 255

[17] Balick, B. 1987, AJ, 94, 671

[18] Balser, D.S., McMullin, J.P. & Wilson, T.L. 2002, ApJ, 572, 326

[19] Baud, B., Habing, H.J., Matthews, H.E. & Winnberg, A. 1981, A&A, 95, 156

[20] Baud, B. & Habing, H.J. 1983, A&A, 127, 73

[21] Becker, S.A. & Iben, I.Jr. 1980, ApJ, 237, 111

[22] Beckwith, S., Gatley, I. & Persson, S.E. 1978, ApJ, 219, L33

[23] Bedijn, P.J. 1987, A&A, 186, 136

[24] Bergeat, J., Knapik, A. & Rutily, B. 2002, A&A, 390, 967

[25] Bessell, M. S., Castelli, F. & Plez, B. 1998, A&A, 333, 231

[26] Black, J.H. & van Dishoeck, E.F. 1987, ApJ, 322, 412

[27] Blöcker, T. 1995, A&A, 299, 755

[28] Blöcker, T. 2001, Ap&SS, 275, 1

[29] Bobrowsky, M., Sahu, K.C., Parthasarathy, M. & García-Lario, P. 1998, Nature, 392, 469

[30] Boesgaard, A.M. 1970, ApJ, 161, 1003

[31] Boffin, H.M.J., Abia, C., Isern, J. & Rebolo, R. 1993, A&AS, 102, 361

[32] Bond, H.E. & Livio, M., 1990, ApJ 355, 568

[33] Bujarrabal, V., Gómez-González, J., Bachiller, R. & Martín-Pintado, J. 1988, A&A, 204, 242

[34] Burstein, D. & Heiles, C. 1982, AJ, 87, 1165

[35] Burton, M.G., Hollenbach, D.J. & Tielens, A.G.M.M. 1990, ApJ, 365, 620

[36] Burton, M.G. 1992, Aust. J. Phys., 45, 463

[37] Burton, M.G., Hollenbach, D.J. & Tielens, A.G.M.M. 1992, ApJ, 399, 563

[38] Burton, M.G., Howe, J.E., Geballe, T.R. & Brand, P.W.J.L. 1998, Publ. Astron. Soc. Aust., 15, 194

[39] Busso, M., Picchio, G., Gallino, R. & Chieffi, A. 1988, ApJ, 326, 196

[40] Busso, M., Gallino, R., Lambert, D.L., Travaglio, C. & Smith, V. V. 2001, ApJ, 557, 802

[41] Cameron, A.G.W. & Fowler, W.A. 1971, ApJ, 164, 111

[42] Cardelli, J.A., Clayton, C. & Mathis, J.S. 1989, ApJ, 345, 245

[43] Catchpole, R.M. & Feast, M.W. 1971, MNRAS, 154, 197

[44] Catchpole, R.M. & Feast, M.W. 1976, MNRAS, 175, 501

[45] Catchpole, R.M. 1982, MNRAS, 199, 1

[46] Cenarro, A.J., Gorgas, J., Cardiel, N., Vazdekis, A. & Peletier, R.F. 2002, MNRAS, 329, 863

[47] Cernicharo, J., Guélin, M. & Kahane, C. 1999, A&AS, 142, 181

[48] Chen, P.S., Wang, X.H. & Xiong, G.Z. 1998, A&A, 333, 613

[49] Chen, P.S., Szczerba, R., Kwok, S. & Volk, K. 2001, A&A, 368, 1006

[50] Chengalur, J.N., Lewis, B.M., Eder, J. & Terzian, Y. 1993, ApJS, 89, 189

[51] Cohen, J.G., Persson, S.E., Elias, J.H. & Frogel, J.A. 1981, ApJ, 249, 481

[52] Cohen, M., Barlow, M.J., Liu, X.-W. & Jones, A.F. 2002, MNRAS, 332, 879

[53] Colangeli, L., Mennella, V., Palumbo, P., Rotundi, A. & Bussoletti, E. 1995, A&AS, 113, 561

[54] Conlon, E.S., Dufton, P.L., McCausland, R.J.H. & Keenan, F.P. 1993, ApJ, 408, 593

[55] D'Antona, F. & Mazzitelli, I. 1996, ApJ, 470, 1093

[56] Davis, C.J., Smith, M.D., Gledhill, T.M. & Varricatt W.P. 2005, MNRAS (in press, astro-ph/0503327)

[57] De Marco, O. & Soker, N. 2002, PASP, 114, 602

[58] De Marco, O., Barlow, M.J. & Cohen, M. 2002, ApJ, 574, 83

[59] Decin, L. 2000, Ph D. Thesis, Catholic University of Leuven

[60] Decin, L., Vandenbussche, B., Waelkens, C., Eriksson, K., Gustafsson, B., Plez, B., Sauval, A.J. & Hinkle, K. 2003a, A&A, 400, 679

[61] Decin, L., Vandenbussche, B., Waelkens, C., Decin, G., Eriksson, K., Gustafsson, B., Plez, B, & Sauval, A.J. 2003b, A&A, 400, 709

[62] Dinerstein, H.L. 2001, ApJ, 550, L223

[63] Dinerstein, H.L. & Geballe, T.R. 2001, ApJ, 562, 515

[64] Doublier, V., Billeres, M., Lo Curto, G., Weilenmann, U., Kaufl, U., Sterzick, M. & Hainaut, O. 2005, LSO-MAN-ESO-9XXXX-X/X.0, in preparation

[65] Draine, B.T. & Lee, H.M. 1984, ApJ, 285, 89

[66] Engels, D. 1979, A&AS, 36, 337

[67] Engels, D., Kreysa, E., Schultz, G.V. & Sherwood, W.A. 1983, A&A, 124, 123

[68] Engels, D. & Lewis, B.M. 1996, A&AS, 116, 117

[69] Evans, N.J. 1980. IAU Symp. 87, "*Interstellar molecules*", Dordrecht, D. Reidel Publishing Co. p.1

[70] Field, D. 1985, MNRAS, 217, 1

[71] Forestini, M., & Charbonnel, C. 1997, A&AS, 123, 241

[72] García-Hernández, D.A., Manchado, A., García-Lario, P., Domínguez-Tagle, C., Conway, G.M. & Prada, F. 2002, A&A, 387, 955

[73] García-Hernández, D.A., Abia, C., García-Lario, P. & Manchado, A. 2006, A&A (submitted)

[74] García-Lario, P., Manchado, A., Pottasch, S.R., Suso, J. & Olling, R. 1990, A&AS, 82, 497

[75] García-Lario, P., Manchado, A., Riera, A., Mampaso, A. & Pottasch, S.R. 1991, A&A, 249, 223

[76] García-Lario, P. 1992. Ph.D. Thesis, La Laguna University

[77] García-Lario, P., Manchado, A., Parthasarathy, M. & Pottasch, S.R. 1994, A&A, 285, 179

[78] García-Lario, P., Manchado, A., Pych, W. & Pottasch, S.R. 1997a, A&AS, 126, 479

[79] García-Lario, P., Parthasarathy, M., de Martino, D., Sanz Fernández de Córdoba, L., Monier, R., Manchado, A. & Pottasch, S.R. 1997b, A&A, 326, 1103

[80] García-Lario, P., Riera, A. & Manchado, A. 1999, ApJ, 526, 854

[81] García-Lario, P., D'Antona, F., Lub, J., Plez, B., Habing, H.J. 1999a, IAU Symp. 191, "*Asymptotic Giant Branch Stars*", eds. T. Le Bertre, A. Lebre and C. Waelkens, PASP, p. 91

[82] García-Lario, P., Manchado, A., Ulla, A. & Manteiga, M. 1999, ApJ, 513, 941

[83] García-Lario, P. & Perea Calderón, J. V. 2003, in "*Exploiting the ISO Data Archive. Infrared Astronomy in the Internet Age*, eds. C. Gry, S. Peschke, J. Matagne, P. García-Lario, R. Lorente and A. Salama. ESA SP-511, p. 97

[84] García-Segura, G., Langer, N. & Rozyczka, M. 1999, ApJ, 517, 767

[85] García-Segura, G. & López, J.A. 2000, ApJ, 544, 336

[86] Gatley, I., Depoy, D.L. & Fowler, A.M. 1988, Science, 242, 1264

[87] Gillet, D. 1988a, A&A, 190, 200

[88] Gillet, D. 1988b, A&A, 192, 206

[89] Goriely, S. & Mowlavi, N. 2000, A&A, 362, 599

[90] Grevesse, N. & Sauval, A.J. 1998, SSRv, 85, 161

[91] Groenewegen, M.A.T. & Whitelock, P.A. 1996, MNRAS, 281, 1347

[92] Groenewegen, M.A.T. & de Jong, T. 1998, A&A, 337, 797

[93] Groenewegen, M.A.T., Blommaert, J.A.D.L., Cioni, M.-R., Okumura, K., Habing, H.J., Trams, N.R. & van Loon, J.T. 2000, Mem. Soc. Astron. Ital., 71, 639

[94] Groenewegen, M.A.T., Sevenster, M., Spoon, H.W.W. & Pérez, I. 2002, A&A, 390, 511

[95] Guerrero, M.A. & Manchado, A. 1998, ApJ, 508, 262

[96] Guerrero, M.A., Villaver, E., Manchado, A., García-Lario, P. & Prada, F. 2000, ApJS, 127, 125

[97] Gustafsson, B., Bell, R.A., Eriksson, K. & Nordlund, *Å*. 1975, A&A, 42, 407

[98] Henyey, L., Vardya, M.S. & Bodenheimer, P. 1965, ApJ, 142, 841

[99] Herman, J. & Habing, H.J. 1985, A&AS, 59, 523

[100] Herwig, F., Blöcker, T., Schönberner, D. & El Eid, M. 1997, A&A, 324, L81

[101] Herwig, F., Blöcker, T., Langer, N. & Driebe, T. 1999, A&A, 349, 5

[102] Herwig, F. 2000, A&A, 360, 952

[103] Herwig, F. 2001, Ap&SS, 275, 15

[104] Herwig, F. 2004, ApJ, 605, 425

[105] Hinkle, K., Wallace, L., Valenti, J. & Harmer, D. 2000, *Visible and Near Infrared Atlas of the Arcturus Spectrum 3727-9300 Å*, eds. K. Hinkle, L. Wallace, J. Valenti, and D. Harmer. (San Francisco: ASP) ISBN: 1-58381-037-4

[106] Höfner, S., Gautschy-Loidl, R., Aringer, B. & Jörgensen, U.G. 2003, A&A, 399, 589

[107] Holweger, H. & Müller, E.A. 1974, Sol. Phys., 39, 19

[108] Hora, J.L., Latter, W.B. & Deutsch, L.K. 1999, ApJS, 124, 195

[109] Hrivnak, B.J., Kwok, S. & Su, K.Y.L. 1999, ApJ, 542, 849

[110] Hrivnak, B.J., Volk, K. & Kwok, S. 1999, BAAS, 31, 1536

[111] Hrivnak, B.J., Volk, K. & Kwok, S. 2000, ApJ, 535, 275

[112] Hrivnak, B.J., Kelly, D.M. & Su, Y.L. 2004, in "*Asymmetrical Planetary Nebulae III: Winds, Structure and the Thunderbird*", eds. M. Meixner, J.H. Kastner, B. Balick and N. Soker. ASP Conference Proceedings, Vol. 313, p.175

[113] Huber, K.P. & Herzberg, G. 1979, in "*Molecular spectra and molecular structure, IV. Constants of diatomic molecules*", Van Nostrand Reinhold Company, New-York

[114] Huggins, P.J. & Healy, A. 1989, ApJ, 346, 201

[115] Huggins, P.J., Bachiller, R., Cox, P. & Forveille, T. 1996, A&A, 315, 284

[116] Iben, I. Jr. 1991, IAU Symp. 145, "*Evolution of Stars: the Photospheric Abundance Connection*", eds. G. Michaud and A.V. Tutukov. Kluwer Academic Publishers, Dordrecht, 1991, p.257

[117] Jiménez-Esteban, F.M. 2004, Ph D. Thesis, Universidad Autónoma de Madrid

[118] Jiménez-Esteban, F.M., Agudo-Mérida, L., Engels, D. & García-Lario, P. 2005, A&A, 431, 779

[119] Jones, T.J., Bryja, C.O., Gehrz, R.D., Harrison, T.E., Jhonson, J.J., Klebe, D.I. & Lawrence, G.F. 1990, ApJS, 74, 785

[120] Jörgensen, U.G., Almlöf, J., Gustafsson, B., Larsson, M. & Siegbahn, P. 1985, J. Chem. Phys. 83, 3034

[121] Jura, M. 1988, ApJS, 66, 33

[122] Jura, M., Chen, C. & Plavchan, P. 2002, ApJ, 569, 964

[123] Justtanont, K., Barlow, M.J., Skinner, C.J., Roche, P.F., Aitken, D.K. & Smith, C.H. 1996, A&A, 309, 612

[124] Kastner, J.H., Forveille, T., Zuckerman, B. & Omont, A. 1993, A&A, 275, 163

[125] Kastner, J.H., Weintraub, D.A., Gatley, I., Merril, K.M. & Probst, R.G. 1996, ApJ, 462, 777

[126] Kelly, D.M., Hrivnak, B.J., Kwok, S. & Hinkle, K. 2004, in "*Asymmetrical Planetary Nebulae III: Winds, Structure and the Thunderbird*", eds.

M. Meixner, J.H. Kastner, B. Balick and N. Soker. ASP Conference Proceedings, Vol. 313, p.343

[127] Kholopov, P.N., Samus, N.N., Frolov, M.S. et al. 1998, GCVS, "*Combined General Catalogue of Variable Stars*"

[128] Klochkova, V.G., Szczerba, R., Panchuk, V.E. & Volk, K. 1999, A&A, 345, 905

[129] Koike, C., Hasegawa, H. & Manabe, A. 1980, Ap&SS, 67, 495

[130] Käufl, H.-U., Sterzik, M.F., Siebenmorgen, R., Weilenmann, U., Relke, H., Hron, J. & Sperl, M. 2003, SPIE 4841, 117

[131] Kupka, F., Piskunov, N.E., Ryabchikova, T.A., Stempels, H.C. & Weiss, W.W. 1999, A&ASS, 138, 119

[132] Kurucz, R.L. 1993, SAO, Cambridge, (CDROM 18)

[133] Kurucz, R.L. 1994, SAO, Cambridge, (CDROM 20-22)

[134] Kwok, S., Purton, C.R. & FitzGerald, M.P. 1978, ApJ, 219, L125

[135] Kwok, S. 1994, PASP 106, 344

[136] Kwok, S., Hrivnak, B.J. & Geballe, T.R. 1995, ApJ, 454, 394

[137] Kwok, S., Volk, K. & Bidelman, W.P. 1997, ApJS, 112, 557

[138] Kwok, S. 2001, in "*Post-AGB Objects as a Phase of Stellar Evolution*", eds. R.Szczerba and S.K. Gorny. Astrophysics and Space Science Library Vol. 265, ISBN 07923-71453. Kluwer Academic Publishers,Boston/Dordrecht/London, 2001.

[139] Kwok, S. 2003, IAU Symp. 209, "*Planetary Nebulae: Their Evolution and Role in the Universe*", eds. S. Kwok, M. Dopita and R. Sutherland. ASP, p. 3

[140] Lattanzio, J. C. 2003, IAU Symp. 209, "*Planetary Nebulae: Their Evolution and Role in the Universe*", eds. S. Kwok, M. Dopita and R. Sutherland. ASP, p. 73

[141] Latter, W.B., Kelly, D.M., Hora, J.L. & Deutsch, L. K. 1995, ApJS, 100, 159

[142] Le Bertre, T. 1993, A&AS, 97, 729

[143] Leuenhagen, U. & Hamann, W.-R. 1998, A&A, 330, 265L

[144] Lewis, B.M., Eder, J. & Terzian, Y. 1990, ApJ, 362, 634

[145] Lewis, B.M. 1994, ApJS, 93, 549

[146] Lewis, B.M., David, P. & Le Squeren, A.M. 1995, A&AS, 111, 237

[147] Likkel, L., Forveille, T., Omont, A. & Morris, M. 1991, A&A, 246, 153

[148] Lindqvist, M., Schöier, F.L., Lucas, R. & Olofsson, H. 2000, A&A, 361, 1036

[149] Lockwood, G.W. 1985, ApJS, 58, 167

[150] Loidl, R., Lancon, A. & Jörgensen, U.G. 2001, A&A, 37, 1065

[151] Loup, C., Forveille, T., Nyman, L.A. & Omont, A. 1990, A&A, 227, L29

[152] Loup, C., Forveille, T., Omont, A. & Paul, J.F. 1993, A&AS, 99, 291

[153] Luck, R.E., Bond, H.E. & Lambert, D.L. 1990, ApJ, 357, 188

[154] Lugaro, M., Herwig, F., Lattanzio, J.C., Gallino, R. & Straniero, O. 2003, ApJ, 586, 1305

[155] Mampaso, A. 2004, in "*Asymmetrical Planetary Nebulae III: Winds, Structure and the Thunderbird*", eds. M. Meixner, J.H. Kastner, B. Balick and N. Soker. ASP Conference Proceedings, Vol. 313, p. 265

[156] Manchado, A., Pottasch, S.R., García-Lario, P., Esteban, C. & Mampaso, A. 1989, A&A, 214, 139

[157] Manchado, A., Villaver, E., Stanghellini, L. & Guerrero, M. A., 2000, in "*Asymmetrical Planetary Nebulae II: From Origins to Microstructures*", eds. J.H. Kastner, N. Soker, and S. Rappaport. ASP Conference Series, Vol. 199, p. 17

[158] Manchado, S. 2003, IAU Symp. 209, "*Planetary Nebulae: Their Evolution and Role in the Universe*", eds. S. Kwok, M. Dopita and R. Sutherland. ASP, p. 431

[159] Manchado, A. 2004, in "*Asymmetrical Planetary Nebulae III: Winds, Structure and the Thunderbird*", eds. M. Meixner, J.H. Kastner, B. Balick and N. Soker. ASP Conference Proceedings, Vol. 313, p. 3

[160] Marigo, P., Girardi, L. & Bressan, A. 1999, A&A, 344, 123

[161] Matsuura, M., Zijlstra, A.A., Molster, F.J., Hony, S., Waters, L.B.F.M., Kemper, F., Bowey, J.E., Chihara, H., Koike, C. & Keller, L.P. 2004, ApJ, 604, 791

[162] Mazzitelli, I., D'Antona, F. & Ventura, P. 1999, A&A, 348, 846

[163] Meixner, M., Skinner, C.J., Graham, J.R., Keto, E., Jernigan, J.G. & Arens, J.F. 1997, ApJ, 482, 897

[164] Meixner, M., Ueta, T., Dayal, A., Hora, J.L., Fazio, G. Hrivnak, B.J., Skinner, C.J., Hoffmann, W.F. & Deutsch, L.K. 1999, ApJS, 122, 221

[165] Mellema, G. 1993, Ph D. Thesis, Sterrewacht Leiden

[166] Menzies, J.W. & Wolstencroft, R.D. 1990, MNRAS, 247, 177

[167] Molster, F.J., 2000, Ph.D. Thesis, University of Amsterdam

[168] Molster, F.J., Waters, L.B.F.M., Tielens, A.G.G.M. & Barlow, M.J. 2002a, A&A, 382, 184

[169] Molster, F.J., Waters, L.B.F.M., Tielens, A.G.G.M., Koike, C. & Chihara, H. 2002b, A&A, 382, 241

[170] Mooney, C.J., Rolleston, W.R.J., Keenan, F.P., Dufton, P.L., Pollacco, D.L. & Magee, H.R. 2001, MNRAS, 326, 1101

[171] Moore, C.E., Minnaert, M.G.J. & Hootgast, J. 1966, "*The solar spectrum, 2935 Å to 8770 Å*", NBS Monog. 61, Washington, DC:NBS

[172] Moorwood, A., Biereichel, P., Finger, G. et al. 1986, Msngr, 44, 19

[173] Morris, M. 1987, PASP 99, 115

[174] Mowlavi, N. 1999a, A&A, 344, 617

[175] Mowlavi, N. 1999b, A&A, 350, 73

[176] Mowlavi, N. Jorissen, A. & Arnould, M. 2000. IAU Symp. 177, "*The Carbon Star Phenomenon*", eds. R.F. Wing, Astronomy Department, The Ohio State University, Columbus, USA. Kluwer Academic Publishers, Vol. 177, p.459

[177] Mowlavi, N. & Meynet, G. 2000, A&A, 361, 959

[178] Mowlavi, N. 2002. IAU Symp. 187, "*Cosmic Chemical Evolution*", eds. K. Nomoto and J.W. Truran. Kluwer Academic Publishers, ISBN 1-4020-0448-6, 2002, p. 57

[179] Nakashima, J., Jiang, B.W., Deguchi, S., Sadakane, K. & Nakada, Y. 2000, PASJ, 52, 275

[180] Neckel, H. 1999, Solar Physics, 184, 421.

[181] Neri, R., Kahane, C., Lucas, R., Bujarrabal, V. & Loup, C. 1998, A&AS, 130, 1

[182] Nyman, L.-A., Booth, R.S., Carlstrom, U., Habing, H.J., Heske, A., Sahai, R., Stark, R., van der Veen, W.E.J.C. & Winnberg, A. 1992, A&AS, 93, 121

[183] Nyman, L.-A., Hall, P.J. & Olofsson, H. 1998, A&AS, 127, 185

[184] Olnon, F.M., Raimond, E., Neugebauer, G. et al. 1986, A&AS, 65, 607

[185] Oudmaijer, R.D., Waters, L.B.F.M., van der Veen, W.E.C.J. & Geballe, T.R. 1995, A&A, 299, 69

[186] Paczyński, B. 1971, Acta Astr., 21, 417

[187] Palla, F., Bachiller, R., Stanghellini, L., Tosi, M. & Galli, D. 2000, A&A, 355, 69

[188] Palla, F., Galli, D., Marconi, A., Stanghellini, L. & Tosi, M. 2002, ApJ, 568, 57

[189] Pascoli, G. 1992, PASP, 104, 350

[190] Pauzat, F., Talbit, D. & Ellinger, Y. 1997, A&A, 319, 318

[191] Pavlenko, Y. 1996, in "*Cool stars, stellar systems, and the sun*", eds. R. Pallavicini and A.K. Dupree, ASP Conference Series, Vol.109, p.569

[192] Peeters, E., Hony, S., Van Kerckhoven, C., Tielens, A.G.G.M., Allamandola, L.J., Hudgins, D.M. & Bauschlicher, C.W. 2002, A&A, 390, 1089

[193] Peimbert, M. 1978, in "*Planetary nebulae*", Dordrecht, D. Reidel. Publishing Co, p. 215.

[194] Plez, B. 1990, MmSAI, 61, 765

[195] Plez, B., Brett, J.M. & Nordlund, *Å*. 1992, A&A, 256, 551

[196] Plez, B., Smith, V.V. & Lambert, D.L. 1993, ApJ, 418, 812

[197] Pottasch, S.R. 1980, A&A, 89, 336

[198] Pottasch, S.R. 1990, in "*From Miras to planetary nebulae: Which path for stellar evolution?*", Gif-sur-Yvette, France, Editions Frontieres, p. 306

[199] Pottasch, S.R. 1992, A&AR, 4, 215

[200] Ramsay, S.K. 1993, Ph D. Thesis, University of Edinburgh

[201] Reddy, B.E., Bakker, E.J. & Hrivnak, B.J. 1999, ApJ, 524, 831

[202] Reimann, H.-G., Linz, H., Wagner, R., Relke, H., Käufl, H.-U., Dietzsch, E., Sperl, M. & Hron, J. 2000, SPIE 4008, 1132

[203] Riera, A., García-Lario, P., Manchado, A., Pottasch, S.R. & Raga A.C. 1995, A&A, 302, 137

[204] Riera, A., García-Lario, P., Manchado, A., Bobrowsky, M. & Estalella, R. 2003, A&A, 401, 1039

[205] Sackmann, I.J., Smith, R.L. & Despain, K.H. 1974, ApJ, 187, 555

[206] Sackmann, I.-J. & Boothroyd, A.I. 1992, ApJ, 392, L71

[207] Sahai, R., Hines, D., Kastner, J.H. et al. 1998, ApJ, 492, L163

[208] Sahai, R., Zijlstra, A.A., Bujarrabal, V. & te Lintel Hekkert, P. 1999a, AJ, 117, 1408

[209] Sahai, R., Bujarrabal, V. & Zijlstra, A.A. 1999b, ApJ, 518, L115

[210] Sahai, R., Su, K.Y.L., Kwok, S., Dayal, A. & Hrivnak, B.J. 2000, in "*Asymmetrical Planetary Nebulae II: From Origins to Microstructures*", eds. J.H. Kastner, N. Soker, and S. Rappaport. ASP Conference Series, Vol. 199, p. 167

[211] Schönberner, D. 1979, A&A, 79, 108

[212] Schönberner, D. 1981, A&A, 103, 119

[213] Schönberner, D. 1987, in "*Late stages of stellar evolution*", Dordrecht, D. Reidel. Publishing Co, p. 337

[214] Schwarzschild, M. & Härm, R. 1965, ApJ, 142, 855

[215] Scoville, N.Z. & Kwan, J. 1976, ApJ, 206, 718

[216] Sevenster, M.N., Chapman, J.M., Habing, H.J., Killeen, N.E.B. & Lindqvist, M. 1997, A&AS, 122, 79

[217] Sivagnanam, P., Le Squeren, A.M., Foy, F. & Tran Minh, F. 1989, A&A, 211, 341

[218] Slootmaker, A., Habing, H.J. & Herman, J. 1985, A&AS, 59, 465

[219] Smith, V.V. & Lambert, D.L. 1985, ApJ, 294, 326

[220] Smith, V.V. & Lambert, D.L. 1989, ApJ, 345, L75

[221] Smith, V.V. & Lambert, D.L. 1990a, ApJ, 361, L69

[222] Smith, V.V. & Lambert, D.L. 1990b, ApJS, 72, 387

[223] Smith, V.V., Plez, B., Lambert, D.L. & Lubowich, D.A. 1995, ApJ, 441, 735

[224] Sneden, C. 1973, Ph.D. thesis, Univ. of Texas at Austin

[225] Sneden, C., Johnson, H.R. & Krupp, B.M. 1976, ApJ, 204, 281

[226] Soker, N. & Harpar, A., 1992, PASP, 104, 923

[227] Speck, A.K. & Hofmeister, A.M. 2003, IAU Symp. 209, "*Planetary Nebulae: Their Evolution and Role in the Universe*", eds. S. Kwok, M. Dopita and R. Sutherland. ASP, p. 315

[228] Sterling, N.C. & Dinerstein H.L. 2004, to appear in "*Cosmic Abundances as Records of Stellar Evolution and Nucleosynthesis*", eds. T. Barnes and F. Bash, ASP Conf. Ser. (in press)

[229] Sternberg, A. & Dalgarno, A. 1989, ApJ, 338, 197

[230] Straniero, O., Gallino, R., Busso, M., Chieffi, A., Raiteri, C. M., Limongi, M. & Salaris, M. 1995, ApJ, 440, L85

[231] Straniero, O., Limongi, M., Chieffi, A., Dominguez, I., Busso, M., Gallino, R. 2000, MmSAI, 71, 719

[232] Suárez, O. 2004, Ph.D. thesis, Universidad de Vigo

[233] Su, K. Y. L., Kwok, S., Hrivnak, B.J., & Sahai, R. 2000, in "*Asymmetrical Planetary Nebulae II: From Origins to Microstructures*", eds. J.H. Kastner, N. Soker, and S. Rappaport. ASP Conference Series, Vol. 199, p. 163

[234] Su, K.Y.L., Hrivnak, B.J. & Kwok, S. 2001, AJ, 122, 1525

[235] Su, K.Y.L., Hrivnak, B.J., Kwok, S. & Sahai, R. 2003, AJ, 126, 848

[236] Surendiranath, R. 2002. A&A, 390, 667

[237] Sylvester, R.J., Kemper, F., Barlow, M.J., de Jong, T., Waters, L.B.F.M., Tielens, A.G.G.M. & Omont, A. 1999, A&A, 352, 587

[238] te Lintel Hekkert, P., Versteege-Hensel, H.A., Habing, H.J. & Wiertz, M. 1989, A&AS, 78, 399

[239] te Lintel Hekkert, P. 1991, A&A, 248, 209

[240] te Lintel Hekkert, P., Caswell, J.L., Habing, H.J., Haynes, R.F. & Norris, R.P. 1991, A&AS, 90, 327

[241] te Lintel Hekkert, P. & Chapman, J.M. 1996, A&A, 119, 459

[242] Trams, N.R., van Loon, J.Th., Waters, L.B.F.M., Zijlstra, A.A., Loup, C., Whitelock, P.A., Groenewegen, M.A.T., Blommaert, J.A.D.L., Siebenmorgen, R., Heske, A. & Feast, M.W. 1999, A&A, 346, 843

[243] Treffers, R.T., Fink, U.F., Larson, H.L. & Gautier, N.T. 1976, ApJ, 209, 793

[244] Tsuji, T. 1973, A&A, 23, 411

[245] Ueta, T., Meixner, M. & Bobrowsky, M. 2000. ApJ, 528, 861

[246] Ueta, T., Meixner, M., Hinz, P.M., Hoffmann, W.F., Brandner, W., Dayal, A., Deutsch, L.K., Fazio, G.G. & Hora, J.L. 2001, ApJ, 557, 831

[247] van Belle, G.T., Lane, B.F., Thompson, R.R., Boden, A.F., Colavita, M.M., Dumont, P.J., Mobley, D.W., Palmer, D., Shao, M., Vasisht, G.X., Wallace, J.K., Creech-Eakman, M.J., Koresko, C.D., Kulkarni, S.R., Pan, X.P. & Gubler, J. 1999, AJ, 117, 521

[248] van Belle, G.T., Thompson, R.R. & Creech-Eakman, M.J. 2002, AJ, 124, 1706

[249] van de Steene, G.C. & Pottasch, S.R. 1993, A&A, 274, 895

[250] van de Steene, G.C., van Hoof, P.A.M. & Wood, P.R. 2000a, A&A, 362, 984

[251] van de Steene, G.C., Wood, P.R. & van Hoof, P.A.M. 2000b, in "*Asymmetrical Planetary Nebulae II: From Origins to Microstructures*", eds. J.H. Kastner, N. Soker, and S. Rappaport. ASP Conference Series, Vol. 199, p. 191

[252] van de Steene, G.C. & van Hoof, P.A.M. 2003, A&A, 406, 773

[253] van der Veen, W.E.C.J., Habing, H.J. & Geballe, T.R. 1989, A&A, 226, 108

[254] Van Eck, S. & Jorissen, A. 2000, A&A, 360, 196

[255] van Loon, J. Th. 2000, A&A, 354, 125

[256] van Winckel, H. 1997, A&A, 319, 561

[257] van Winckel, H. & Reyniers, M. 2000, A&A, 354, 135

[258] van Winckel, H. 2003, ARA&A, 41, 391

[259] Vanture, A.D. & Wallerstein, G. 2002, ApJ, 564, 395

[260] Vassiliadis, E. & Wood, P.R. 1994, ApJS, 92, 125

[261] Ventura, P., D'Antona, F. & Mazzitelli, I. 2000, A&A, 363, 605

[262] Volk, K.M. & Kwok, S. 1989, ApJ, 342, 345

[263] Wallace, L., Hinkle, K. & Livingston, W. 1993, "*An atlas of the photospheric spectrum from 8900 to 13600 cm*$^{-1}$ *(7350 to 11230 Å)*", NSO Technical Report 93-001, Tucson: National Solar Observatory

[264] Wallace, L., Hinkle, K. & Livingston, W. 1998, "*An atlas of the spectrum of the solar photosphere from 13500 to 28000 cm*$^{-1}$ *(3570 to 7405 Å)*", Tucson, AZ: National Optical Astronomy Observatories

[265] Wallerstein, G. & Knapp, G.R. 1998, ARA&A, 36, 369

[266] Wasserburg, G.J., Boothroyd, A.I. & Sackmann, I.J. 1995, ApJ, 447, L37

[267] Waters, L.B.F.M., Cami, J., de Jong, T., Molster, F.J., van Loon, J.Th., Bouwman, J., de Koter, A., Waelkens, C., Van Winckel, H. & Morris, P.W. 1998, Nature, 391, 868

[268] Waters, L.B.F.M., Beintema, D.A., Cami, J. et al. 1999, in "*The Universe as seen by ISO*", eds. P. Cox and M.F. Kessler. ESA SP-427, p. 219

[269] Webster, B.L., Payne, P.W., Storey, J.W.V. & Dopita M.A. 1988, MNRAS, 235, 533

[270] Weintraub, D.A., Huard, T., Kastner, J. & Gatley, I. 1998, ApJ, 509, 728

[271] Whitelock, P.A., Menzies, J., Feast, M., Marang, F., Carter, B., Roberts, G., Catchpole, R. & Chapman, J. 1994, MNRAS, 267, 711

[272] Whitelock, P.A., Feast, M.W., van Loon, J.Th. & Zijlstra, A.A. 2003, MNRAS, 342, 86

[273] Willson, L.A. 2000, ARA&A, 38, 573

[274] Winters, J.M., Le Bertre, T., Jeong, K.S., Helling, Ch. & Sedlmayr, E. 2000, A&A, 361, 641

[275] Wood, P.R., Bessell, M.S. & Fox, M.W. 1983, ApJ, 272, 99

[276] Wood, P.R., Habing, H.J. & McGregor, P.J. 1998, A&A, 336, 925

[277] Yamamura, I., Dominik, C., de Jong, T., Waters, L.B.F.M. & Molster, F.J.. 2000, A&A, 363, 629

[278] Zijlstra, A.A., te Lintel Hekkert, P., Pottasch, S.R., Caswell, J.L., Ratag, M. & Habing, H.J. 1989, A&A, 217, 157

[279] Zijlstra, A.A., Gaylard, M.J., te Lintel Hekkert, P., Menzies, J., Nyman, L.-A. & Schwarz, H.E. 1991, A&A, 243, L9

[280] Zijlstra, A.A. 2001, Ap&SS, 275, 79

[281] Zuckerman, B. & Gatley I. 1988, ApJ, 324, 501

A

Li detected sources

We present here the best fit model and the observed spectrum in the region 6670−6730 Å of the 21 O-rich AGB stars in our sample with Li detections for which a fitting could be done. The best fit shown corresponds to the Li abundance quoted in Table 5.1. The synthetic spectra corresponding to Li abundances shifted by +0.2 dex and −0.2 dex from the adopted value are also shown. The parameters of the best fit model atmosphere are indicated at the top of each Figure. The flux units are arbitrary. The plots are displayed in increasing R.A. order and each page corresponds to one object.

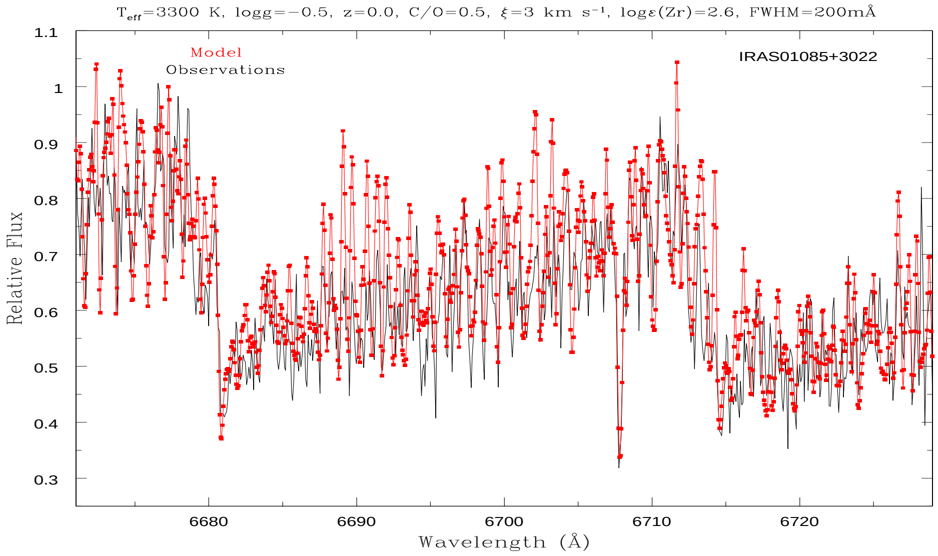

FIGURE A.1—

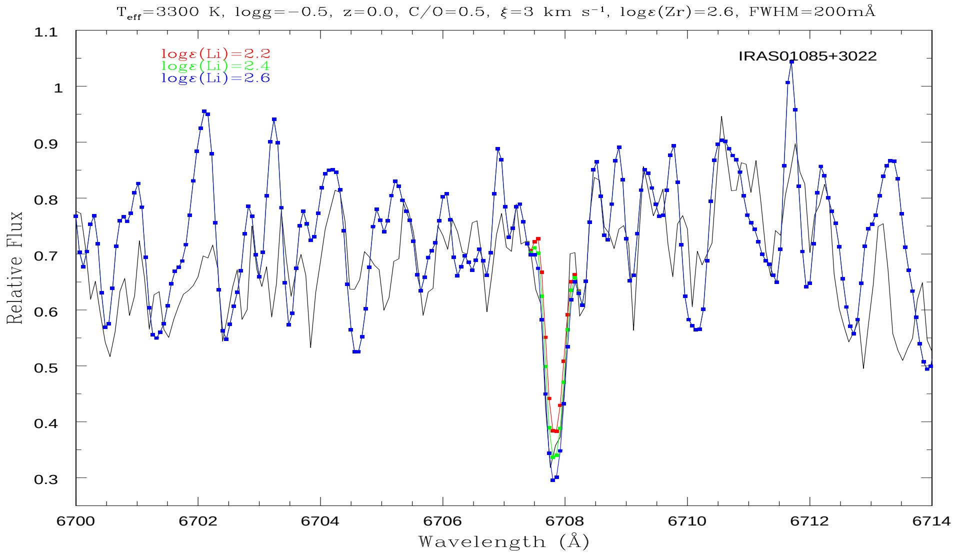

FIGURE A.2—

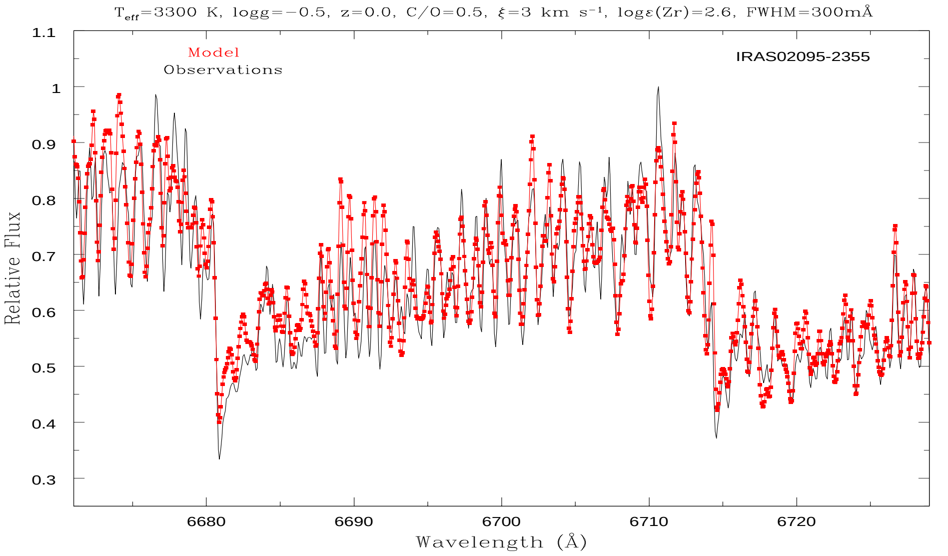

Figure A.3—

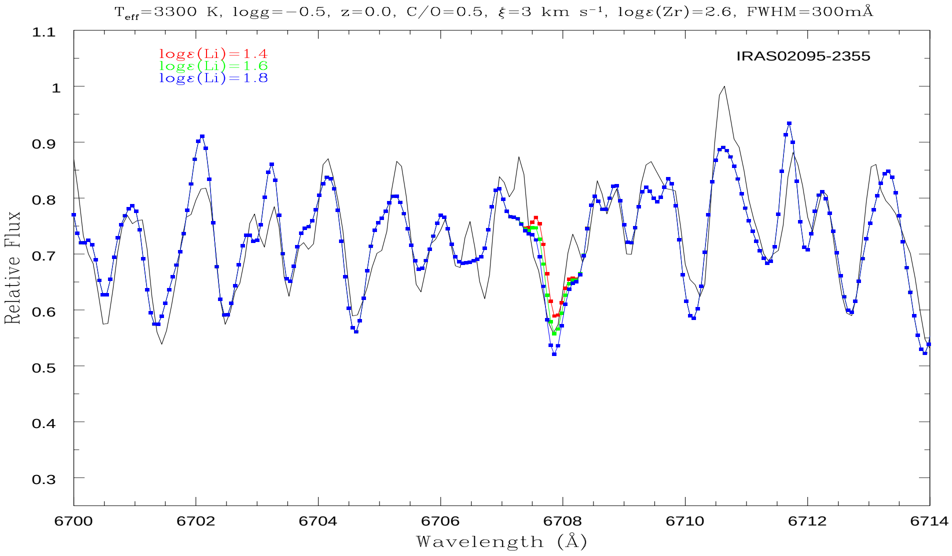

Figure A.4—

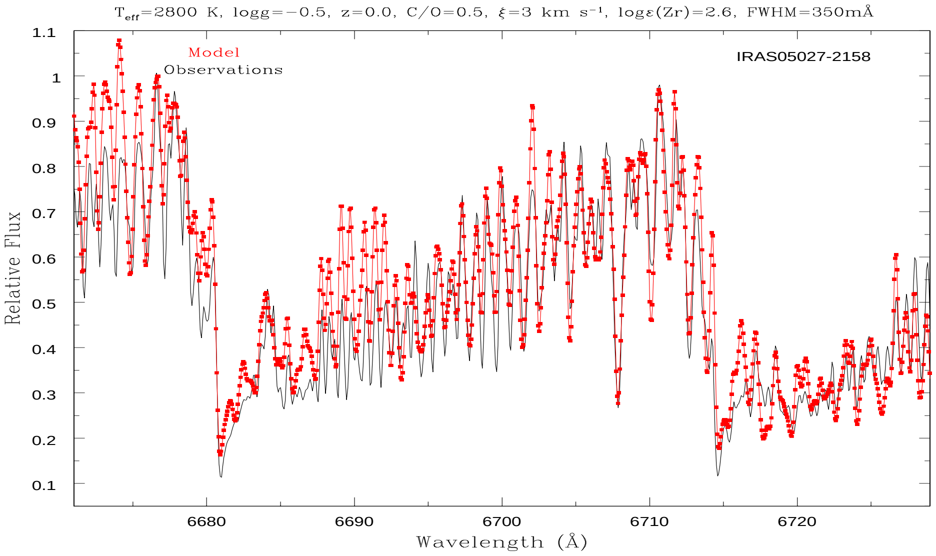

FIGURE A.5—

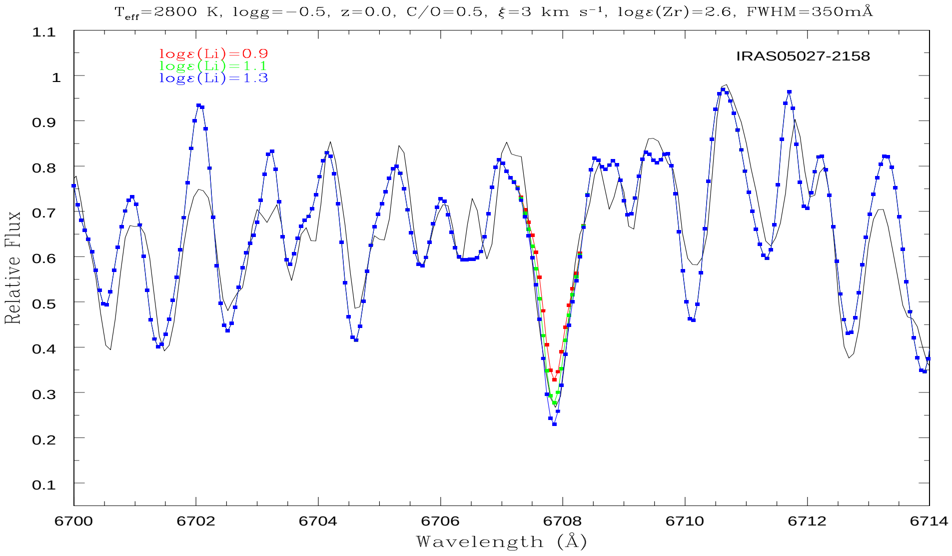

FIGURE A.6—

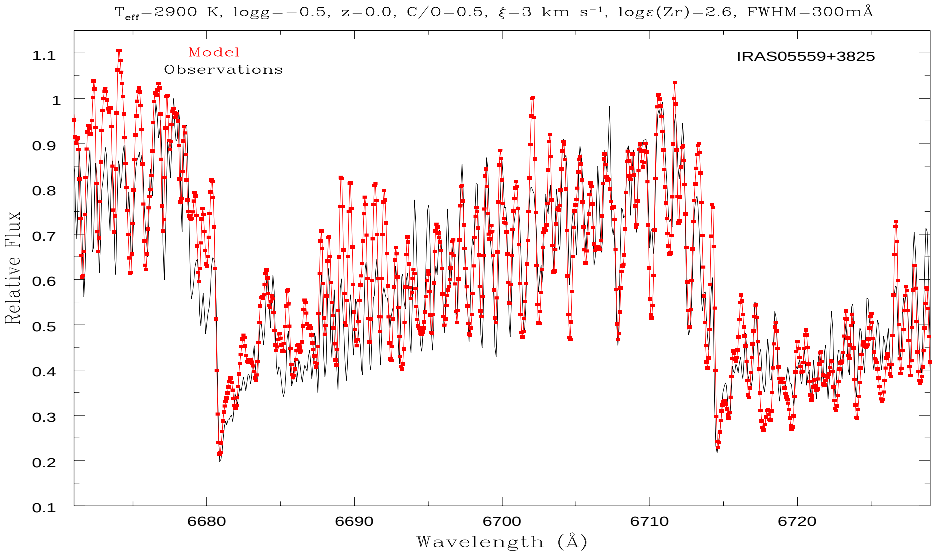

Figure A.7—

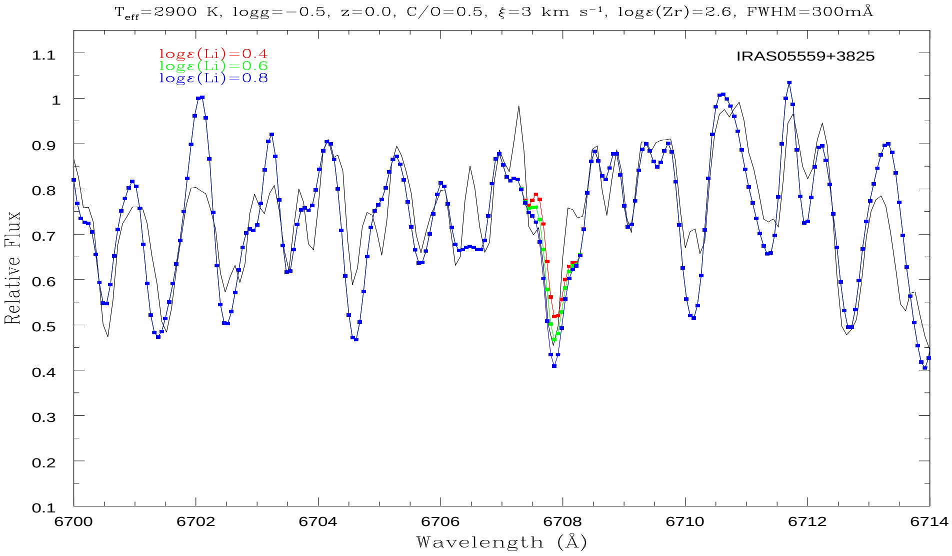

Figure A.8—

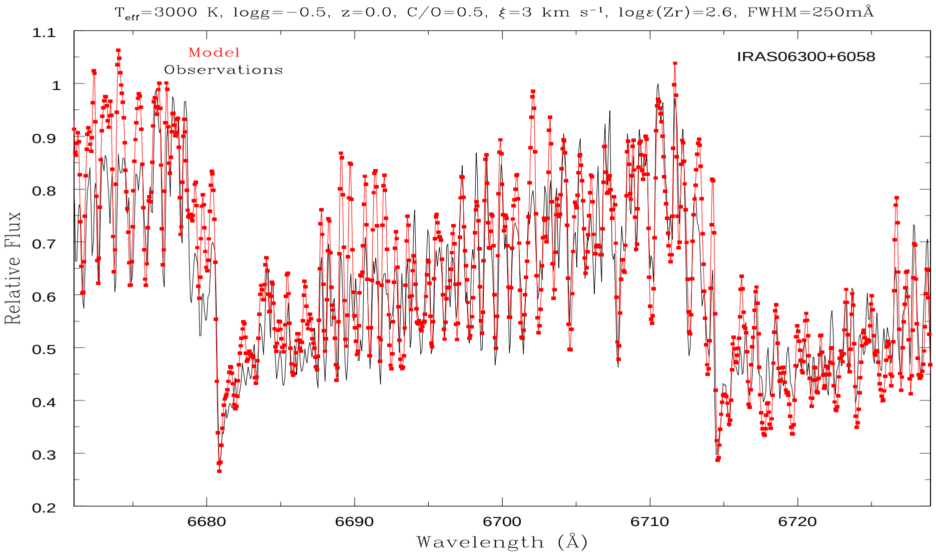

FIGURE A.9—

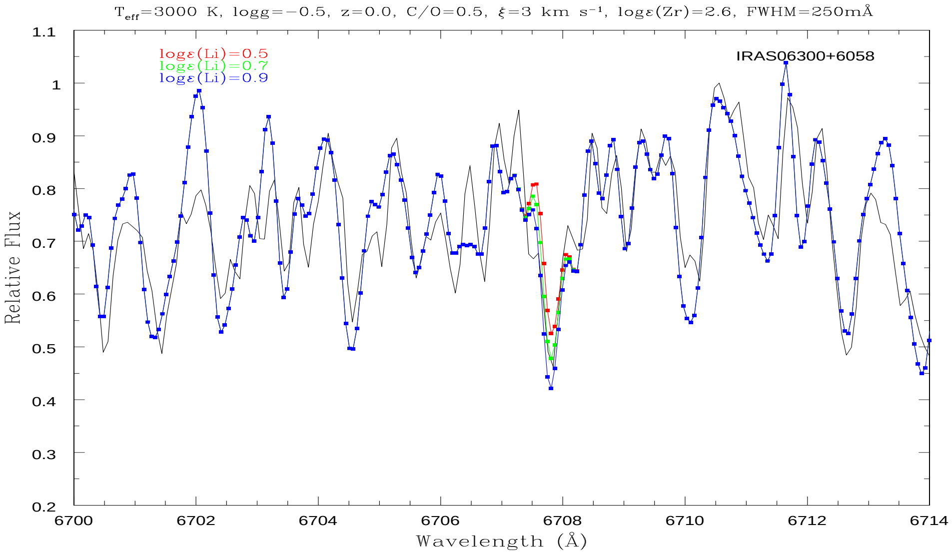

FIGURE A.10—

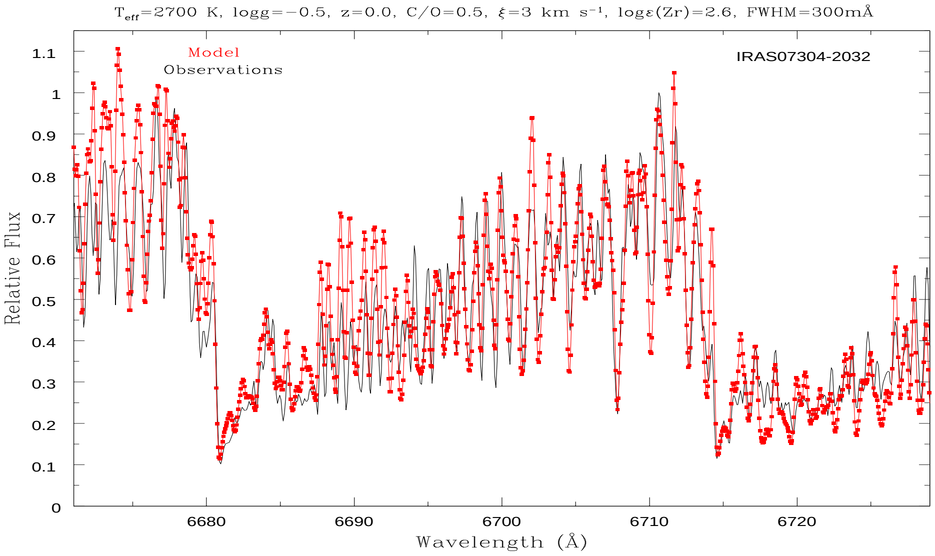

FIGURE A.11—

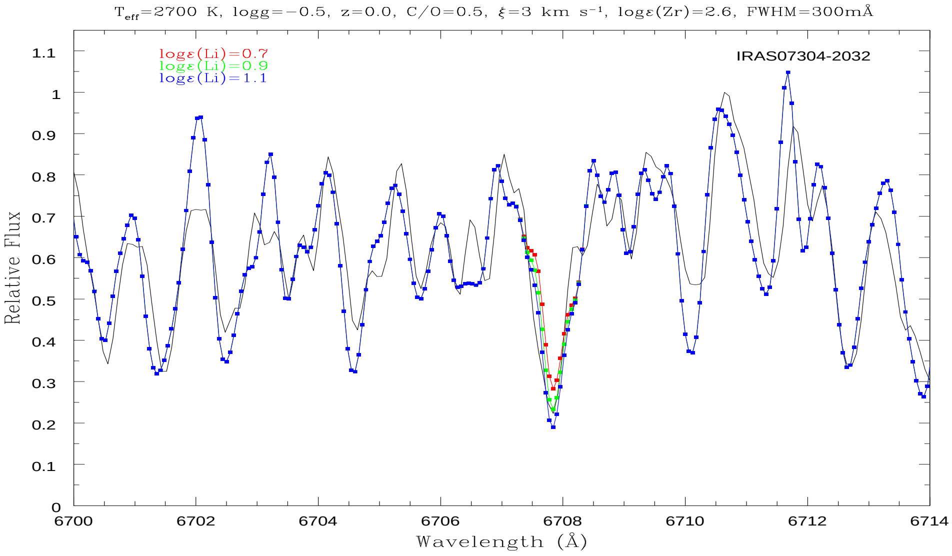

FIGURE A.12—

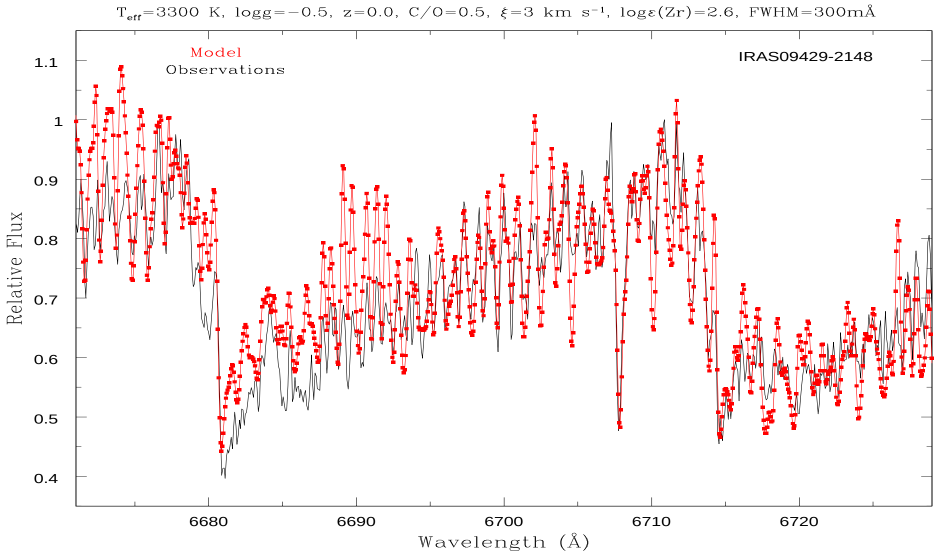

FIGURE A.13—

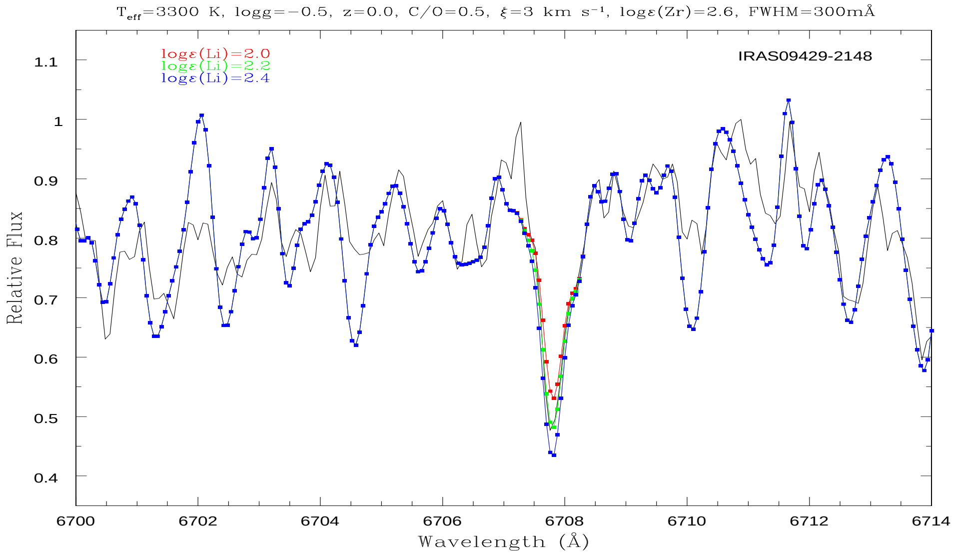

FIGURE A.14—

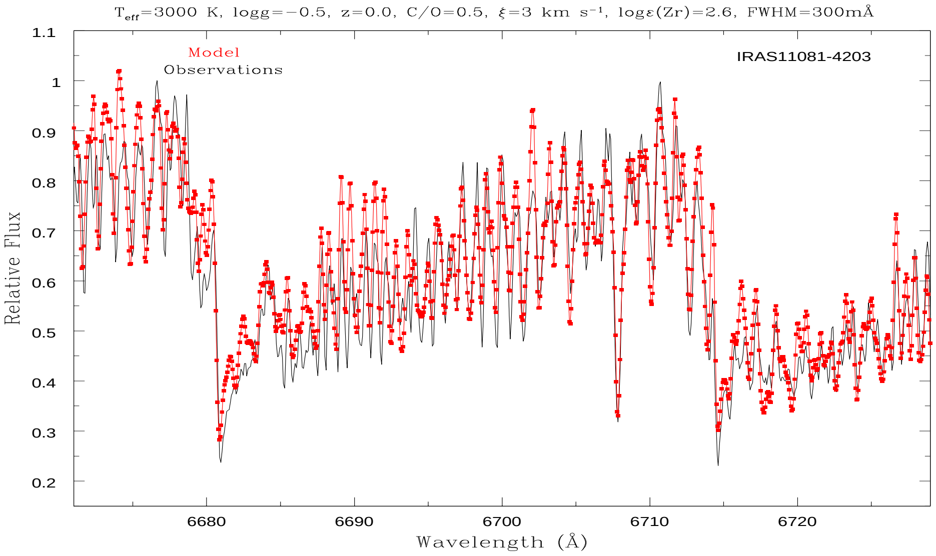

FIGURE A.15—

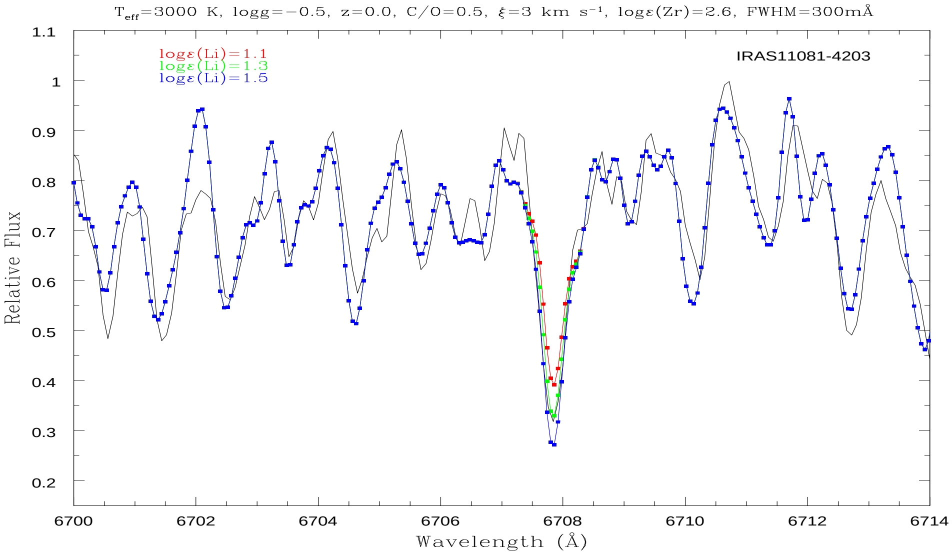

FIGURE A.16—

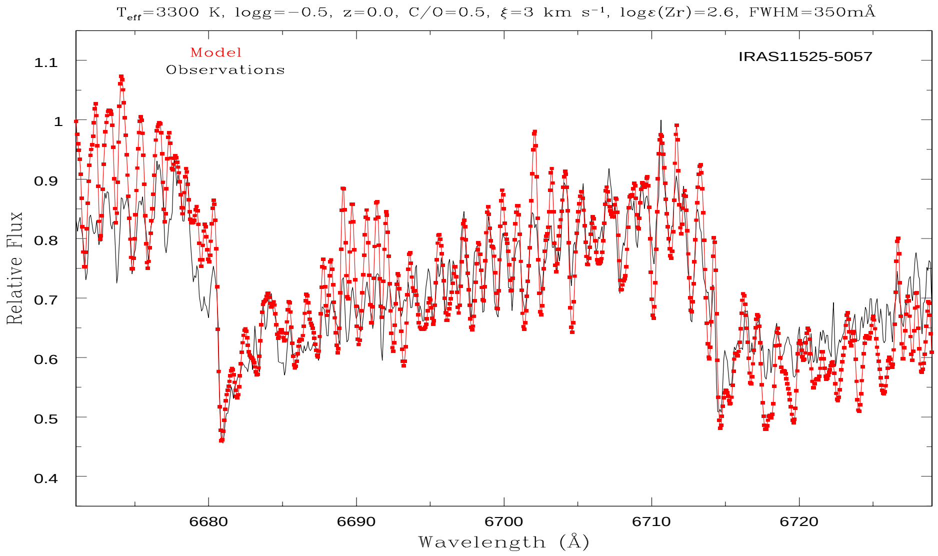

FIGURE A.17—

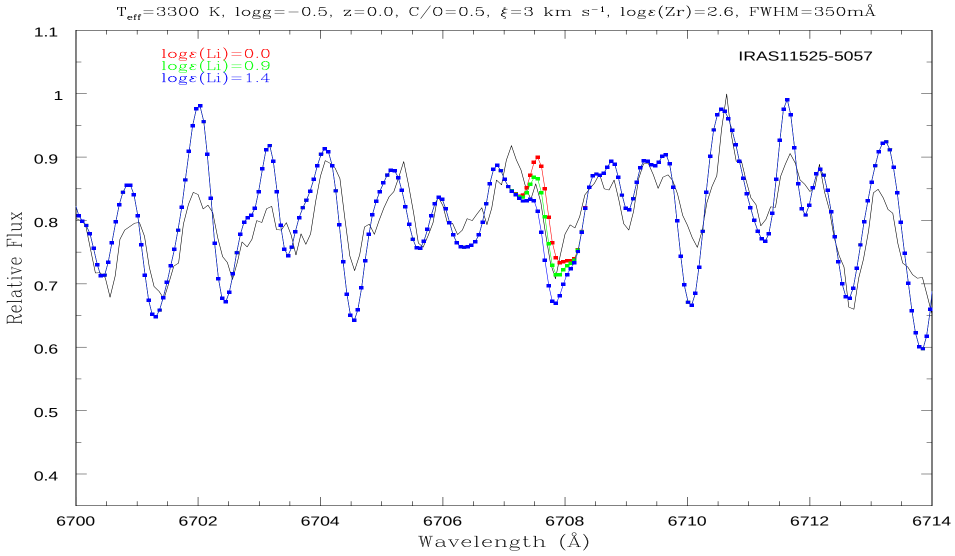

FIGURE A.18—

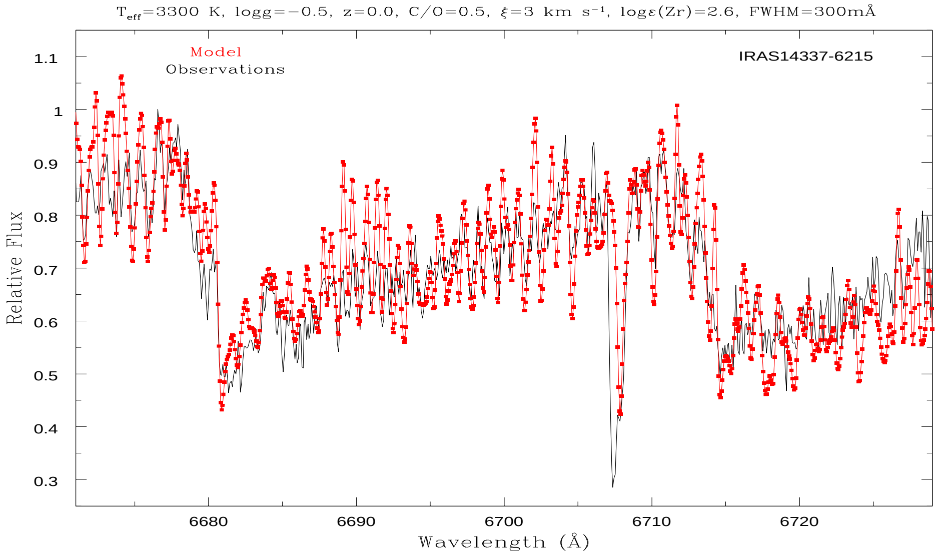

FIGURE A.19—

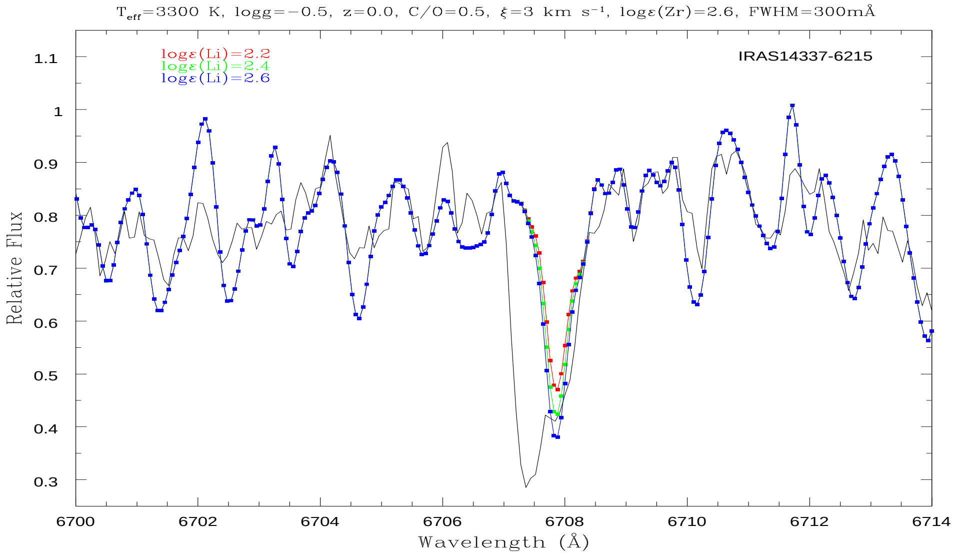

FIGURE A.20—

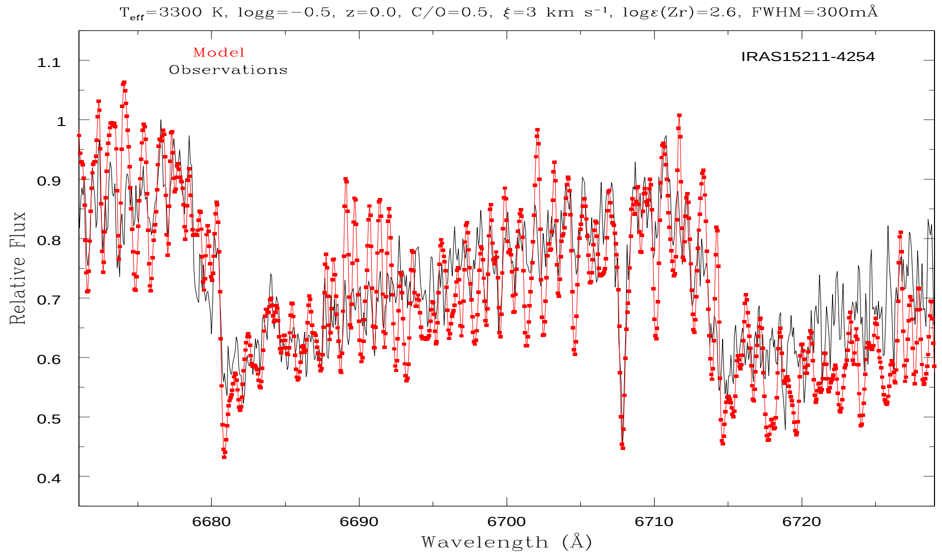

FIGURE A.21—

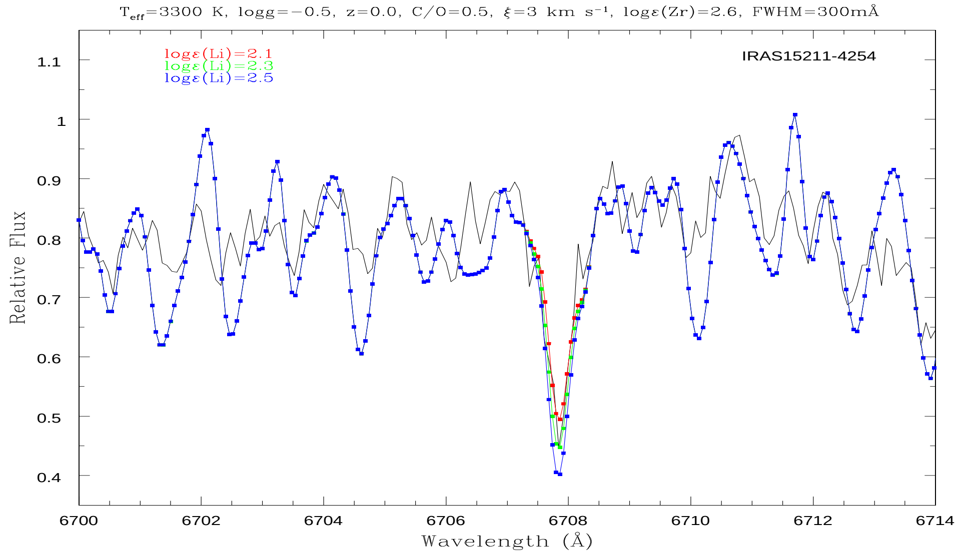

FIGURE A.22—

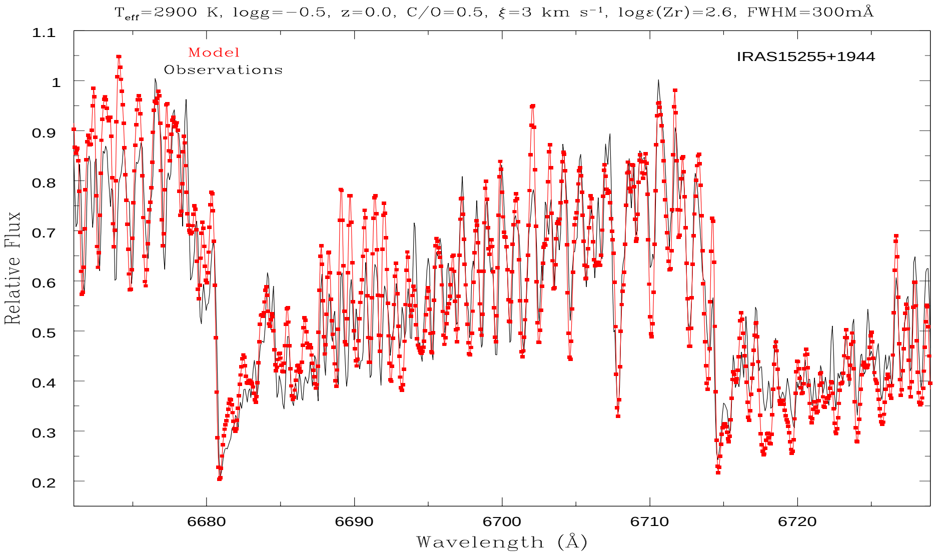

FIGURE A.23—

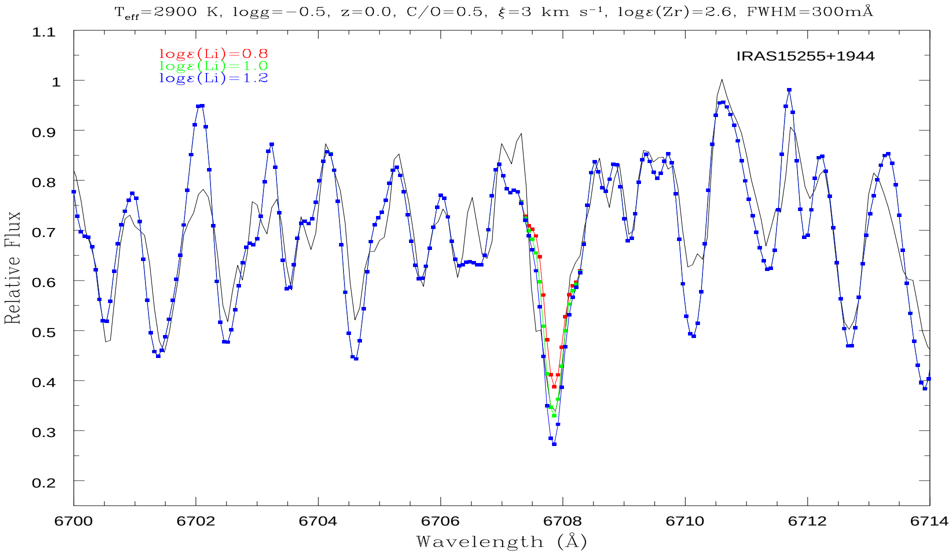

FIGURE A.24—

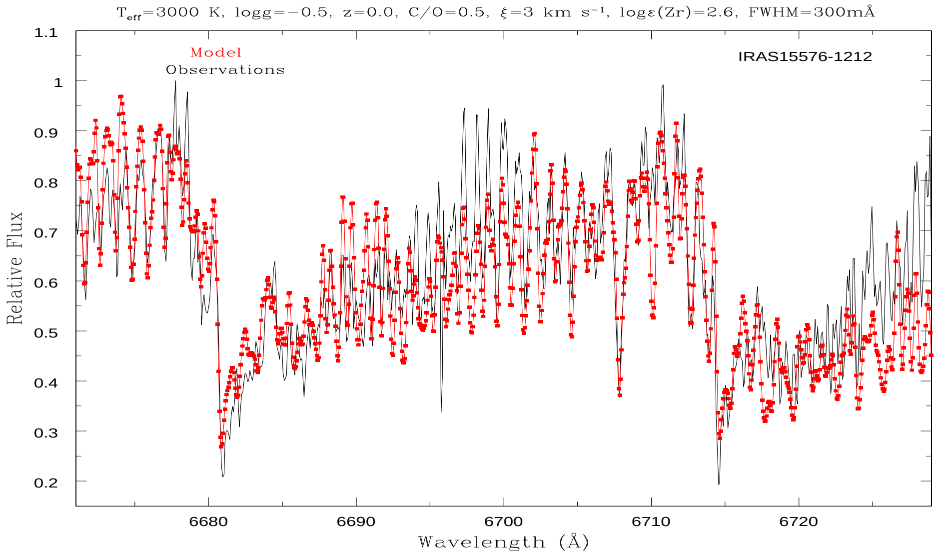

FIGURE A.25—

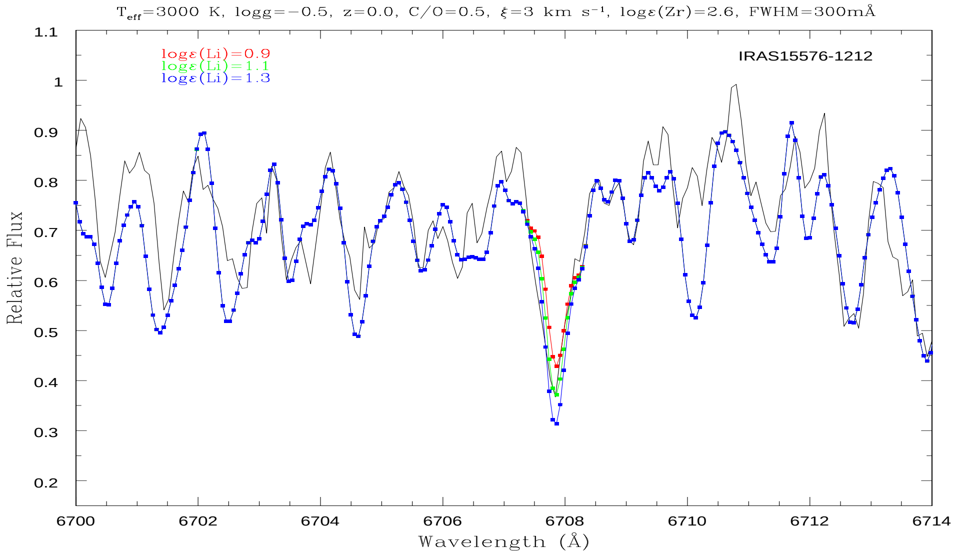

FIGURE A.26—

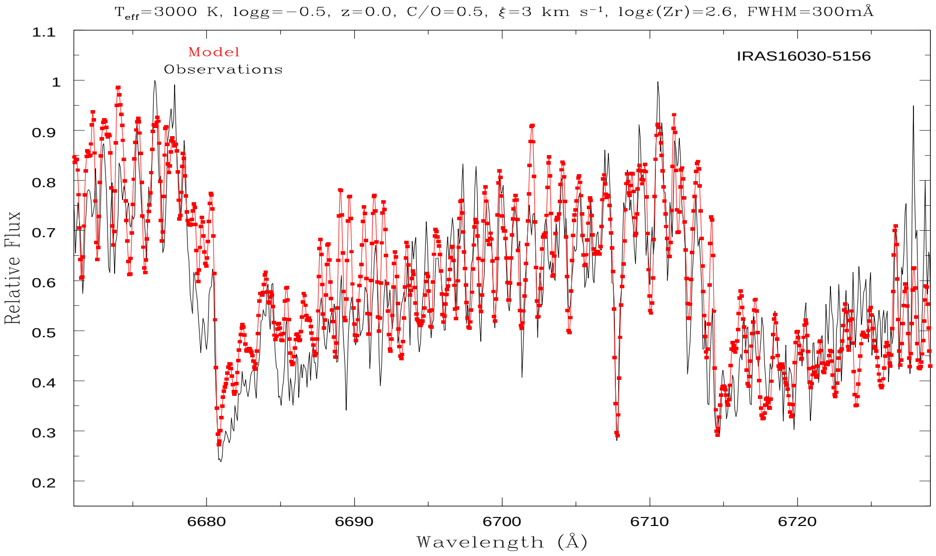

Figure A.27—

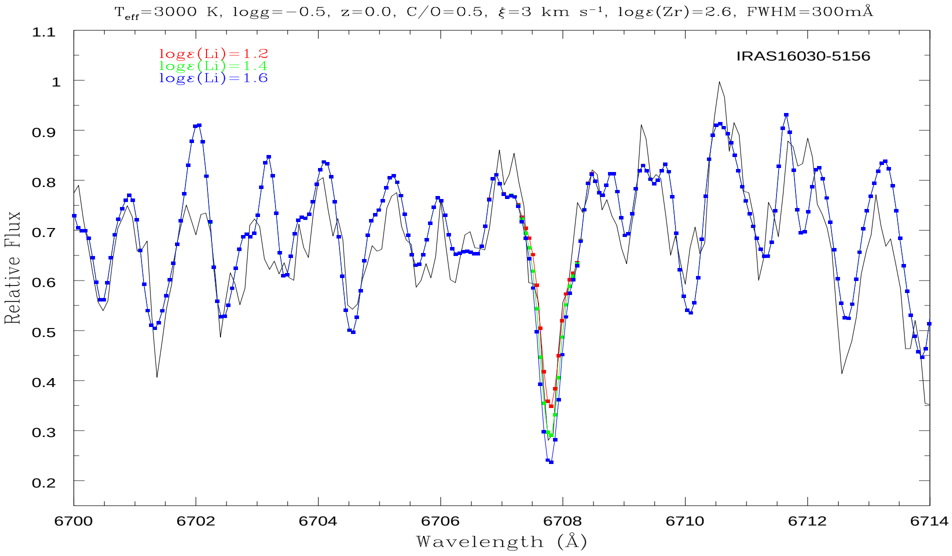

Figure A.28—

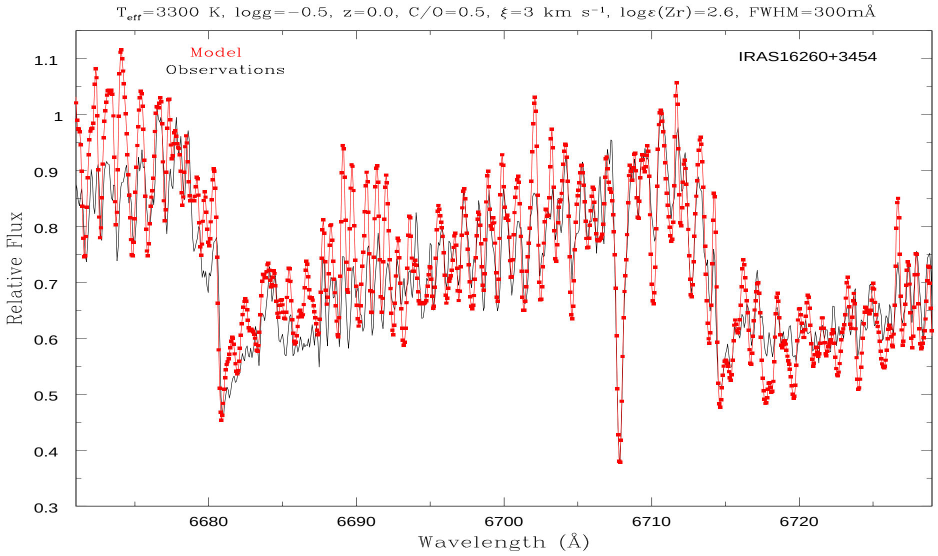

FIGURE A.29—

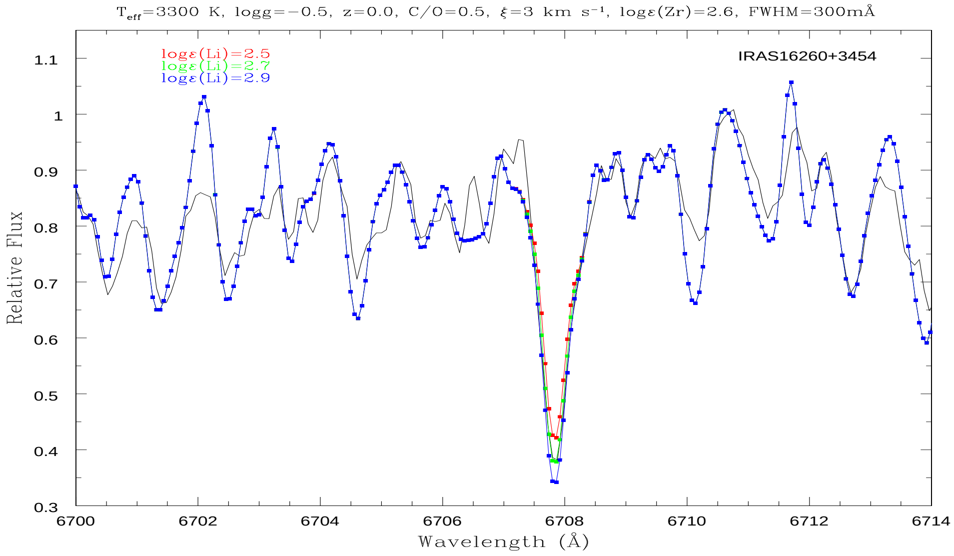

FIGURE A.30—

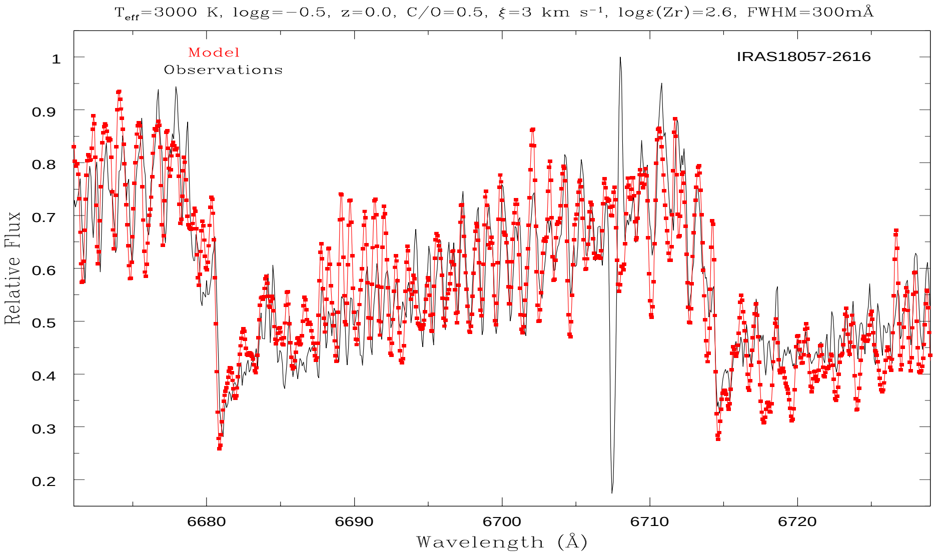

FIGURE A.31—

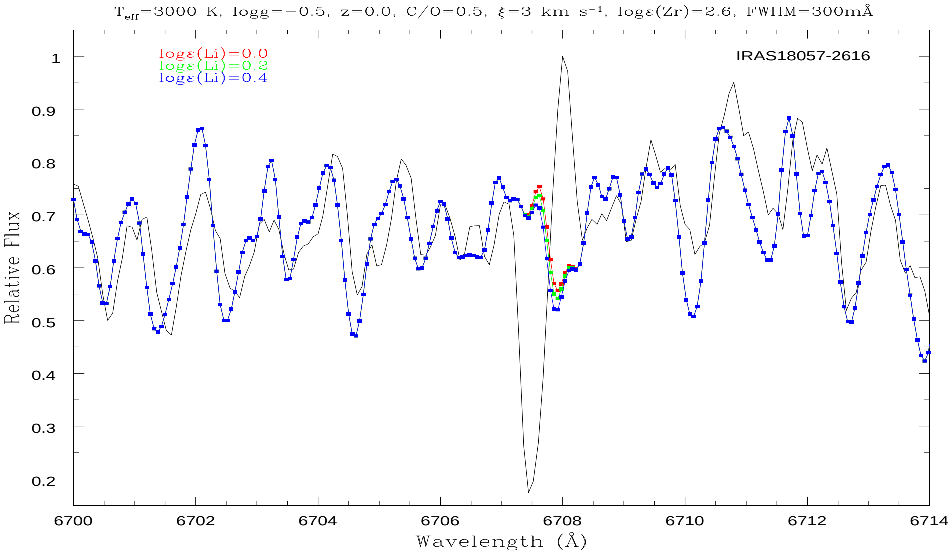

FIGURE A.32—

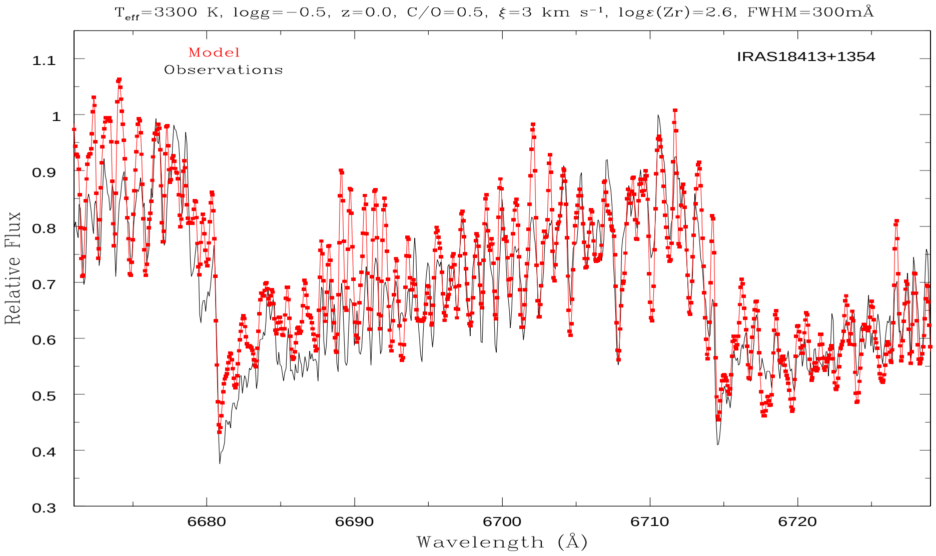

FIGURE A.33—

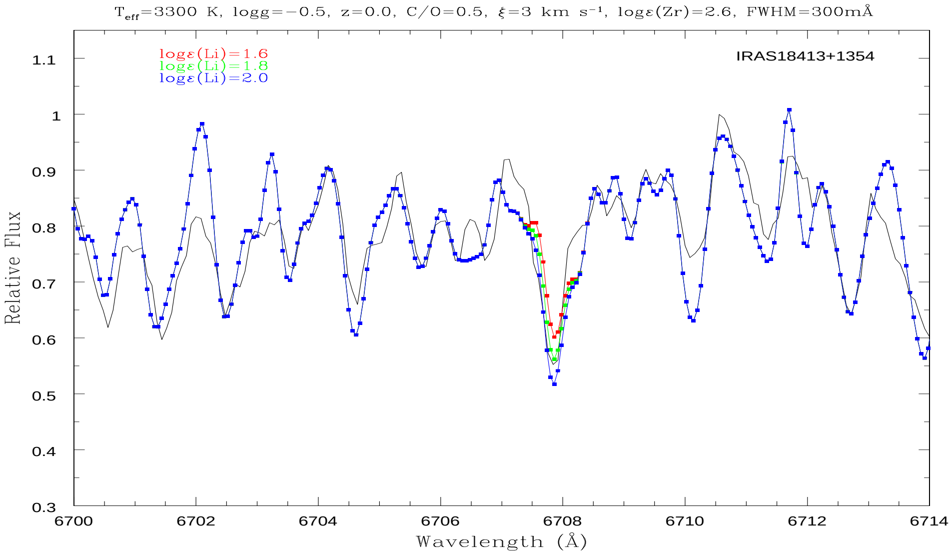

FIGURE A.34—

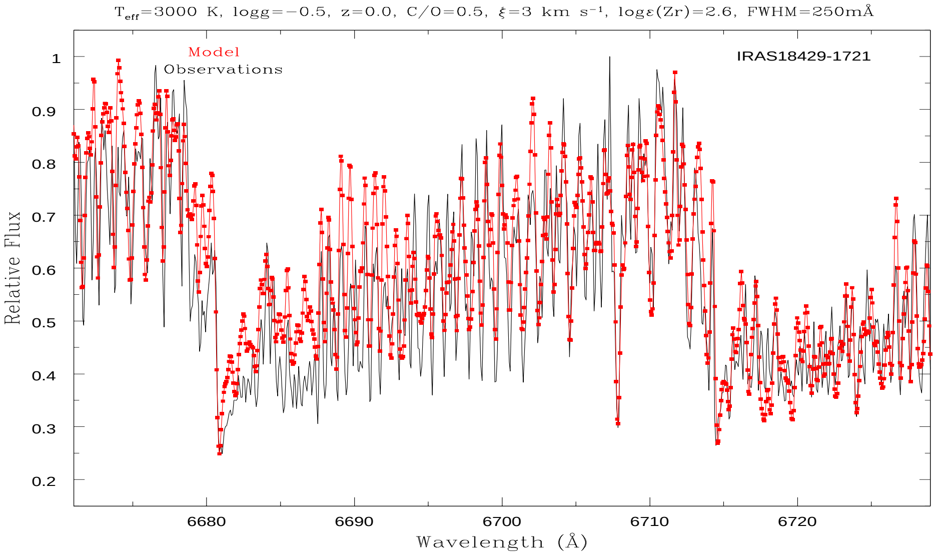

FIGURE A.35—

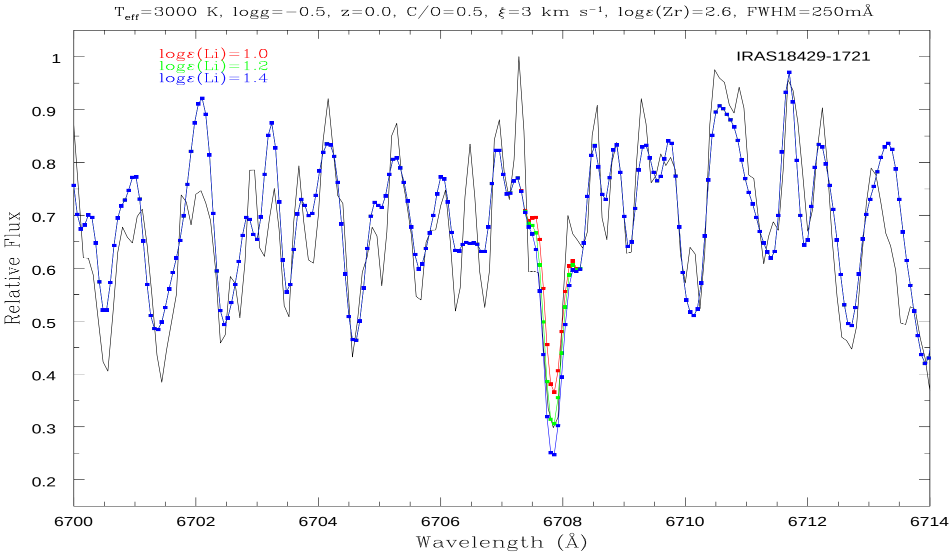

FIGURE A.36—

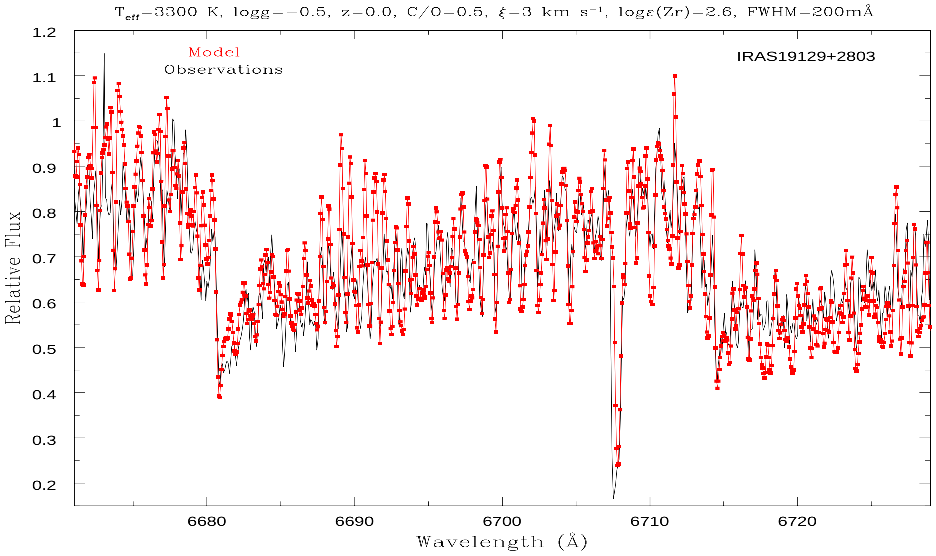

FIGURE A.37—

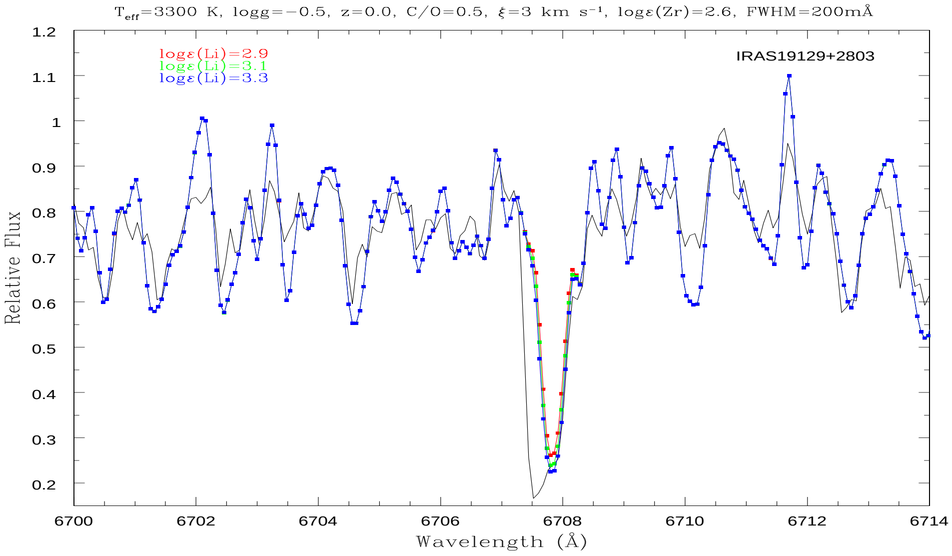

FIGURE A.38—

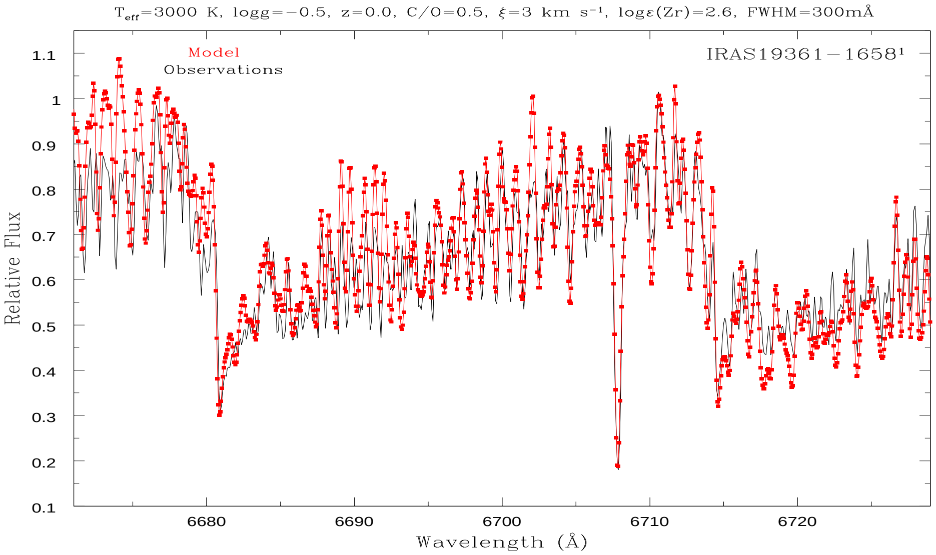

FIGURE A.39—

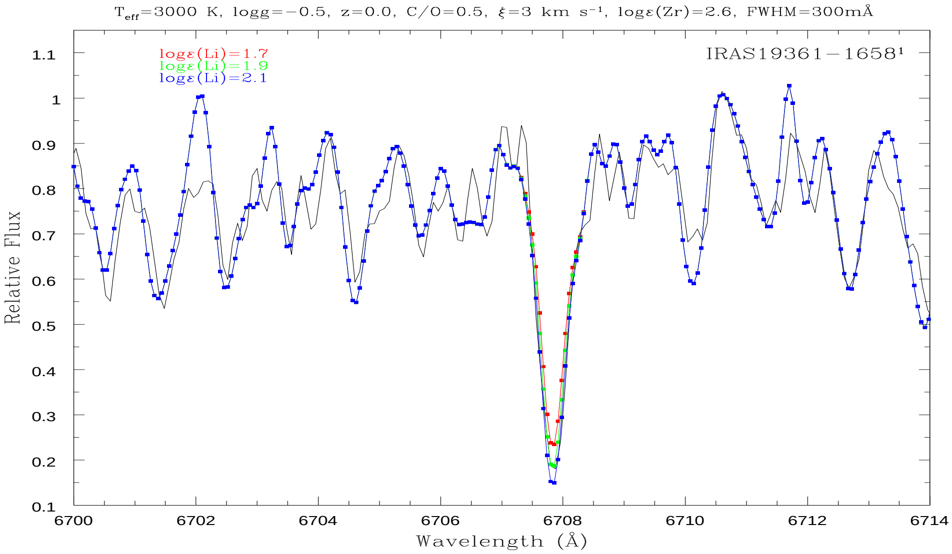

FIGURE A.40—

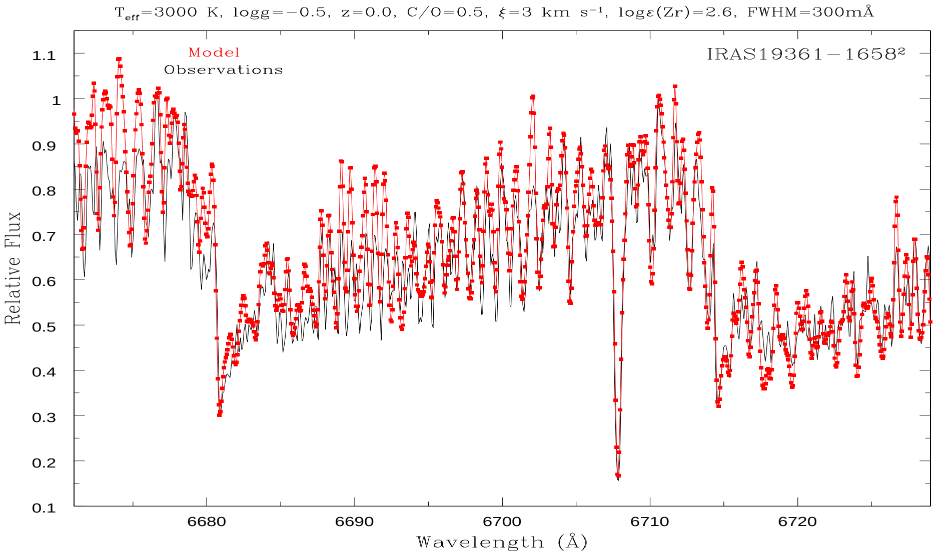

FIGURE A.41—

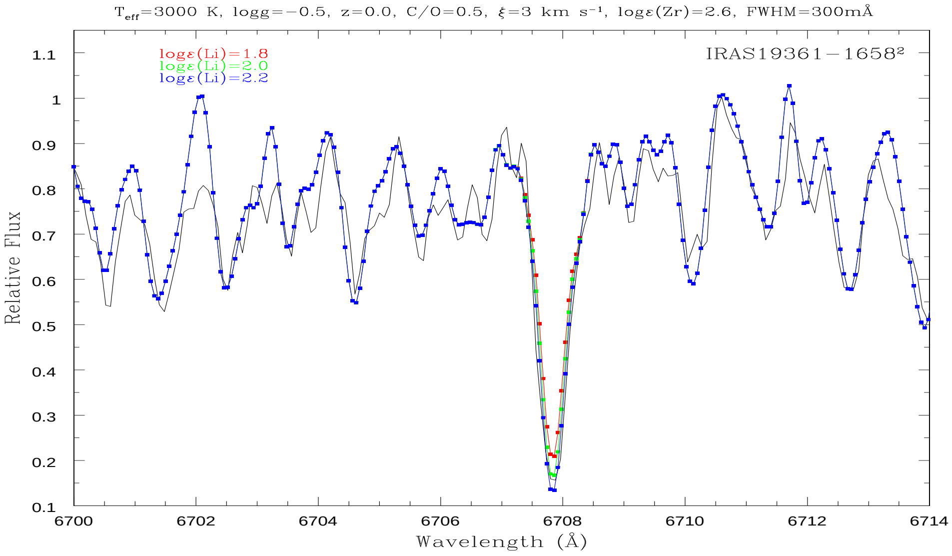

FIGURE A.42—

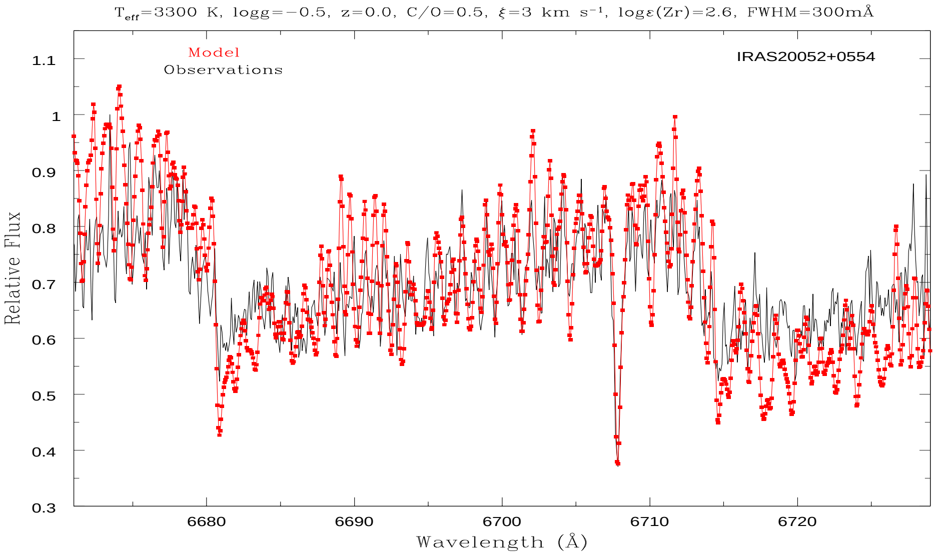

Figure A.43—

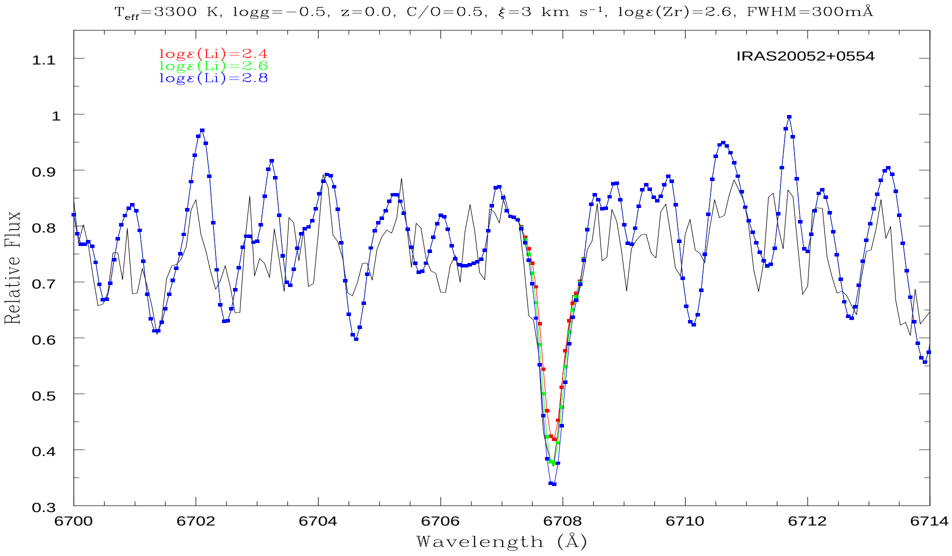

Figure A.44—

B

Li non-detected sources

We present here the best fit model and the observed spectrum in the region 6670−6730 Å of the 27 O-rich AGB stars in our sample with Li non-detections for which a fitting could be done. The best fit shown corresponds to the upper limit of the Li abundance quoted in Table 5.1. The synthetic spectra corresponding to Li abundances shifted by ±0.5−2 dex (depending on the star considered) from this value are also shown. The parameters of the best fit model atmosphere are indicated at the top of each Figure. The flux units are arbitrary. The plots are displayed in increasing R.A. order and each page corresponds to one object.

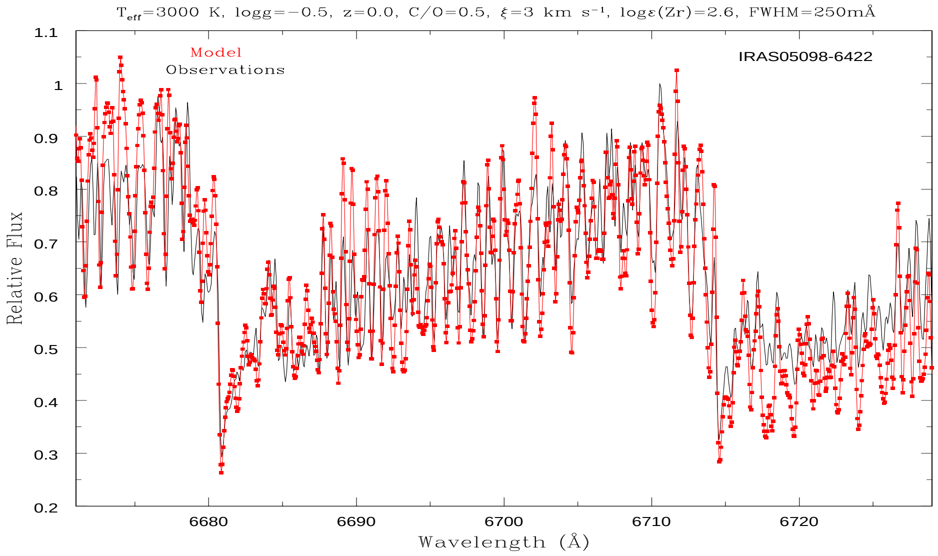

FIGURE B.1—

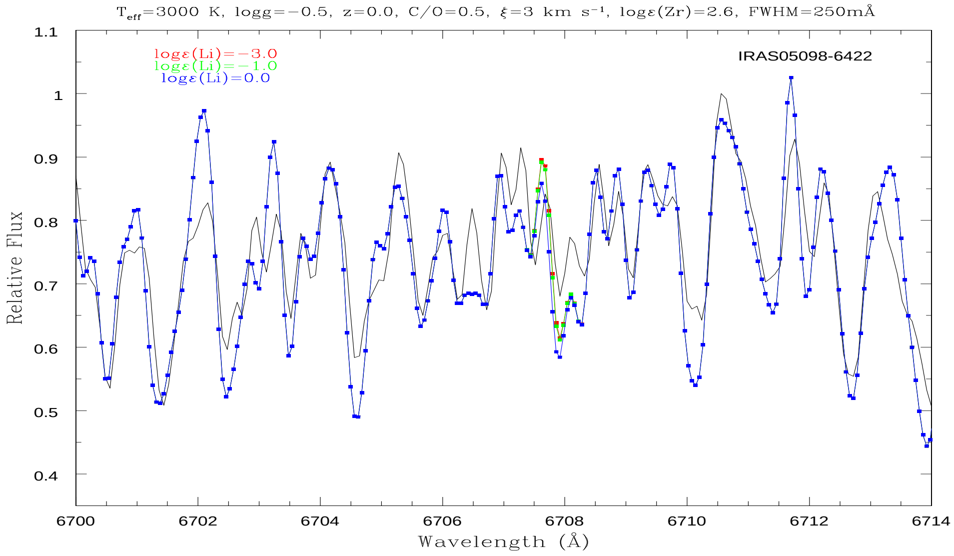

FIGURE B.2—

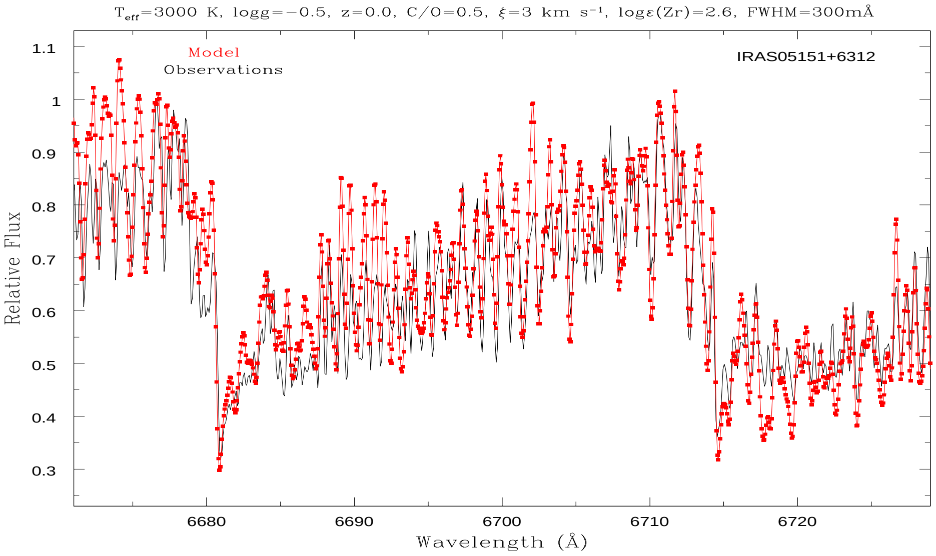

FIGURE B.3—

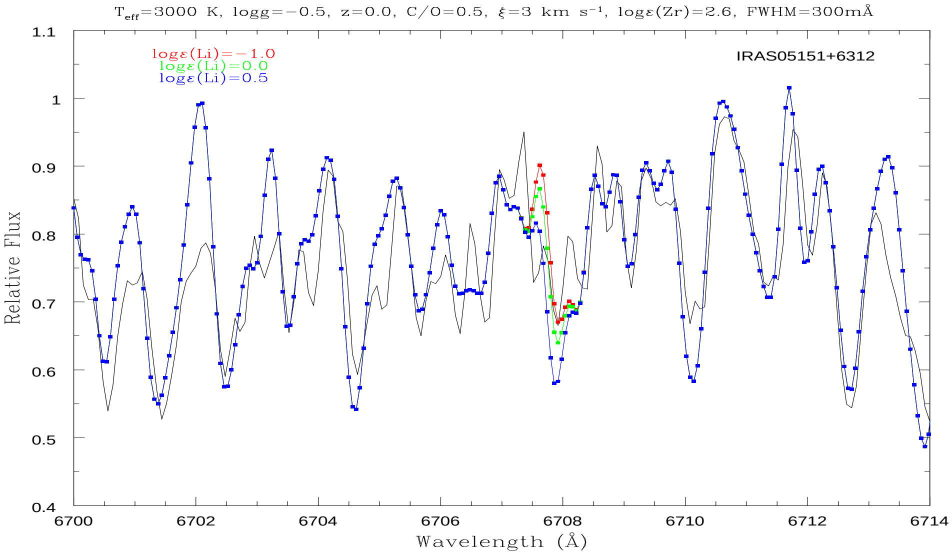

FIGURE B.4—

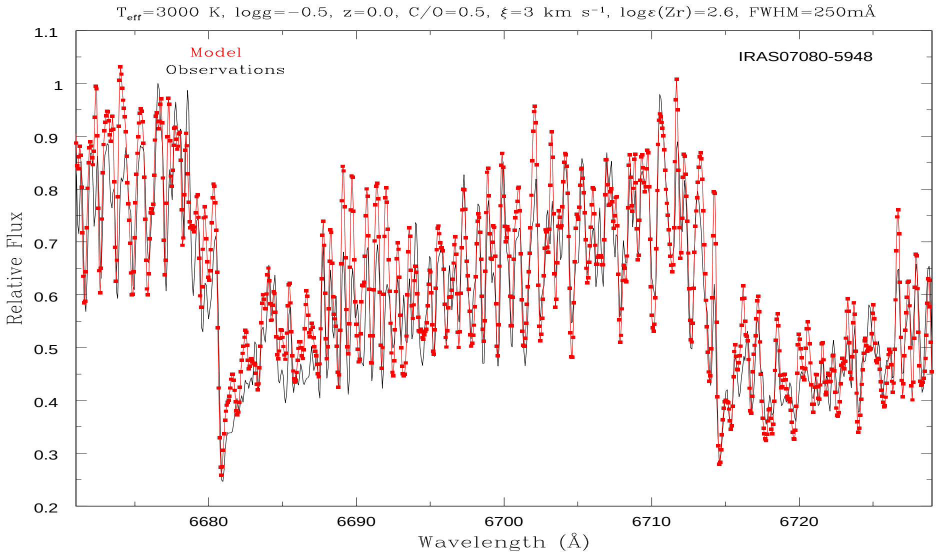

FIGURE B.5—

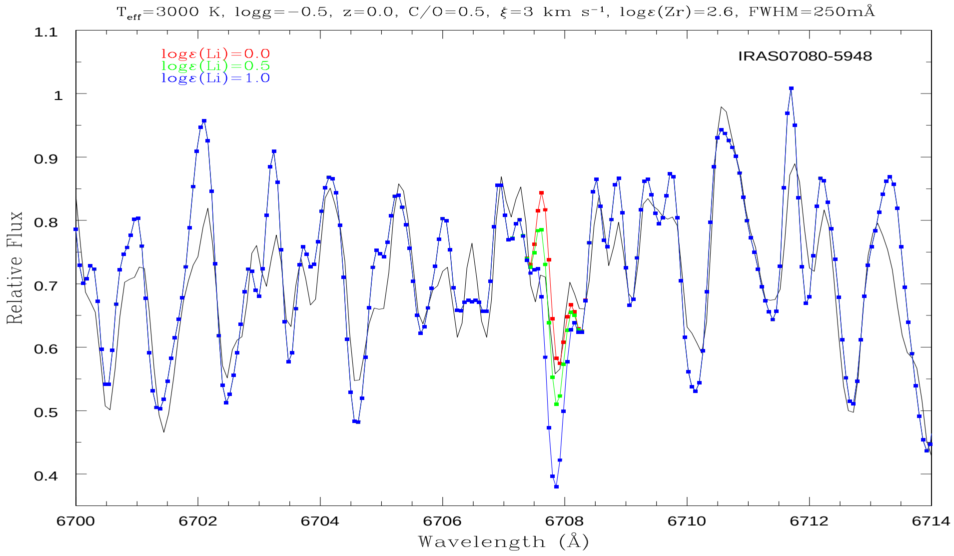

FIGURE B.6—

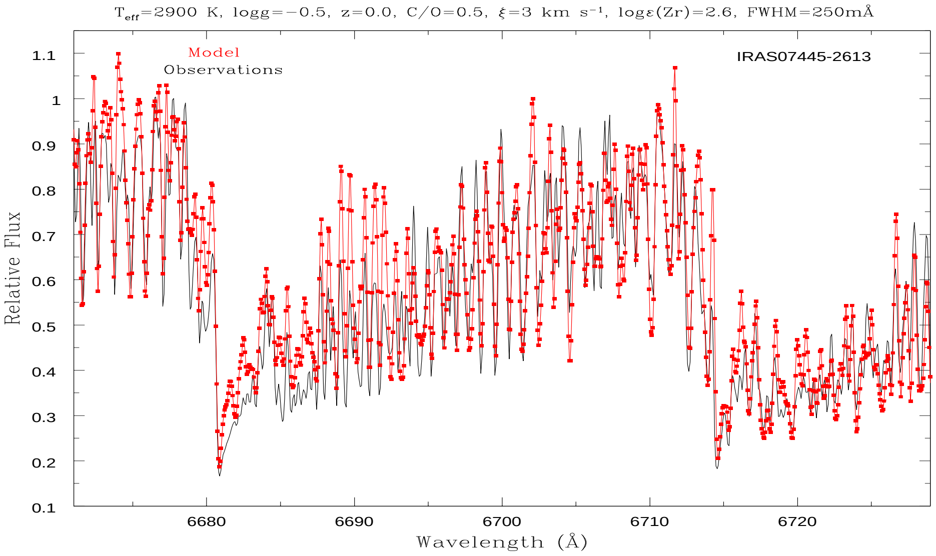

FIGURE B.7—

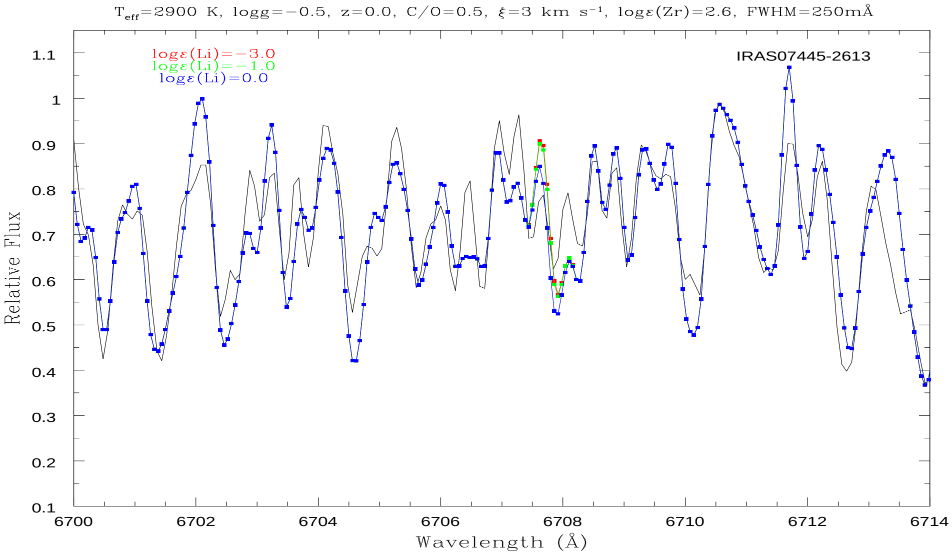

FIGURE B.8—

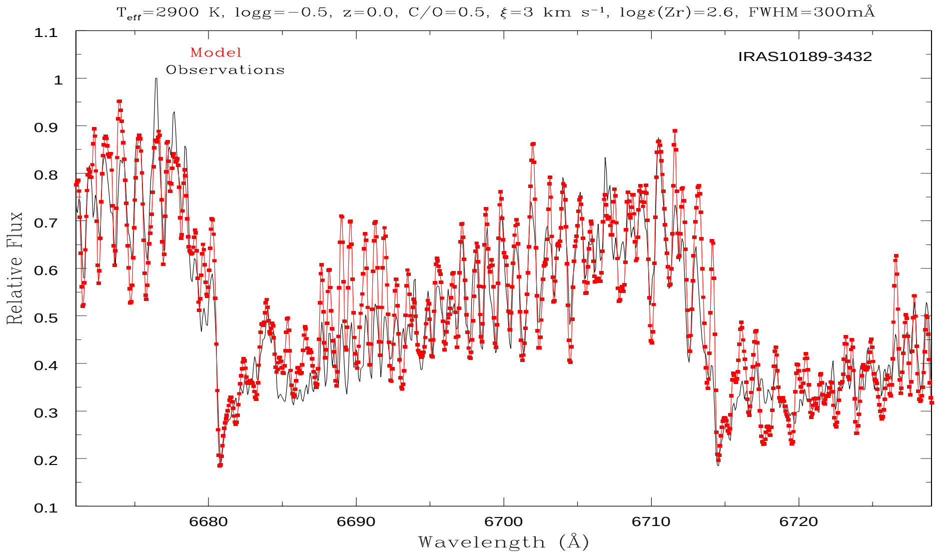

Figure B.9—

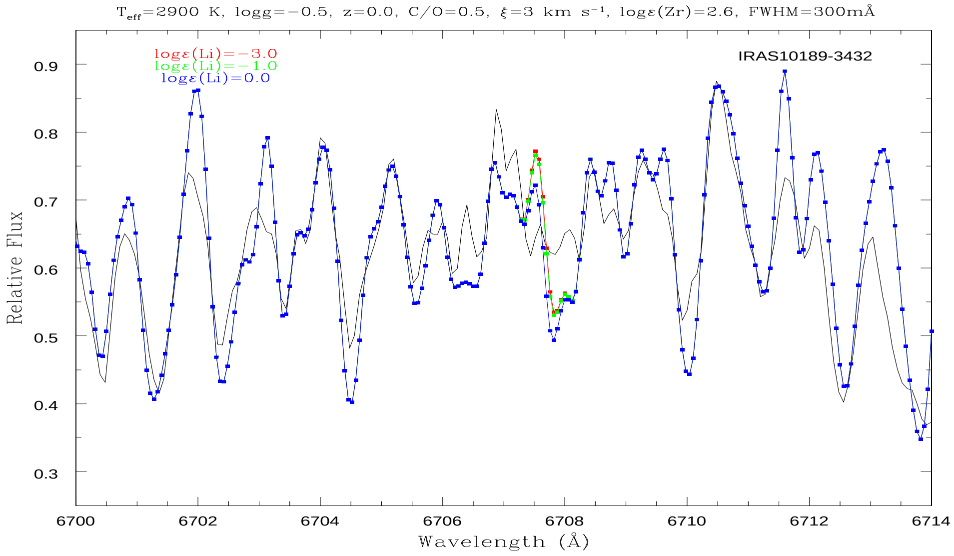

Figure B.10—

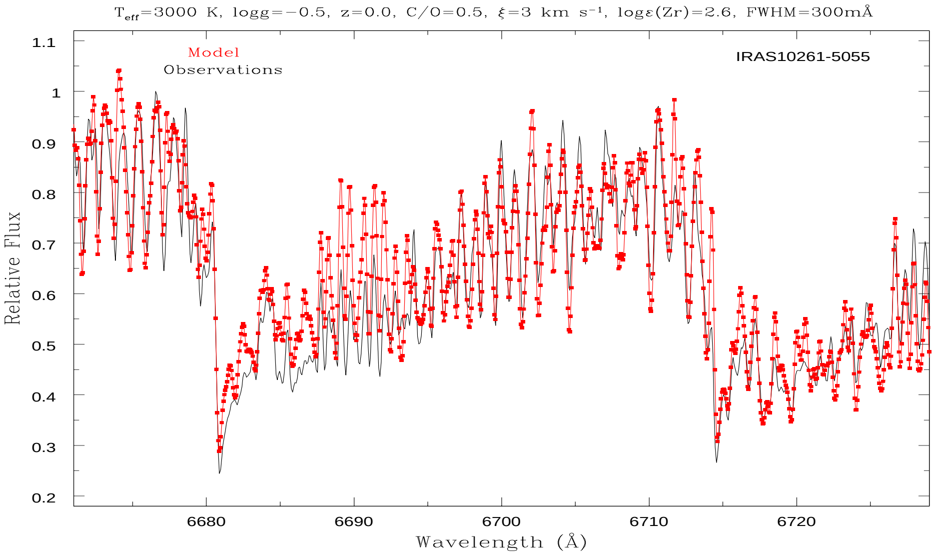

FIGURE B.11—

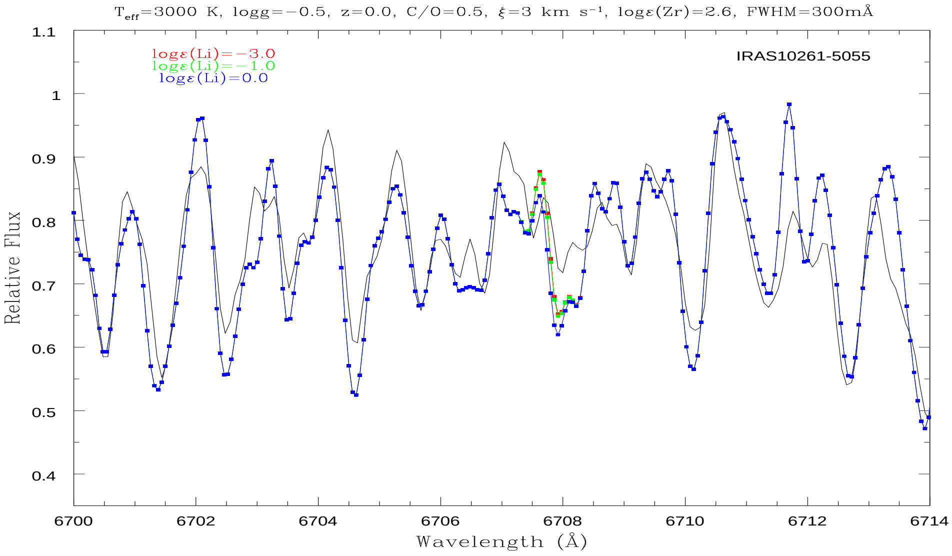

FIGURE B.12—

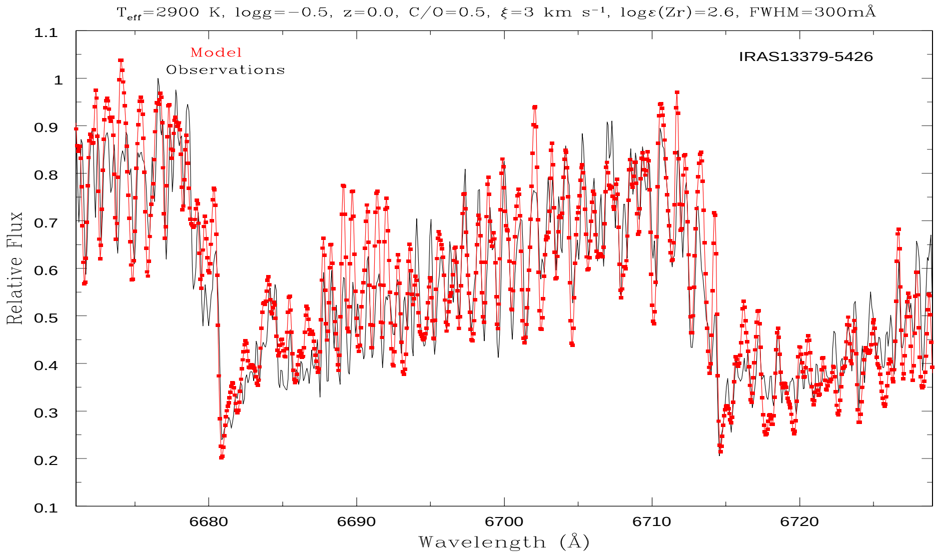

FIGURE B.13—

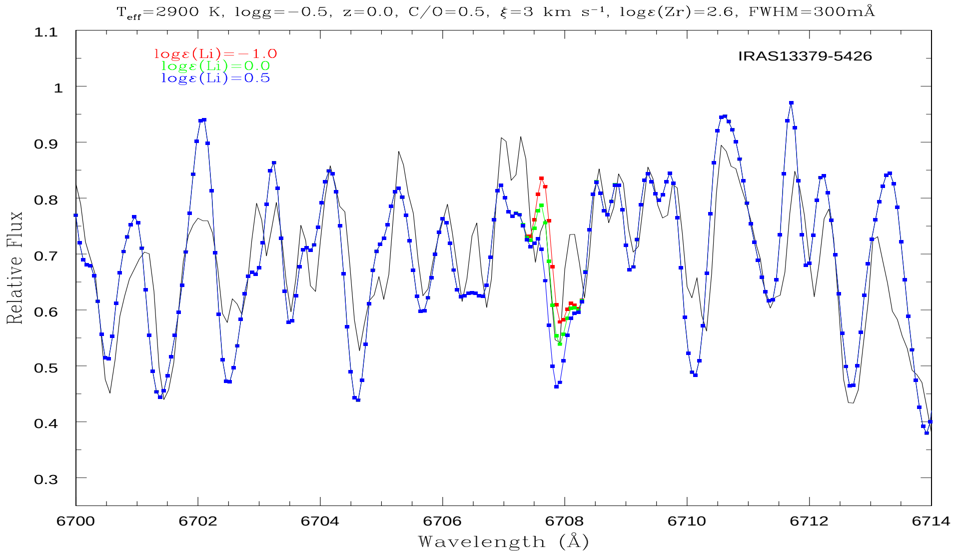

FIGURE B.14—

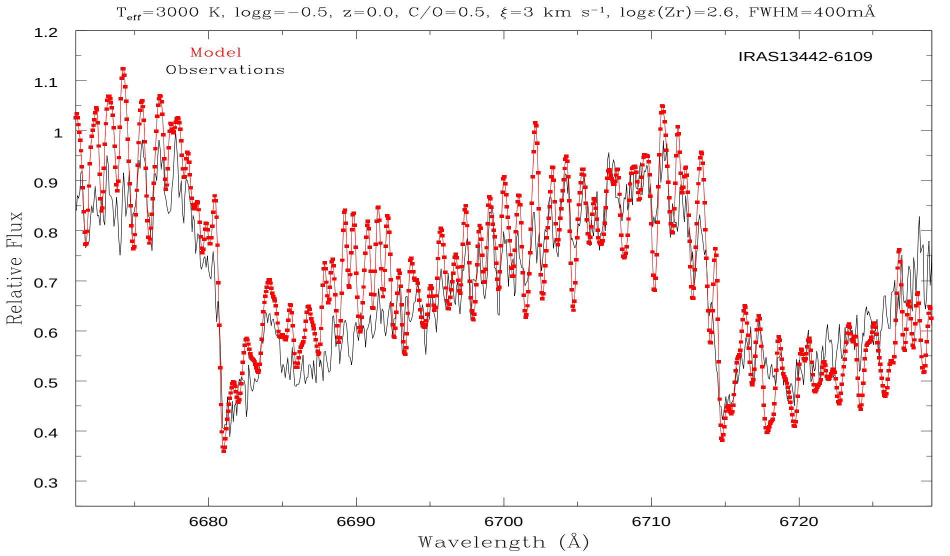

FIGURE B.15—

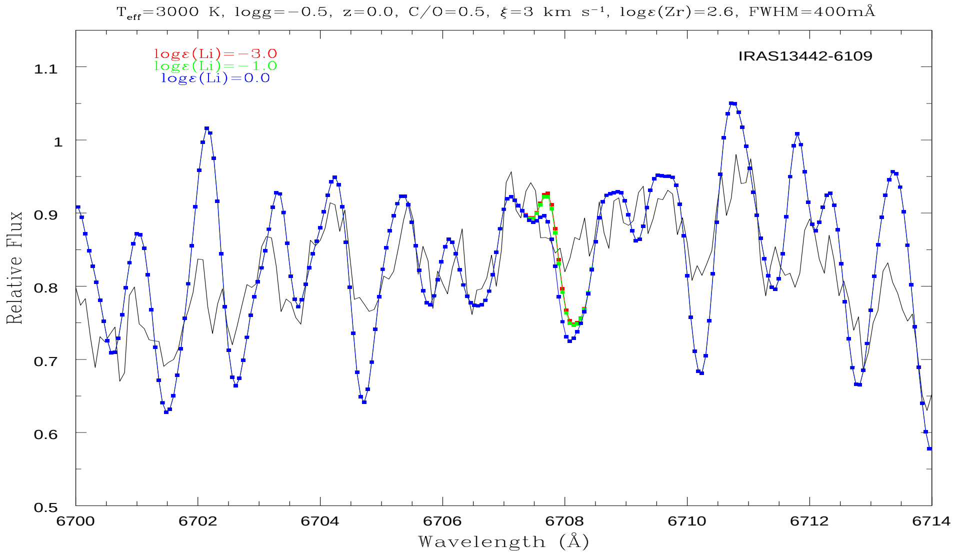

FIGURE B.16—

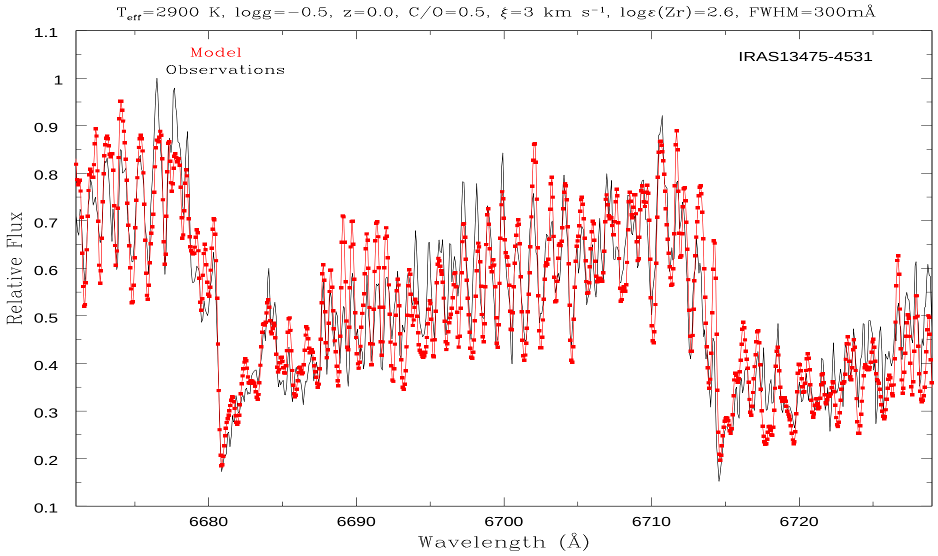

FIGURE B.17—

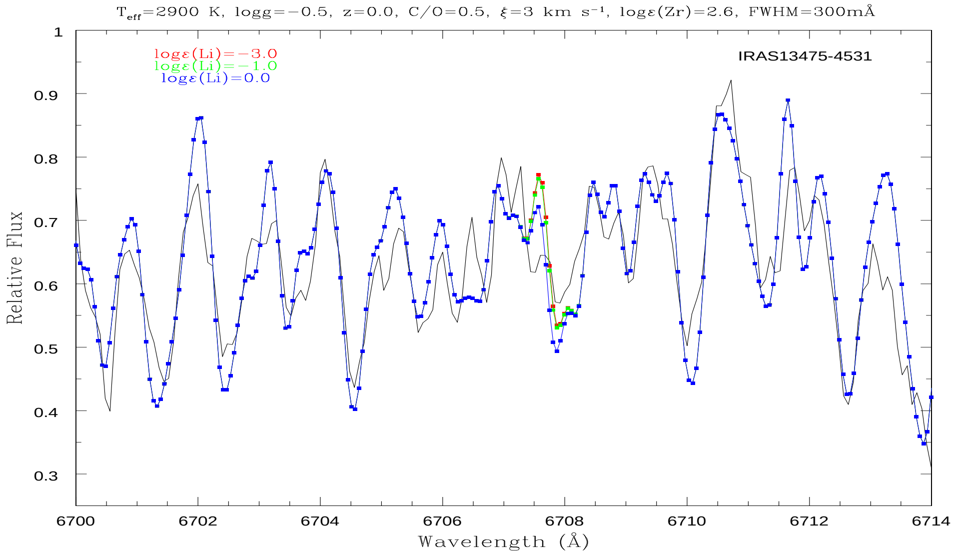

FIGURE B.18—

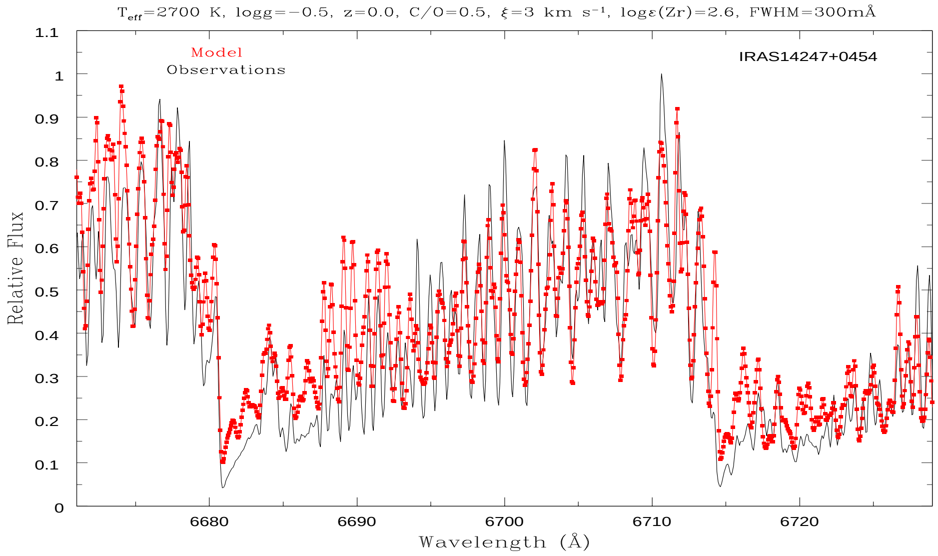

Figure B.19—

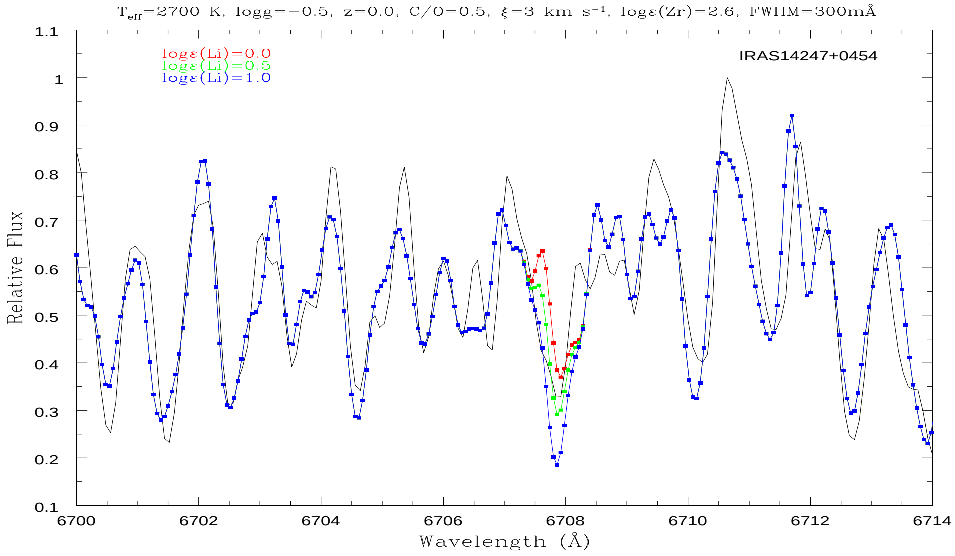

Figure B.20—

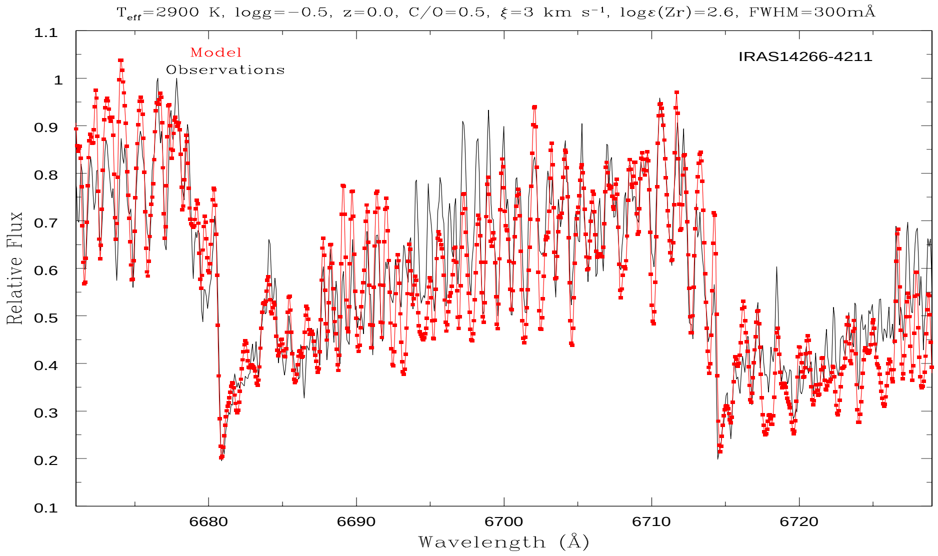

FIGURE B.21—

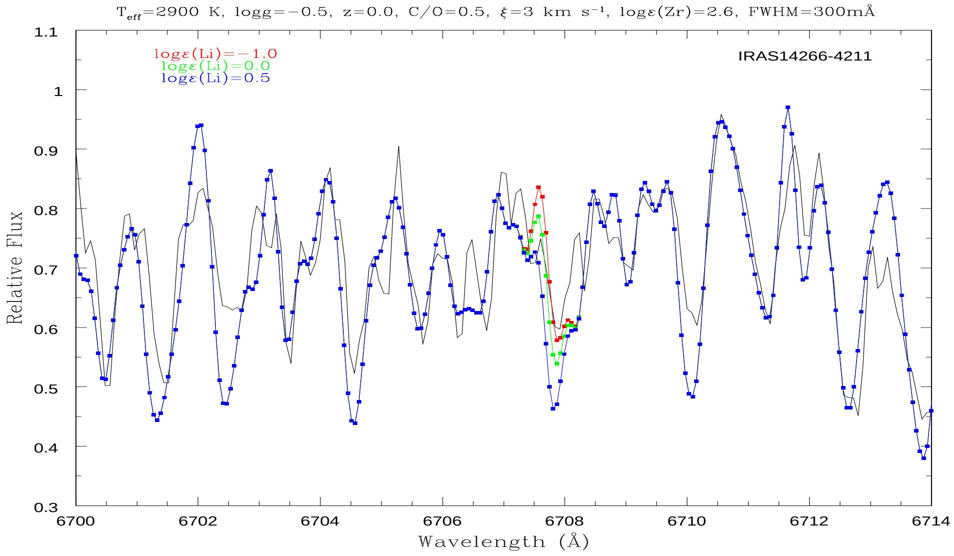

FIGURE B.22—

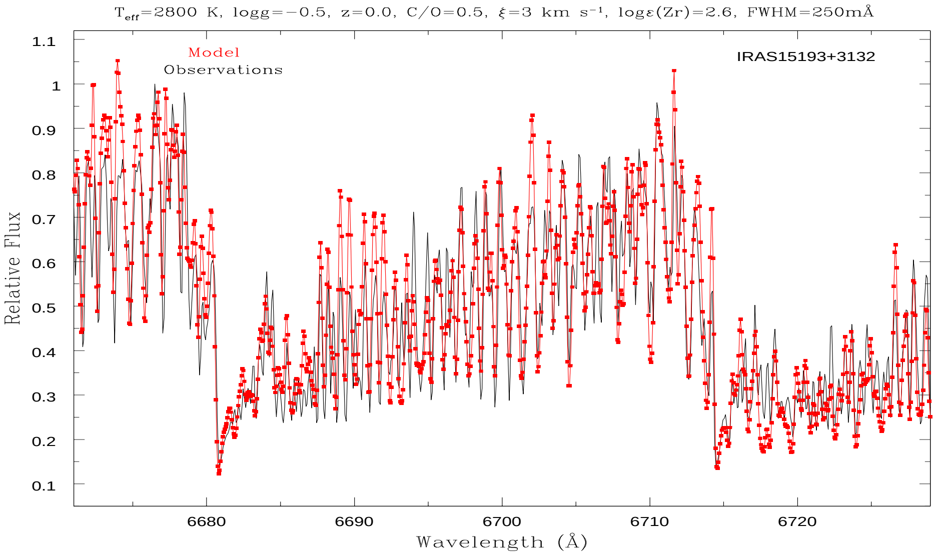

FIGURE B.23—

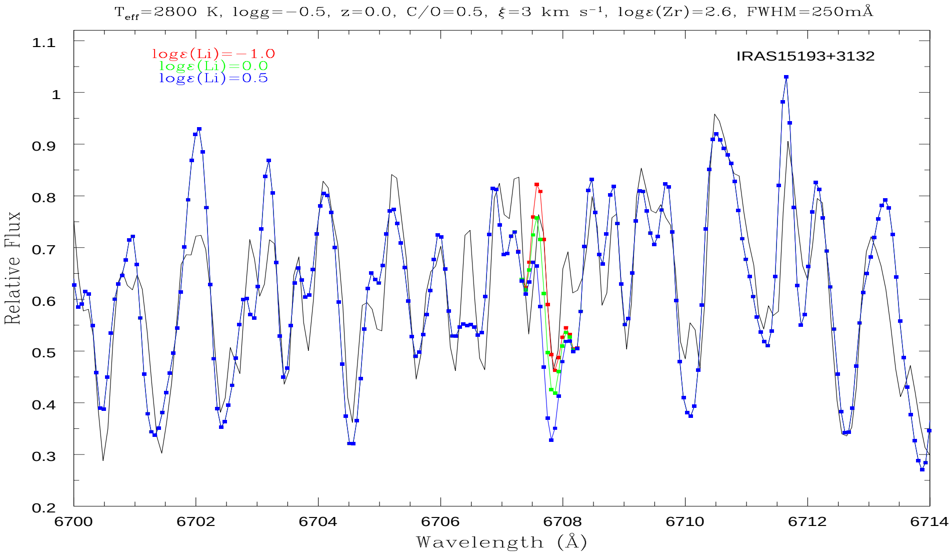

FIGURE B.24—

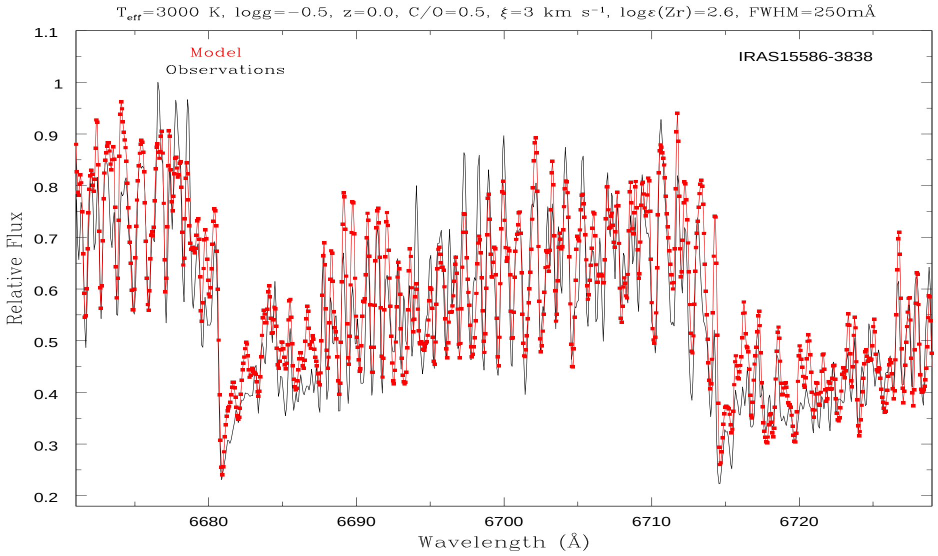

Figure B.25—

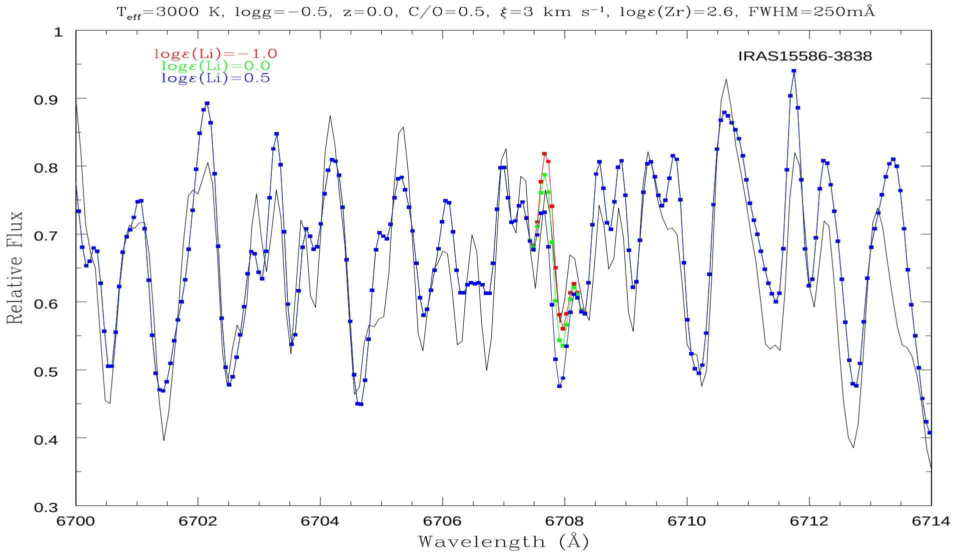

Figure B.26—

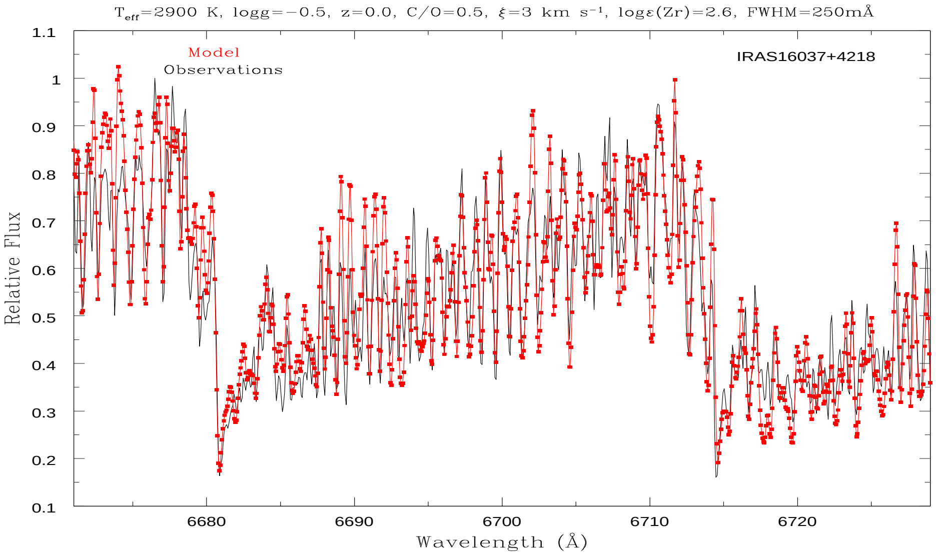

FIGURE B.27—

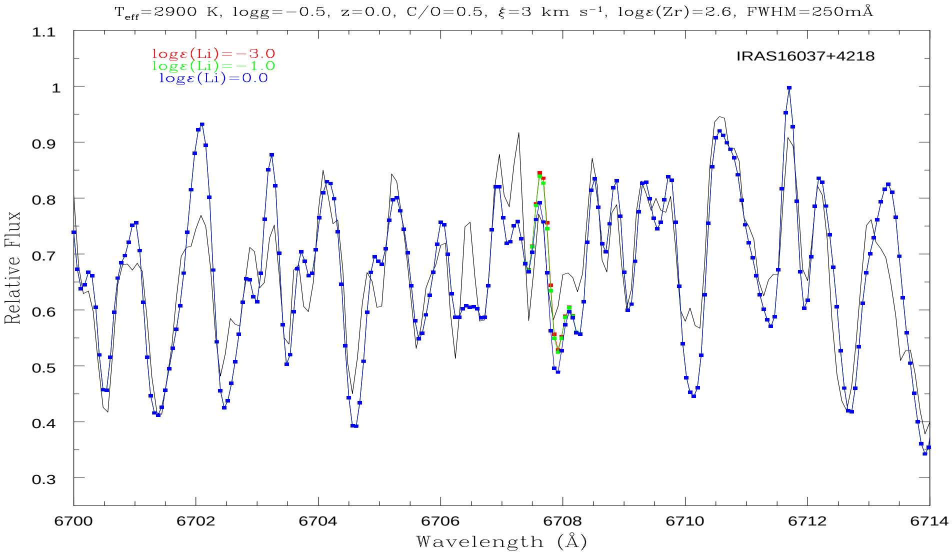

FIGURE B.28—

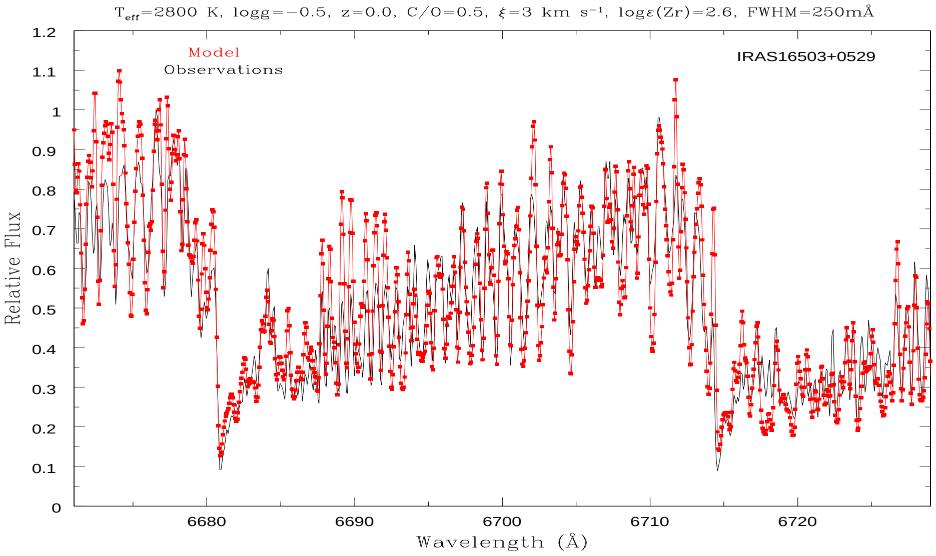

FIGURE B.29—

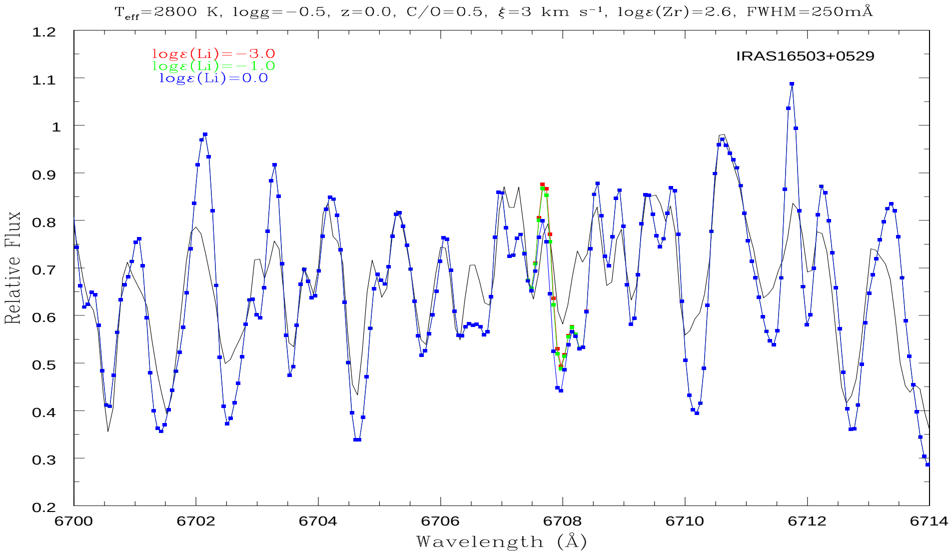

FIGURE B.30—

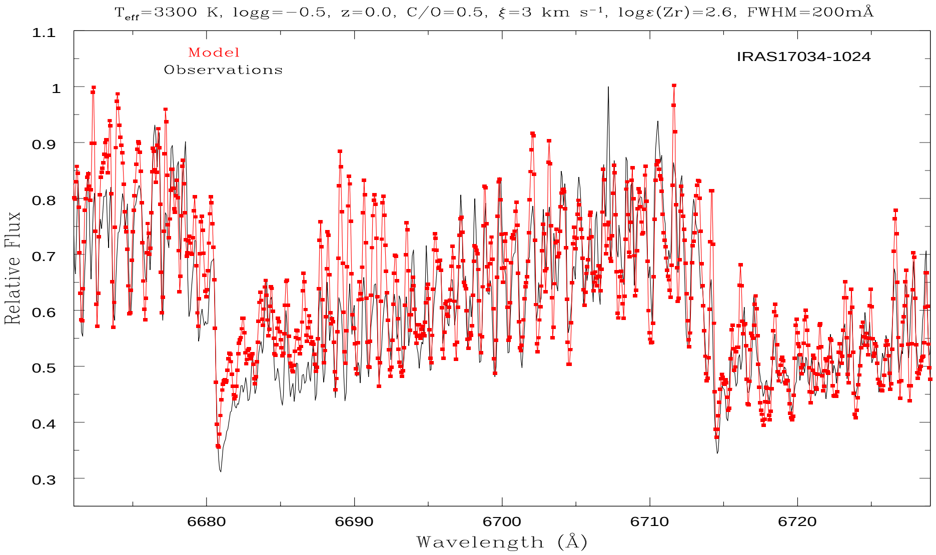

FIGURE B.31—

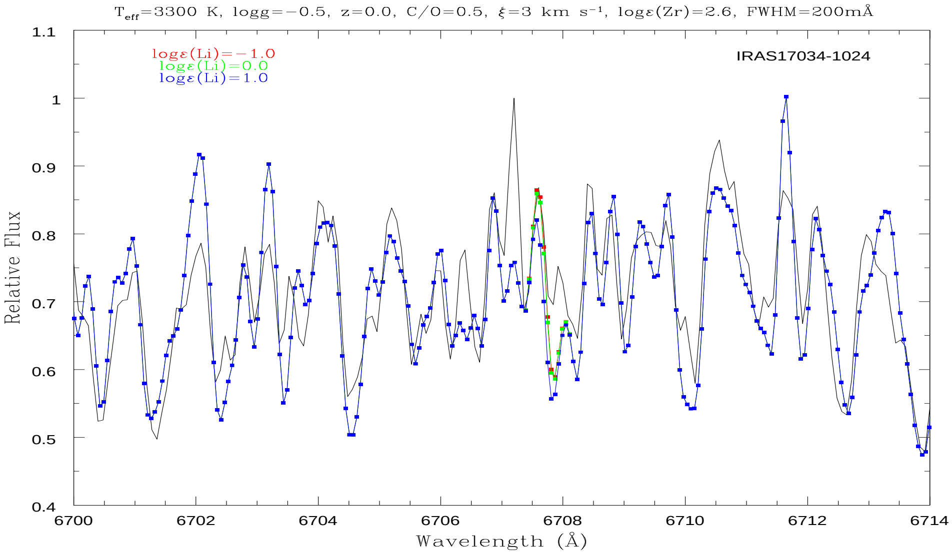

FIGURE B.32—

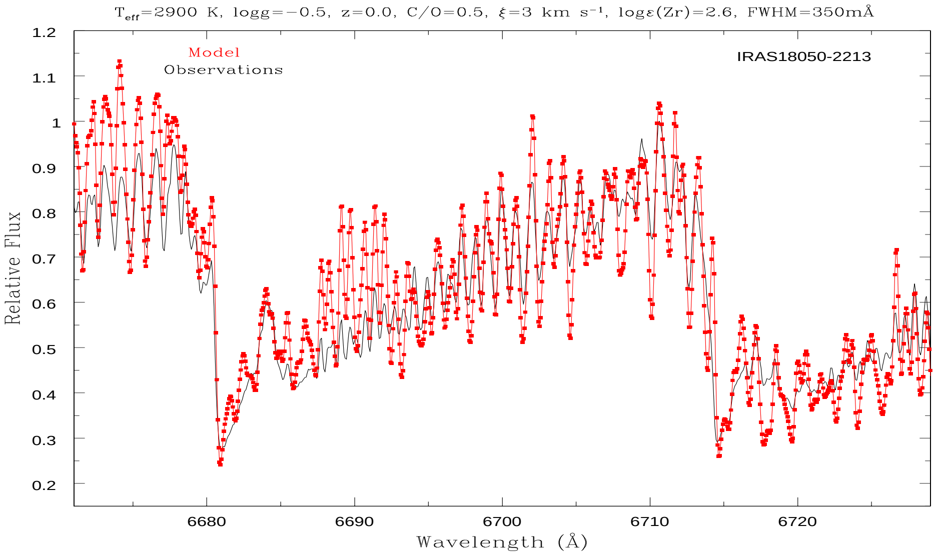

FIGURE B.33—

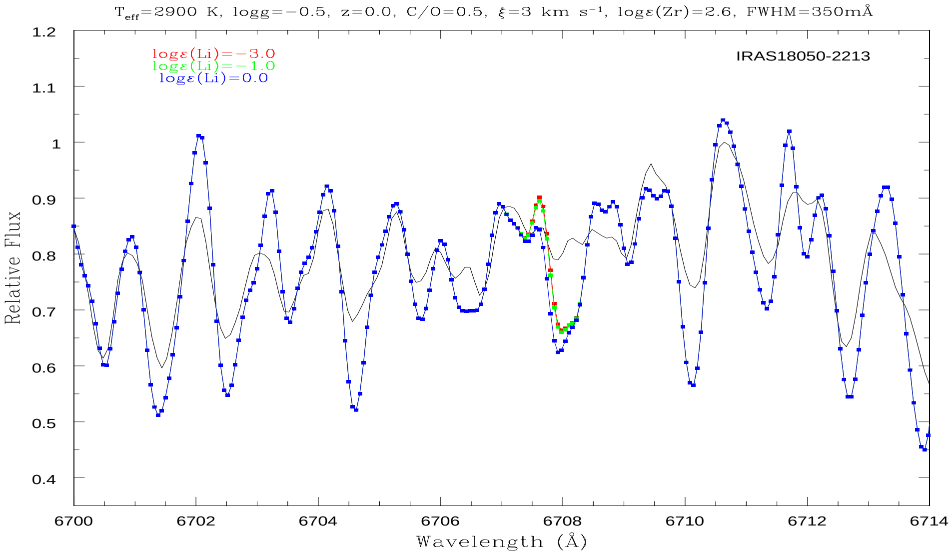

FIGURE B.34—

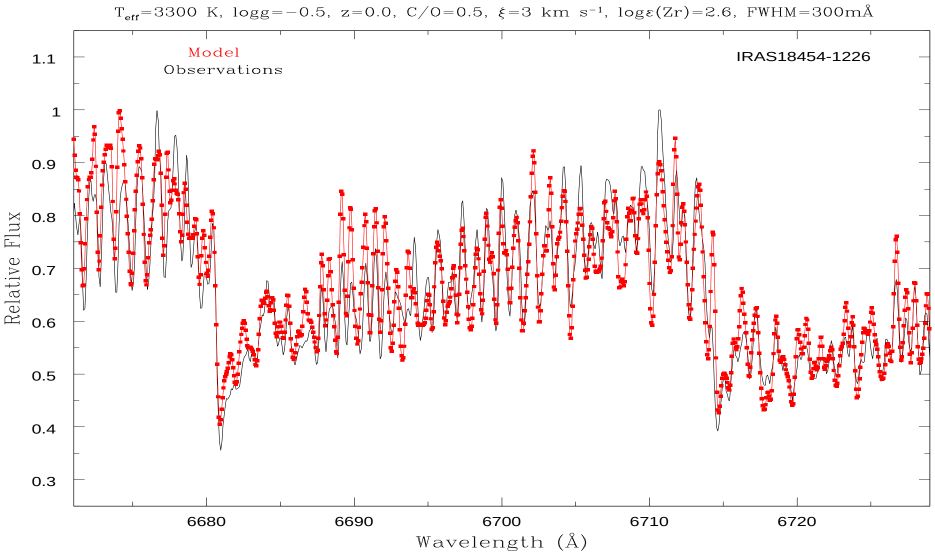

FIGURE B.35—

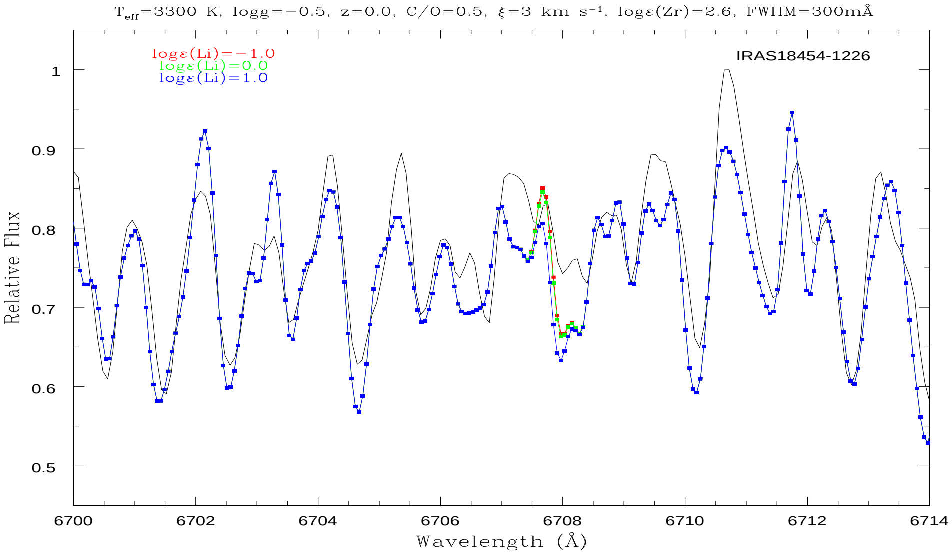

FIGURE B.36—

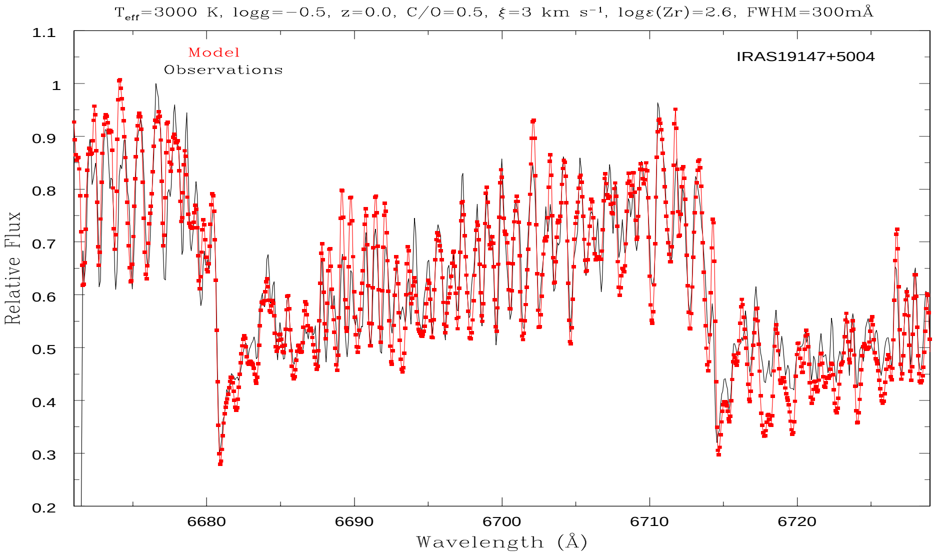

FIGURE B.37—

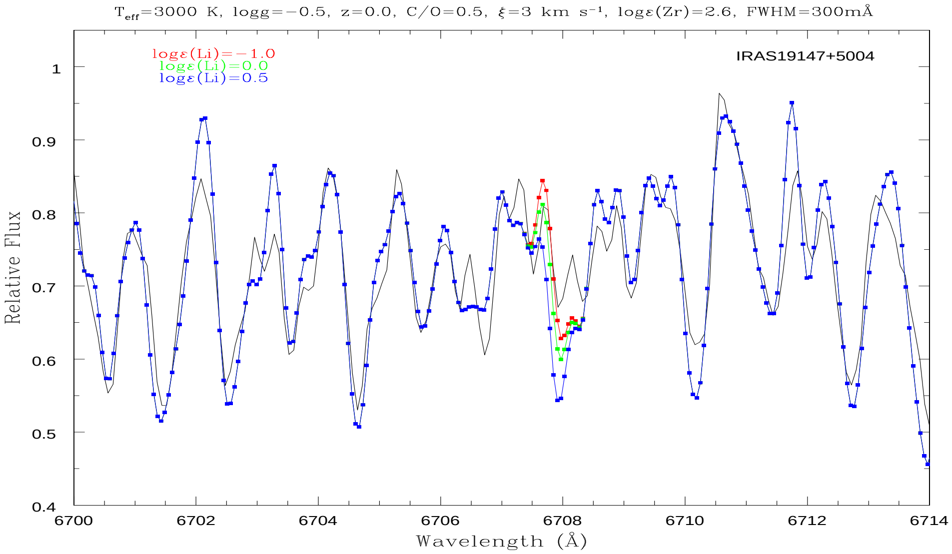

FIGURE B.38—

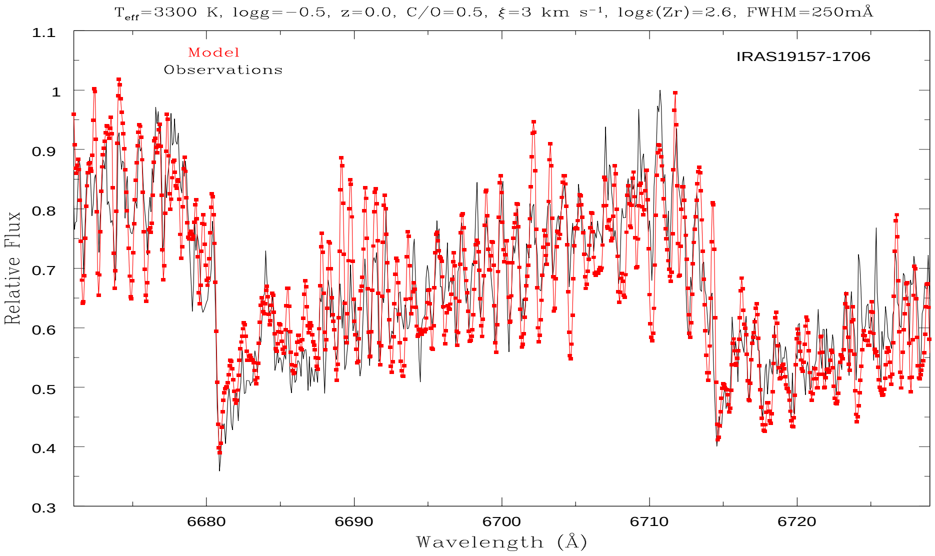

FIGURE B.39—

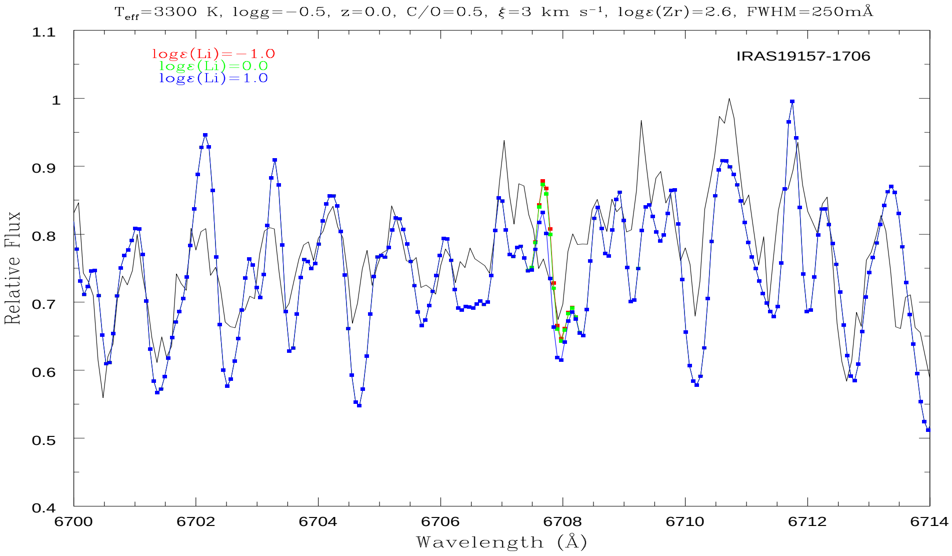

FIGURE B.40—

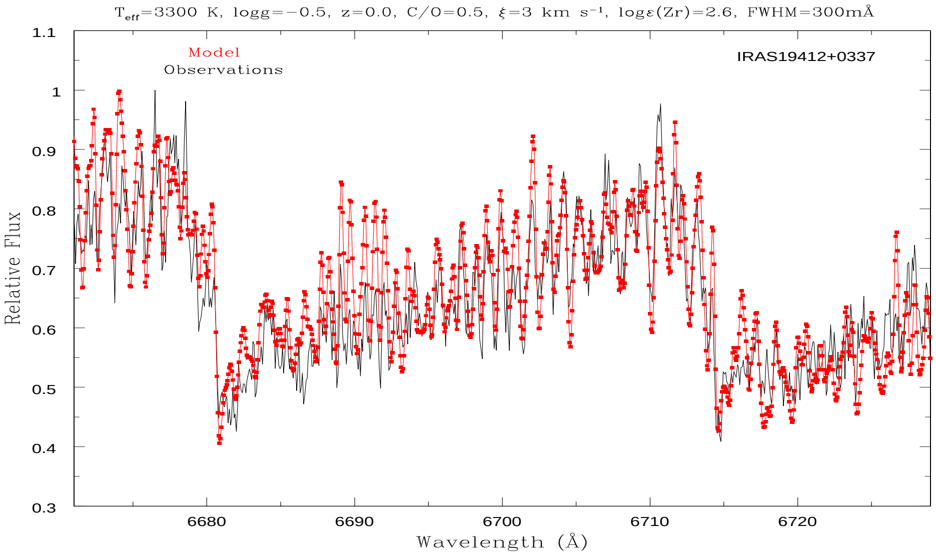

Figure B.41—

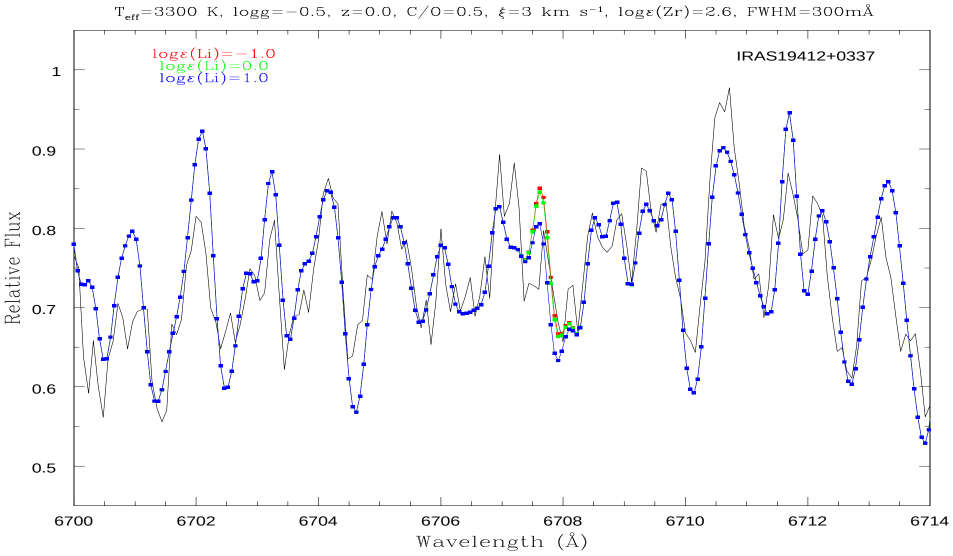

Figure B.42—

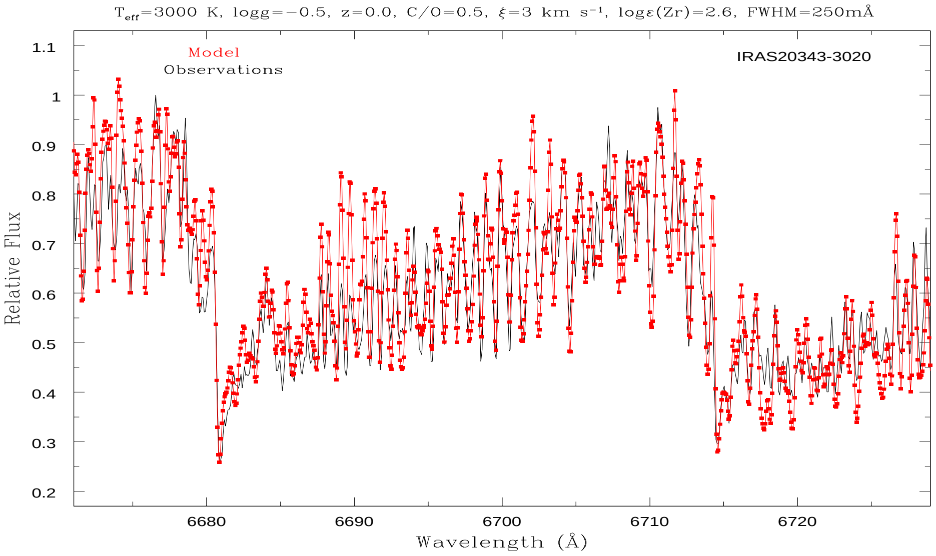

FIGURE B.43—

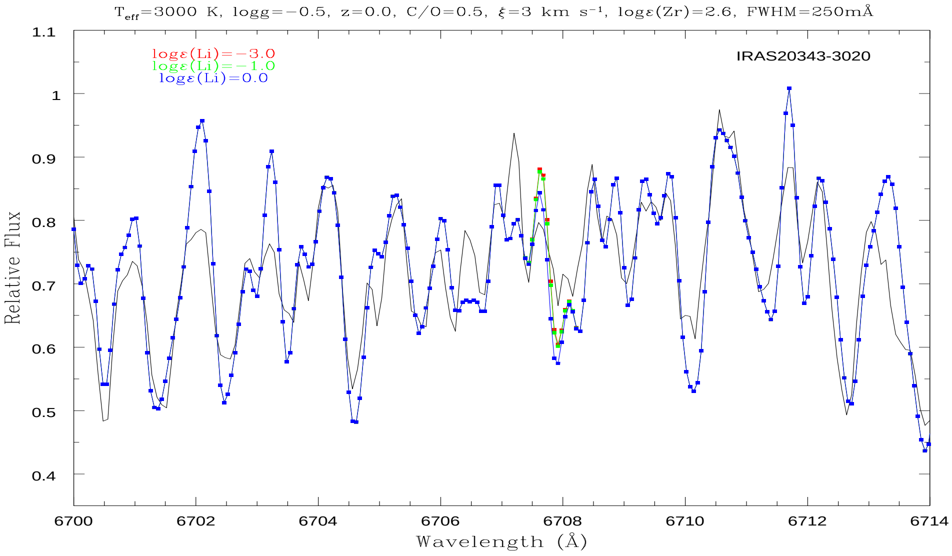

FIGURE B.44—

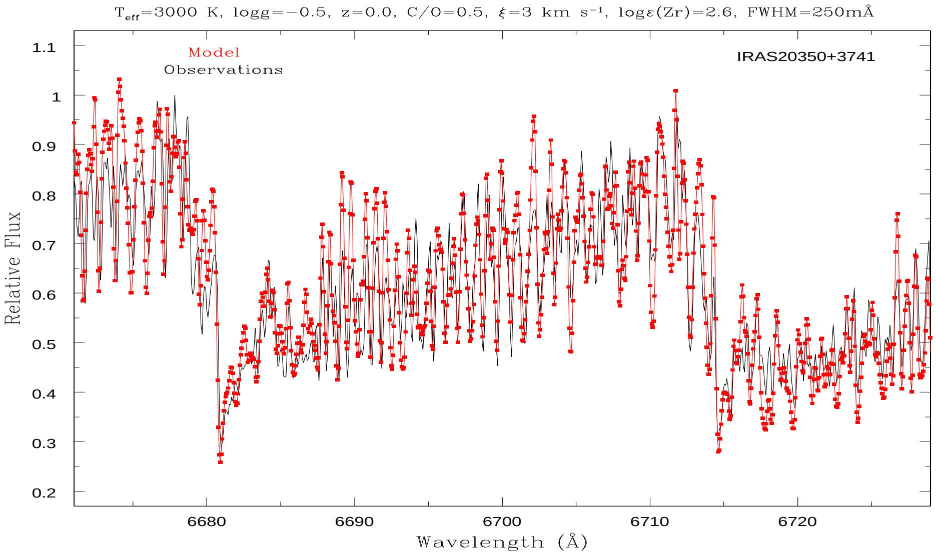

FIGURE B.45—

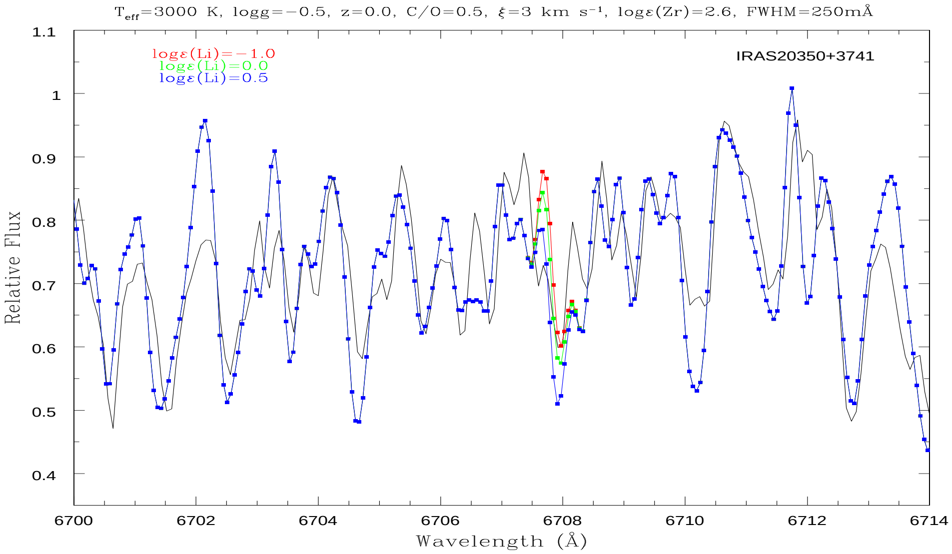

FIGURE B.46—

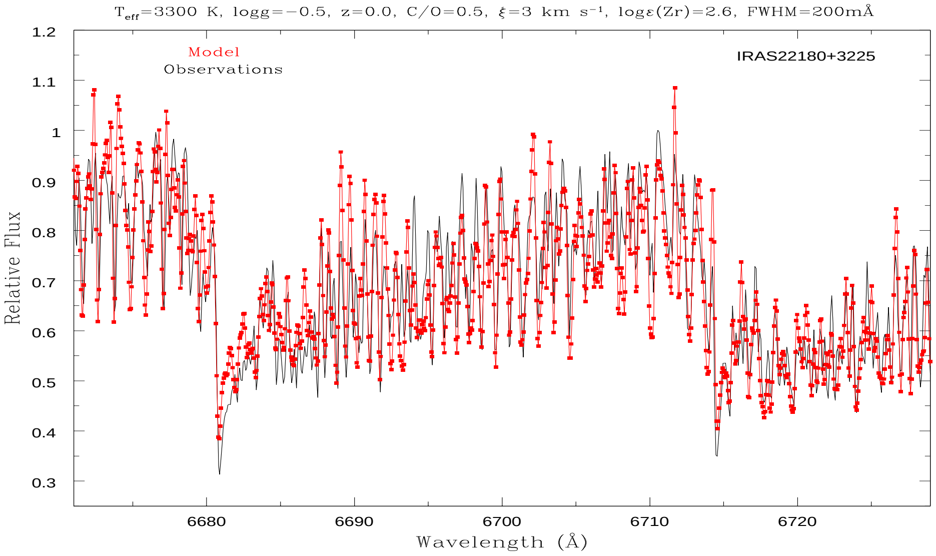

FIGURE B.47—

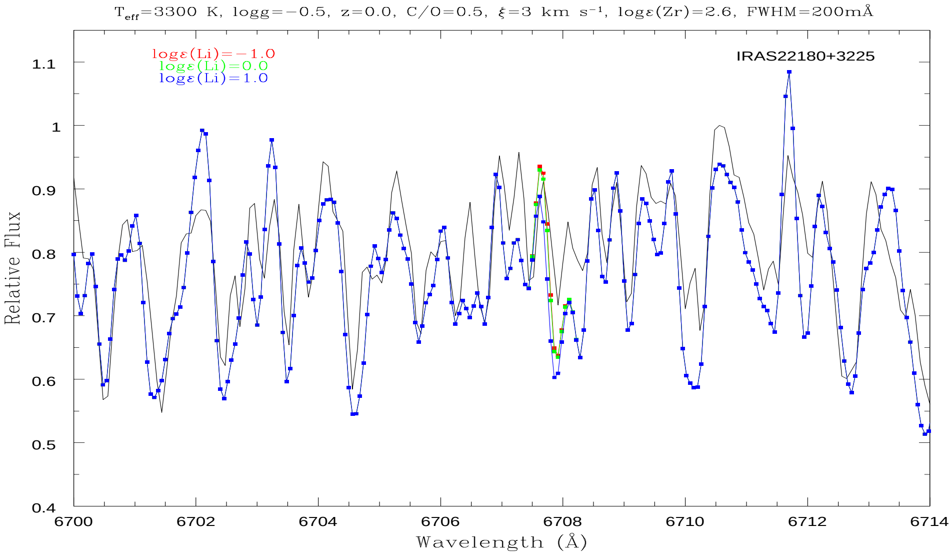

FIGURE B.48—

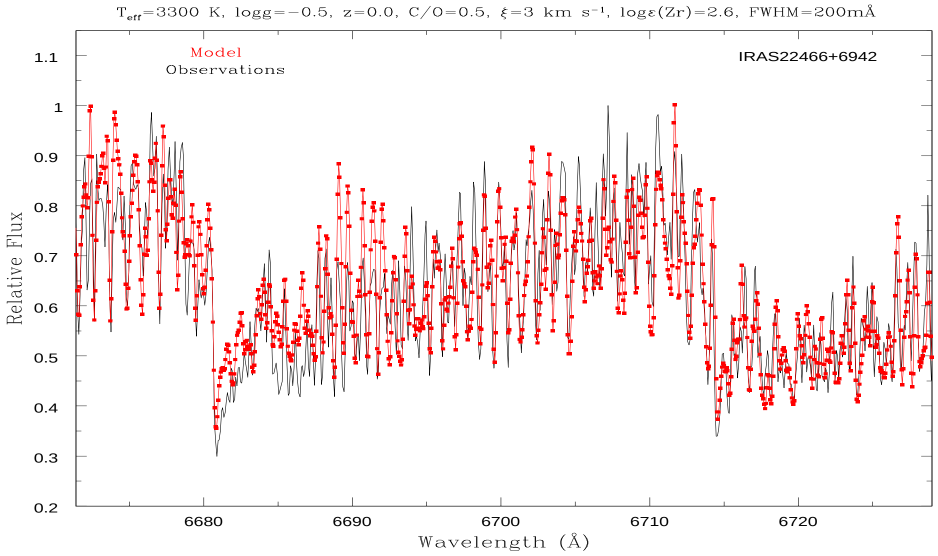

FIGURE B.49—

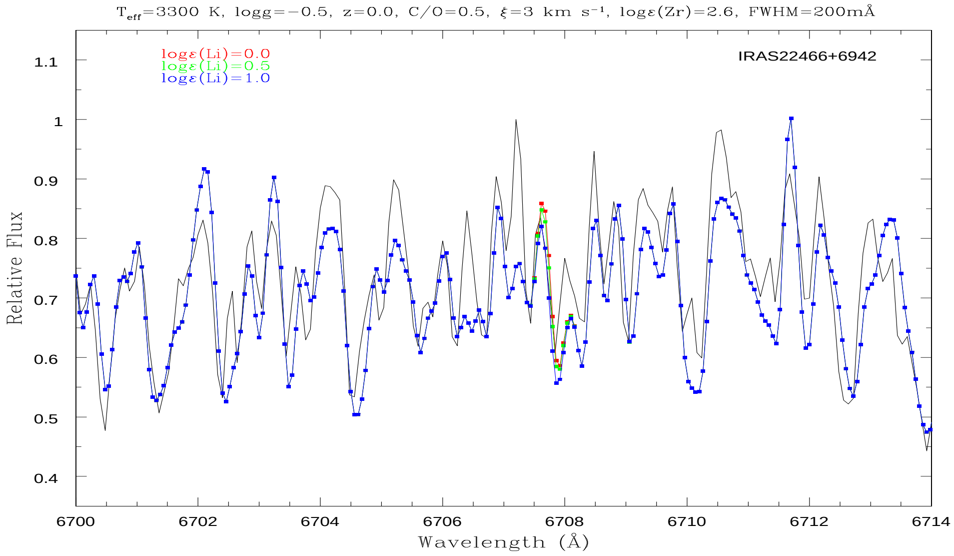

FIGURE B.50—

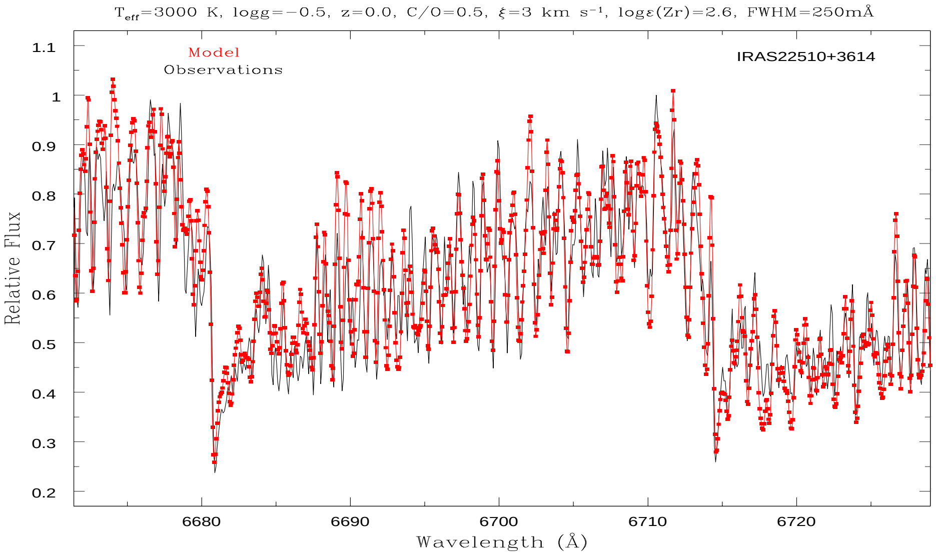

FIGURE B.51—

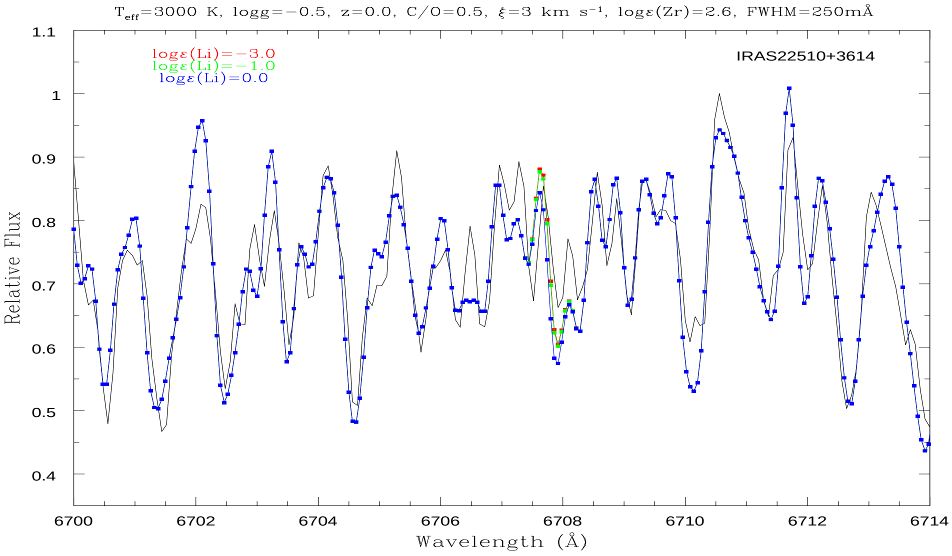

FIGURE B.52—

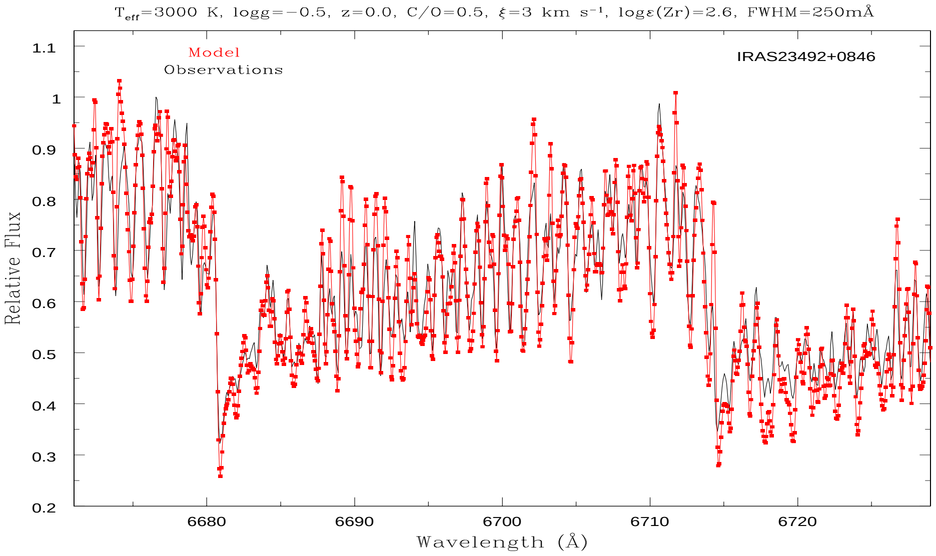

FIGURE B.53—

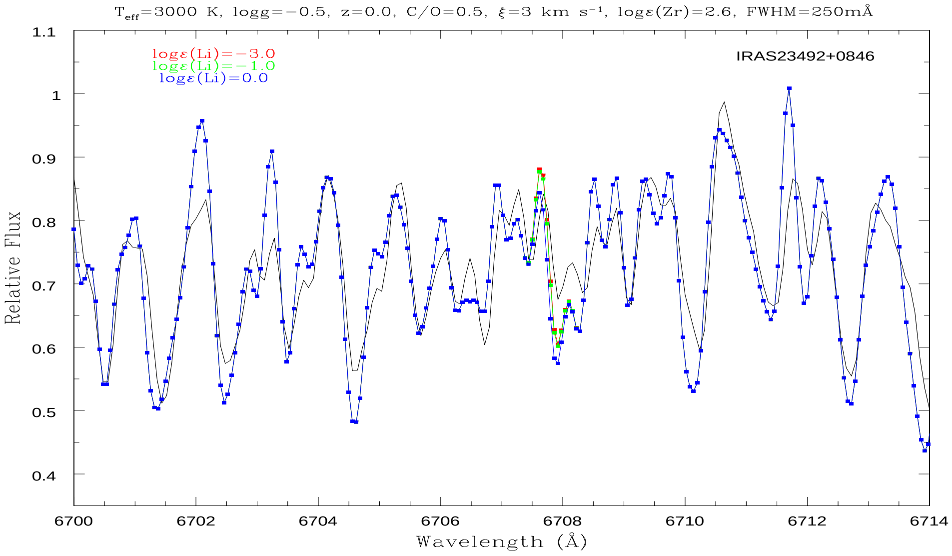

FIGURE B.54—